Optomechatronics Design and Control for Confocal Laser Scanning Microscopy

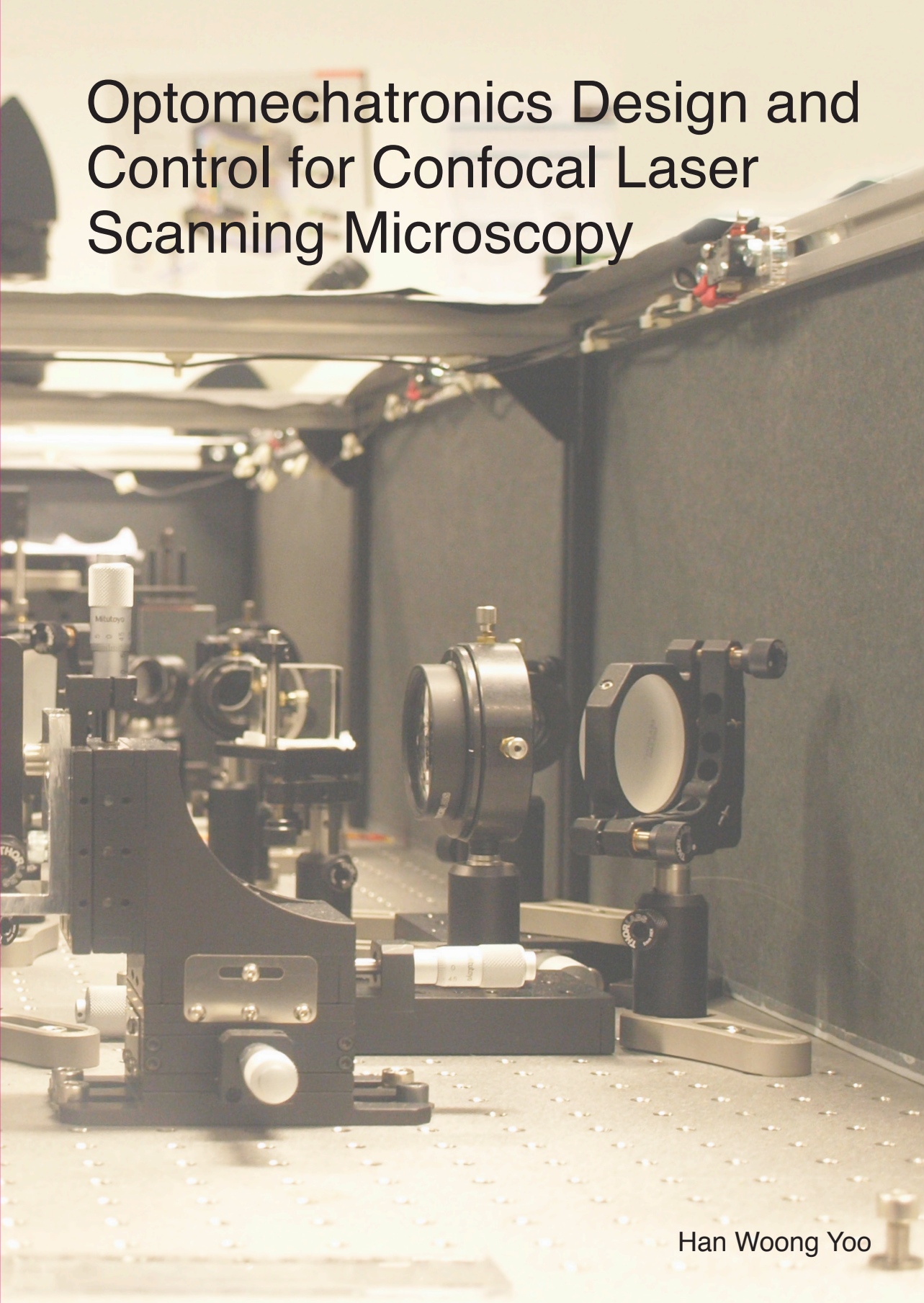

Han Woong Yoo

Optomechatronics Design and Control for Confocal Laser Scanning Microscopy

Han Woong Yoo

Cover: Developed experimental setup for Leica SP5 confocal laser scanning microscope,
Cover design: Jaehee Lee.

Optomechatronics Design and Control for Confocal Laser Scanning Microscopy

Proefschrift

ter verkrijging van de graad van doctor
aan de Technische Universiteit Delft,
op gezag van de Rector Magnificus prof.ir. K.C.A.M. Luyben,
voorzitter van het College van Promoties,
in het openbaar te verdedigen op

maandag 30 maart 2015 om 10:00 uur

Door

Han Woong YOO,

Master of Science in Electrical Engineering and Computer Science,
Seoul National University, Seoul, Zuid-Korea.
geboren te Seoul, Zuid-Korea.

Dit proefschrift is goedgekeurd door de promotoren:

Prof.dr.ir. M. Verhaegen
Univ.Prof.Dr.sc.techn. G. Schitter

Samenstelling promotiecommissie:

Rector Magnificus	voorzitter
Prof.dr.ir. M. Verhaegen	Technische Universiteit Delft, promotor
Univ.Prof.Dr.sc.techn. G. Schitter	Vienna University of Technology, promotor

Onafhankelijke leden:

Prof.dr.ir. G. V. Vdovin	Technische Universiteit Delft
Prof. A. B. Houtsmuller	Erasmus University Medical Center
Prof.dr.ir. M. Steinbuch	Technische Universiteit Eindhoven
Prof.ir. R. H. Munnig Schmidt	Technische Universiteit Delft
Prof.dr. P. J. French	Technische Universiteit Delft (reservelid)

Enabling new technology

This research is supported by the Integrated Smart Microscopy project in the Smart Optics Systems program of Technologiestichting STW, the Netherlands and is partly supported by Ernst-Mach-Stipendien of the Austrian Agency for International Cooperation in Education & Research.

Published and distributed by: Han Woong Yoo
E-mail: kohito80@gmail.com

ISBN: 978-94-6203-812-7

Keywords: Confocal Laser Scanning Microscopy, Iterative Learning Control, Galvanometer Scanner, Coverslip Correction Collar, Adaptive Optics, Confocal Wavefront Sensing.

Printed by CPI-Koninklijke Wöhrmann B.V., Zutphen, The Netherlands.

일기일회(一期一會),
단 한 번의 기회, 단 한 번의 만남.
이 고마움을 세상과 나누기 위해
우리는 지금 이렇게 살아가고 있다.

법정 (法頂, 1932-2010)

Ichi-go ichi-e,
fated meeting that occurs in your lifetime.
We live now as we are
for sharing this gratitude of life with you.

Bopjong (1932-2010)

Acknowledgements

This thesis introduces some researches on optomechatronics design and control research for the confocal laser scanning microscopy, mainly conducted in Delft Center for Systems and Control (DCSC) of Delft University of Technology and also partly in Automation and Control Institute (ACIN) of Vienna University of Technology. I owe thanks to many people who supported and encouraged me during my PhD study and inevitably led to the completion of this thesis.

First of all, I would like to thank my promoters, Prof. Michel Verhaegen and Prof. Georg Schitter, for providing me with the opportunity, support, and encouragement to finalize this PhD project. For the development of the system they were always good partners for discussing issues in detail, bringing me new insight, and supporting the implementation and evaluation. Moreover, they were open to being good friends and supporting me in personal matters when I was having difficulties outside of work. It was my pleasure to work with them for 4 years and I believe this work could eventually meet its end with this thesis owing to their support.

I would like to thank Martin van Royen for the discussions and support of experiments with biological specimens. All protocols for the specimen preparation were designed by him, which resulted in nice figures in the thesis. I also thank Gert van Cappellen, Prof. Adriaan Houtsmuller, Ihor Smal, and Erik Meijering for sharing problems in biological imaging and bringing ideas for the research. I would like to thank Darko Simonovic for his participation on the development of adaptive optics systems with his expertise on physics.

I also appreciate supports from industrial partners of Integrated Smart Microscopy (ISM) project. I would like to thank Tanjef Szellas, Andrea Pfeifer, Frank Houdijk, Henk den Hartog, Barry Selles, Frank Sieckmann in Leica Microsystems in Mannheim and the Netherlands for providing a confocal laser scanning microscope, allowing us to modifying it for our research, and supporting with interfaces and customized detectors. I also would like to thank to Prof. Gleb Vdovin, Mikhail Loktev, and Oleg Soloviev in Flexible Optical B.V. for the discussions and help for designing imaging system and adaptive optics.

During the project, I have met many colleagues, sharing thoughts, ideas, and feelings. I am grateful to Jacopo Antonello for being with me in the dark optics lab most of time, sharing experience and knowledge on adaptive optics and microscopy. I also appreciate his colleague Tim van Werkhoven for the open discussions and advices on practical implementation of the adaptive optics system. I thank Patricio Torres, Arne Dankers, who started working at similar time in DCSC, for sharing lunches and dinners with precious stories. I also want to thank Stefan Kuiper for the discussions on the mechatronics design and analysis, pleasant drinks in Delft and Vienna, and the translation of the summary of this thesis. For the development of the lab, I have received crucial support from Ron van Puffelen, Will van Geest, Kee Slinkman, Rob Luttjeboer, Patrick van Holst, and Harry Jansen. I really

appreciate it. I would like to thank Kitty, Esther, Saskia, Marieke, and Olaf for their support on administrative issues during the time in DCSC and Delft. Furthermore, I would like to thank the members of my PhD committee for constructive comments to improve this thesis.

I want to thank Hong, Ruxandra, Elisabeth, Jeroem, Hans Verstraete, Alexandar, Tope, Visa, Zhe, Yu, Yihui, Noortje, Shu, Alfredo, Mohammadraza, Bart, Andrea, Arturo, Tamas, Alessandro, Gijs, Ilhan, Pieter, Hildo, Edwin, Ivo, Solomon, Mernout, Yue, Le, Jia, Marko, Ilya, Sadegh, and Yashar for being nice colleagues and friends with great memories during my stay in DCSC. While my staying in ACIN, I would like to thank Shingo, Markus, Rene, Dominik, Thomas, Ingo, Martin, Reinhard, Rudolf, and Jürgen for nice collaborations in work and mugs of beer and punsch we drank with a lot of pleasant moments.

I also appreciate all the support from my friends. I would like to thank Kiki and her family Anton, Betty, and Lee for their warm hospitality and sharing Dutch traditions e.g. Sinterklaas party and delicious homemade oliebollen. It was always great moments that I never forget. I want to thank Matijn Kalf for sharing his experience on computer engineering with me and translating the propositions. I am grateful to Hyeonsu Yang for a number of short trips together in the Netherlands, and provide me knowledge on the architecture and art history. I also thank Jae Wook Chung for playing sports: table tennis and basketball time-to-time, coming to me when I need urgent help, and being my paranimf during my defense.

I would like to thank friends in the Netherlands: Youngkwan Kim, EunHui Park, Eun-Seong Cho, Junwon Koo, Seil Kim, Hyoshin Jun, Xiaolin Chen, Xiaohui Zhang, Prof. Chirlmin Joo, Youngchul Chae, Minjae Kim, Chang Ho Yeo, Prof. Nam Seok Kim, BongJun Choi, Dukje Bang, Jungsoo Kim, Chajoong Kim, Hyoungsoo Kim, Hyung Jun Noh, Do Yun Kim, Myung-Jae Lee, Vitnarae Kang, Younggon Cho, Sang-Myung Park, Jason Hwang, KyungHo Choes, Jaewoo Lee, SeungKyu Ha, Joo Young Jung, JungKyoon Yoon, Byeong Jun Kim, Junhyeon Lee, Jooyoun Yoon, Dong Min Lee, Keonsoo Koh, Yae-jin Lee, Junwoo Lee, Gyeong Oh Chung, Tae Jin Lee, Hansol Moon and all other friends that I could not mention all here for sharing the happiest moments in the Netherlands. I also would like to thank Friends in Vienna: Hyungjin Park, Il Hong, and Siwoong Song for providing attentions in music and arts for me to recover from the deep slump, and Taesoo Jang and Jiho Cho for encouragement to finish PhD. I would like to thank Jaehee Lee for designing this nice cover of the thesis. I also thank friends in Korea: Wonyoung, Yoon, Rim, Changhyun, Junhee, Kibae, Yoonkyung, Mingu, Daejin, Soojung, and Byungchan for their encouragement. I also thank Euikyung in Japan for providing valuable comments about my PhD life.

I would like to thank Prof. Wook Hyun Kwon for providing me an opportunity to work in DCSC and valuable advices for my study and career when we met in ECC 2013. I also appreciate support of Junjin Kong and Prof. Ken Tomiyama, allowing me to leave the Netherlands for this new challenge. I am grateful to Prof. Soohee Han, Prof. Young Sam Lee, Prof. Bokyu Kwon, and all alumni of CISL for sharing their expertise and supporting my study abroad.

Last but not least, I want to thank my father, mother, and brother for their unconditional love and support to me. Without them, I could not imagine finishing my work as successfully.

Han Woong Yoo,
Vienna, March 2015.

Contents

Chapter 1

Introduction

1.1 Confocal Laser Scanning Microscopy

Confocal laser scanning microscopy (CLSM) is considered as one of the major advancement in microscopy in the last century as the first high resolution technique with optical sectioning ability [1, 2]. Confocal microscopy is the standard reference of microscopy with sectioning ability when new methods are developed such as two photon excitation microscopy [3], second harmonic generation microscopy [4], structured illumination microscopy [5], and stimulus emission depletion microscopy [6]. With its high resolution and 3D imaging ability and with the developments of various fluorescence marking techniques, confocal laser scanning fluorescence microscopy is getting popular in biology research groups as an essential tool for research.

The basic principle of confocal microscopy studied by Luckosz [7], showing that a higher resolution than the classical limit of wide-field microscopy can be obtained by sacrificing the field of view. This leads to two types of improved microscopy, one is placing a pinhole close by the specimen, called near-field scanning optical microscopy (NSOM, also refer to SNOM) [8], and placing the pinhole at the light source and at the imaging plane, called confocal microscopy [9]. In confocal microscopy, only one point in the specimen is illuminated and only light at the focus can pass through the conjugated pinhole, rejecting the light from outside of the focus volume. The term of "confocal" is originated from this structure since both the illumination (excitation) and the detection (emission) light is focused on the same point of the object [10].

Fig. 1.1 shows a simplified optical path of confocal laser scanning fluorescence microscopy. Due to practical reason, CLSM is often designed with epi-illumination type, sharing most optics including an objective and scanners for both illumination and detection path. The image of the illumination spot, made by the illumination pinhole, is focused on the object and illuminates the focus volume, then the specimen generates the fluorescence. The fluorescence is collected by the same objective, separated by the dichroic mirror and the filter system based on Stokes shift. Then the filtered fluorescence is focused on the detection pinhole and the fluorescence in the tight small volume is imaged. The scanning mirror moves the illumination and detection point on the specimen, which allows an image of a given range of the specimen. Fig. 1.2 summarizes the main components with the light

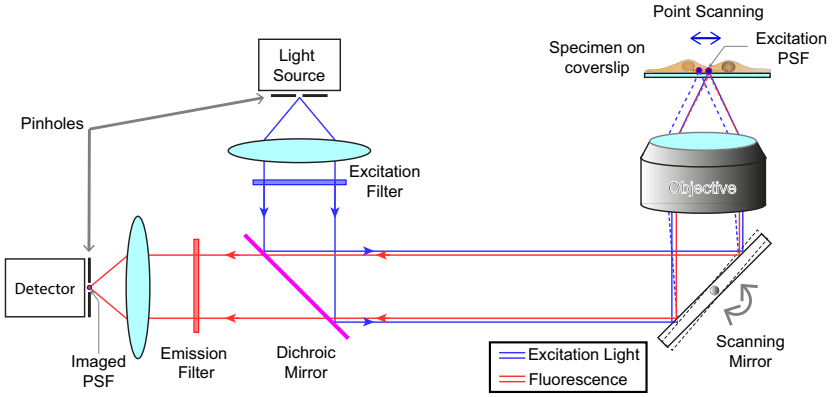

Figure 1.1: The optical path of the confocal laser scanning microscope, epi-illumination type. The optical path is separated into illumination (excitation, blue solid line) path and detection (emission, solid red) path. The excitation beam after the pinhole is focused on the specimen, illuminates a point of the specimen, and generates fluorescence in a small area near by focus. The fluorescence light is imaged on the pinhole is only in-focus light is detects the image. Scanning mirrors moves this focus through the specimen and allows to generate an image of fluorescence of the specimen. For the separation of the excitation beam and fluorescence, a dichroic mirror with both excitation and emission filter is used using Stokes shift.

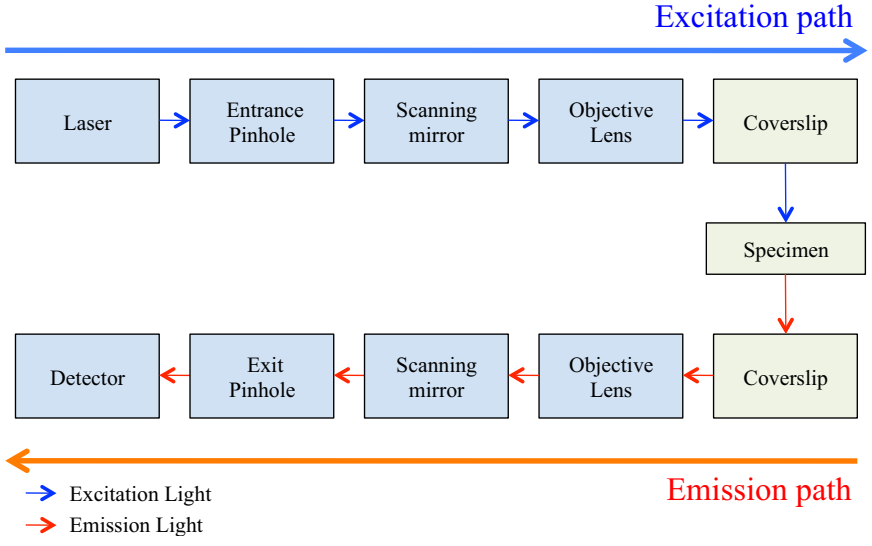

Figure 1.2: Block diagram of the confocal laser scanning fluorescence microscope

path as a block diagram.

1.1.1 Scanning Point by Point for Image

Because confocal microscopy only illuminates a point at once, the point-by-point scanner is a crucial component to complete an image by measuring multiple points of the specimen. Since high speed imaging enables for confocal miscopy to capture rapid biological phenomena such as cardiac cycles of the mouse [11], the development of scanning systems pursue higher speed of scanning as well as keeping the flexibility in scanning such as zoom of the imaging range and arbitrary random scanning [12].

The first suggestion of scanning system in the Minsky's patent was sample scanning [9]. In the patent, he insists sample scanning is beneficial because it can record a wide area of specimen regardless the optics and simpler design of objective with a small field of view and less support of chromatic aberrations. The scanning speed is innately limited by the inertia of the stage and specimen. In addition, fast motion of specimen is usually not desirable in biological imaging due to mechanical damages of the soft biological specimen.

Another idea for scanning image system is moving the pinhole by spinning disk [13–15]. In principle of confocal microscopy point light source at the entrance pinhole is imaged onto specimen and the illumination point on specimen follows as the point light source moves. To generate movement of the point light source, a disk with perforated pinholes (called Nipkow disk) rotates with a given constant speed under a wide light source illuminating the disk. This method provides relatively fast scanning speed for video rates (30 frames/sec) [14] since the scanning speed can be fast by increasing the speed of the disk, which is not depending on the inertia of the disk. As drawback, this method suffers from less light transmission and the pinholes at the disk are fixed i.e. the system is inflexible in the range of imaging [1].

After laser is employed in confocal microscopy, laser beam scanning method is a popular way for confocal image [1, 16]. The idea is use two galvanometer scanning mirrors at the back focal plane to provide tip and tilt on the back focal plane of the objective, leading to the lateral shift of the point illumination on the specimen. This mechanism of confocal microscope is called confocal laser scanning microscope (CLSM), which is a representative name of confocal microscopy. Since this galvanometer scanner provides high precision and reasonable speed, this beam scanning methods was commercialized by microscope manufacturers and became popular in the market [1, 10, 12]. For high speed scanning over 1000 line/s, however, the inertia and dynamics of the scanner limits the scanning speed, results in distortions in the image [17].

1.1.2 Resolution, Point Spread Function, and Aberrations

Since the configuration of scan can define the pixel size (a voxel in 3D image case) of the image, the attainable resolution of confocal microscopy is theoretically bounded by the diffraction of the light [18]. The diffraction limit depends on the wavelength and numerical aperture (NA) and can be expressed as a point spread function (PSF), the spatial distribution of a point light source at 3D imaging region through the optical system [18]. For high spatial resolution, a small point spread function is desirable. To achieve high resolution, microscope manufacturers provide high NA objectives with high refractive index immersion

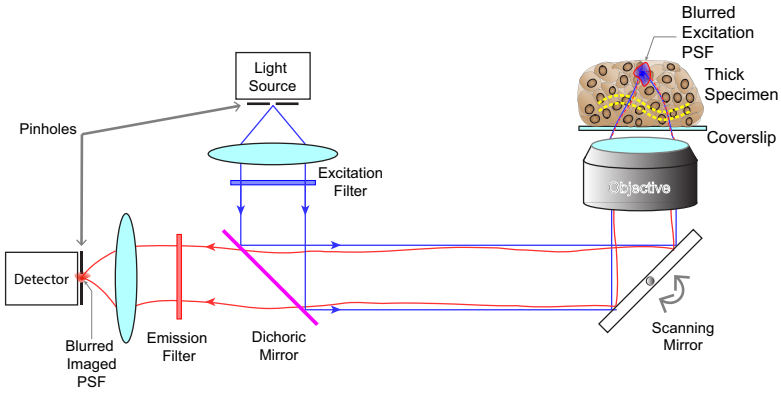

Figure 1.3: The optical path of confocal laser scanning microscope for deep specimen imaging. Due to the aberrations induced by the optical structure of the specimen, e.g. coverslip thickness variation [19] and optical composition of the tissue [20], the point spread function of the excitation path (blue region at the specimen) is blurred, leading to degradation of the resolution and image intensity. The imaged point spread function of fluorescence is also degenerated at the detection pinhole (red region at the detection pinhole), making the resolution of the image worse.

media such as oil. For confocal microscopes, commercial available high NA oil immersion objectives can attain lateral resolution less than half of the wavelength and axial resolution about a wavelength under optimal measurement conditions [18].

In a practical setting with deep specimen imaging, however, the diffraction limited resolution is hardly obtained due to various aberrations in the microscope [19–21]. Fig. 1.3 illustrates the blurred PSFs in both excitation and detection path due to the specimen induced aberrations, leading to dark, noisy, and vague images [19]. The specimen induced aberrations can be caused by the optical path error due to refractive index mismatch of the media [19, 20] and non-homogeneous cellular and subcellular structures [21, 22]. In addition, high NA objectives with aberrations also do not guarantee high resolution images, since the aberrations degrade the resolutions more significantly as the NA of the objective increases. Fig. 1.4(a) shows a 3D image of 100 *nm* red fluorescence beads for the measurements of the actual point spread function along the imaging depth (Fig. 1.4(b)). Fig. 1.4(c) shows that the axial full width at half maximum (FWHM) is two times larger when imaging in 100 μm depth. This degradation of the imaging quality by depth increases the uncertainty in the localization of the targeted molecules and reduces the signal intensity of the fluorescence from the cells in the tissue, hampering the precise analysis on life activities in the deep tissue [23].

1.1.3 Fluorescence for Biological Imaging

The most attractive applications for confocal microscopy are in biology and medical science with fluorescence marking techniques [24]. The availability of a large variety of fluorescent

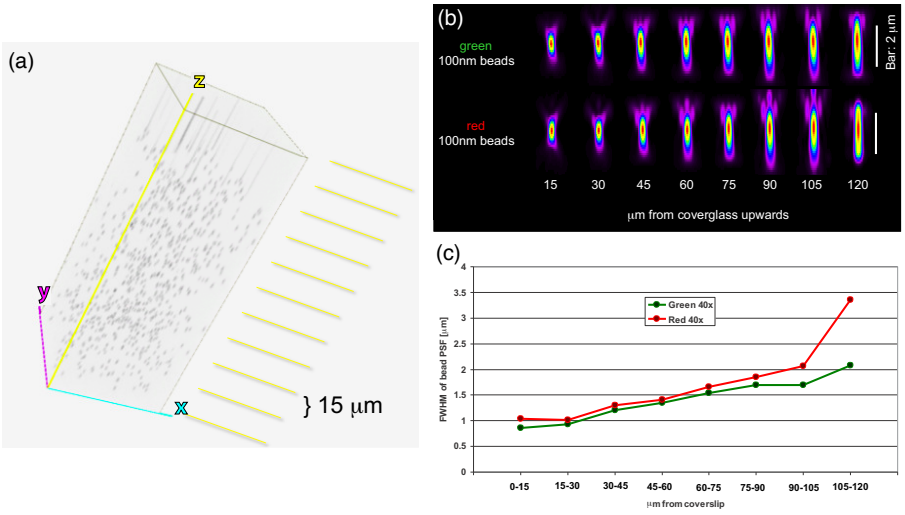

Figure 1.4: (a-b) Measured PSF (Distilled by Huygens Software of Scientific Volume Imaging B. V., Hilversum, the Netherlands) along the imaging depth from 100 *nm green and red fluorescence beads in polyacrylamide (PA) gel (refractive index = 1.38) via Plan-Apo 40×/1.3 NA oil immersion objective with 1 airy unit (AU) detection pinhole by Leica SP5 CLSM. (c) The axial full width at half maximum (FWHM) of the measured PSF. Provided courtesy of M.E. van Royen.*

proteins, including photoactivatable and -switchable mutants, has revolutionized live cell imaging [24, 25]. With confocal microscopy, quantitative investigation of molecular mechanisms responsible for normal biological function of living cells and organisms [26, 27] can be imaged with precise localization of active factors inside subcellular organelles, including the structure and dynamics of active chromatin sites inside the cell nucleus. The fluorescence marking technique allows to image and diagnose aberrant processes because of diseases such as cancer [28, 29] or neurodegenerative diseases [30, 31].

Sir George Gabriel Stokes (1819-1903), who initiated modern explanation and analysis on fluorescence, was aware of its potential in biology and he mentioned “on the application of the optical properties to detection and discrimination of organic substances” [32]. Since Osamu Shimomura discovered the green fluorescence protein (GFP), GFP and its derivatives have been widely used in biology and medical science [33, 34]. Various experiments, markers, and techniques are developed not only for detecting the location and function of specific molecules [35] but also for figuring out reactions between multiple biomolecules such as Ca+ ionic distribution for neuron reaction [36] and stages of cells [37]. Due to such a huge leap with this tool in biology, three scientists have been award the Nobel Prize in Chemistry 2008 for “Discovery and development of the green fluorescent protein, GFP” [38]. By separation of excitation from the emission, fluorescence microscopy has intrinsic high signal to noise ratio, selectivity and specificity [39–41]. In contrast to other techniques, such as electron microscopy, fluorescence enables *in vivo* imaging, i.e. observation of the targeted bio-molecules in the living cell, allowing to observe both spatial and functional

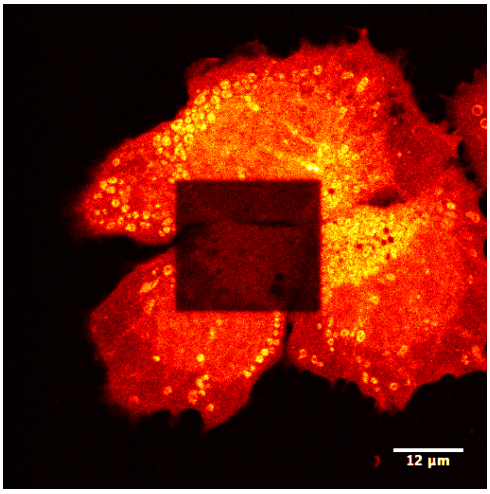

Figure 1.5: Photobleached MitoTracker Deep Red^{TM} on Hepatocellular Carcinoma cells by after running image process. The dark square area at the image center used to have similar intensity as the surroundings do before the imaging center for minutes, showing the loss of intensity by photobleaching.

information of the actual bio-reaction close to the real life conditions [42].

To use of the fluorescence for biological imaging, one should bare in mind that long-term stable imaging and observation of fluorescence is usually unavailable due to photobleaching. Photobleaching is a phenomenon that the fluorescence molecule loses its intensity permanently during observation due to photochemical modification [1]. Fig. 1.5 shows a bleached florescence dye at the image center after minutes of imaging that region. Although physical mechanisms of photobleaching are different by every single fluorescence dye, photobleaching of fluorescence is usually unavoidable [2]. The intensity loss due to photobleaching is a problem in practical fluorescence microscope imaging due to the loss of the signal to detect. It also limits the time of experiments and hampers precise intensity comparison between images taken at a different time because later measurements have usually lower intensity. One solution is to reduce the excitation intensity to slow down the photobleaching process, which however leads to low fluorescence intensity with a low signal to noise ratio (SNR). In practice, excitation intensity and imaging time should be adjusted considering the sensitivity and noise level of the detector and the speed of photobleaching.

1.2 Scope of the Thesis

As knowledge about life activity increases and tools for biological research are improved, biologists strive to analyze faster biological processes occurring in deep living tissue, i.e. in optically harsh conditions [43]. To meet such needs, conventional confocal laser microscope has to be adapted. The main scope of thesis is optomechatronics design and control for improving both imaging speed and spatial resolution of the CLSM.

One of the main challenges is fast imaging and scanning control of conventional gal-

vanometer scanners. Galvanometer scanning system is the dominant scanning device installed in most commercial confocal microscopes [1, 10, 16]. This popularity is due to the reasonable performance, affordable cost, and high flexibilities [1]. Improving scanning speed and accuracy of the given galvanometer scanner could significantly broaden the coverage of the default galvanometer scanners for observation of faster biological process. Since the computing and software cost is relatively low, a controller change that improves the performance considerably can be done by the minor update of the currently installed CLSM without changing scanner or optics inside. This leads to the following main question as

Main research question #1
Can control algorithms improve the imaging speed and precision of the conventional galvanometer scanning system for fast confocal laser scanning microscopy?

The other challenge is aberrations deteriorate the spatial resolution of CLSM. As discussed in Chapter 1.1.2, there are various source of aberrations deteriorate the microscope image. These aberrations impair the image quality and blur the localization of the targeted cellular structure and bio processes, which may not be conclusive for biologists for their research question. Therefore the correction of the aberration in the CLSM imaging could provide high-quality information of the life activities vividly regardless of the specimen and measurement conditions. This leads to the next main research question as follows.

Main research question #2
Can optomechatronics design and control improve imaging quality of confocal laser scanning microscopy with given aberrations due to undesirable measurement environments?

1.3 State of the Art

Since this thesis is focused on the confocal microscopy in both spatial and temporal resolution, the developments and techniques on the confocal microscopy is discussed first in this section. Then learning control is discussed for the scanning control algorithms in imaging techniques. Finally adaptive optics development for microscopy is discussed with approaches of direct or indirect wavefront sensing.

1.3.1 Confocal Laser Scanning Microscopy

Fast Scanning and Imaging

The needs for high speed of the imaging, i.e. high temporal resolution of the microscopy, are increasing as the knowledge of biology increases. From video-rate CLSM imaging of the biological reactions such as cardiac cycle [11], sub-millisecond random access scanning is required for the current biological researches such as Ca^{+} imaging of function of

the brain tissue [43]. To improve temporal resolution, three approaches are discussed in this subsections: software improvement of the popular galvanometer scanner, fast scanner developments, and focal multiplexing.

Due to high flexibility to scanning and cost effective solution, default scanners of the most commercial confocal microscopes are galvanometer scanners [1]. However due to the inertia of the rotor and the sharp turnaround action, the speed of normal galvanometer scanner usually have less than 1600 lines per second [44, 45]. In addition unidirectional scanning is usually used to obtain a uniform and accurate line scan since dynamics due to the mechanical structure causes phase mismatch between lines and stimulate the high order modes that distorts the images [46]. For the fast scanning by galvanometer scanner Duma et al studied smooth trajectories of turnaround for the bi-directional scan to improve the accuracy of the scanning motion in high speed tracking [17, 47] and analyzed with optical coherence tomography [45]. A line switching methods is studied to hide the difference between trace and retrace scans while keeping the speed of bidirectional scanning at the same time [48].

For the fast scanning and imaging new scanners are developed by removing turnaround motion, using resonances of the scanners and exploiting a dynamic-free scanning method. Since sharp turnaround at high scan rates needs large force, polygon mirrors [49, 50] and spinning disks [13] are used for the fast scanning methods by removing turnaround motion and rotating constantly. As a trade off, these types of scanners usually have less flexibility: range of imaging is fixed without optical zooming [10] and the configuration of the pinholes are fixed [12]. Resonance dynamics of scanners can be used in the fast scanning, e.g. resonance galvanometer scanners [12, 51], which is also commercially available over 8000 lines per second [44]. As a drawback the wavefront distortion due to deflection of the mirror plate and the linearity of the scanning region is limited since the scanning trajectory is sine like by only one mode at high frequency [12]. The other approach remove the inertia in scanning principle such as acousto-optic deflectors (AOD), allowing extreme fast scanning speed over 100 kHz [1, 52, 53]. Instead of moving structure for beam scanning, AOD uses birefringent crystals and sound wave to control the deflections. Since the deflection process is inertia free, AOD provides fast scanning in 2D [54] and 3D [55] imaging as well as discontinuous (random, arbitrary) scanning modes [56].

As scanning speed becomes faster by new hardware and software, dwelling time per each pixel is getting shorter to obtain sufficient number of photons per pixel [12, 43]. To secure enough number of photon, imaging with multiple points at the same time, called focal multiplexing, is necessary. The multiple illumination CLSM can be implemented by pinhole arrays [57–59], micro-lenslet arrays [60], and micro mirror array [61]. For this multiple illumination in high speed, wide field image detector such as electron multiplying charge coupled device (EMCCD) are usually used to record the multiple point simultaneously [1]. Since this optical parallelism may cause interference in imaging, the specimen has to be transparent and with small scattering, which limits imaging depth of the microscope [43].

Super Resolution

In biological images, the optical microscope can have about 200 nm resolution by diffraction limit while the targeted bio-molecule such as protein and DNAs are usually only about 10 nm [1, 43, 62]. This hampers the imaging precisely a small biological structure such

as virus and interactions in molecular scales (e.g. reactions hormones and chromatins) while optical microscope has benefits for imaging living biological specimen [62]. From this needs, several approaches to tackle the diffraction limit of the microscope are devised, which is called super-resolution microscopy or optical nanoscopy [63, 64]. The approaches for the super-resolution can be categorized into four based on the main concept to break the diffraction limit: confined illumination, structured illumination, stimulated emission depletion, and molecular switching.

One approach to break the diffraction limit is reduce the size of illumination by confining the illumination by near field effect or evanescent light. Near-field scanning optical microscopy (NSOM) is similar technique with scanning probe microscope but has optics at the scanning probe that is smaller than the diffraction limit by the wavelength [8, 65]. The optical probes are approached approximately 10-20 nm from the surface of the specimen and illuminate only a small area to achieve high resolution (typically 20-50 nm) [43, 66]. NSOM is versatile with type of fluorophore while the possible objects for imaging are limited in depth because NSOM can measure only the surface of the specimen where the optical probes can reach. The other technique with limited illumination is total internal reflection fluorescence (TIRF) microscopy using evanescent waves. When total internal reflection occur at the interface of two media, usually coverslip glass and the aqueous specimen, at the surface of the reflection the evanescent wave are generated but attenuated quickly so that only small depth approximately 100 nm are illuminated [1]. This allows high axial resolution of the specimen but the object for imaging is defined by the surface of reflection.

Another approach uses modulations of the light fields to doubling the bandwidth of the spatial frequencies of the specimen imaging. This technique is called structured illumination microscopy (SIM), which can achieve twice higher resolution in all axis of widefield microscope than diffraction limit by imaging with multiple illumination (typically Moirè patterns) pattern and processing the image afterwards [1, 67, 68]. The advantage of SIM is that any fluorophore can be used for imaging and it can image also weak intensities of fluorescence, leading to the commercialized product in the market now [43]. Since the confocal also improve the spatial frequency contents in doubled manner, confocal microscopy can be regarded as a variant of the SIM [2]. In general, however, the contents at high spatial frequencies are more emphasized with SIM, leading to the higher resolution than confocal microscopy. In this regards, it can be said that SIM does not break the diffraction limit but extend it with twice rich contents in frequency domain [2, 43, 62].

One of the successful super-resolution techniques is stimulated emission depletion (STED) microscopy that literally break the diffraction limit in resolution [6, 69, 70]. Stimulated emission depletion is a phenomenon that the energy level of excited fluorophore drops near grounded state by given additional light (depletion laser), whose wavelength is usually matched with downward transition of fluorophore [2]. This stimulated emission depletion can be used to resize the point spread function up to 30 nm in lateral and 100 nm in axial by depleting the fluorophore in the surrounding volume to the focus [6, 63]. In theory, STED microscopy can provide infinitely small point spread function so that the diffraction limit does not plays any role to the resolution. In practice there are problems of selecting proper fluorescence dyes and high intensities of depletion laser but they does not limit the principle and can be improved successively [62].

The last representative super-resolution technique is a fine localization with photoswitchable fluorescence mutants, named as photoactivated localization microscopy (PALM)

or stochastic optical reconstruction microscopy (STORM) [71–73]. Basically the localization of the single fluorescence molecule can be much precise than the resolution of the system but this highly precise localization is only available with sparse enough fluorophore density, i.e. the distance in between fluorophore should be larger than diffraction limit [62]. With photoswitchable fluorophore that actively 'turn on' or 'turn off' the fluorescence, this sparsity can be manipulated and the super-resolution can be attained sequentially turning off the fluorophore. PALM and STORM is beneficial since the implementation is extremely simple in optics and hardware while has also disadvantages because it needs special photoswitchable dyes and the imaging time can be long since multiple images with different activated fluorophore are used to generate a high resolution image [2].

Currently those super-resolution techniques are available in the markets for biologist and produce much results for revealing the scientific questions in biology [62]. As the response to the results, the development of STED microscopy and PALM are award the Nobel Prize in Chemistry 2014 for "the development of super-resolved fluorescence microscopy". Optical nanoscopy is still young and on developing with new techniques and coverage in biology [62].

Leica SP5 Confocal Laser Scanning Microscope

A Leica SP5 confocal microscope is used for experiments. In the Leica SP5 CLSM, two galvanometer scanners are attached for lateral scanning and a galvanometer-driven z stage can be used for fast axial scanning while motorized z stage also can be used for slow axial imaging. The lateral scanning speed is 400 lines/s up to 1400 lines/s for 512×512 image, i.e. the frame rate is up to 0.4 s. The dwelling time for each pixel is below 1.4 μs at 1400 lines/s (4.9 μs at 400 lines/s) considering turn-around of the x (fast) scanner.

1.3.2 Learning Control for Scanning Imaging System

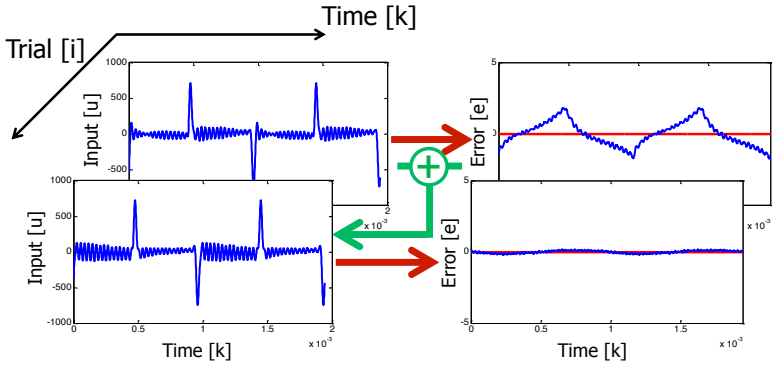

Figure 1.6: Operation of the iterative learning control. The new input is updated based on the input and residual error of previous trials, which leads to the smaller residual error. By increasing iteration, the properly design ILC adapt the input signal for minimizing the error.

To boost the scanning speed and accuracy by managing dynamics of the scanner in

CLSM, iterative learning control (ILC) has much potential as a scanning controller. ILC is a feedforward type of control that compensates the periodic errors in the repetitive process by learning from the error of the previous process. Fig. 1.6 shows the concept of the ILC, in time and trial axis. Fist an input is applied in time axis and the error is recorded. Based on the recorded residual error and the applied input in the previous trial, the new input for the next trial is calculated and applied to the system for the better residual error. As iterations increase, the tracking error can be minimized. Since ILC was firstly proposed by Uchiyama in 1978 in Japanese [74] and introduced by Arimoto et al. in English [75], ILC are applied in various applications of robotics, rotary systems, chemical process, actuators, power electronics, and precision mechatronics [76].

Due to the learning nature of repetitive error, ILC sometimes confused with repetitive control (RC). Longman [77] argued that they are not much different in practice while literatures highlight the differences. Wang et al. [78] provides a comparison of ILC and RC in various aspect, in problem, model, output, input and control structure. According to Wang, the ILC problem is only batch process with the same initial condition, and the model is in state space model while RC runs periodic continuous process and the model is usually transfer function. Fleming and Leang [79] pointed out the ILC runs in the iteration domain while RC runs in feedback manner in time domain with definite delay of period. They argue that due to this structural difference between trial and time domain in control, i.e. offline (ILC) and online (RC) manner of learning, the instability of ILC means divergence and ILC can stop learning after the detection of divergence [80] while RC results in instability of the system.

There are advantages of ILCs compared to the conventional feedback control in scanning control. The benefit of ILC is that the bandwidth of the feedforward control can be wider than the conventional closed loop control, enabling a fast and accurate scanning. That is because the stability is not limited by the gain or phase margin of the system, but the accuracy of the system model, which is used in the learning filter design. ILC can also efficiently remove the phase and gain mismatch in the tracking error and repetitive disturbances during the scanning.

The learning control for galvanometer scanners of CLSM is firstly shown in [81]. While the paper does not mention the exact term of 'learning control', the technique for enhancing the random scanning clearly shows main factors of learning control: a feedback by the mean error of the receding horizon in the previous actual trajectories, improvement of the scanning trajectories by a number of iterations, and stopping the iteration when the improvement reach 'good enough'. The experiments with 600 Hz scanning shows less than 1.5 pixel error compared to the raster images. Since this approach only changes the reference for feedback control, the speed of the scanning is still bounded by the feedback control bandwidth. For the piezoelectric optical scanners, ILC is also applied for accurate scanning while the scanning speed is limited by the feedback control bandwidth by design. For different application of the galvanometer scanner, iterative learning control is applied for a microvia drilling machine for precise integrated circuit correction to suppress vibration [82].

ILC as a scanning controller has been actively studied for scanning probe microscopy (SPM) such as atomic force microscopy (AFM) [83–85] to gain a high control bandwidth and compensate for the dynamics and nonlinearity of the piezoelectric actuators [86, 87]. Traditionally SPMs are slow in imaging, tens of lines per second, to achieve an accuracy in nanometer scale even it uses piezoelectric actuators for high speed control. Using the

wide control bandwidth in ILC over kHz, more than 100 Hz of scanning speed can be achieved in nanometer scale error [84]. Nonlinearities of piezoelectric actuators can be also compensated for by ILC [83]. To cope with specimen changes during experiments, non-model based ILC in frequency domain is developed for maintain fast scanning image [80].

1.3.3 Adaptive Optics

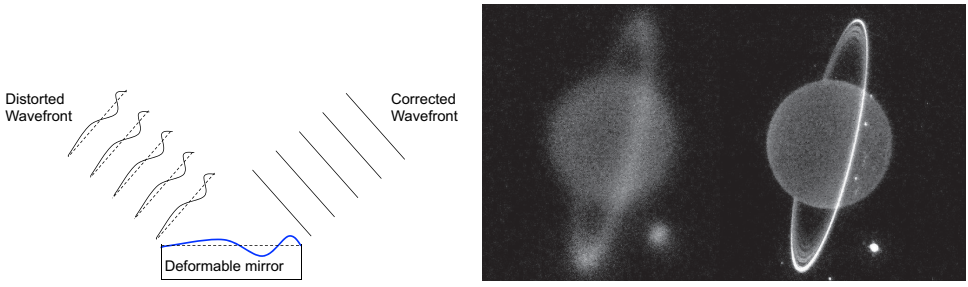

Figure 1.7: (a) Concept of adaptive optics and (b) near-infrared images of Uranus without adaptive optics (left) and with adaptive optics turned on (right). With adaptive optics, a vague single ring turns out an assembly of multiple rings and the atmospheric phenomena could be imaged from ground-based telescopes. Courtesy of Heidi B. Hammel, Imke de Pater and the W.M. Keck Observatory [88].

Adaptive optics (AO) is a method that compensates aberrations to improve the imaging quality. Aberrations of the beam degrade the focus, resulting in dark, blurry, and even distorted images. These aberrations can be explained as a distortion of the wavefront, which is a line at the same phase of the light in the pupil function and should be flat for the best image performance. Fig. 1.7(a) illustrates the concept of adaptive optics that compensates for incoming aberrations (wrinkled solid line) by deformable mirror with the inverse of the aberrations (solid blue line), leading to the flat wavefront for improved sharp and clear images. Fig. 1.7(b) shows near-infrared images of Uranus before adaptive optics applied (left) and after (right), discovering more features and details of the planet [88].

Though adaptive optics (AO) is a quite recently developed technology proved late 1960s, the idea dreamed up from the early 16th century that people know turbulence in atmosphere imposes an serious limitation the angular resolution of telescopes for astronomy [89]. Isaac Newton clearly mention this limitation by turbulence in his book, Optiks, published in 1704 [89] and Herschel practically suffered from the effect of the turbulence after building up the 18.8 inch (0.48m) and the 48 inch (1.2m) telescopes [89]. The only ways to reduce the optical disturbance by turbulence were finding a good site to observe the sky, e.g. high mountains near the equator. Besides, measurements of the wavefront distortion by atmosphere were studied from late 1850 based on Knife-edge test [89]. Hartmann test, which is one of the popular wavefront sensing techniques, was developed in 1900, before the complete development of the optics system.

The first image compensation by AO technique was the Real-Time Atmospheric Compensation system (RTAC), whose first operation is done in 1973, developed by Itek Optical System [89, 90]. As other technologies such as telecommunication and cryptography, AO were seriously investigated first for the military purpose. After huge success of the launch of Sputnik I from Soviet Union, Unite States needed better images of satellites from ground, as well as better images of the enemy's territory from satellites to collect aerial intelligence [90]. RTAC has a 21 channel monolithic piezoelectric deformable mirror and a shearing interferometer for detecting wavefront distortion, and successfully demonstrated its performance with a HeNe laser through 300m of ground distance. The success from RTAC led to the next development of AO, Compensated Imaging System (CIS) with 168 actuators and also a shearing interferometers. CIS was installed on the 1.6-meter telescope on top of Mt. Haleakala on the island of Maui in Hawaii. After declassified in 1991, AO became a proven technique for astronomical imaging as Fig 1.7(b) [91].

Currently adaptive optics are extensively investigated for various research fields and industrial applications: optical microscopy [92], ophthalmoscopy [93], optical coherent tomography [94], optical tweezers [95], laser communications [96], and holographic data storages [97].

Structure of Adaptive Optics and Wavefront Sensing

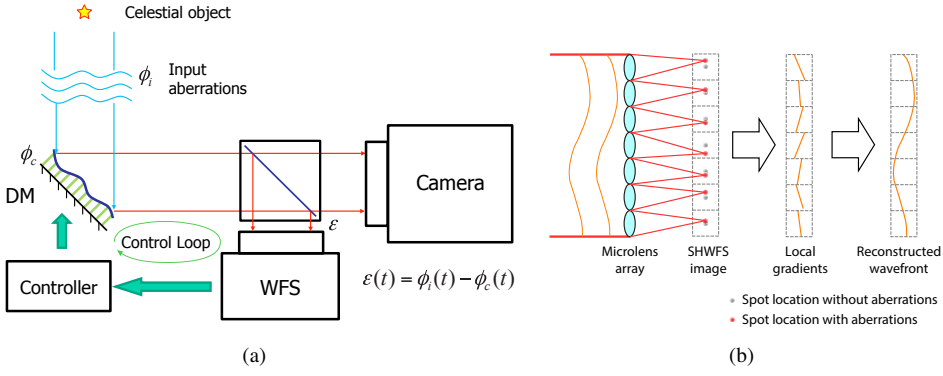

Figure 1.8: (a) A closed loop AO system consisting of wavefront sensor, wavefront corrector, and its control unit to achieve aberration corrected image at the camera. (b) A schematic of Shack Hartmann wavefront sensor with wavefront reconstruction process.

Adaptive optics system usually consists of three main components. Fig. 1.8(a) illustrates a closed loop AO system wavefront sensing, wavefront correction, and the control unit [98]. After the light with aberration shines to the wavefront corrector, the wavefront sensor measures residual aberrations of beam. The recorded image of the wavefront sensor is interpreted by the controller. The controller also computes the desired correction in wavefront and determines the input of the deformable mirror. By compensating in this loop, the wavefront error is reduced in real time and the image quality at the camera can be improved.

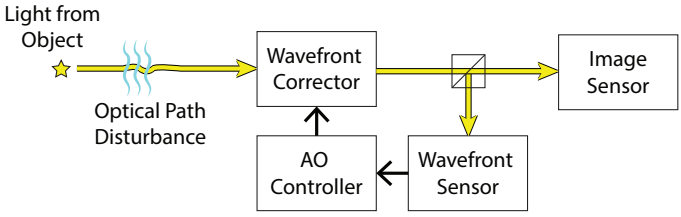

(a) Received Adaptive Optics System: wavefront compensation

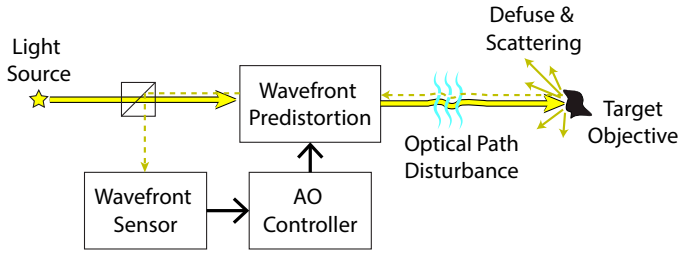

(b) Transmitted Adaptive Optics System: phase conjugation

Figure 1.9: Adaptive optics system of received and transmitted optical system.

Among those components, wavefront sensor is one key element that detects the aberrations of the system. It can be direct or indirect, depending on the raw measurement. Direct wavefront sensing uses an explicit wavefront sensor that directly measures the pupil function. Shack-Hartmann wavefront sensor (SHWFS) is one of the popular wavefront sensors using a lenslet array, measuring local wavefront gradients by the displacements of the local focal spots [98] as Fig 1.8(b) shows. Indirect wavefront sensing uses the measurement of the image plane side such as intensity after point detector [99, 100], average image intensity or image sharpness [101, 102]. There are also a technique known as phase diversity, which retrieves wavefront information based on the multiple images with different known aberrations, usually defocus, i.e. displacement of the focal plane [103, 104].

Adaptive Optics for Received and Transmitted Optical System

There are mainly two kinds of adaptive optics considering the objective of the optical system and the location of the aberration: a received type and a transmitted type as shown in Fig. 1.9 [98]. The objective of the received type of optical systems is to image the light source outside of the optical system through wavefront distortion media, while the objective of transmitted optical system is to transfer the focused light power from the light source in the optical system to the target. The main difference between them is the location of aberration generation. A received optical system has the source light with applied aberrations while transmitted optical system has a clear source light, which suffers from the future aberrations before reaching the target. Since the objectives of each system are different, AO objective is different: to generate the best image by compensate aberrations from the source light, and to transmit the higher power to the target by predistortion of wavefront to the outgoing light.

AO development for the received optical system is straight forward as discussed in previous subsection. For the transmitted optical system, however, the wavefront distortion in the media is not available from the beam path of the optical system. Fig. 1.9(b) shows phase conjugation technique for the transmitted optical system. The idea is using the glint like reflection from the small area of the target for the wavefront sensing. The reflection of the small area of the target can be regarded as a point source from the target and it contains the same aberrations as the transmitted light.

For the received optical system, this phase conjugation technique is also used for overcome its given limit, named "laser guide star (LGS)" in astronomical telescope application [98]. For observation of dark stars in the sky, the received light can be insufficient for wavefront sensing. To get photons for wavefront sensing, an artificial star is projected from the laser on the ground to a certain layer of the atmosphere, e.g. sodium layers in the mesosphere around 92 km from the ground [105–107]. Then measured wavefront distortion from the LGS is used for compensation of the received dark star image, improving the image quality.

Adaptive Optics for Microscopy

As discussed in Section 1.1.2, the diffraction limited imaging is hardly attainable for deep imaging through the biological specimen due to the aberrations. Adaptive optics is suggested as a solution of the such aberrations and received much attention in last decade [92, 108]. Adaptive optics is applied to the various microscopy technique such as confocal laser scanning microscopy (CLSM) [109, 110], multi-photon excitation (MPE) microscopy [109], widefield microscopy [111–113], Harmonic generation microscopy (HGM) [114], fluorescence spectroscopy [115], coherent anti-Stokes Raman spectroscopy (CARS) [116], light sheet fluorescence microscopy (LSFM) [117]. Since aberrations are also problematic in super-resolution microscopy, adaptive optics are investigated as a cure for image degradation [118] in various structured illumination microscopy (SIM) [119], photo activated localization microscopy (PALM) [120], and Stimulated emission depletion (STED) microscopy [121]. For the STED, adaptive optics technique is used for improving the point spread function in both lateral and axial axis [121].

Indirect vs. Direct Wavefront Sensing in AO for Microscopy

The main challenge in AO for microscopy is the way to measure the aberrations that degrade the microscope image [43]. Adaptive optics development for the microscopy can be categorized by the wavefront sensing method: indirect and direct sensing [122]. Indirect wavefront sensing, also called wavefront sensorless approach, does not use explicit wavefront sensors but the information from the image to obtain the optimum image [101, 102, 109, 123–125]. Pupil segmentation can be regarded as indirect sensing since it does not have wavefront sensor in AO system while its principle is similar with Shack Hartmann wavefront sensor [126–129]. The benefits of the indirect sensing are less complex in system and optical path, and no light loss since the light from the specimen can be fully used for the image. As a drawback, the convergence is slow in general and needs many images to correct the aberrations in quality, which may cause the photobleaching of the specimen during the aberration correction.

Direct wavefront sensing approach exploits the wavefront sensors such as interferometry and Shack Hartmann wavefront sensor that measures the aberrations from the specimen. It can be categorized by the type of the wavefront sensor, the type of the light source for wavefront sensing, and the method to refine the light only at the focal point. As light sources for wavefront sensing, back-scattered light and fluorescence can be used and coherence-gate and a pinhole can be used to restrict the light for wavefront sensing only from the focal point [130]. Interferometry is applied based on coherent gaged back scattered light [131, 132] and Shack Hartmann-based approach with pinhole [133, 134]. Based on the fluorescence guided star technique, shack Hartmann wavefront sensor is used for the aberration measurement from the fluorescence sample [110, 112, 117, 135–139]. These direct wavefront sensing methods usually fast since aberrations in the system can be obtained from a single measurement. This fast correction allows in less photobleaching and photo damage of the specimen [137], and also real time compensation for dynamic changes of aberrations induced by living specimen [138]. As a drawback the imaging quality after correction may not be the optimum due to the alignment of the system [133] and error in reference of the wavefront sensor. For the scattering light the sensitivity of odd-symmetry aberrations is usually weak [134] and for fluorescence the intensity is usually weak and also signal intensity degraded due to photobleaching [137].

A comparative study [133] of the indirect and direct sensing AO for microscope shows the benefits and drawbacks of each method. *Bourgenot et. al.* shows transient responses of image sharpness by the sensorless AO (Nedler-Mead simplex algorithm) and direct sensing AO (Shack Hartmann wavefront sensor). The results shows that direct sensing AO converges fast in 3 iteration with the suboptimal final image while indirect methods takes long, 250 iteration for the convergence. This convergence time can be improved by the modal based algorithms [101] but at least N+1 is necessary where N denotes the number of modal modes to compensate for [100]. (e.g. 16 iteration is necessary at least for correcting 15 Zernike modes) In this sense, direct wavefront sensing AO would be beneficial for the living specimen imaging which need high temporal resolution or venerable fluorescence dyes to photobleaching.

1.4 Contribution and Thesis Outline

Fig. 1.10 shows the outline of the thesis with the connections between chapters. The contribution can be separated in 4 parts: fast scanning control of galvanometer scanner (Chapter 2 and 3), automated spherical aberration correction via motorized coverslip correction ring (Chapter 4), general aberration measurement and compensation via adaptive optics system (Chapter 5 and 6), and pupil function recovery via adjustable square pinhole. Each part corresponds to the separate scientific questions and can be read independently.

- In Chapter 2, iterative learning control (ILC) for a galvanometer scanner is proposed to achieve a high speed, linear, and accurate bidirectional scanning for scanning laser microscopy. Experimental results verify the benefits of ILCs, achieving up to a 73 times smaller root mean square (RMS) error than a conventional feedback controller. Research Question: Can ILC improve the speed and accuracy of the conventional galvanometer scanners? How the performance can be improved by handling the non-minimum phase zero of the galvanometer in design of learning filter?

Reference: [140] Han Woong Yoo, Shingo Ito, Michel Verhaegen, and Georg Schitter. Iterative Learn- ing Control of a Galvanometer Scanner for Fast and Accurate Scanning Laser Microscopy. In Mechatronics 2012, 17-19 Sep, Linz, Austria, pages 537-543, 2012.
Han Woong Yoo, Shingo Ito, Michel Verhaegen, and Georg Schitter. Iterative Learning Control of a Galvanometer Scanner for Fast and Accurate Scanning Laser Microscopy. Mechatronics, submitted.

- In Chapter 3, transformation-based ILC approach is proposed to achieve accurate image scanning for the non-collocated dynamics of a galvanometer scanner. Experimental results with the proposed ILC show a 7.5 times better tracking accuracy in RMS error as compared to the ILC design based on non-collocated sensing.
  Research Question: Can reference transformation filter improve the accuracy of beam scanning of the galvanometer scanner with ILC due to non-collocated sensing by the encoder?
  Reference: [141] Han Woong Yoo, Shingo Ito, Michel Verhaegen, and Georg Schitter. Transformation-based iterative learning control for non-collocated sensing of a galvanometer scanner. In 2013 European Control Conference (ECC), pages 1204-1209. IEEE, July 2013.

- In Chapter 4, an automated adjustment of the coverslip correction collar is proposed for scanning confocal microscopy. The benefits of the proposed automated correction are demonstrated with various coverslips with biological specimens, shows that it tracks better image quality of the confocal microscope.
  Research Question: How can the correction of coverslip mismatch be automized for the coverslip with biological specimen?
  Reference: [142] Han Woong Yoo, Michel Verhaegen, Martin E van Royen, and Georg Schitter. Automated Adjustment of Aberration Correction in Scanning Confocal Microscopy. In IEEE International Instrumentation and Measurement Technology Conference, pages 1083-1088, 2012.
  [143] Han Woong Yoo, Martin E van Royen, Wiggert A van Cappellen, Adriaan B Houtsmuller, Michel Verhaegen, and Georg Schitter. Automated spherical aberration correction in scanning confocal microscopy. Review of Scientific Instruments, 85(12):123706, December 2014.

- In Chapter 5 and 6, an adaptive optics development for the commercial CLSM is discussed. The developed adaptive optics contains an adjustable pinhole, that can be used in calibration of AO and evaluate the AO correction quality. Experimental results shows that the proposed referencing can improve the axial resolution of point spread function. For 40 um deep in biological specimen, the axial resolutions are improved with 5 AU, while for 1 AU pinhole the lateral resolutions are improved.
  Research question: Is it feasible to build an interface between AO development and the commercial Leica SP5 CLSM? Does developed AO system improves the resolution? How can adjustable pinholes be used for the AO system for CLSM? Can adjustable pinhole be used for evaluation of the aberration correction quality?

- In Chapter 7 pupil function retrieval with the finite square pinhole is proposed from on the complex pupil measurements. Simulation results with various pinhole size show that the proposed pupil function retrieval reduce phase and magnitude error from the original measurement.
  Research question: Can the distortion of aberrations due to a small pinhole be recovered by the measurement of complex pupil function? Can diversified measurements improve the quality of recovery?

- Chapter 8 summarizes the developments and results of this thesis and outlines the directions for the future research.

Fig, 1.11 shows the developments of the hardware and software in this thesis, as an extension of the conventional CLSM block diagram in Fig. 1.2.

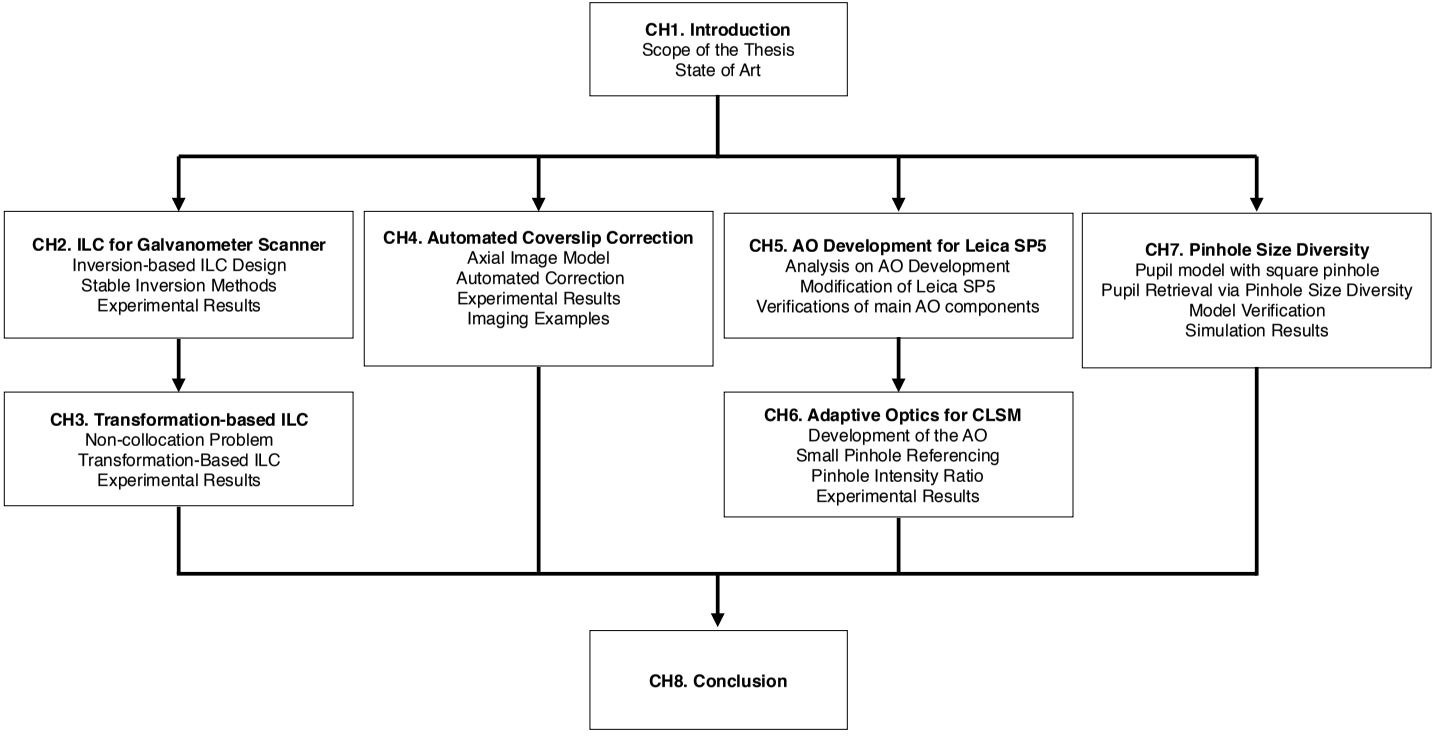

Figure 1.10: Outline of the thesis

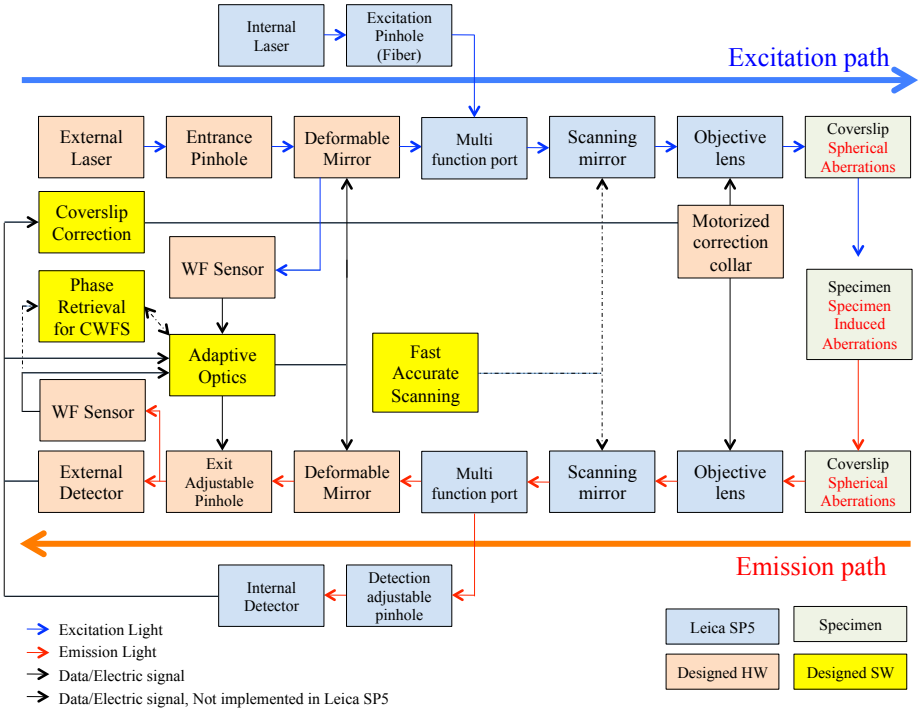

Figure 1.11: Diagram of the system developments with respect to excitation and emission path of the commercial Leica SP5 CLSM. There are four major developments in terms of systems. They are the fast accurate scanning control system ([yellow] Fast Accurate Scanning), an automated coverslip correction system ([orange] Motorized Correction collar, [yellow] Coverslip Correction), an adaptive optics system (All the other orange blocks, [yellow] Adaptive Optics), and a phase retrieval algorithm with finite square pinhole ([yellow] Phase Retrieval for CWFS). The fast scanning control and the phase retrieval algorithm are not implemented with Leica SP5 and AO system, whose connections are represented with dotted-dash lines.

Chapter 2

ILC of a Galvanometer Scanner for Fast and Accurate Scanning Laser Microscopy *

Iterative learning control (ILC) for a galvanometer scanner is proposed to achieve high speed, linear, and accurate bidirectional scanning for scanning laser microscopy. The marginally stable galvanometer scanner is stabilized by a feedback control while ILC is applied for fast scanning motion control at over 2000 lines per second. Two different approaches to compute a stable inverse model of the non-minimum phase dynamics of the galvanometer are derived and implemented for comparison. Experimental results verify the benefits of ILC, enabling a faster, more linear and more accurate scanning without a phase lag and a gain mismatch, where the root mean square (RMS) error can be reduced by a factor of up to 73 in comparison with the feedback controlled galvanometer scanner of the commercial system.

2.1 Introduction

Galvanometer based scanning mirrors are the most widely used scanning systems for high-precision in vivo biological imaging systems, such as scanning confocal and two-photon excitation microscopes [1, 12, 144]. In principle, these microscopes record an image by scanning a laser point by point to achieve a high spatial resolution. A high temporal resolution of microscopic images is desirable for capturing rapid biological phenomena such as a cardiac cycle [11] or tracking the single molecule movements in living organisms [145]. Fast imaging in scanning laser microscopes, however, is challenging in practice due to the dynamic behavior of the scanner and limited bandwidth of the controller [43, 45]. To minimize the imaging time and increase the temporal resolution, fast and accurate scanning is a

*Part of chapter is published,
H. W. Yoo, S. Ito, M. Verhaegen, and G. Schitter, Iterative Learning Control of a Galvanometer Scanner for Fast and Accurate Scanning Laser Microscopy, In Mechatronics 2012, 17-19 Sep, Linz, Austria, pages 537-543, 2012.
H. W. Yoo, S. Ito, M. Verhaegen, and G. Schitter, Iterative Learning Control of a Galvanometer Scanner for Fast and Accurate Scanning Laser Microscopy, Mechatronics, submitted.

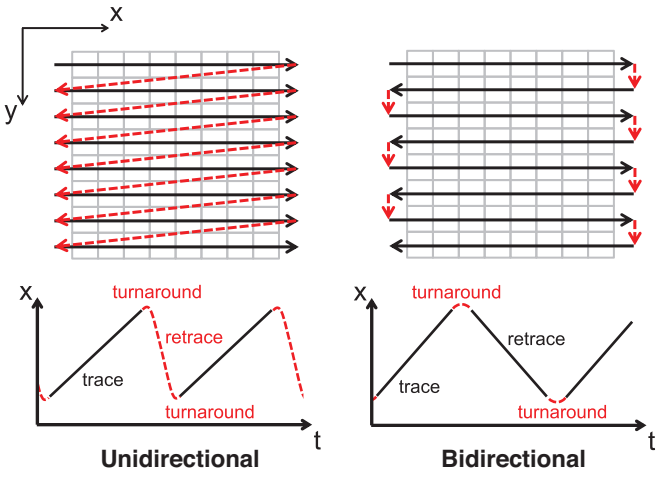

Figure 2.1: Unidirectional scanning (left top) and bidirectional scanning (right top) of laser scanning microscope imaging, which correspond to sawtooth scanning (left bottom) and triangular scanning (right bottom) over the time t for the fast x-scan. The focused laser beam is moved linearly over the specimen (gray squares) for recording an image along the active scanning region (black solid line). Since unidirectional scanning has to turn and retrace without imaging (red dotted line), bidirectional scanning is advantageous in terms of a large active scanning area with a small turnaround (red dotted line).

crucial requirement for galvanometer scanners.

Fig. 2.1 shows two ways of scanning: unidirectional and bidirectional scanning, which are also called sawtooth and triangular scanning, respectively. For laser scanning microscopes, unidirectional scanning is often used due to the long linear slope [45, 146]. However, retracing faster than tracing may cause overheating of the actuator and damage to the scanning system. Furthermore beam blocking is necessary to avoid unnecessary bleaching of the specimen while retracing [1]. In addition, a big retracing portion reduces the effective exposure time per pixel in the active linear scan region, which would lead to a large photon noise due to the reduced number of photons. Duma et al [17, 47] intensively studied various types of bidirectional scanning trajectories for a large linear scan area and compared them to optical coherence tomography [45]. They point out that triangular scanning is desirable comparing to unidirectional scanning, but it is difficult to obtain an accurate scan at a high scanning speed in reality due to high frequencies induced by the sharp turnaround. They also mention that the sharp turnaround at high scan rates causes nonlinearities which decrease the linear active scan region. Furthermore, the phase lag of the scanner causes a misalignment between the trace and retrace of the active scan region. A manufacturer of scanning laser microscopes with a bidirectional scan option provides a phase correction control bar for users to compensate for this mismatch manually [147]. However vibrational dynamics of the scanner is completely ignored so far.

As a solution to compensate for these drawbacks of the triangular scanning motion, iterative learning control (ILC) can be applied, which is feed-forward control for tracking a

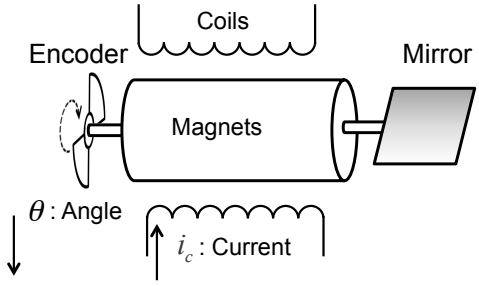

Figure 2.2: Mechanical structure of a moving-magnet galvanometer scanner. The rotor of a galvanometer scanner consists of magnets, a mirror and an encoder connected by a steel shaft, and coils surrounding the magnets. The Lorentz force induced by the coil current i_c with magnets rotates the mirror at one end and the encoder at the other end measures the mirror angle θ.

repetitive reference by updating the control signal based on tracking error measurements obtained at previous trials. For fast scanning ILC has been applied to atomic force microscopy [83–85] and to an optical scanning system [148] to compensate for the dynamics and nonlinearity of the piezoelectric actuators. For a galvanometer scanner, iterative optimization methods have been proposed by Trepte and Liljeborg [81, 146] for a sawtooth, a triangular, and an arbitrary scanning reference for a laser scanning microscope. They compensate for a phase and trajectory error to obtain the optimal input for the closed-loop galvanometer scanner. However, compensation of the vibrational modes due to the internal modes of the galvanometer scanner for a fast and accurate scanning in optical microscopy has not been studied much yet, which is the main contribution of this article.

The goal is to develop ILC for bidirectional scanning beyond 1 kHz, i.e. 2000 lines per seconds, to be applied to fast and distortion-free laser scanning microscope imaging [140]. Section 2.2 describes the stabilized galvanometer scanner, consisting of the galvanometer scanner and a feedback controller, and its linear model is derived. Based on the model of the stabilized galvanometer scanner, ILC design is investigated in Section 2.3 and two approaches for deriving a stable inversion of the non-minimum phase scanner dynamics are presented. Experimental results verify the benefits of the proposed ILC approach in Section 2.4, and conclusions are drawn in Section 2.5.

2.2 Stabilized Galvanometer Scanner

2.2.1 Galvanometer Scanner

For the experiments, a high performance galvanometer scanner (6210H, Cambridge Technology Inc., Lexington, MA, USA) is used, which is widely installed in commercial laser confocal microscopes [1, 144]. The galvanometer scanner is a moving-magnet type as shown in Fig. 3.1, i.e. magnets along the shaft are rotated by the Lorentz force created by the current i_c through the fixed coils. A scanning mirror is attached at one end of the shaft for directing a laser beam. At the other end of the shaft an encoder is attached for the precise angle measurement of the mirror by the passed light through the blocking but-

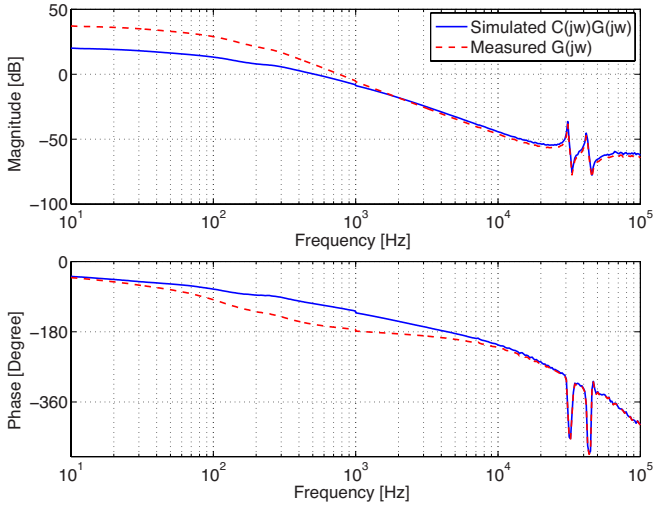

Figure 2.3: Measured Bode plot of the galvanometer scanner from the system input to the system output (red dash line) and the simulated frequency response of open-loop transfer function with a tamed PD controller $C(j\omega)P(j\omega)$ (blue solid line).

terfly [144]. The mechanical actuation range of the galvanometer scanner is $\pm 5^\circ$, $\pm 10^\circ$ of optical angle. The servo driver (MicroMax 671, Cambridge Technology Inc.) consists of a current driver for the coil of the galvanometer scanner, the decoder for the encoder signal, and a closed loop control. The system input and the system output are given by the input to the current driver and the encoder signal through the decoder, respectively. The closed loop control of the servo driver is only used as a benchmark for comparison with the ILC in Section 2.4, but is disabled for all other experiments.

The galvanometer scanner is marginally stable since the rotor of the galvanometer can be regarded as a floating mass with a weak stiffness and friction at low frequency. Fig. 2.3 shows the frequency response of the galvanometer $G(s)$ from the control input to the encoder output is measured by a Dynamic Signal Analyzer (HP3562, Agilent Technologies, Santa Clara, CA, USA). The frequency response shows the dynamics between 300 Hz and 30 kHz is dominated by the inertia of the rotor, providing a -40 dB/dec line in the Fig. 2.3. At low frequencies, however, the magnitude does not show a slope of -40 dB/dec due to the friction, stiction, and weak suspension springs. Due to the marginal stability and low-frequency drift, a feedback controller is designed and implemented before ILC is applied.

2.2.2 Feedback Control Design for Stabilization

Fig. 2.4 illustrates the overall structure of the control system, where G, C, and ILC blocks represent the galvanometer scanner, a stabilizing feedback controller, and the iterative learning controller, respectively. The ILC is applied in parallel to the servo driver with the stabilizing feedback control by an analog summing amplifier with 1.5 MHz bandwidth (-3dB). This structure allows a broad bandwidth of the ILC, regardless of the stabilizing feedback controller. Before the ILC design a PD feedback controller is designed and implemented

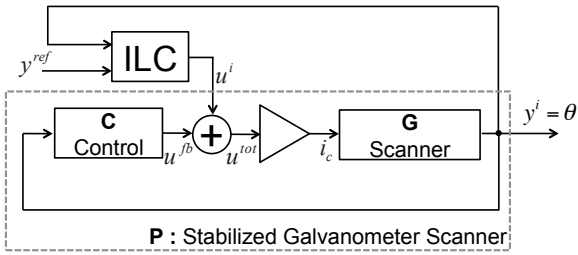

Figure 2.4: Overall architecture of the system with ILC. The galvanometer scanner G is stabilized by the feedback controller C and forms a stabilized galvanometer-based scanning system P, which is the process sensitivity $P(s) = G(s)/(1+G(s)C(s))$. The control signal from ILC u^i for high frequency scanning is summed with the control signal from the feedback controller u^{fb}, resulting in the total input u^{tot} for the galvanometer. The total input, $u^{tot} = u^{fb} + u^i$, is applied to the current driver.

for stabilizing the marginally stable galvanometer scanner.

For the stabilization of the galvanometer scanner, a lead compensator, i.e. a tamed PD controller, is selected as the feedback controller $C(s)$ for providing a phase margin around the unit gain crossover frequency [149]. The controller is tuned, such that the cross-over frequency of the open-loop transfer function $G(s)C(s)$ is about 500 Hz with a sufficient phase margin as shown in Fig. 2.3. The simulation shows that the gain of $G(s)C(s)$ crosses the 0 dB line at 500 Hz with a phase margin of 72 degrees and the gain margin is 36 dB. The controller is implemented as an analog circuit with operational amplifiers and passive components.

Note that the feedback controller is intentionally tuned to have a large gain and phase margins, resulting in a relatively low control bandwidth. With this setting, uncertainties at low frequencies such as a deflection dependent friction and drift are compensated by the feedback control. In addition, the sensor noise, which gets more dominant with high frequencies, stays low in the stabilized galvanometer scanner [150]. This is beneficial for the ILC design since it makes the dynamics of the stabilized galvanometer scanner more deterministic. Based on this ILC is applied to the stabilized galvanometer scanner to control the fast scanning motion at high frequencies.

2.2.3 Linear System Modeling

For the design of inversion based ILC, the stabilized galvanometer scanner model $P(s)$ from the ILC input to the encoder output is necessary. Fig. 2.5 illustrates measured Bode plot of the encoder output of the stabilized galvanometer scanner from the control input by the Dynamic Signal Analyzer (HP3562, Agilent Technologies) and the Bode plot of its manually fitted linear model. The manually fitted linear model is obtained based on multiple second order systems by adjusting each natural frequency and damping parameter in Matlab (The MathWorks, Inc., Natick, Massachusetts, USA). The transfer function from the system input, given by the current through the coils of the galvanometer, to the encoder output is

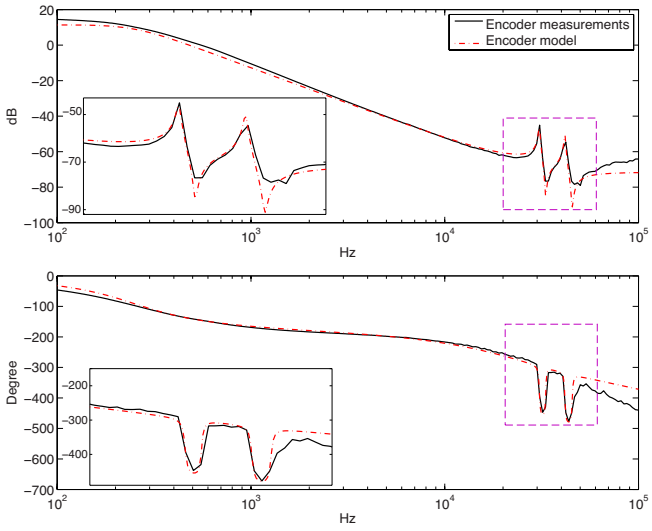

Figure 2.5: Measured Bode plots of the encoder output (solid black line) of the stabilized galvanometer from the input for ILC (u^i) and the Bode plot of the linear model with non-minimum phase zeros (dash-dotted red line). The zoomed Bode plots (violet dashed box in original Bode plot) shows the by resonance and anti-resonances of the galvanometer scanner dynamics.

given as follows [140].

$$\hat{P}(s) = \frac{K\prod_{i_z=1}^{n_z}(s^2+2\zeta_{i_z}\omega_{i_z}s+\omega_{i_z}^2)}{\prod_{i_p=1}^{n_p}(s^2+2\zeta_{i_p}\omega_{i_p}s+\omega_{i_p}^2)}e^{-t_d\times 10^{-6}s}, \tag{2.1}$$

where K denotes a gain, t_d is a time delay in μs. n_p and n_z denotes the number of pole and zero pairs, respectively.

Table 2.1 provides all parameters for the transfer function in Eq. (3.41), and its Bode plot is shown by the red dashed-dot line in Fig. 2.5. A pair of non-minimum phase zeros occurs at 25 kHz. These non-minimum phase zeros provides a fundamental limit of the bandwidth of the feedback controller in practice [150]. Non-minimum phase zeros are also problematic in the feedforward control design such as ILC, but several stable design techniques are available [82, 151, 152] to overcome the limit. By such design techniques ILC can achieve a wide control bandwidth for high tracking performance in fast beam scanning. In the following section ILCs using stable inversion methods are discussed for the fast and accurate scanning of the galvanometer scanner.

Table 2.1: Parameters of the Stabilized Galvanometer Scanner Model

	Poles		Zeros		t_d	K
	$\omega_{i_p}/2\pi$	ζ_{i_p}	$\omega_{i_z}/2\pi$	ζ_{i_z}		
	250	0.65	25000	-0.85		
$P(s)$	30800	0.0087	33200	0.0069	1	2.64×10^{-4}
	41700	0.008	45500	0.0084		

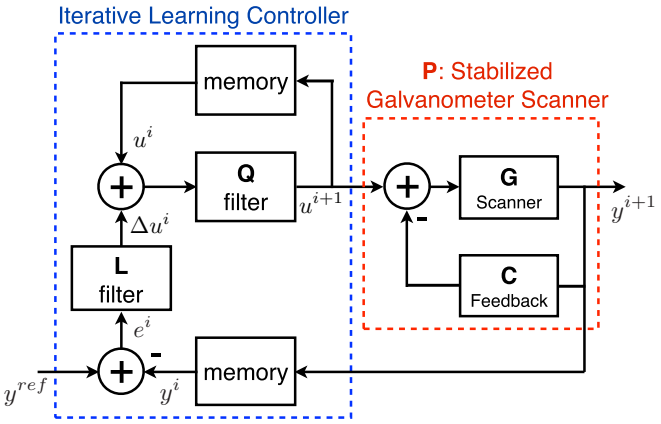

Figure 2.6: A schematic diagram of the iterative learning controller. A learning filter L calculates a required update $\Delta\mathbf{u}^i$ based on the error $\mathbf{e}^i$ between the previous system output $\mathbf{y}^i$ and the reference trajectory $\mathbf{y}^{ref}$. The update $\Delta\mathbf{u}^i$ is added to the current ILC input $\mathbf{u}^i$, which is saved in the memory, and used as a new ILC $\mathbf{u}^{i+1}$ in the next iteration after a robustness filter Q is applied.

2.3 Iterative Learning Control Design

In this section a design of ILC is discussed for the control of the fast and accurate scanning motion control based on the linear model of the galvanometer scanner. ILC is beneficial for scanning motion control since non-unity magnitude and phase lags at each harmonics can be corrected by its learning nature and periodic disturbances and nonlinearities can be compensated for over a wide bandwidth. In the first half of this section, two design methods of inversion based ILC are discussed for the linear model with non-minimum phase zeros.

2.3.1 Inversion based Iterative Learning Control with Non-minimum Phase Zeros

Fig. 2.6 shows a schematic diagram of the iterative learning control with a learning filter L and a Q-filter [153]. The structure leads to the following equation as

$$\mathbf{u}^{i+1}[k] = Q(q)\left(\mathbf{u}^i[k] + L(q)\,\mathbf{e}^i[k]\right), \tag{2.2}$$

$$\mathbf{e}^i[k] = \mathbf{y}^{ref}[k] - \mathbf{y}^i[k], \tag{2.3}$$

$$\mathbf{y}^i[k] = P(q)\mathbf{u}^i[k], \tag{2.4}$$

where $u^i[k]$, $y^i[k]$ and $e^i[k]$ denote the ILC input, output, and tracking error at the discrete time k in ith trial. $L(q)$, $Q(q)$, and $P(q)$ denote the LTI dynamics of the learning filter, Q-filter, and the plant with the forward time-shift operator q, i.e. $x[k+1] = qx[k]$. $y^{ref}[k]$ is the desirable scanning trajectory at time k.

Then the error evolution equation in the frequency domain is as follows,

$$E^{i+1}(\mathrm{z}) \quad = \quad Q(\mathrm{z})\,(1-P(\mathrm{z})L(\mathrm{z}))\,E^i(\mathrm{z}) + (1-Q(\mathrm{z}))\,Y^{ref}(\mathrm{z}), \tag{2.5}$$

where $Y^{ref}(\mathrm{z})$ and $E^i(\mathrm{z})$ are the z-transform of the reference trajectory and of the error at ith trial with $\mathrm{z} = e^{j\omega T_s}$ with sampling time T_s. This provides two well-known characteristics of ILC. The first is that the straight forward solution for the learning filter design is the inversion of the process dynamics $P(\mathrm{z})$ to make the error zero [153]. In general, a learning filter $L(\mathrm{z})$ is designed with a learning gain ρ multiplied with an inverse dynamics, i.e. $L(\mathrm{z}) = \rho\hat{P}^{-1}(\mathrm{z})$ where $\hat{P}(\mathrm{z})$ denotes the system dynamics model. As the learning gain gets smaller, the robustness to modeling errors is improved, albeit sacrificing on the learning speed. The second is that the ILC algorithm converges if the maximum spectral radius of the error evolution operator in trial axis is smaller than 1, which leads to a following renowned ILC convergence criterion [154],

$$|Q(\mathrm{z})\,(1-P(\mathrm{z})L(\mathrm{z}))| < 1,\ \forall\omega. \tag{2.6}$$

From Eq. (2.6), $Q(\mathrm{z})$ denotes a robustness filter, also called Q-filter, which is usually designed to suppress the modeling and design error of L compared to the actual dynamics P. By considering the modeling error in phase, Eq. (2.6) for $\rho = 1$ leads to following necessary condition as [84]

$$\left|\arg(\hat{P}(\omega)) - \arg(P(\omega))\right| < \frac{\pi}{2},\ \forall\omega, \tag{2.7}$$

where $\arg(\cdot)$ denotes the phase of the complex value. Eq. (2.7) means that the uncertainty and modeling error of the system dynamic model should be less than $\pm 90^\circ$ in phase for the convergence of ILC. For this reason the modeling error in phase needs to be small not only in the magnitude but also the phase.

In this straightforward and inversion based design of the learning filter $L(\mathrm{z})$, one of the major challenges lies on the stable inversion of the plant model $\hat{P}^{-1}(\mathrm{z})$ when the plant has non-minimum phase zeros. Fig. 2.7 shows pole-zero plots of the discretized stabilized galvanometer scanner model (black x and o marks at the locations of poles and zeros, respectively), and the non-minimum phase zeroes at 25 kHz (black o marks in black dotted line box) are observed outside of the unit circle. Direct inversion of such non-minimum phase zeros leads to an unstable learning filter. Among the stable inversion methods [155], zero phase approximation and time delay approximation are chosen due to their simplicity [156, 157] and discussed for stable L filter design in the following subsections.

Zero Phase (ZP) Approximation

To cope with non-minimum phase zeros, the idea of zero phase error tracking control (ZPETC) can be used for a stable inversion [151]. Assume that the numerator of the plant model can be factorized by the terms of minimum phase zeros $B^s(\mathrm{z})$ and non-minimum

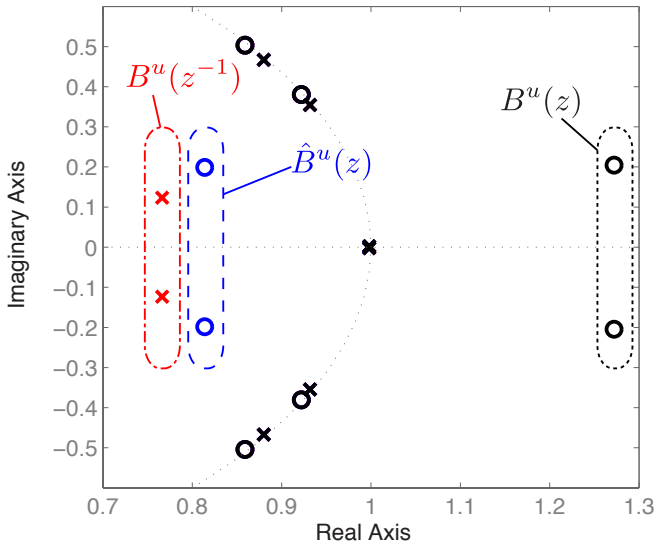

Figure 2.7: Pole-zero plot of the stabilized galvanometer scanner model $\hat{P}(\mathrm{z})$ with non-minimum phase zeros ($B^u(\mathrm{z})$, black dotted line box), zero phase approximation $\hat{P}_{zp}(\mathrm{z})$ with stable poles ($B^u(\mathrm{z}^{-1})$, red dashed-dot line box) and an invertible model with minimum phase zeros ($\hat{B}^u(\mathrm{z})$, blue dashed line box) for the delay approximation $\hat{P}_{td}(\mathrm{z})$.

phase zeros $B^u(\mathrm{z})$, i.e.

$$\hat{P}(\mathrm{z}) = \frac{B^u(\mathrm{z})B^s(\mathrm{z})\mathrm{z}^{-k_d}}{A(\mathrm{z})}, \tag{2.8}$$

with the denominator $A(\mathrm{z})$ and the time delay in discrete time $k_d = \mathrm{round}(t_d/(T_s \times 10^6))$, where $\mathrm{round}(\cdot)$ denotes the round-off of the time delay into the integer delay in discrete time. Then a zero-phase approximation of the stable model inversion is given as follows,

$$\hat{P}_{zp}^{-1}(\mathrm{z}) = \frac{A(\mathrm{z})B^u(\mathrm{z}^{-1})\mathrm{z}^{k_d}}{B^s(\mathrm{z})\left(B^u(1)\right)^2}. \tag{2.9}$$

It is note that the time delay is changed into the time advance by the inversion. In the ILC implementation the time advance can be a simply applied by shifting the input signal of next trial or output signal of the previous trial. In this paper, the increment of input for the update is shifted for realization of the time advance.

In Fig. 2.7 this approximation can be observed by minimum-phase poles (red x marks in red dashed-dot line box) in lieu of original non-minimum phase zeros. This leads to the zero phase error in the model inversion, but the magnitude error of the model inversion increases at the rate of 40 dB per decade from the frequency of the pair of non-minimum phase zeros onwards. The Bode plot of the zero phase approximation (green dashed-dot line) in Fig. 2.8 shows the identical phase with the original model with the non-minimum phase zeros (red solid line) while the magnitude does not fit anymore at frequencies higher than the replaced

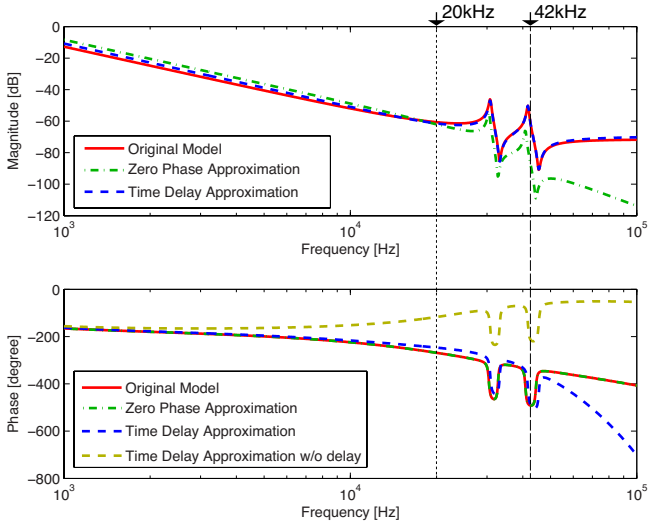

Figure 2.8: Bode plots of a model with non-minimum phase zeros (red solid line), zero phase approximation of ZPETC (green dashed-dot line), delay approximation method without time delay (dark yellow dashed lines in phase diagram) and with time delay (blue dashed line). The arrows of 20 *and* 42 kHz *represent the cutoff frequency of the ILC designs with the zero-phase and delay approximations, respectively*

non-minimum phase zeros. This magnitude mismatch can violate the convergence criterion (2.6) of the ILC and mainly limits the bandwidth of the ILCs, degrading the tracking performance.

Time Delay (TD) Approximation

Another approach to treat the non-minimum phase zeros for a stable model inversion is a time delay approximation [82, 158]. The system with non-minimum phase zeros can be approximated by a system with minimum phase zeros and a time delay as follows [82, 152, 159]

$$\hat{P}_{td}^{-1}(\mathrm{z}) = \frac{A(\mathrm{z})\mathrm{z}^{k_d+k_a}}{B^s(\mathrm{z})\hat{B}^u(\mathrm{z})}, \tag{2.10}$$

where $\hat{B}^u(\mathrm{z})$ is an approximated minimum phase zeros (blue o marks in blue dashed line box) instead of non-minimum phase zeros as shown in Fig. 2.7,and k_a denotes the discretized delay of an additional input delay t_a in μs for the phase adjustment by phase correction, i.e. $k_a = \mathrm{round}((t_d + t_a)/(T_s \times 10^6)) - k_d$. This inversion can provide a small magnitude error as shown in Fig. 2.8 (blue dashed line) [156, 158]. In contrast to the zero phase approximation, the phase error can be large without delay (dark yellow dashed line in Fig. 2.8) which may cause divergence of the ILC by Eq. (2.7). By adding a time delay to the approximated model the phase lead due to the stable zeros can be compensated up to a certain frequency, providing a good approximation of the model in a wide frequency range

(blue dashed line in Fig. 2.8). At high frequencies, i.e. beyond the ILC bandwidth the phase lag starts to diverge from the dynamics of the galvanometer.

In practice $\hat{B}^u(z)$ and t_d are determined in a trade off between the magnitude and phase error of the model inversion for satisfying the convergence criterion Eq. (2.6) and Eq. (2.7). For high performance of ILC, $\hat{B}^u(z)$ can be initially chosen by $B^u(z^{-1})$ for the zero magnitude error [156, 159] and further finely tuned referring to the frequency responses for better fitting. Then the time delay is chosen to compensate the phase lead by the zeros [158]. Compared to the optimization [152] and online adaptation [159] of the time sequences, and system identification with a delay [82], the delay is simply chosen by frequency responses to satisfy Eq. (2.7) until the desired frequency, which is the upper bound of the control bandwidth of ILC considering convergence. As a result, the time delay approximation in Fig. 2.7 and Fig. 2.8 is obtained by replacing damping coefficient -0.85 with 0.6 for the zeros at 25 kHz (See Table 2.1) and the total input delay, $t_d + t_a$, is chosen as 18.5 μs, which corresponds the zero phase error crossing at 36 kHz to the original model to secure wider bandwidth. This time delay can be applied as a time advance as the zero phase approximation case.

2.3.2 Iterative Learning Control Design

Since the stabilized galvanometer scanner model $P(\mathrm{z})$ has a pair of non-minimum phase zeros, the model are approximated for the stable inversion methods. Zero-phase approximation ILC_{ZP} and the stable inversion with an input delay ILC_{TD} are investigated in this section. The ILC design is divided into two steps: stable learning filters L for the galvanometer scanner and Q filter design based on the modeling error.

For the design of inversion-based ILCs, the learning filters are designed by two different stable inversion methods. ILC_{ZP} is designed by Eq. (2.9) from the model with non-minimum phase zeros. For the conversion of continuous time model $\hat{P}(s)$ to the discrete time model $\hat{P}(\mathrm{z})$, Tustin's method is used since the stable region of the s-plane is exactly mapped into the stable region of the z plane. The learning filter of the zero-phase approximation is obtained by Eq. (2.9), i.e. $L_{ZP}(\mathrm{z}) = \hat{P}_{zp}^{-1}(\mathrm{z})$. ILC_{TD} uses the time delay approximation model with only minimum phase zeros in Eq. (2.10), i.e $L_{TD}(\mathrm{z}) = \hat{P}_{td}^{-1}(\mathrm{z})$. This time delay approximation is designed in the continuous time domain $\hat{P}(s)$ and the approximated continuous time model is converted to the discrete time model by Tustin's method as ILC_{ZP}. The learning gain ρ is set to 1 in both cases.

For the Q filter design of each ILC, a zero-phase 8th order Butterworth IIR filter is used as shown in Fig. 2.9. The frequency response of the robustness filter $Q(\mathrm{z})$ is designed to satisfy the convergence criterion (2.6) for all frequencies. Based on the measured Bode plot and the model error, the cutoff frequencies of the Q-filters for ILC_{ZP} and ILC_{TD} are determined as 20 kHz and 42 kHz, respectively, as marked in Fig. 2.8. The higher bandwidth is achieved with ILC_{TD} due to a smaller stable inversion error than the zero phase error approximation in ILC_{ZP}. The benefits of the broader control bandwidth of ILC are demonstrated in the following section.

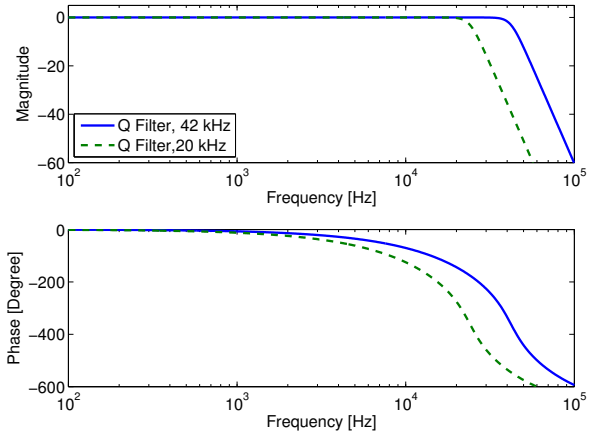

Figure 2.9: Q filter for ILC_{ZP} *and* ILC_{TD}*, which are 8th order Butterworth IIR filter with 20 kHz and 42 kHz, respectively.*

2.4 Experimental Results

2.4.1 Implementation of ILC

For ILC implementation for the galvanometer scanner, a data acquisition system consisting of a DAQ card (DAQ-2010, ADLink Technology Inc., New Taipei City, Taiwan) is used. The measurement data are processed in Labview (National Instruments Co., Austin, Texas, USA) that is capable of the seamless streaming of the scanning signal [160] while calculating the updated scanning signal via ILC in Matlab. The angle of the mirror is sampled and recorded from the encoder output at a sampling frequency f_s of 526 kHz, i.e. the sampling time T_s of 1.9 μs. Accordingly, the delays in the discrete time learning filters are set as $k_d = 1$ and $k_a = 9$ samples.

For output measurements for the ILC update, the encoder signals of 512 triangular scans are averaged to reduce the influence of measurement noise [85]. The reference trajectory $\mathbf{y}^{ref}$ is used for the initial ILC input $\mathbf{u}^0$, and the learning of ILC stops at the 20th iteration, when ILC is already converged to its error limit.

2.4.2 Preparation of the Triangular Scanning Reference

A triangular scanning reference is desirable for a fast scanning, however, it include high frequency components due to the sharp turnaround [149, 161], which can lead to errors in the active scan area and a large input peak [161]. To reduce the unwanted high frequency errors, input-shaping methods [162, 163] can be used. For high speed atomic force microscopy, an input shaping method reduces the resonance in the active scan area and results in less image distortion [164]. For the galvanometer scanner, polynomials and triangular functions are studied for the effective turnaround [47].

To reduce the high frequency content of the reference signal, an input shaping filter is implemented in the form of an finite impulse response (FIR) filter for the triangular scanning

reference [161, 162]. FIR filters have desirable properties such as a linear phase all over the frequency and a constant group delay, which can be easily corrected by zero phase filtering in advance. The innate finite response structure, only finite number of samples near the turnaround is smoothened while the active scanning region is kept linear.

In the experiments, a 5th order FIR filter is used as follows

$$R(\mathrm{z}) = \frac{10}{32}\mathrm{z}^{-3} + \frac{5}{32}\mathrm{z}^{-2} + \frac{1}{32}\mathrm{z}^{-1} + \frac{1}{32}\mathrm{z}^{0} + \frac{5}{32}\mathrm{z}^{1} + \frac{10}{32}\mathrm{z}^{2}. \tag{2.11}$$

This FIR filter has the first zero at 63 kHz and the magnitude is $-6.3dB$ at 42 kHz. This FIR filter only change ± 5 samples of the linear scan region near the turnaround.

For evaluation of ILC three pre-filtered triangular reference signals with a scanning rate of 1.03 kHz (512 samples per a triangular scan), 2.06 kHz (256 samples per a triangular scan) and 4.11 kHz (128 samples per a triangular scan) are examined, which corresponds to 2056, 4112, and 8224 lines per second for scanning laser microscopes. The scanning amplitudes in optical angle are 0.235°, 0.185° and 0.111°, respectively.

2.4.3 Tracking Results

Experimental results of the designed ILC_{ZP} and ILC_{TD} are presented for the galvanometer scanner and compared with the closed-loop controller (CLC_{UC}, CLC_{CP}) of the conventional servo driver.

Fig. 3.8 shows the scanning angle and error trajectory for each controller at the 2.06 kHz scan rate, i.e. 4112 lines per second. Fig. 3.8(a) shows the final angle trajectory of ILC_{TD} (black solid line), ILC_{ZP} (magenta dashed line), and CLC_{UC} (green dash-dot line). First, both ILCs automatically track the trajectory without any phase lag and magnitude error while the CLC_{UC} has about a 74 μs time lag and 40% gain mismatch. Both ILC can compensate this phase and gain mismatch while the performance of ILC can outperform the conventional feedback controller, even when this gain and phase margin is compensated by prior knowledge in advance [146]. Therefore, the closed loop controller with the phase and magnitude mismatch compensation, denoted by CLC_{CP} (blue dash-dot line in Fig. 3.8(a)), is used for further comparison. The gain and phase lag are compensated based on the position and average gradient of 11 data points that are centered closely to the zero degree line, denoting the center of the scanning laser microscope image. Assuming that the system is linear, CLC_{CP} obtains the same results shifting the reference and gain adjustments.

Though the phase and gain errors are compensated for CLC_{CP}, ILCs outperform CLC_{CP} with a better tracking performance by a smaller RMS error as well as a smaller peak to peak tracking error. Fig. 3.8(b) shows that the error trajectory of ILC_{TD} and ILC_{ZP} are much smaller than CLC_{CP}. The high bandwidth of ILC_{TD} leads to the smallest error, followed by ILC_{ZP} and the largest error for CLC_{CP} in all cases. The peak to peak errors of ILC_{TD} and ILC_{ZP} are up to 46 and 8 times smaller than that of CLC_{CP}, respectively. For the RMS errors the improvements are even better. At 2.06 kHz scan rate, the RMS error of ILC_{TD} is 73 times smaller than that of CLC_{CP}. ILC_{ZP} shows less improvement of tracking performance than ILC_{TD}, but its RMS errors are also up to 10 times smaller than that of CLC_{CP}.

Not only does ILC result in smaller errors, but it also enables the rejection of periodic disturbance and nonlinearity compensation. The control signals as shown in Fig. 3.8(c) il-

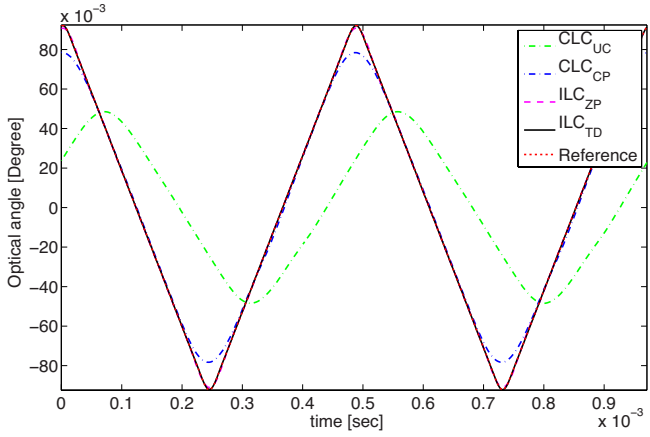

(a) Output trajectory

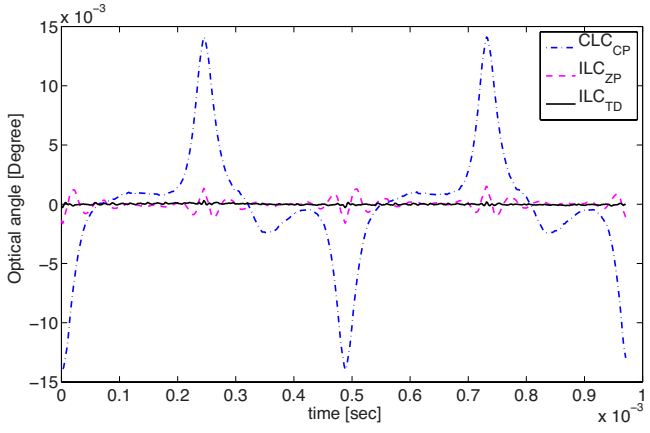

(b) Residual error trajectory

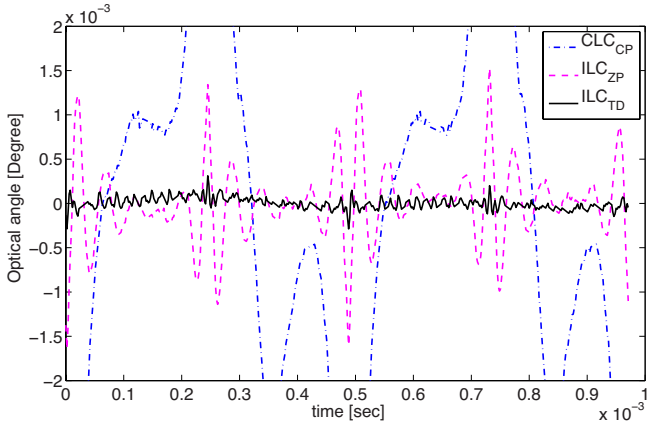

(c) Zoomed residual error trajectory

Figure 2.10: Output and error trajectories of ILC_{TD} *(black solid line),* ILC_{ZP} *(magenta dashed line),* CLC_{CP} *(blue dash-dot line) and* CLC_{UC} *(green dash-dot line) at a 2.06kHz scanning frequency (4112 lines per second). The error trajectory is zoomed to better compare the error between* ILC_{TD} *and* ILC_{ZP}.

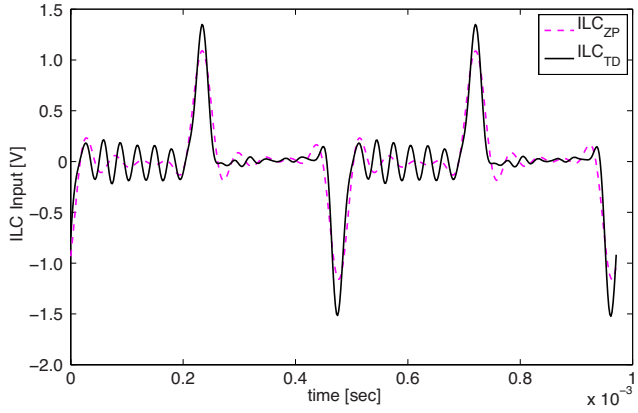

Figure 2.11: Input trajectories of ILC_{TD} *(black solid line) and* ILC_{ZP} *(magenta dashed line) at a 2.06kHz scanning frequency.*

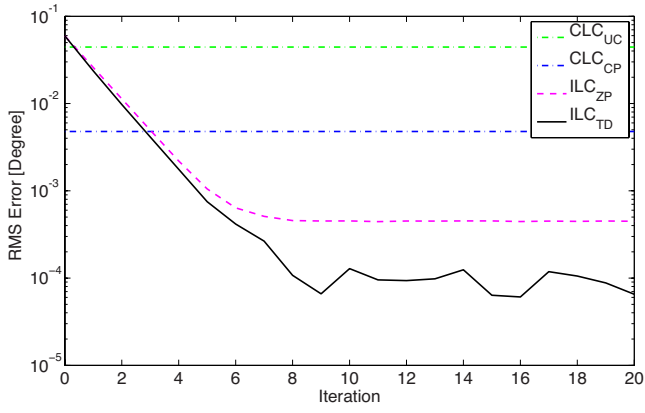

Figure 2.12: RMS error as a function of ILC iterations

Table 2.2: The final RMS error (e_{rms}) and peak to peak error (e_{pp}) for different controllers, taken with respect to the amplitude of the reference triangle command at three different scan rates.

e_{rms} (e_{pp}) [%]	1.03 kHz	2.06 kHz	4.11 kHz
CLC_{UC}	15.84 (56.48)	24.04 (58.41)	38.22 (53.84)
CLC_{CP}	0.64 (4.85)	2.59 (11.93)	5.29 (11.70)
ILC_{ZP}	0.090 (0.88)	0.24 (1.35)	0.83 (2.02)
ILC_{TD}	0.026 (0.13)	0.035 (0.25)	0.11 (0.36)

lustrate that the final inputs between the trace and retrace scan region are asymmetric. This indicates that there are nonlinearities or a periodic disturbance in the galvanometer actuation. Besides, the error trajectories of the CLC_{CP} in Fig. 3.8(b) illustrates the asymmetrical residual errors between the trace and retrace scan region, which leads to a misalignment of the individual lines in the image.

Fig. 3.9 illustrates the evolution of the RMS error along the iteration axis for ILC at 2.06 kHz scan rate. Four to five more iterations are required for ILC_{TD} to reach the final value in all cases than for ILC_{ZP}, but the convergence speed of both ILC is similar and ILC_{TD} can attain the smaller RMS error. The RMS errors of the CLC_{UC} and CLC_{CP} are given for comparison. The final RMS errors and peak to peak errors of 1.03 kHz, 2.03 kHz, and 4.03 kHz is summarized in Table 4.1. For the case of ILC_{TD} scanning at 4112 lines per second the RMS error is a factor of 73 smaller than controlling the galvanometer scanner with the conventional feedback controller, clearly demonstrating that ILC enables scanning at a high speed with a significantly reduced tracking error.

2.5 Conclusion

Iterative learning control (ILC) schemes are proposed for a galvanometer scanner in scanning laser microscopy, achieving a fast, linear, and accurate bidirectional scanning. Two inversion types of ILC, zero phase approximation ILC_{ZP} and delay approximation ILC_{TD}, are designed based on the linear model of the stabilized galvanometer scanner system with non-minimum phase zeros and implemented with a control bandwidth of 20 kHz and 42 kHz, respectively. The designed ILCs are evaluated using a high performance galvanometer scanner at high scanning speed, and are compared to a conventional closed loop controller. Both ILCs outperform the conventional closed loop control in terms of the root mean square (RMS) error and peak to peak tracking error. ILC_{TD} show an RMS error that is up to 73 times smaller as compared to the gain and phase corrected closed loop control CLC_{CP} of the commercial system. ILC_{ZP}, which has a narrower control bandwidth than ILC_{TD}, outperforms the CLC_{CP} by an up to 10 times smaller RMS error. This result clearly demonstrates the potential of ILC for fast and accurate motion control of the galvanometer scanner at scanning speeds, enabling distortion free imaging at improved temporal resolution in conventional scanning laser microscopy.

Chapter 3

Transformation based ILC of Galvanometer Scanner *

A transformation-based iterative learning control (ILC) approach is proposed to achieve accurate image scanning for the non-collocated dynamics of a galvanometer scanner. The non-collocation between the encoder and beam scanning mirror results in a tracking error of the actual beam position although the encoder measurement matches the reference signal. The proposed ILC is extended from the conventional ILC design by adding a reference transformation filter, which is based on the transfer functions between the measured and the controlled output. An error analysis shows that the proposed method can reduce the error of the actual controlled output, especially for applications of a large tracking reference such as image scanning. Experimental results with the proposed ILC show a better tracking accuracy as compared to conventional ILC design with non-collocated sensing.

3.1 Introduction

Temporal resolution of confocal laser scanning microscopy has been improved for recording rapid biological processes such as a cardiac activity and the growth of intracellular structures [11, 12, 145]. To achieve the high temporal resolution, fast scanning devices such as a resonance scanner [51], a spinning disk [13], an acousto-optic deflector [52] have been applied. Changing the pinhole structure for a multiple illumination and detection has also been studied for fast imaging [11, 58, 59, 165].

In addition, there are approaches that improve control for fast confocal imaging with a conventional galvanometer based optical scanner. Galvanometer based optical scanners are most popular scanning systems for biological laser scanning confocal microscopes, which are usually provided as a default scanner [1, 144]. A modified bidirectional scanning function is studied for fast and undistorted imaging and applied to optical coherent tomography

*Part of chapter is published,
H. W. Yoo, S. Ito, M. Verhaegen, and G. Schitter. Transformation-based iterative learning control for non-collocated sensing of a galvanometer scanner. In 2013 European Control Conference (ECC), pages 1204-1209. IEEE, July 2013.

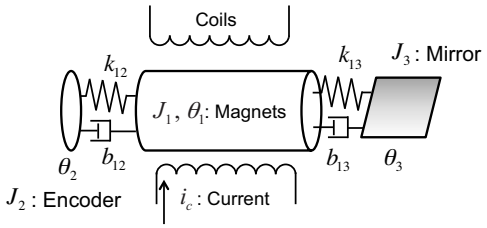

Figure 3.1: A mechanical model of a moving magnet galvanometer scanner. The rotor of a galvanometer scanner consists of a magnet, a mirror and an encoder connected by the shaft. This shaft can be regarded as a spring (K_{12} and K_{13}) with damping (B_{12} and B_{13}) causing non-collocation between the encoder and the mirror.

[17, 45, 47]. In a controller design of the galvanometer scanner, an indirect run to run (R2R) digital control has been studied for more accurate unidirectional, bidirectional, arbitrary scanning functions [81, 146]. Iterative learning control (ILC) is proposed for fast and accurate scanning confocal microscopy [140]. Due to non-collocation between the galvanometer scanner's encoder sensor and the actual scanning mirror, however, the beam position corresponding to the scanning mirror shows a distinct mismatch from the encoder sensor output at a high frequency, which results in image distortion in high speed microscope imaging with a galvanometer scanner. For measuring the actual beam position, an additional sensor requires not only cost and space, but a beam sampler is also not suitable for biological confocal fluorescence microscopy, because of the limited number of photons in fluorescence imaging and the risk of photobleaching when increasing the laser power for a better image contrast.

In this chapter, a transformation-based iterative learning control is proposed to compensate for the non-collocated sensing when applying iterative learning control [141]. Non-collocation between the desired and the measured output has been studied by an observer-based structure in [166, 167] and applied to a robot control. Their method estimates the controlled output from the measured output by applying the transfer function between these two outputs, and their tracking error performance is intensively analyzed. Instead of filtering the output or adding an observer, the proposed method modifies the reference signal to the desired measured output reference based on the internal model theorem [168]. This approach is simple in design, as the ILC and the reference transformation filter can be designed separately, even though the convergence criterion is still the same with conventional ILC. The proposed method is also computationally efficient since the reference transformation can be done once and in advance for a given reference. The final error with a bounded measurement uncertainty is analyzed. Experimental results with a commercial galvanometer scanner demonstrate the benefits of the proposed ILC, and are compared to the conventional ILC based on both the measured and controlled output directly.

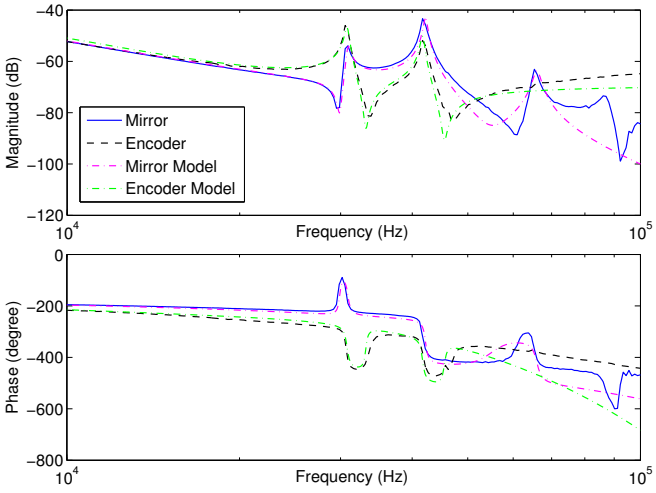

Figure 3.2: Bode plot of the encoder and mirror position of the closed loop galvanometer with respect to the galvanometer input. The position of the anti-resonances varies for the two different outputs, which shows that the mirror position is not collocated with the encoder. The DC offset of the mirror position is adjusted. The fitted model for each output is discussed in Section 3.4.2.

3.2 Non-collocated Dynamics of Galvanometer Scanner

3.2.1 Structure of Galvanometer Scanner

Fig. 3.1 shows a mechanical model of a moving-magnet galvanometer scanner, which is typically used in confocal laser scanning microscopy [1, 144]. A scanning mirror is attached at one end of the shaft for beam positioning. At the other end, an encoder is placed for the measurement of the deflection angle. The magnets with the encoder and the mirror are rotated by the Lorentz force exerted by the current through the surrounded fixed coils.

Fig. 3.2 illustrates measured Bode plots of the encoder output and mirror position of the stabilized galvanometer scanner of Fig. 3.1, measured by a Dynamic Signal Analyzer (HP3562, Agilent Technologies, Santa Clara, CA, USA) using a swept-sine signal as an input. At a low frequency, the shaft is stiff enough and both output signals follow the mass line of the total mass. At high frequencies, however, the encoder and the scanning mirror are decoupled due to limited stiffness of the shaft as shown in Fig. 3.1. This can be explained by a combination of multi-body dynamical systems [169], which is discussed in the following subsection.

3.2.2 Model of Galvanometer Scanner

For the analytical description of three-body structure in Fig. 3.1, the balance of force for each body is derived as the two body mass spring system [149]. The magnet is the source of the input by the current i_c with a torque constant τ, while the encoder and the mirror follows the motion of the magnet. By the second law of Newton, these motions lead to the

following second order ordinary differential equations as

$$\begin{aligned} J_1\frac{d^2\theta_1}{dt^2} &= \tau i_c - b_{12}\left(\frac{d\theta_1}{dt}-\frac{d\theta_2}{dt}\right)-b_{13}\left(\frac{d\theta_1}{dt}-\frac{d\theta_3}{dt}\right) \\ &- k_{12}(\theta_1-\theta_2)-k_{13}(\theta_1-\theta_3), \end{aligned} \tag{3.1}$$

$$J_2\frac{d^2\theta_2}{dt^2} = -b_{12}\left(\frac{d\theta_2}{dt}-\frac{d\theta_1}{dt}\right)-k_{12}(\theta_2-\theta_1), \tag{3.2}$$

$$J_3\frac{d^2\theta_3}{dt^2} = -b_{13}\left(\frac{d\theta_3}{dt}-\frac{d\theta_1}{dt}\right)-k_{13}(\theta_3-\theta_1). \tag{3.3}$$

By applying Laplace transform to (3.1)-(3.3), the transfer functions from the current to the each angle of the magnet, mirror, and encoder are as follows,

$$\frac{\Theta_1(s)}{I_c(s)} = \frac{\tau(J_2s^2+b_{12}s+k_{12}))(J_3s^2+b_{13}s+k_{13})}{s^2(\alpha s^4+\beta s^3+\gamma s^2+\delta s+\epsilon)}, \tag{3.4}$$

$$\frac{\Theta_2(s)}{I_c(s)} = \frac{\tau(k_{12}+b_{12}s)(J_3s^2+b_{13}s+k_{13})}{s^2(\alpha s^4+\beta s^3+\gamma s^2+\delta s+\epsilon)}, \tag{3.5}$$

$$\frac{\Theta_3(s)}{I_c(s)} = \frac{\tau(k_{13}+b_{13}s)(J_2s^2+b_{12}s+k_{12}))}{s^2(\alpha s^4+\beta s^3+\gamma s^2+\delta s+\epsilon)}, \tag{3.6}$$

where

$$\alpha = J_1J_2J_3, \tag{3.7}$$

$$\beta = (J_1(J_2b_{13}+J_3b_{12})+J_2J_3(b_{12}+b_{13})), \tag{3.8}$$

$$\gamma = (J_1(J_2k_{13}+J_3k_{12})+J_2J_3(k_{12}+k_{13})+b_{12}b_{13}(J_1+J_2+J_3)), \tag{3.9}$$

$$\delta = (J_1+J_2+J_3)(b_{12}k_{13}+b_{13}k_{12}), \tag{3.10}$$

$$\epsilon = k_{12}k_{13}(J_1+J_2+J_3). \tag{3.11}$$

At low frequencies, i.e. s is small, all the transfer functions show the standard mass-line by the sum of all inertias as

$$\left.\frac{\Theta_1(s)}{I_c(s)}\right|_{s\to 0} \approx \left.\frac{\Theta_2(s)}{I_c(s)}\right|_{s\to 0} \approx \left.\frac{\Theta_3(s)}{I_c(s)}\right|_{s\to 0} \approx \frac{1}{s^2(J_1+J_2+J_3)}. \tag{3.12}$$

By assuming that a small damping in the each connection compared to the stiffness, i.e. $b_{12} \ll k_{12}$ and $b_{13} \ll k_{12}$. The transfer functions at high frequencies, i.e. at high values of s, are approximately by

$$\left.\frac{\Theta_1(s)}{I_c(s)}\right|_{s\to\infty} \approx \frac{1}{J_1s^2}, \left.\frac{\Theta_2(s)}{I_c(s)}\right|_{s\to\infty} \approx \frac{k_{12}}{J_1J_2s^4}, \left.\frac{\Theta_3(s)}{I_c(s)}\right|_{s\to\infty} \approx \frac{k_{13}}{J_1J_3s^4}. \tag{3.13}$$

This means that the angles of the magnet, the mirror, and the encoder are synchronized at the low frequencies, while the encoder and mirror at the high frequencies unable to follow the rotation of the magnet, i.e. decoupling of the mirror and the encoder. From (3.5)-(3.6) the anti-resonance of the angle of the encoder θ_2 and the mirror θ_3 is determined by the

other side of inertia as

$$f_{a_{\theta_2}} = \frac{1}{2\pi}\sqrt{\frac{k_{13}}{J_3}},\ f_{a_{\theta_3}} = \frac{1}{2\pi}\sqrt{\frac{k_{12}}{J_2}} \tag{3.14}$$

where $f_{a_{\theta_2}}$ and $f_{a_{\theta_3}}$ denote the anti-resonance frequency of the mirror angle θ_2 and the encoder angle θ_3. This means that the order of decoupling of the mirror and the encoder from the magnet is determined by the inertia and the stiffness of the other end, i.e. the encoder and the mirror, respectively. For example, by assuming that the stiffness of the shaft is similar at the both end, i.e. $k_{12} \approx k_{13}$, the anti-resonance frequency is solely determined by the inertia of the mirror J_2 and the encoder J_3. In this case the body with large inertia will cause the first anti-resonance at the lower frequency and the anti-resonance is measured in the motion of the body with the small inertia. Similarly, the second anti-resonance at the higher frequency is caused by the body with small inertia and is measured in the motion of the body with the large inertia.

The resonances in (3.4)-(3.6) is difficult to analyze as it is since it is 4th order equation with full parameters. Assume that the torsional stiffness and damping of the connection to the mirror and the encoder with the magnet, i.e. $k_{12} = k_{13} = k_l$ and $b_{12} = b_{13} = b_l$mass are only factor that influence the resonances and anti-resonances. Without changing the roots of the characteristic equation of (3.4)-(3.6), define new coefficients by applying $1/(J_1+J_2+J_3)$ for all coefficients in (3.7)-(3.11) as

$$\frac{1}{J_1+J_2+J_3}\left(\alpha s^4+\beta s^3+\gamma s^2+\delta s+\epsilon\right) = \left(\alpha_s s^4+\beta_s s^3+\gamma_s s^2+\delta_s s+\epsilon_s\right), \tag{3.15}$$

where

$$\begin{aligned}
\alpha_s &= \frac{J_1J_2J_3}{(J_1+J_2+J_3)}, && (3.16)\\
\beta_s &= b_l\frac{(J_1J_2+J_1J_3+2J_2J_3)}{(J_1+J_2+J_3)}, && (3.17)\\
\gamma_s &= k_l\frac{(J_1J_2+J_1J_3+2J_2J_3)}{(J_1+J_2+J_3)}+b_l^2, && (3.18)\\
\delta_s &= 2b_lk_l, && (3.19)\\
\epsilon_s &= k_l^2, && (3.20)
\end{aligned}$$

Let define effective inertias J_{M1} and J_{M2} and assume that the characteristics equation is given as the following form,

$$\begin{aligned}
&\left(J_{M1}s^2+b_ls+k_l\right)\left(J_{M2}s^2+b_ls+k_l\right)\\
=\ & J_{M1}J_{M2}s^4+b(J_{M1}+J_{M2})s^3+(k(J_{M1}+J_{M2})+b_l^2)s^2+2b_lk_ls+k_l^2. \qquad (3.21)
\end{aligned}$$

Since (3.15) is the same with (3.21), J_{M1} and J_{M2} are the solutions of the following second order equation as

$$0 = (J_1+J_2+J_3)x^2-(J_1J_2+J_1J_3+2J_2J_3)x+J_1J_2J_3, \tag{3.22}$$

and the solutions are given (3.24)-(3.26). Since $\Xi > 0$ for all positive J_1, J_2, and J_3, all the transfer functions (3.4)-(3.6) always has two distinctive pairs of resonances as (3.24) and (3.26).

$$f_{r1} = \frac{1}{2\pi}\sqrt{\frac{k_l}{J_{M1}}},\ f_{r2} = \frac{1}{2\pi}\sqrt{\frac{k_l}{J_{M2}}}, \tag{3.23}$$

where

$$J_{M1} = \frac{(J_1J_2 + J_1J_3 + 2J_2J_3) + \sqrt{\Xi}}{2(J_1 + J_2 + J_3)}, \tag{3.24}$$

$$J_{M2} = \frac{(J_1J_2 + J_1J_3 + 2J_2J_3) - \sqrt{\Xi}}{2(J_1 + J_2 + J_3)}, \tag{3.25}$$

$$\Xi = J_1^2(J_2 - J_3)^2 + 4J_2^2J_3^2. \tag{3.26}$$

Since the first effective inertia is larger than the second effective inertia, $J_{M1} > J_{M2} > 0$, the resonances frequencies from the first effective inertia is lower than the resonance frequencies from the second effective inertia, i.e. $f_{r1} < f_{r2}$.

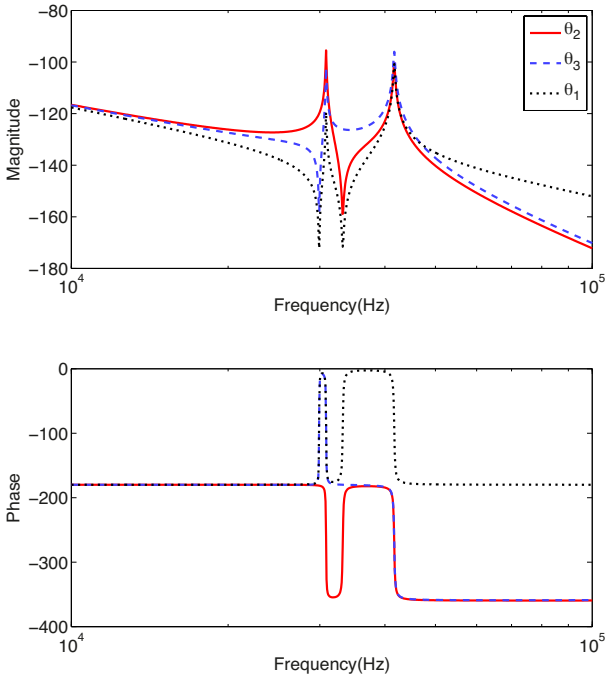

Figure 3.3: The simulated Bode plot of the system with $k_{13} = 2k_{12}$ and $J1 = 3.876J_2$. The resonance peaks are 30.8 kHz and 41.7 kHz, which are identical to the resonance and antiresonance peaks of the measurements in Fig. 3.2.

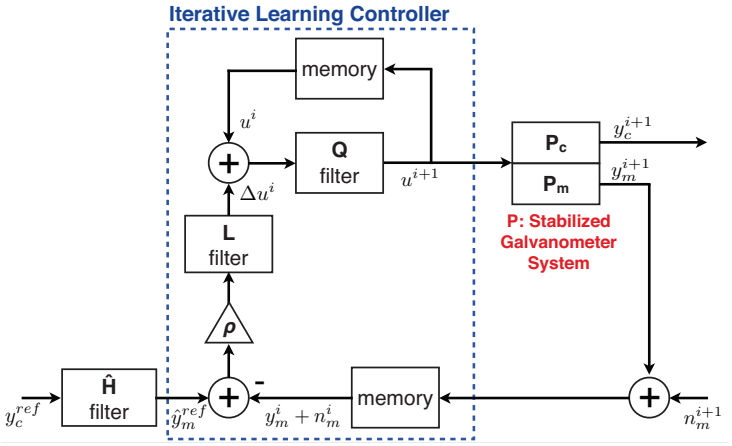

Figure 3.4: A structure of transform-based iterative learning control with non-collocated sensing. The stabilized galvanometer scanning system has two outputs, a measured output from an encoder and a controlled output from an actual beam position. The differences in dynamics are represented by each transfer functions, P_m, P_c. The reference transformation filter $\hat{H}$ is applied to achieve the desired reference of controlled output $\mathbf{y}_c^{ref}$ using an ILC with measured output.

In practice, the spring constant and damping constants of each link are not equal and need a refinement by relaxing the condition of $k_{12} = k_{13}$. Fig. 3.3 shows a simulated Bode plot of the galvanometer scanner with $k_{13} = 2k_{12}$ and $J_1 = 3.876J_2$, which are obtained by matching the distance between resonances and adjusting the relative spring constants of each end. For example by increasing k_{13} compared to k_{12}, the first resonance moves toward the first anti-resonance. J_1 is chosen based on the distance of the two resonances. The resonance peaks are 30.8 kHz and 41.7 kHz, which is identical to the measured resonance peaks in Fig. 3.2. This results in complete fitting of the resonances and anti-resonances based on the lumped model (3.4)-(3.6) for the actual galvanometer scanner from two bode plot measurements of the encoder θ_2 and the mirror θ_3.

This analysis explains resonance and anti-resonances in Fig. 3.2, showing that the encoder output and the scanning mirror angle may not have the same response, resulting in non-collocated sensing. The difference become evident as the frequency is getting higher, beyond 20 kHz, where the ILC tries to compensate the harmonics. Especially the anti-resonance at 33 kHz appears only in the Bode plot for the mirror output, which is the clear evidence of this decoupling. This non-collocated sensing from the encoder output causes uncompensatable errors by a common ILC, limiting its tracking performance. A transformation-based ILC is proposed in the following section, given with an error analysis.

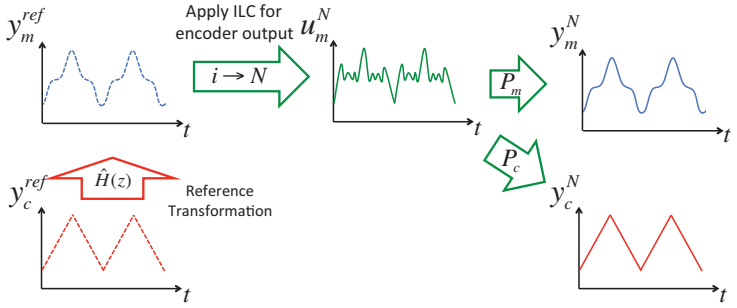

Figure 3.5: A concept of the transformation-based ILC. The reference is modified based on the reference transformation filter $\hat{H}$ and applied to the ILC with the measured output. If the ILC reaches the final iteration N that ILC does not reduce the tracking error anymore by iteration, the controlled output also converges to the desired reference by the non-collocation between two systems of the measured and controlled output.

3.3 Transformation-based Iterative Learning Control for Non-collocated Sensing

Fig. 3.4 shows the structure of the transformation-based iterative learning control with a stabilized galvanometer scanner [140, 153]. The structure leads to the following equations

$$\mathbf{u}^{i+1}[k] = Q(q)\left(\mathbf{u}^i[k] + \rho L(q)\left(\mathbf{e}_m^i[k] - \mathbf{v}_m^i[k]\right)\right), \tag{3.27}$$

$$\mathbf{e}_m^i[k] = \hat{\mathbf{y}}_m^{ref}[k] - \mathbf{y}_m^i[k], \tag{3.28}$$

$$\mathbf{e}_c^i[k] = \mathbf{y}_c^{ref}[k] - \mathbf{y}_c^i[k], \tag{3.29}$$

$$\mathbf{y}_m^i[k] = P_m(q)\mathbf{u}^i[k], \tag{3.30}$$

$$\mathbf{y}_c^i[k] = P_c(q)\mathbf{u}^i[k], \tag{3.31}$$

where $\mathbf{u}^i[k]$, $\mathbf{y}_c^i[k]$, $\mathbf{y}_m^i[k]$, $\mathbf{e}_c^i[k]$ and $\mathbf{e}_m^i[k]$ denote the ILC input, controlled output, measured output, tracking error of the beam position, and measured tracking error of the encoder signal at the discrete time k in the i-th trial. $\rho L(q)$, $Q(q)$, and $P_m(q)$ denote the LTI dynamics of the learning filter with a scalar learning gain ρ, the Q-filter, and the dynamics of the galvanometer scanner with the forward time-shift operator q, i.e. $\mathbf{x}[k+1] = q\mathbf{x}[k]$. $\hat{\mathbf{y}}_m^{ref}$ and $\mathbf{y}_c^{ref}$ are the desired reference trajectories for the measured output and controlled output, respectively. $\mathbf{v}_m^i[k]$ is a measurement noise at the measured output. It is assumed that the magnitude of the measurement noise at any frequency w and any iteration i is bounded by an arbitrary function δ, i.e. $|\mathbf{n}_m^i(\omega)| < \delta(\omega), \forall\omega$ and $\forall i$ [170]. The design of the learning filter $L(q)$ of a minimum phase SISO plant dynamics is simply obtained by the inversion of the system, which is called an inversion based ILC. The Q filter is designed to cut off the learning at a certain frequency considering the convergence of ILC [154].

The goal of the transformation-based ILC is to minimize the tracking error of the beam position output via controlling the encoder measurement output by designing a reference

transformation filter $\hat{H}(q)$, i.e.

$$\hat{\mathbf{y}}_m^{ref}[k] = \hat{H}(q)\mathbf{y}_c^{ref}[k]. \tag{3.32}$$

Fig. 3.5 illustrates the concept of the transformation-based ILC. Based on the desired trajectory for the laser beam, the reference transformation filter generates a new reference for the encoder measured output. Once the ILC designed for the measured output converges to the transformed reference, the output representing the beam position follows the actual desired reference $\mathbf{y}_c^{ref}$. The boundedness of the final error of the ILC and of the bounded measurement noise is studied in Lemma 1 of [170]. Based on that, the following lemma provides the bounded final error of the proposed method.

Lemma 3.1 *The limit of residual controlled output error is bounded by the following affine function of the reference function $\mathbf{y}_c^{ref}(j\omega)$ and the noise effect $\delta(w)$,*

$$\begin{aligned}
|\mathbf{e}_c^{\infty}(j\omega)| &= \lim_{i\to\infty}|\mathbf{e}_c^{i}(j\omega)| \\
&\leq \left(\left|H^{-1}(j\omega)\hat{H}(j\omega)\frac{1-Q(j\omega)}{1-\Phi(j\omega)}\right| + \left|1-H^{-1}(jw)\hat{H}(j\omega)\right|\right)|\mathbf{y}_c^{ref}(j\omega)| \\
&+ \left|H^{-1}(j\omega)\frac{P_m(j\omega)Q(j\omega)L(j\omega)}{1-\Phi(j\omega)}\right|\delta(w), \qquad (3.33) \\
H(j\omega) &= P_m(j\omega)P_c^{-1}(j\omega), \qquad (3.34)
\end{aligned}$$

provided that the ILC with the measured output converges, i.e.

$$\Phi(j\omega) = Q(j\omega)(1-\rho P_m(j\omega)L(j\omega)) < 1, \forall\omega. \tag{3.35}$$

□

Proof : From (3.28), (3.30) and (3.27), the measured error dynamics along iteration axis is given as follows.

$$\begin{aligned}
\mathbf{e}_m^{i+1}[k] &= Q(q)(1-\rho P_m(q)L(q))\mathbf{e}_m^{i}[k] \\
&+ \hat{H}(q)(1-Q(q))\mathbf{y}_c^{ref}[k] \\
&+ \rho P_m(q)Q(q)L(q)\mathbf{v}_m^{i}[k], \qquad (3.36)
\end{aligned}$$

(3.34) can be rewritten by $y_c^i = H^{-1}y_m^i$ from (3.30) and (3.31). Based on this, the controlled tracking error (3.29) can be rewritten by the measured tracking error (3.28) regarding the transformed reference (3.32) as

$$\mathbf{e}_c^{i}[k] = H^{-1}(q)\mathbf{e}_m^{i}[k] + \left(1-H^{-1}(q)\hat{H}(q)\right)\mathbf{y}_c^{ref}[k]. \tag{3.37}$$

Assuming that the ILC converges, the final controlled tracking error in the frequency domain can be bounded as follows [170].

$$\lim_{i\to\infty}\mathbf{e}_m^{i}(j\omega) \leq \hat{H}(j\omega)\frac{1-Q(j\omega)}{1-\Phi(j\omega)}\mathbf{y}_c^{ref}(j\omega)$$

$$+ \quad \frac{P_m(j\omega)Q(j\omega)L(j\omega)}{1-\Phi(j\omega)}\delta(w). \tag{3.38}$$

Substituting (3.38) with (3.37), the final controlled output error is obtained,

$$\begin{aligned}\lim_{i\to\infty}\mathbf{e}_c^i(j\omega) \quad &\leq \quad H^{-1}(j\omega)\hat{H}(j\omega)\frac{1-Q(j\omega)}{1-\Phi(j\omega)}\mathbf{y}_c^{ref}(j\omega)\\ &+ \quad \left(1-H^{-1}(j\omega)\hat{H}(j\omega)\right)\mathbf{y}_c^{ref}(j\omega)\\ &+ \quad H^{-1}(j\omega)\frac{P_m(j\omega)Q(j\omega)L(j\omega)}{1-\Phi(j\omega)}\delta(w).\end{aligned} \tag{3.39}$$

By triangular inequality, (3.33) is obtained from (3.39). □

Remark 3.2 Assuming that the desired controlled output reference and the complement of Q filter are orthogonal by design, i.e. $(1-Q(jw))\,\mathbf{y}_c^{ref}(j\omega)=0, \forall\omega$, the design of $\hat{H}(j\omega)$ is simply obtained by $H(j\omega)$. □

Remark 3.3 The final tracking error of the non-collocated system with a conventional ILC is obtained by applying $\hat{H}(j\omega)=1$. Assuming an ideal case that a best design of the ILC is given with the perfect knowledge of the system $P_m(j\omega)$, the reference being designed to be orthogonal to the Q filter and $\hat{H}=H$, and zero noise $\mathbf{v}_m^i[k]=0$, $\forall i$ and $\forall k$, the error by non-collocation sensing is rewritten as follows:

$$|\mathbf{e}_c^*(j\omega)| \quad \leq \quad |\mathbf{e}_m^*(j\omega)|+|1-H^{-1}(j\omega)||\mathbf{y}_c^{ref}(j\omega)|, \tag{3.40}$$

where $\mathbf{e}_c^*$ and $\mathbf{e}_m^*$ denote the optimal tracking errors of the controlled output and measured output. This corresponds to the results presented in [166]. □

Remark 3.4 Since $H(j\omega)$ represents the difference in dynamics between the measured output and the controlled output, in conventional ILC whose measured output equals to the controlled output, (3.34) degenerates $H(j\omega)=1$. With $\hat{H}(j\omega)=1$, this cancels the second term in (3.33), i.e. $1-H^{-1}(j\omega)\hat{H}(j\omega)=0$, which leads to (5) in [170]. □

Corollary 3.3 shows that the reference transformation filter can provide a smaller error than conventional ILC when the filter is designed appropriately. Moreover, it also implies that the error of non-collocated sensing depends on not only the mismatch by non-collocation between measured and controlled output but also on the tracking reference. This means that the proposed reference transformation filter is more beneficial with a large varying tracking reference such as an imaging scanning application.

In implementation, the proposed reference transformation method is beneficial because of the simplicity of the design, without online computation for a given reference. The ILC can be designed and verified separately with the reference transformation filter, reducing the design effort and complexity. In addition, the computation of the transformation is only necessary when the reference changes. The following section presents experimental results for a fast and accurate beam scanning application with a high performance galvanometer scanner.

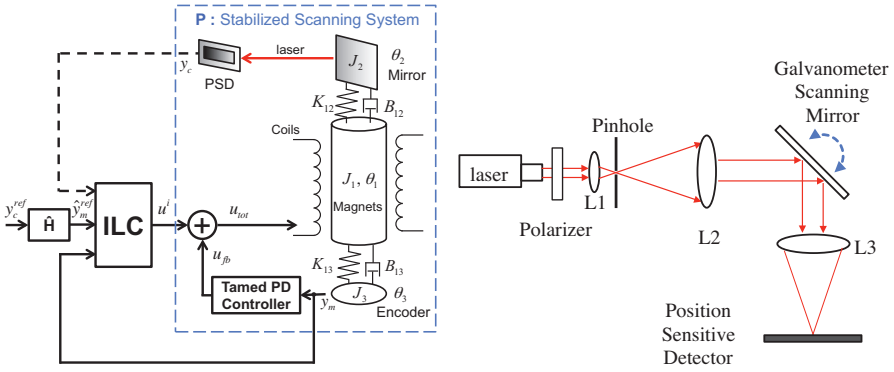

(a) Overall System (b) Optical System

Figure 3.6: (a) A diagram of the overall system with a PD stabilized scanning system. The marginally stable galvanometer scanner is stabilized by a tamed PD controller, which regulates the galvanometer at less than 1kHz. ILC is applied to the feedback stabilized galvanometer scanner up to a bandwidth of 42 kHz, i.e. far beyond the feedback bandwidth. The reference transformation filter $\hat{H}$ is applied to the desired reference of the controlled output y_c^{ref}. (b) Schematic of a beam scanning system to measure the mirror angle (θ_2) directly. The beam is filtered by a pinhole and expanded by the lenses L1 and L2 before and after the pinhole . The mirror angle is projected onto a lateral beam position at the position sensitive detector (PSD) by the lens L3.

3.4 Experimental Results

The transformation-based ILC is examined for a high performance galvanometer scanner (6210H, Cambridge Technology Inc., Lexington, MA, USA), which is a moving magnet type. Aforementioned, the encoder and actual mirror position, which is measured by the beam position, are non-collocated and show different dynamics. To illustrate the benefits of the transformation based ILC (ILC-PSDEst), a conventional ILC based on the encoder output without reference transformation (ILC-ENC) and based on the directly measured beam position output (ILC-PSD) are examined for comparison.

3.4.1 Experimental Setup

A high performance galvanometer scanner (6210H, Cambridge Technology Inc., Lexington, MA, USA) with a mirror for a laser beam diameter of 3*mm* is used, which is applied as laser scanning system in commercial laser confocal microscopes [1]. As shown in Fig. 3.6(a), the galvanometer is driven by a servo driver (MicroMax 671, Cambridge Tech). The server driver applies the total input u^{tot} as a coil current, which is the summation of the ILC signal u^i and the output of the analog tamed PD controller u^{fb}.

Fig. 3.6(b) shows a beam scanning system to measure the mirror angle of the galvanometer, θ_2, directly. A red laser is emitted from a laser diode and passes through the pinhole (25 μm, Edmund optics) with collimating lenses L1 (Aspheric Lens, f = 11 mm, Thorlabs) and

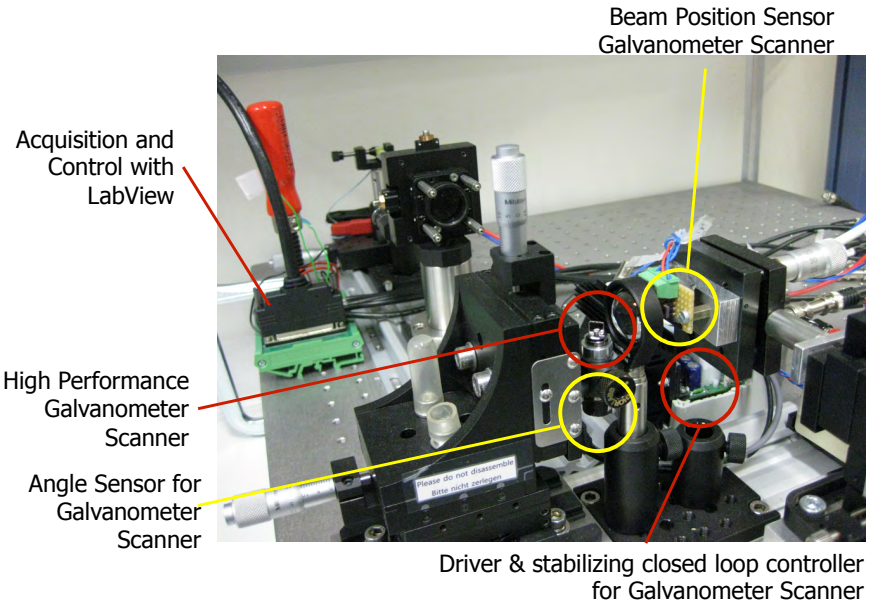

Figure 3.7: A picture of the experimental setup

L2 (plano convex lens, f = 40 mm, Thorlabs). Then the beam is reflected by the scanning mirror and collimated to a position sensitive detector (PSD, S3932, Hamamatsu Photonics K.K., Hamamatsu, Japan) by the lens L3 (Plastic Aspheric, f =17.50 mm, Edmund optics). Fig. 3.7 shows a picture of the experimental setup.

Both encoder output and PSD output are sampled with $f_s = 526$ kHz, $T_s = 1.9\ \mu s$ by a data acquisition card (DAQ-2010, ADLink Technology Inc., New Taipei City, Taiwan). The measurements are processed in Labview (National Instruments Co., Austin, TX, USA) that manages the seamless streaming of the scanning signal while calculating the updated scanning signal via ILC in Matlab. A 2.06 kHz FIR-filtered triangular signal with a scanning amplitude for an optical angle of 0.190° is used as a reference y^{ref} [140].

3.4.2 System Modeling and Inversion-based ILC Design

For design of an inversion based ILC, the plant models of encoder output P_{enc} and PSD output P_{psd} are necessary. From the measured Bode plots shown in Fig. 3.2, the models are obtained by manually fitting multiple second order systems with a time delay. For example, the transfer function from the system input, given by the current through the coils of the galvanometer, to the encoder output P_{enc} is given as follows [140].

$$P_{enc}(s) = \frac{K \prod_{i_z=1}^{n_z} (s^2 + 2\zeta_{i_z}\omega_{i_z}s + \omega_{i_z}^2)}{\prod_{i_p=1}^{n_p} (s^2 + 2\zeta_{i_p}\omega_{i_p}s + \omega_{i_p}^2)} e^{-t_d \times 10^{-6} s},$$

Table 3.1: Parameters of the Galvanometer Scanner Output Models

	Poles		Zeros		t_d	K
	$\omega_{i_p}/2\pi$	ζ_{i_p}	$\omega_{i_z}/2\pi$	ζ_{i_z}		
P_{ENC}	280	0.65	25000	0.6	18.5	3.32×10^{-4}
	30800	0.0087	33200	0.0069		
	41700	0.008	45500	0.0084		
P_{PSD}	250	0.65	29900	0.0069	5.5	2.81×10^{18}
	30900	0.0087	55000	0.07		
	42200	0.008				
	66000	0.015				

Table 3.2: The Final RMS Errors of ILC-ENC, ILC-PSD, and ILC-PSDEST

	ILC-ENC	ILC-PSD	ILC-PSDEst
RMS Error [10^{-3} °]	5.193	0.416	0.686

(3.41)

where K denotes a gain, t_d is a time delay in μs. n_p and n_z denotes the number of poles and zero, respectively. The transfer function from the same input to the actual position of the laser beam P_{psd} is represented in the same way with different parameters. Table 3.1 provides all parameters for each transfer function, and their Bode plots are shown by the magenta and the green dashed-dot line in Fig. 3.2.

The learning filter L is designed by inverting the respective model. The learning filter of L_{enc} of ILC-ENC and ILC-PSDEst is obtained by the inversion of P_{enc} [140]. The learning filter of ILC-PSD, L_{psd} is the inversion of the beam position model, P_{psd}^{-1}. For designing the Q-filter, a zero-phase 8th order Butterworth IIR filter with a bandwidth of 42kHz is used in all case, which is the position of the second resonance shown in Fig. 3.2. The learning gains of ILC-ENC, ILC-PSD, and ILC-PSDEst are set as 1, 0.2, and 0.5 respectively, considering the convergence of each ILC. The final trajectory is chosen where the ILC cannot improve the tracking performance anymore. The final iteration is chosen at the 30th iteration in ILC-ENC and ILC-PSDEst. For ILC-PSD, the 60th iteration is chosen, considering the slower convergence due to the smaller learning gain. The reference transformation filter is designed by dividing two models, i.e. $\hat{H} = P_{enc}/P_{psd}$.

3.4.3 Tracking Results

Fig. 3.8 shows the tracking result of ILC-ENC (magenta dashed line), ILC-PSD (blue dash-dot line), and ILC-PSDEst (black solid line) at the final iteration. The final root mean square (RMS) tracking error of each ILC is summarized in Table 4.1. Not only ILC-PSD but also ILC-PSDEst in Fig. 3.8(a) tracks without phase-lag while ILC-ENC has a constant lag which is mainly due the the time delay of the encoder sensor output discussed in Section II. Fig. 3.8(b) and Table 4.1 shows that ILC-PSDEst results in a 7.5 times smaller tracking error than ILC-ENC. However, the tracking error is still 1.65 times larger than ILC-PSD.

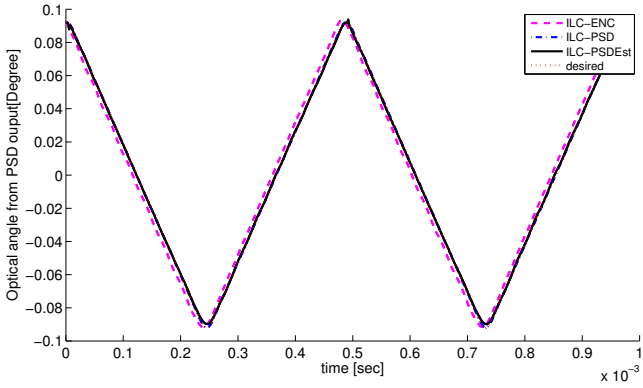

(a) Beam position trajectory

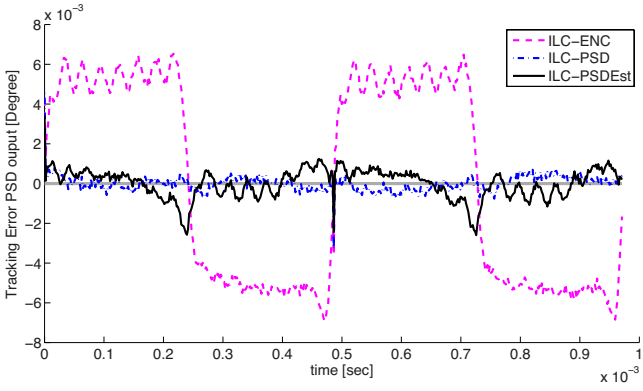

(b) Beam position error trajectory

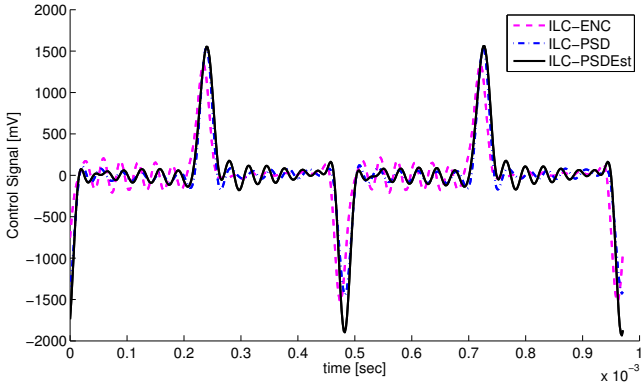

(c) Input Trajectory

Figure 3.8: Final trajectories of ILC − PSDEst *(black solid line),* ILC − PSD *(blue dash-dot line), and* ILC − ENC *(magenta dashed line) at a 2.06kHz scanning frequency.*

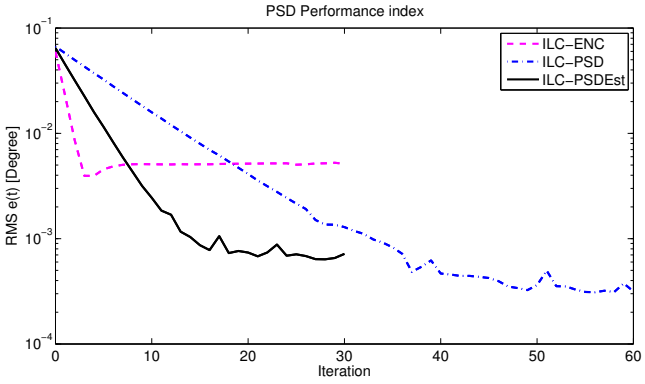

Figure 3.9: RMS beam position error along ILC iterations. The variation in the convergence speed is due to different learning gains, depending on the stability conditions for the various ILC inputs.

This is expected because ILC-PSD exploits full information of the desired output of the laser beam position, while ILC-PSDEst does not. ILC-PSDEst is still practically advantageous considering the fact that this beam position output is not available during operation of the confocal microscope. The control signal obtained via ILC also show that the input of ILC-PSDEst is more similar with ILC-PSD than ILC-ENC. The proposed ILC-PSD and its alternative solution ILC-PSDEst for the galvanometer scanner is beneficial for a fast and accurate imaging of scanning microscopes providing high temporal resolution and distortion free imaging.

3.5 Conclusion

In this chapter, a transformation-based iterative learning control approach is proposed for non-collocated sensing of a galvanometer scanner. The dynamic mismatch introduced by the non-collocation of the galvanometer scanner's outputs is addressed as a bottleneck of iterative learning control design. An analysis of multi-body dynamics of the galvanometer scanner is given based on the measured Bode plots. The proposed transformation-based iterative learning control improves the tracking performance of the beam position output using the measured encoder output, by transforming the desired scanning reference. The upper bound of the final tracking error is analyzed, and the desired transformation filter is driven derived under the assumption of zero output noise. Experimental results show that the proposed transformation-based ILC, ILC-PSDEst, reduces the tracking error up to 7.5 times as compared to ILC based directly on the encoder output, ILC-ENC, and is only 1.65 times larger than ILC with the directly measured laser beam position, which is used only for this evaluation but is not available when operating the confocal microscope. This proposed ILC is suitable for fast and distortion-free imaging in scanning confocal microscopy.

Chapter 4

Automated Adjustment of Spherical Aberration Correction *

Mismatch between the refractive indices of immersion media and glass coverslips introduces spherical aberrations in microscopes especially for high numerical aperture (NA) objectives. This chapter demonstrates an automated adjustment of the coverslip correction collar in scanning confocal microscopy to compensate for spherical aberrations due to coverslip thickness mismatch. With a motorized coverslip correction collar, the adjustment procedure consists of *xz* image scans, image processing, correction quality evaluation, the mismatch estimation, and eventually the optimal adjustment of the correction collar. For fast correction with less photodamage, coarse-fine Gaussian fitting algorithms are proposed and evaluated with various specimen for their estimation accuracy. The benefits of the proposed automated correction are demonstrated for various coverslips with biological specimens, showing the optimized resolution of the confocal microscope.

4.1 Introduction

Like most optical microscopy, the optimal resolution of confocal microscopy is theoretically limited by the diffraction of the light [1, 2]. Since the diffraction limit is defined by the wavelength and numerical aperture of the objective lens, high-numerical-aperture objective lenses are used for fining specimen imaging to obtain high spatial resolution. In a practical setting, however, the diffraction limited resolution can be hardly obtained for such high-numerical-aperture objective lenses due to the aberrations induced by mismatch between the refractive index of the objective lens and the refractive index of the specimen [19, 171].

One common aberration occurring in optical microscopy is spherical aberration, mainly

*Part of chapter is published,
Han Woong Yoo, Michel Verhaegen, Martin E van Royen, and Georg Schitter. Automated Adjustment of Aberration Correction in Scanning Confocal Microscopy. In IEEE International Instrumentation and Measurement Technology Conference, pages 1083-1088, 2012.
Han Woong Yoo, Martin E van Royen, Wiggert A van Cappellen, Adriaan B Houtsmuller, Michel Verhaegen, and Georg Schitter. Automated spherical aberration correction in scanning confocal microscopy. Review of Scientific Instruments, 85(12):123706, December 2014.

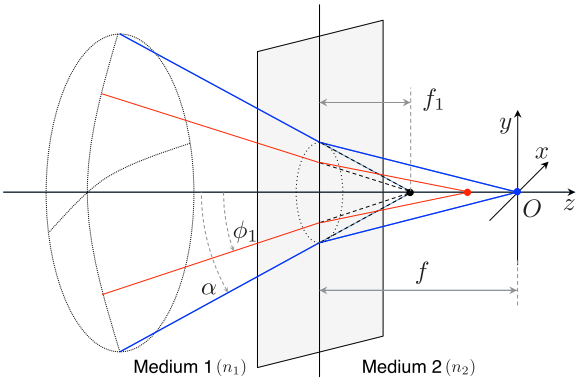

Figure 4.1: Geometrical optics interpretation of the spherical aberrations caused by focusing a beam through two media ($n_2 > n_1$). The designed focal point of the lens in medium 1 (black dot) is diverged into two foci (red and blue dots), leading to image degradation.

introduced by layered structures such as coverslip glass and skin[171–173]. Fig. 4.1 shows a spherical aberration generated by focusing through two different media. With a water immersion objective, for example, the refraction index mismatch between the immersion medium (water) and the coverslip (glass) generates spherical aberrations. Perfect compensation is difficult to achieve by a static objective design since the level of spherical aberrations is mainly fluctuated by the thickness variation of the coverslip. To cope with the varying spherical aberrations induced by coverslip thickness mismatch, microscope manufacturers provide an objective lens with a coverslip correction collar that allows adjustment of a lens block in the objective [174], which can be motorized [175]. Microscope manufacturers recommend users to maximize the intensity of the interface reflection between the coverslip and specimen to find the best adjustment [171]. Some commercial systems utilize additional sensors that measure the coverslip thickness [176] or the spherical aberrations directly [177] to adjust the correction collar. Another approach adds a relay optics between the objective and tube lens for correcting spherical aberrations for deep specimen imaging [178]. However the sensors do not use the same optical path of microscope imaging, and the auxiliary sensors and devices add complexity to the microscope system. A correction based on image quality measures of these reflection is defined and evaluated without biological specimen by maximizing image sharpness find the optimal adjustment by Gaussian fitting [179]. However, the manual adjustment is difficult, imprecise and time consuming, causing photodamage to the specimen. Moreover, the spatial fluctuation of reflection by specimen makes it difficult for users to find the best correction.

In this chapter an automated correction of spherical aberrations is proposed based on a motor driven correction collar [142, 143] in combination with algorithms on a generalized correction quality measure. The chapter is organized as follows: Section 4.2 describes the setup with a new motorized correction collar. In Section 4.3, an axial image model is derived to design a noise reduction filter and to analyze the residual spherical aberration. A sequence of normalized axial images is recorded and the optimal correction collar adjustment is determined by the correction quality measures and correction methods presented

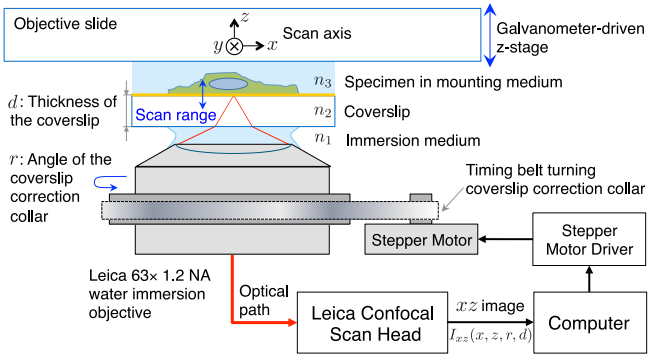

Figure 4.2: A diagram of the automated adjustment system for coverslip thickness mismatch correction.

in Section 4.4. Section 4.5 demonstrates the performance of the correction methods and improved image resolution of fluorescent specimen by experimental results obtained by the automatically adjusted confocal microscope.

4.2 System Description

The overall structure of the automatic coverslip thickness mismatch correction system is illustrated in Fig. 4.2. An excitation laser is focused by an objective lens (HCX PL λ_{BL} APO 63$\times$ 1.20 NA water immersion, Leica Microsystems, Mannheim, Germany). The reflections between the coverslip and specimen are collected by the same objective lens, and detected by the photo multiplier tube (PMT) with a wavelength window between 485 μm and 491 μm in the confocal scanhead (TCS SP5, Leica Microsystems). For obtaining axial scans, the specimen slide is linearly translated by a galvanometer-driven z-stage (Super Z-Galvo Stage, Leica Microsystems). The axial images are recorded by a computer, which also controls the microscope. To actuate the coverslip correction collar, a stepper motor (15HS-012, Mclennan Servo Supplies Ltd., Surrey, United Kingdom) driven by a pulse generator (Stellaris Stepper Motor Reference Design Kit, Texas Instruments, Dallas, TX, USA) adjusts the angle of the coverslip correction collar r through a timing belt with a gear ratio of $1/6$, providing a resolution of 0.33°/step over the full rotational range of 115° of the correction collar.

4.3 Axial Image Model of the Coverslip Mismatch Problem

4.3.1 Axial Image Model of the Reflective Planar Interface

Imaging with coverslip mismatch can be modeled as imaging through two different media as shown in Fig. 4.1, where n_1 is the reflective index of the immersion media, and n_2 is that of the coverslip [1, 19, 20, 180, 181]. An axial scan model, based on the aberration model

[180], is derived for a matched filter design (cf. Section 4.4).

The imaging intensity of a uniform reflective plane in confocal microscopy depends on the point spread function (PSF) and is given as follows [2],

$$I(x,y,z,f) = k^{-2}|\zeta|^2 \Omega I_{\mathcal{L}} \mathrm{PSF}(2\gamma z, f), \tag{4.1}$$

where x, y, and z are the coordinates at the imaged point as depicted in Fig. 4.1. $\mathrm{PSF}(z,f)$ denotes the one-dimensional point spread function along the z axis through two media and f denotes the actual focal depth in the second medium, which is the distance from the media interface to the actual focus position. γ denotes the vertical direction ratio between the shifted actual focus position f, and the nominal focus position f_1 of the lens in medium 1, i.e. $f = \gamma f_1$, approximated to $\gamma = \frac{n_2}{n_1}$ [182]. The term γz reflects the compression of the actual axial profile in the second medium [183, 184] due to the shift of the z position by the galvanometer-driven z-stage as seen in Fig. 4.2. The scaling factor of 2 is obtained by the imaged focus movements against the reflective mirroric surface. The wave vector k, the reflectance ζ at the interface, the solid angle Ω of the aperture pupil as seen from either the object or image plane, and the illumination intensity $I_{\mathcal{L}}$ at pupil are assumed to be constant.

Applying the Debye approximation [180], the axial PSF with aberrations of a linearly polarized light source is obtained as follows,

$$\mathrm{PSF}(z,f) = A^2 I_0(z,f)\bar{I}_0(z,f), \tag{4.2}$$

where I_0 denotes a diffraction integral (see Eq. 4.3), and $\bar{I}_0$ denotes the complex conjugate of I_0. A is a constant amplitude factor determined by the focal length of the lens *in vacuo* and the wavenumber of the first medium. The diffraction integral can be simplified as follows,

$$I_0(z,f) = \int_{\cos\alpha}^{1} F_0(\beta) e^{ik_0 \Psi(\beta,f,z)} d\beta, \tag{4.3}$$

where

$$F_0(\beta) = 2\sqrt{\beta^3}\left(\frac{1}{\eta(\beta)+\beta} + \frac{\gamma^{-2}\eta(\beta)}{\beta+\gamma^{-2}\eta(\beta)}\right), \tag{4.4a}$$

$$\Psi(\beta,f,z) = n_1\{f(\eta(\beta)-\beta)+z\eta(\beta)\}, \tag{4.4b}$$

$$\eta(\beta) = \sqrt{\beta^2+\gamma^2-1}, \tag{4.4c}$$

with $\beta = \cos\phi_1$, corresponding to the radial coordinate in the pupil plane (back focal plane). As shown in Fig. 4.1, ϕ_1 is the incident angle of the original focal point neglecting the refraction at the second medium. α is the maximum angle of ϕ_1, which is determined by the numerical aperture (NA) of the objective lens and the refractive index of the immersion medium n_1. $\Psi(\beta,f,z)$ is called the aberration function, representing the wavefront along the radial coordinate β at the axial position z with the actual focal depth f in the second medium. Here, the aberration function Ψ represents spherical aberrations only, since Ψ is solely dependent on the radial coordinate β.

From Eq. (4.3), it can be seen that the actual focal depth through the second medium influences the amplitude of the aberration function Ψ. By adjustment of the angular position r of the coverslip correction collar, it should compensate for this nominal focal depth

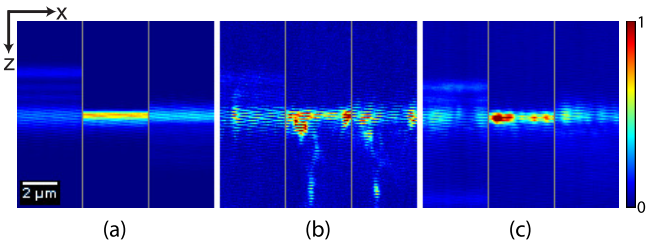

Figure 4.3: Axial xz images of the reflection of the coverslip interface with (a) pure water as specimen, (b) a specimen of convallaria majalis rhizome (CMR), (c) a specimen of fixed mouse embryonic fibroblasts (MEFs). Each image consists of three interface images at the optimal correction (center), −12.8 µm (left), and +12.8 µm mismatch (right). The axial image is the brightest and sharpest at the optimal correction although the axial images with biological specimen fluctuated over x axis due to the inhomogeneous optical structure of the specimen.

at the reflective surface between coverslip and specimen. A linear relation between the adjustment r and the thickness of the coverslip d is assumed [174]. Then, the effective actual focal depth for the spherical aberration can be rewritten as

$$f = \underbrace{d - d_0}_{d_m} + br + \gamma z, \tag{4.5}$$

where b denotes the coefficient between the correction collar angle and the coverslip thickness mismatch. For the objective in Fig. 4.2 $b = 0.5\ \mu m/^\circ$. d_m is the residual mismatch at $r = 0$ and $z = 0$, where the intensity along the z axis is at its maximum. This can be obtained by d with an initial coverslip mismatch correction at $r = 0$, defined by d_0. γz denotes the compressed focus movement due to vertical displacements.

Substituting Eq. (4.5) into Eq. (4.1), the xz image, as recorded by the microscope, can be modeled as

$$I_{xz}(x,z,r,d_m) = k^{-2}|\zeta|^2 \Omega I_{\mathcal{L}} \mathrm{PSF}(2\gamma z, d_m + br + \gamma z), \tag{4.6}$$

where $\mathrm{PSF}(\cdot,\cdot)$ is defined in Eq. (4.2) and Eq. (4.3).

4.3.2 Sample Induced Distortion in Axial Image Measurements

Considering the gain and offset of the detector, the axial imaging intensity of Eq. (4.6) can be rewritten as

$$\hat{I}_{xz}(x,z,r,d_m) = K_g \Big\{ I_{xz}(x,z,r,d_m) + v(x,z) \Big\} + K_{off}(r), \tag{4.7}$$

where K_g and K_{off} denote a gain and offset of the detector and the term $v(x,z)$ represents the noise in the image, such as dark current and readout noise [40].

Fig. 4.3 illustrates measured axial images of the coverslip specimen interface with (a) pure water as specimen, (b) a specimen of convallaria majalis rhizome (CMR)[142], and (c) a specimen of fixed mouse embryonic fibroblasts (MEFs, cf. Section 4.5). Each reflection

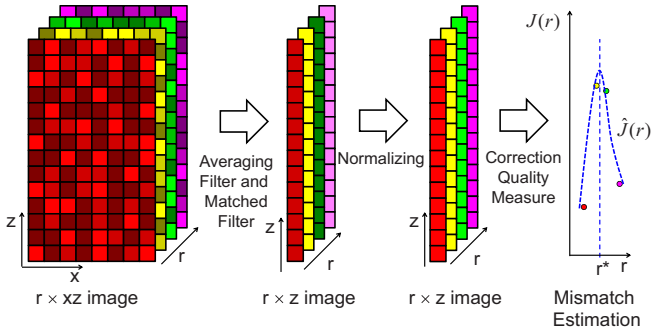

Figure 4.4: Adjustment procedure of the proposed system. The small squares represent individual pixels of the image, the pixel colors (red, yellow, green, violet) indicate different adjustment angles r of the correction collar and the shadowing of each pixel color represents the intensity fluctuation and noise. First, a specified number of xz images are recorded at different adjustment angles r. Each xz image is compressed into a z image vector by averaging in x, followed by matched filtering. The z image vectors are normalized to remove influences of measurement conditions. Finally, the z image vectors are evaluated with quality functions and a fitting algorithm is applied to find the best adjustment angle r^*.

of specimen contains three sets of the coverslip correction collar setting, which are optimal correction (center), $-12.8\ \mu m$ (left), and $+12.8\ \mu m$ mismatch (right), corresponding to $r = \pm 25.2°$. All images are made with the same laser power and detector gain setting and the pinhole at 1 airy unit. For all specimen the reflection is the brightest at the optimal adjustment of the correction collar and blurred interference patterns are observed with a coverslip mismatch. Axial images with biological specimens Fig. 4.3(b) and Fig. 4.3(c) show a large noise level along the x axis, which is mainly caused by fluctuations in the refractive index of the specimen. The varying reflection due to the specimen, shown as bright irregular spots in Fig. 4.3, may cause erroneous mismatch estimates. In order to avoid signal saturation and low signal to noise ratio (SNR), which can cause an estimation error, measurement conditions such as laser intensity and detector gain need to be adjusted during the automated correction. To cope with these practical problems and to automate the spherical aberration correction, image processing steps are discussed in the following section.

4.4 Automated Adjustments of Coverslip Thickness Mismatch

The proposed automation of the coverslip mismatch correction should enable a fast and reliable correction with as low as possible photodamage to the specimen. Therefore the number of axial scans that have to be recorded should be small only. For reliable correction, the correction accuracy should not depend on the kind of specimen and the measurement noise. Recording only a small number of image for obtaining the correction reduces the adjustment time while it also minimizes photodamage and photobleaching[102]. In addition, the

axial scans for correction should use low laser intensity to reduces the photodamage while low laser intensity leads to low SNR.

Fig. 4.4 illustrates the overall workflow for obtaining the best adjustment angle r^* obtained from a set of noisy xz images. A specified number of xz images are recorded at different adjustment angles r. These images are further processed by two filters. The first filter averages the images along the x axis, reducing the x-position dependent intensity fluctuations. The second filter is a matched filter that reduces high frequency noise, which cannot be imaged by diffraction. Then a normalizer decreases the influence of the measurement conditions in order to provide comparable axial images. Finally, the correction quality of the filtered and normalized images are evaluated, and the optimal adjustment angle r^* of the correction collar is obtained by a fitting algorithm.

4.4.1 Noise Reduction and Image Alignment

To improve the SNR of the measured axial image, an averaging filter and a matched filter [185] are applied with an offset rejection. The offset-corrected filtered image can be written as

$$I_h(z,r,d_m) \quad = \quad \left(\frac{1}{2x_m}\int_{-x_m}^{x_m}\hat{I}_{xz}(x,z,r,d_m)dx\right) * h_m(z) - \hat{K}_{off}, \tag{4.8}$$

where x_m denotes the half of the averaging range of the x axis, $*$ is the convolution operator, $h_m(z)$ is a matched filter, and $\hat{K}_{off}$ is the offset to be corrected for. The matched filter $h_m(z)$ is designed based on the axial image model without mismatch, i.e. $h_m(z) = \mathrm{PSF}(2\gamma z, 0)$. This is because the spatial frequency response of axial images is bounded by the spatial frequency response of mismatch free images

For every xz image, averaging over x axis is applied along the x axis, generating a z image vector per each adjustment r, reducing the x dependency due to inhomogeneous specimen. Additionally, the averaging filter also reduces the noise term $v(x,z)$ of Eq. (4.7). .

To compare the obtained z image vectors, their maximum intensity position are aligned along the center ($z = 0$), and the edges of each axial image is removed symmetrically from a distance z_m. An offset rejector subtracts the background offset $\hat{K}_{off}$ of the detector, which is obtained by the mean intensity at either ends of the respective z image. An rz image is generated by stitching the z image vectors along the collar angle r to illustrate the evolution of the z image along r as Fig. 4.4. For the rz image generation, 71 xz images that are equally spaced along the correction collar's full angular range are recorded and processed.

Fig. 4.5 illustrates the rz images and corresponding correction quality measures (c.f. Section 4.4.3) without any noise filter (left), only with an averaging filter (center), and with averaging and matched filters (right image). For comparison the correction measures are rescaled between 0 and 1. Filtering smoothens the noisy rz images and many local minima in the quality measures reduces. Therefore this is advantageous to determine the optimal correction.

4.4.2 Normalization of the Axial Image

Saturation and low signal intensity may affect the evaluation of z images during the measurement of the xz images. At a lower signal intensity, i.e. the detection gain or the laser

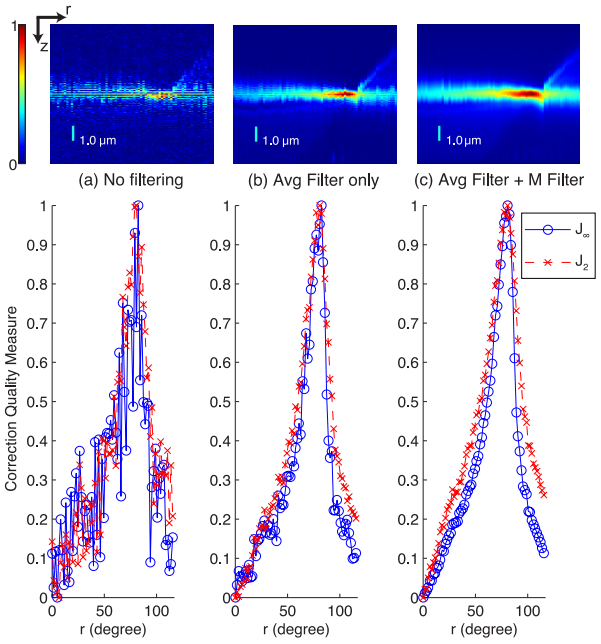

Figure 4.5: rz images and corresponding correction quality measures of the Leica standard sample of Convallaria majalis rhizome in case of (a) no filtering, (b) averaging filter only, (c) both averaging filter and matched filter. The averaging size is 50 pixels, which corresponds to 4 *µm.*

intensity are low, the detector noise dominates the evaluation of z images. Detector saturation can occur during the correction due to the increased intensity by correction, which means loss of information at the peak of the image and results in wrong mismatch estimation as well. To solve this problem, a normalizer based on the integration of the axial image is applied as follows [186],

$$I_n(z,r,d_m) \quad = \quad \frac{I_h(z,r,d_m)}{\int_{-z_m}^{z_m} I_h(z,r,d_m)dz}. \tag{4.9}$$

The integral in the denominator corresponds to the summation of the axial image, i.e. the magnitude of zero frequency of optical transfer function [2]. With a normalizer, the detector gain can be freely adjusted to prevent a low signal as well as detector saturation. In addition, a normalizer also allows a comparison between measurements with specimen dependent intensity fluctuation.

Fig. 4.6 shows rz images with a fixed detection gain (left) and with the detection gain adjustment (center) and with the detection gain adjustment after applying a normalizer (right). In Fig. 4.6(b), the gain of the detector is adjusted during the sweep of the correction collar r in order to avoid detector saturation and low signal intensity. Abrupt changes of the maximum intensity along the r axis depict the modification of the detector gain. Fig. 4.6(c) shows that a normalizer removes the dependency on the detection gain, resulting in a pattern

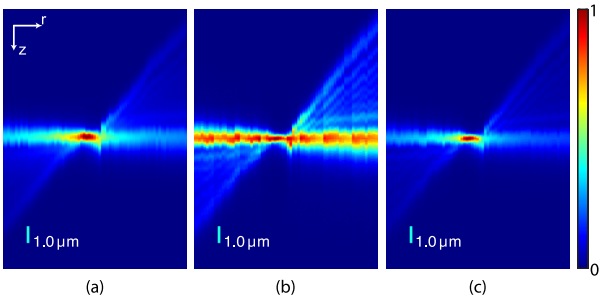

Figure 4.6: rz image of coverslip (a) fixed detection gain and (b) with a detection gain adjustement and (c) after applying the normalizer with the detection gain adjustement. The normalized rz image (right) shows a similar diffraction pattern to the rz image with the fixed detector gain (left) [142]. This allows mismatch estimation and correction regardless of detection gain and laser intensity.

similar to the image with the fixed detection gain in Fig. 4.6(a).

4.4.3 Correction Quality Measures

For the evaluation of the correction quality of the filtered and normalized axial images, three quality measures are defined, $\mathcal{L}_\infty$ and $\mathcal{L}_2$ norm, as well as entropy. A generalized quality measure, combining these three quality measures, is introduced.

$\mathcal{L}_p$ norms are proposed as a correction quality measure for a coverslip correction problem [179], and have been tested for $\mathcal{L}_2$. We evaluate $\mathcal{L}_2$ as well as $\mathcal{L}_\infty$, which are given as

$$J_\infty(r,d_m) = \lim_{p\to\infty}\left(\int_{-z_m}^{+z_m} I_n^p(z,r,d_m)dz\right)^{1/p}, \tag{4.10}$$

$$J_2(r,d_m) = \left(\int_{-z_m}^{+z_m} I_n^2(z,r,d_m)dz\right)^{1/2}. \tag{4.11}$$

The maximum intensity J_∞ corresponds to the Strehl ratio of the imaging system, which is defined as the ratio between the maximum intensity with and without aberrations [89]. J_2 is known as a measure for image sharpness [187, 188].

The entropy is proposed as a correction quality measure of the coverslip mismatch correction, which is defined as [189, 190],

$$J_{ent}(r,d_m) = -\int_{-z_m}^{+z_m} I_n(z,r,d_m)\ln I_n(z,r,d_m)dz. \tag{4.12}$$

An entropy measure can only be used with a normalizer since normalized intensity can be interpreted as a probability density function of the reflection from the interface. Since entropy is known as information of the axial image, a smaller entropy correction measure means less uncertainty of the microscope image regarding the true object. J_{ent} is a concave function with its minimum as optimum, in contrast to the J_∞ and J_2 being optimal at the

corresponding maximum..

In theory, the optimal correction position of the correction quality measures of $\mathcal{L}_\infty$, $\mathcal{L}_2$ and entropy should be the same without aberrations but in practice the optimum are different due to the intensity fluctuation by the specimen and the residual aberrations at the optimal correction. A generalized correction quality measure is proposed as a weighted linear combination of $\mathcal{L}_\infty$, $\mathcal{L}_2$, and inverse entropy measure, defined as

$$J(r,d_m) = q_1 J_\infty(r,d_m) + q_2 J_2(r,d_m) + q_3 J_{ent}^{-1}(r,d_m), \tag{4.13}$$

where q_1, q_2, and q_3 are the weighting for each quality measure. Since each quality measure has different of its value, this weighting can be used for the equalization of the influence of each quality measure. It can be used to emphasize the important quality measure as well. Considering only the image sharpness $\mathcal{L}_2$ for example the weights are chosen as $q_2 = 1$ and $q_1 = q_3 = 0$.

4.4.4 Mismatch Estimation and Optimal Adjustment of Correction Collar

It is desirable to find the optimal correction collar angle based on a low number of xz images to be recorded. Three adjustment algorithms are discussed in detail and evaluated with specimen in the following section.

Sweep Method

For the sweep method, xz images are recorded at different correction collar positions r. This allows to extract a correction quality measure for each collar position and to determine the optimal adjustment by detecting the maximum quality measure [142].

The sweep method is simple and easy to implement but it is time consuming as more xz images have to be recorded. The precision is inversely proportional to the number of sweeping steps. For the above mentioned 71 measurements the correction collar angle can be detected with a resolution of 1.65°, corresponding to 0.8 μm coverslip thickness mismatch.

Gaussian Fitting Method

The Gaussian fitting (GF) method can be understood as an extension of the sweep method. Instead of increasing the accuracy by recording additional images, the optimal correction position is estimated by fitting a Gaussian function, given as [179]

$$r^* = \arg\min_{\hat{s},r} \sum_{t=0}^{m_g-1} \| J(r_t,d_m) - (\hat{s}_1 e^{-(r_t-r)^2/\hat{s}_3^2} + \hat{s}_2) \|^2, \tag{4.14}$$

where m_g is the number of axial images used, $\hat{s} = \begin{bmatrix} \hat{s}_1 & \hat{s}_2 & \hat{s}_2 \end{bmatrix}$ is a parameter vector, and r_t denotes the correction collar position defined by $r_t = t\Delta_g$ where Δ_g is the size of the sweeping step for Gaussian fitting. Gaussian fitting allows to interpolate between measurement points in order to reduce the number of axial images, however, it can also lead to a large estimation error when the Gaussian model does not match the real measured data.

Coarse-Fine Gaussian Fitting and Mixed Gaussian Fitting Method

To minimize the model mismatch of the Gaussian model, an algorithm that is composed of two steps is proposed. In the first step, a coarse sweep of m_c xz images with a sweeping step size of Δ_c is performed to estimate the coarse optimum r_c^*. In the second step, additional xz images are recorded around the coarse optimum and the optimal adjustment is determined. The correction optimum r^* is found by fine fitting of the nonlinear least squares problem

$$r^* = \arg\min_{\hat{\theta},r} \sum_{p=0}^{m_f-1} \|J(r_p,d_m) - (\hat{\theta}_1 \hat{J}(r_p - r) + \hat{\theta}_2)\|^2, \tag{4.15}$$

where $\hat{J}$ denotes a model of the correction quality measure in (4.13) near the optimal correction under ideal measurement conditions. To this end measurements of coverslip with pure water as specimen have been recorded in advance in the range of 16.5° near the optimal adjustments. The model $\hat{J}$ is generated based on the ideal images of the simulation of (4.1) and by applying to the Curve Fitting Toolbox of Matlab to the measurement data. Two methods are defined by the choice of the fitting function, which are coarse-fine Gaussian fitting method (CF-GF) and coarse-fine mixed Gaussian fitting method (CF-MGF) using Gaussian and mixed Gaussian function, respectively. $\hat{\theta} = \begin{bmatrix} \hat{\theta}_1 & \hat{\theta}_2 \end{bmatrix}$ is a parameter vector of a gain and offset of the model. r_p denotes the correction collar position for fine fitting as

$$r_p = r_c^* + \frac{2p - m_f + 1}{m_f - 1}\Delta_c. \tag{4.16}$$

m_f is an odd number of xz images used for the fine fitting, with $m_f \geq 5$. If $m_f = 5$, for example, $\{r_0, r_1, r_2, r_3, r_4\} = \{r_c^* - \Delta_c, r_c^* - 0.5, r_c^*, r_c^* + 0.5\Delta_c, r_c^* + \Delta_c\}$ are used for the fine fitting. The total number of recorded images are $m_c + m_f - 3$ because 3 images of r_c^* and $r_c^* \pm \Delta_c$ are already taken in the coarse sweep. With this two step algorithm significantly less images have to be recorded as compared to the sweep methods while the optimum can be detected at least with the same precision, which is experimentally validated in the next section.

4.5 Experiment Results

4.5.1 Evaluation of the Automatic Coverslip Correction Algorithms

To evaluate the proposed mismatch correction methods, various samples are listed in Table 4.1 are examined. First, two coverslips with pure water as specimen in Section 4.4 are examined as a reference. To demonstrate the robustness of the algorithms against specimen-induced intensity fluctuations, 5 coverslips with specimens are examined, gold particles on poly-L-lysine (GP), Convallaria majalis rhizome (CMR), fixed mouse embryonic fibroblasts (MEFs), and fixed human hepatocellular carcinoma cell line (Hep3B-AR). Particularity for Hep3B-AR, two slides are produced with different coverslips of standard thickness No. 1 (Hep3B-AR #1) and No. 1.5 (Hep3B-AR #1.5) for the comparison.

To obtain the optimal setting of the correction collar and to compare the adjustment methods, a set of 71 xz images at every 1.65° of the correction collar r are recorded. For

Table 4.1: Mean and standard deviation of the estimated optimal correction with sweep method, Gaussian fitting (GF) method, coarse-fine Gaussian fitting (CF-GF) method, and coarse-fine mixed Gaussian fitting (CF-MGF) method. Sweep method provides the reference measured optimum while the other methods estimate the optimal correction. Root mean square (RMS) of mean error and standard deviation describes the accuracy and the precision of the algorithms in diffrent specimens.

[°]	Sweep	GF		CF-GF		CF-MGF	
		Mean (Error)	STD	Mean (Error)	STD	Mean (Error)	STD
Coverslip #1	77.55	69.42 (-8.13)	1.03	75.36 (-2.19)	0.68	77.45 (-0.10)	0.25
Coverslip #1.5	52.8	51.46 (-1.34)	0.87	52.72 (-0.08)	0.69	54.57 (1.77)	0.25
GP	77.55	74.3 (-3.25)	2.33	77.15 (-0.4)	0.61	78.67 (1.12)	0.28
CMR	80.85	72.82 (-8.03)	4.07	78.94 (-1.91)	1.34	78.47 (-2.38)	0.83
MEFs	89.10	101.21 (12.11)	15.52	89.05 (-0.05)	0.83	88.41 (-0.69)	0.98
Hep3B-AR #1	74.25	68.64 (-5.61)	0.87	75.62 (1.37)	0.86	74.29 (0.04)	0.73
Hep3B-AR #1.5	54.45	55.69 (1.24)	1.92	55.38 (0.93)	0.71	54.24 (-0.21)	0.29
RMS Performance		... (6.79)	6.20	... (1.27)	0.85	... (1.23)	0.59

the axial images the 488 *nm* Ar laser is used as light source, except for the Hep3B-AR specimens, where the reflections of the 514 *nm* Ar laser are recorded since this wavelength is used for yellow fluorescent protein (YFP) excitation. The generalized correction quality measure Eq. (4.13) is used to evaluate the quality of correction with coefficients $q_1 = 2.8$, $q_2 = 4.2$, and $q_3 = 1$, which are chosen set all three correction quality measures equal.

Three correction methods in Section 4.4 are evaluated with the following conditions. First, the entire set of *xz* images processed directly by the sweep method for its optimum, which is set as reference. Secondly, 6 image subsets with 11 axial images are selected to evaluate the accuracy of the Gaussian fitting (GF) method. To simulate slightly different coverslip thicknesses and the corresponding shift in the *rz* image, the subsets are equally spaced over r with $m_g = 11$ and $\Delta_g = 9.9°$. Finally in the coarse-fine Gaussian fitting (CF-GF) and mixed Gaussian fitting method (CF-MGF), 10 subsets of 6 axial images, $m_c = 6$ and $\Delta_c = 16.5°$, are chosen for the coarse correction. The optimization of Eq. (4.15) is done with the correction measures of the $m_f = 5$, i.e. with two additional axial images between the selected three images in the coarse correction. Therefore, the coarse-fine correction method uses in total 8 *xz* images, which significantly reduces the recording time as compared to the 71 images of the sweep method.

Table 4.1 shows the mean and standard deviation (STD) of the estimated optimal adjustments each sample. The optimal adjustment obtained by the sweep method is considered as reference since it has a known accuracy of $\pm 1.65°$. From the results, the specimen can be categorized into two groups, thin coverslips (Coverslip #1, GP, CMR, MEFs, Hep3B-AR #1) and thick coverslips (Coverslip #1.5, Hep3B-AR #1.5). GF method shows a large estimation errors for thin coverslips and its standard deviation is always the largest except for Hep3B-AR #1. The estimated optimal adjustment of CF-GF and CF-MGF shows a better accuracy with a small mean error, and the standard deviation of CF-MGF is smaller than CF-GF except for the case of MEFs. To evaluate the overall performance among the different

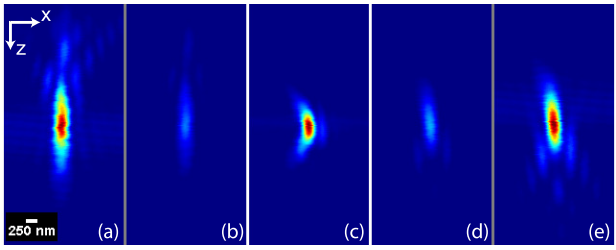

Figure 4.7: xz reflection images of a 20 *nm gold particle with (c) the optimal adjustment, (a,b)* −13.2 *µm mismatch and (d,e)* +13.2 *µm mismatch, corresponding to* ±26.4° *of the correction collar angle. The detector gain is fixed in (b), (c), and (d) , while (a) and (e) are recorded with an increased detector gain to achieve the same maximum intensity as in (c). The difference in the PSF size is clearly visible among (a), (c), and (e).*

Table 4.2: Relative maximum intensity with respect to the optimal adjustments and lateral and axial full width at half maximum (FWHM) of the measured point spread function.

	Optimum	13.2 μm	−13.2 μm
Relative maximum intensity	1	0.30	0.24
Lateral FWHM [μm]	0.20	0.24	0.22
Axial FWHM [μm]	0.52	0.78	0.94

specimen, root mean square (RMS) is used for the mean errors and the standard deviation [189]. RMS of the mean error and RMS of the standard deviation represent the accuracy and the precision of the algorithm, respectively. It shows that the proposed coarse-fine correction methods (CF-GF, CF-MGF) provide the RMS mean error less than the sweep methods step, which is used as a reference and the precision with the smallest RMS mean error and standard deviation, only with 8 *xz* images while the sweep method and the Gaussian fitting method (GF) need 74 and 11 images.

4.5.2 Imaging Examples

Evaluating the PSF

In order to determine the PSF, 20 *nm* gold particles (Gold Colloid, BBInternational, Cardiff, UK), which are sparsely distributed on a Poly-L-Lysine coated coverslip are used as the first specimen, because the refection of particles smaller than the wavelength of the laser shows a squared PSF with spherical aberrations [2]. In addition, gold particles do not bleach so that reflection intensity does not degrade by the former measurement trials, i.e. aberrations are the only factor that degrades the image. An Ar laser with a wavelength of 488 *nm* is used for imaging.

Fig. 4.7 shows axial images of a gold particle recorded with the confocal microscope (c) with the optimal adjustment of the correction collar and (a, b, d, e) with a mismatch of

$\pm 26.5^\circ$ in the correction collar angle, corresponding to a thickness mismatch of $\mp 13.2\ \mu m$. The gain is fixed in (b), (c), and (d) to show the low intensity of the PSF in (b) and (d) due to spherical aberrations. (a) and (e) are recorded at the same condition of the correction collar as in (b) and (d) but with the detector gain adjusted to obtain brighter images, clearly illustrating the enlarged shape of the PSF. This is based on a scenario that users frequently do: not adjusting the correction collar but the detector gain in order to obtain the confocal microscope image with enough brightness. These gain adjusted PSFs are close to the images of inexperienced microscope users who usually adjust the detector gain or the laser intensity to make the image bright rather than manually adjusting the correction collar. Table 4.2 summarizes relative maximum intensity as compared to the optimal adjustments, as well as the lateral and axial full width at half maximum (FWHM) of the measured particle images. It is observed that in the uncompensated case the maximum intensity drops by up to 76% and the axial FWHM also increases significantly by up to 80%.

Automated Optimal Adjustment Correction Collar in Multicolor Images

To demonstrate the improved image quality for the optimally adjusted correction collar, fixed mouse embryonic fibroblasts (MEFs) are used as the second specimen. The cytoskeleton of MEFs is visualized by means of immunofluorescent labeling of beta-tubulin (Alexa488) and with a chromatin staining (DAPI) [191] that are excited by a 488*nm* Ar laser and a 405*nm* diode laser and recorded by each PMT simultaneously. Beta-tubulin as a dimer with alpha-tubulin assemble in cells into a hollow cylindrical structure of approximately 24 *nm* diameter, the microtubules [192]. This is smaller than the diffraction limit of the confocal microscope and can be a useful indicator with a high sensitivity to aberrations.

For a comparison of fluorescence images of MEFs between a spherically aberrated case and the optimally adjusted microscope, the optimal adjustment of Hep3B-AR #1.5 is chosen as the unadjusted case for. This scenario is likely when multiple users share the same microscope and the objective lens but use different coverslips for their experiments. Fig. 4.8 shows *rz* images and the corresponding generalized correction quality of Hep3B-AR #1.5 and MEFs. The optimal adjustments of Hep3B-AR #1.5 and MEFs, r_H^* and r_M^*, differ by 34.7° as shown in *rz* images (a) and (b), corresponding to 17.3 μm thickness mismatch. 3D images of MEFs for the uncompensated and compensated case are taken to have the same voxel height z as width in x and y. The 3D images of the compensated and uncompensated cases are aligned based on the maximization of the cross-correlation between two 3D images, in order to locate the same position as well as to remove the effect of defocus by a different z position. Microtubule images are used for the alignment of images, because of their complex pattern.

Fig. 4.9 shows lateral *xy* fluorescence images and axial *xz* fluorescence images of chromatin (DAPI, Cyan) and beta-tubulin (Alexa488, Green) for (a) the uncompensated case and (b) the optimally adjusted correction collar. In the uncompensated case, the image intensity of both chromatin and beta-tubulin clearly degrades in the lateral image. In the *xz* image, in addition, the image of both fluorophores are elongated and dispersed. Furthermore, a misalignment in the axial position between the images of each color can be observed in the uncompensated case. This denotes that the fluorescence images of different excitation wavelengths have a shifted axial focus when a spherical aberration due to the coverslip thickness mismatch exists. In case of the optimally adjusted correction collar (b), the image

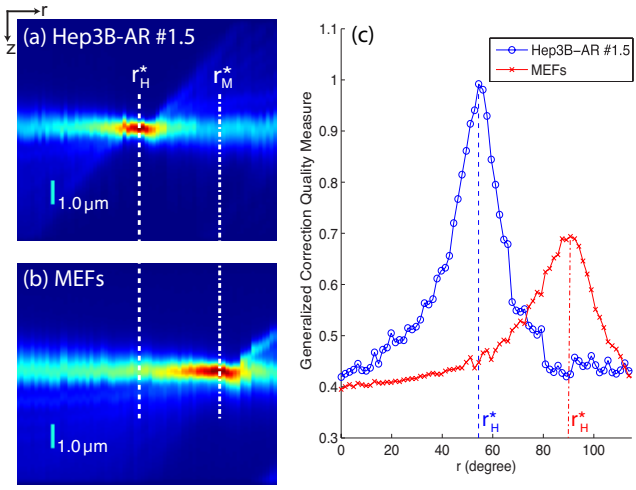

Figure 4.8: Measured rz image of a slide of (a) a fixed human hepatocellular carcinoma cell line with a coverslip of standard thickness No. 1.5 (Hep3B-AR #1.5) and (b) a fixed mouse embryonic fibroblasts (MEFs). The optimal adjustment of Hep3B-AR #1.5, r_H^* (dashed line), is different from that of MEFs, r_M^* (dashed dot line), indicating the necessity of individual adjustment of the correction collar before imaging each sample. (c) The generalized correction quality clearly shows the different maxima in correction quality along r axis.

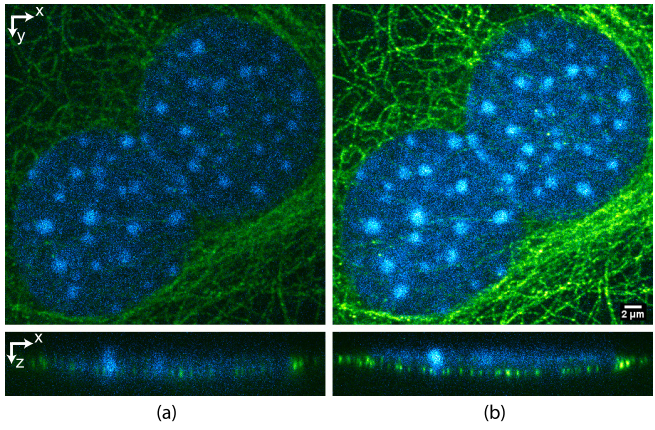

Figure 4.9: Fluorescence images of chromatin (DAPI, Cyan) and beta-tubulin (Alexa488, Green) in fixed mouse embryonic fibroblasts (MEFs) with (a) uncompensated spherical aberrations (r_H^*) and (b) optimally compensated r_M^*. The image degradation is significant in axial xz images, and the axial location of the chromatic cluster is aligned with the beta-tubulin image in (b) while it is not aligned in (a).

intensity, sharpness, as well as the alignment is improved, which is clearly visible in the

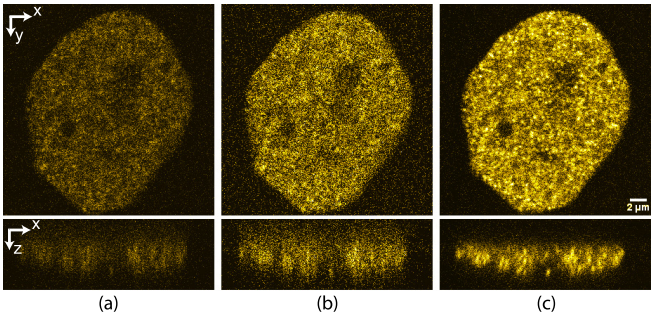

Figure 4.10: Images of fluorescently labeled androgen receptor (YFP, Yellow) in the nucleus of a fixed human Hep3B-AR cell. Spherical aberrations are (a) uncompensated (r_M^*), (b) also uncompensated with an adjusted detector gain, and (c) optimally compensated (r_H^*). Details of fluorescent clusters are blurred in the uncompensated images and cannot be enhanced by increasing the detector gain.

lateral as well as axial images.

Optimal Adjustment of Correction Collar vs Adjustment of Detection Gain

To demonstrate the improvement in image quality by optimally adjusting the correction collar as compared to enhancing the detection gain (cf. Fig 4.7) in a real imaging example, a fixed human hepatocellular carcinoma cell line (Hep3B-AR) is imaged with the confocal microscope. Hep3B-AR is grown on coverslips with the standard thickness No. 1.5 (sample Hep3B-AR #1.5), stably expressing the androgen receptor (AR), double labeled with yellow fluorescent protein (YFP) at the N-terminus and cyan fluorescent protein (CFP) at the C-terminus of the protein [193]. The AR is a hormone activated transcription factor that regulates the expression of genes involved in the development and maintenance of the male phenotype as well as prostate cancer growth. The hormone (R1881) activated AR shows a typical sprinkled distribution which is correlated with transient binding to DNA and is linked to the spatial distribution of transcriptional activity [194]. An Ar laser with a wavelength of 514*nm* is used to excite YFP.

3D images of YFP-labeled AR of Hep3B-AR #1.5 are recorded with the uncompensated system and the optimally adjusted correction collar, respectively, by stacking 320 *xz* image layers to obtain the same *y* voxel width as for the *xz* voxel width and height and aligned by the maximization of the cross-correlation. In the uncompensated case, the images are recorded with two detector gains, which is once the same gain as in the compensated case and once with an adjusted gain for similar brightness as in the compensated case. The uncompensated image with an adjusted detector gain is quite likely in practical imaging application (cf. Fig 4.7).

Fig. 4.10 shows lateral *xy* images and corresponding sectional *xz* image slices of the fluorescently labeled AR (Yellow) in Hep3B-AR cells (coverslip #1.5) with (a) the uncompensated case, (b) the uncompensated case with adjusted detector gain, and (c) the optimally adjusted correction collar. The image degradation is more significant in the axial images due to the shape of the PSF (cf. Fig. 4.7). The elongated and dispersed features are observed,

making their localization difficult while the sample details in the uncompensated images are blurred and distorted.

In summary the automated and optimal adjustment of the correction collar proposed here minimizes the spherical aberrations and enables sharp and bright images with the scanning confocal microscope.

4.6 Conclusion

This chapter presents the automatic adjustment of spherical aberration correction with a motorized correction collar. The proposed approach is evaluated for compensation of spherical aberrations due to coverslip mismatch. After noise filtering and normalization, the measured axial images are evaluated by general correction quality measures, including the maximum intensity, image sharpness, and image entropy. For searching the optimal correction the sweep method, Gaussian fitting method, and coarse-fine Gaussian fitting method are discussed. These algorithms are evaluated with 7 specimens and it is shown that the coarse-fine Gaussian correction has the best adjustment accuracy with least number of images to be recorded, which minimize the adjustment time as well as bleaching of the sample. In a practical lab scenario it is shown that the proposed automated adjustment minimizes spherical aberrations, resulting in the smallest PSF, the highest intensity, and the best alignment of multi-color images. This enables recording of the sharpest lateral as well as axial resolution with a minimized distortion of the confocal microscope images.

Chapter 5

Adaptive Optics Development for Leica SP5 CLSM

As the other optical microscopy, the resolution of the confocal laser scanning microscopy (CLSM) is theoretically defined by diffraction limits. In non-idealistic imaging conditions, however, the theoretical resolution may not be attained due to aberrations and such chance become frequent by emerging needs in biology for deep imaging through the living tissues [43, 108]. As a candidate of the solutions, adaptive optics have recently received much attentions over the last decade and some results shows the improvement of the images by correcting aberrations [108, 122].

In this chapter an AO development is discussed for a commercial CLMS, Leica SP5. The development of AO for the Leica SP5 CLSM is conducted in four parts. First, a general design consideration of AO for CLSM is discussed for its aberrations and optical structure. Based on the literature analysis, design considerations such as the locations of AO components, confocal wavefront sensing, and anisoplanatism are drawn and analyzed. From the literature, the aberrations of AO for CLSM is discussed and analyzed for derive the requirements of AO system to verify the its concept. Second part of the development is a modification of the Leica SP5 scanhead that interfaces the developed AO system. For the design of AO for PSF-engineering at specimen and detection pinhole, multi functional port (MFP) is selected as an interface for AO and Leica SP5 CLSM. An external detector is specially ordered for the sensitive measurement of fluorescence over 650 nm, which is designed for experiments. Third the AO components such as a deformable mirror (DM) and a wavefront sensor are selected based on the budget analysis. A 19ch piezoelectric DM is selected for the AO system design considering the derived requirements from the model. For wavefront sensing, a cooled CCD sensor is selected for weak fluorescence imaging due to its high quantum efficiency (QE) and low thermal noise. An adjustable pinhole is adapted with the wavefront sensor to remove the out of focus light and for a study on the trade off between out of focus light rejection and the wavefront distortion. Finally, verification experiments illustrate the selected components and interface for Leica SP5 can influence the image quality and point spread function of CLSM imaging and measure the wavefront information from the fluorescence, which allows a complete AO system in the Chapter 6.

5.1 Adaptive Optics Design for CLSM

5.1.1 Interface of the Adaptive Optics to CLSM

To design an adaptive optics system to CLSM, the location of two main components of wavefront correctors and wavefront sensors is analyzed. The location of the wavefront corrector directly discussed first for the correction ability of the excitation and detector path. Then the location of the wavefront sensor is discussed based on the decided location of the wavefront corrector.

Wavefront Corrector of AO for CLSM

The early study for AO development for CLSM [109] raises three possible locations of wavefront corrector in only excitation path, only illumination path, or both paths. Fig. 5.1 shows three possible implementations for CLSM of epi-illumination type. As discussed in 1.3, deep imaging through specimen causes various aberrations that blur the point spread function at the specimen as well as the point spread function at the pinhole detector. The aberrations are the same in both path since the fluorescence itself at the specimen acts as a point-like source without aberrations and the fluorescence pass exactly same optical path of the excitation light. For the confocal design, correction of the each path as Fig. 5.1(a) and Fig. 5.1(b) does not complete the image correction. For the epi-illumination type, the common path between scanning system and dichroic mirror is desirable for the wavefront corrector to can both point spread functions [109]. Most AO design for CLSM use this common paths for the wavefront correctors[109, 110, 135].

This is based on the assumption that both excitation paths suffer the same aberrations due to the same optical path in the specimen. Therefore the difference in aberrations in both path may cause the degrades the correction quality. For example, chromatic aberrations of the specimen due to different wavelength of excitation laser and fluorescence should be negligible compared to the common aberrations. This assumption is practically proven from the AO with fluorescence guided stars [110], which uses different wavelength to measure and compensate the aberrations.

Wavefront Sensors of AO for CLSM

To determine the aberrations to compensate the aberrations due to specimen should be measured and the position of the wavefront sensor determines the correction method. For direct measurement of aberrations of specimen, a light source should be point like at the focal point [134]. Scattered light from the specimen [131, 134, 195] and the fluorescence [110, 112, 117, 135–137, 139] can be used. Scattered light has benefit in retaining signal intensity due to no bleaching effect, while the structure of the specimen influences scattering and selection the scattering at focus from other reflections may need special technique such as coherence gating [131, 195]. Fluorescence-based wavefront sensing, also called fluorescence guided star methods, uses the fluorescence light at the focus. The fluorescence source can be injected and expressed in the specimen by user's intention [110, 136] and easily separated from the reflection by a dichroic filter while its intensity is usually weak compared to the excitation light and due to photobleaching the signal intensity degraded during the measurement. In this research fluorescence based wavefront sensing is chosen

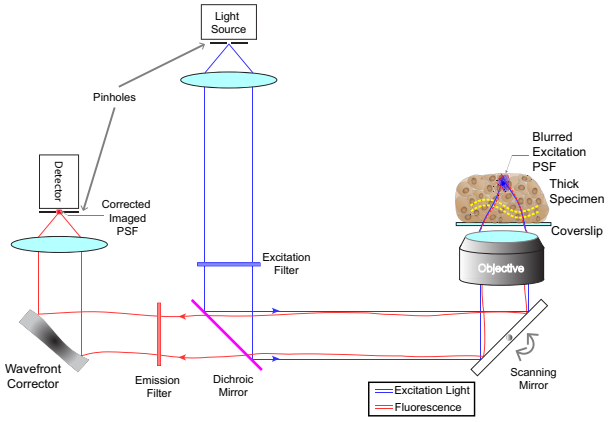

(a) Only detection path

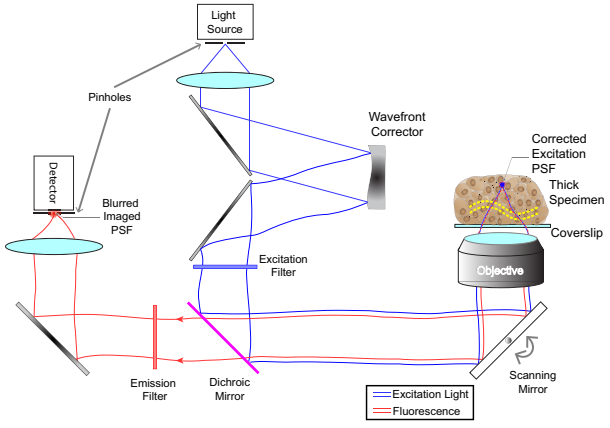

(b) Only illumination path

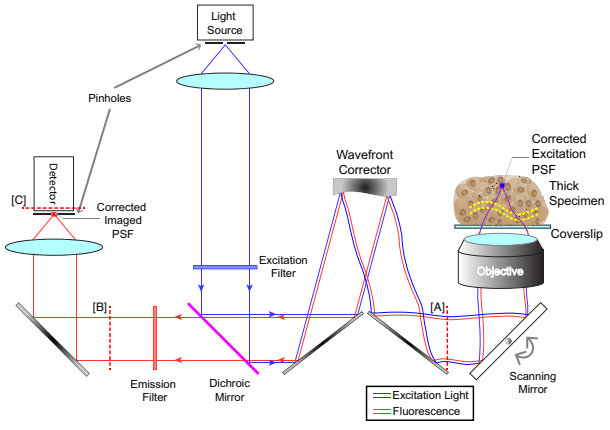

(c) Both detection and excitation path

Figure 5.1: The location of wavefront corrector at (a) emission (detection) path only (b) illumination (excitation) path only (c) both excitation and detection path. The correction of either excitation and detection path corrects the point spread function at the specimen or at the detection pinhole while correction at the both path can improve both point spread function.

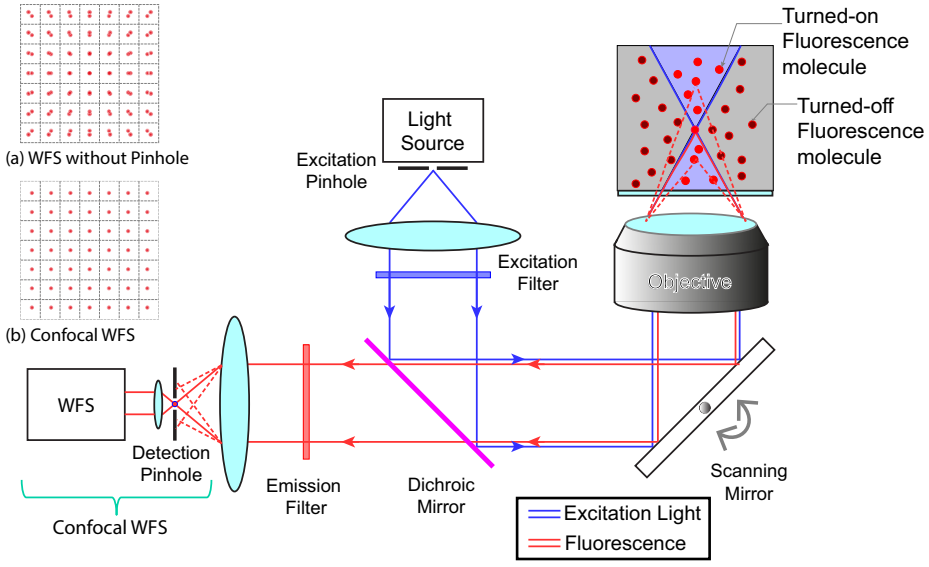

Figure 5.2: Schematics of confocal wavefront sensor. In confocal microscope fluorescence molecule of in the light path, shown as blue triangles in the specimen, are excited and generate fluorescence in a volume, which degrades the wavefront sensor spot images. By adding a pinhole in front of wavefront sensor, fluorescence molecules at the focal region are selected for wavefront sensing and out-of-focus fluorescence are rejected, as the principle of confocal microscopy.

due to the benefits aforementioned and because the dichroic filters for the separation of the fluorescence can be reused for the imaging path.

Fig. 5.1(c) also illustrates possible wavefront sensor locations with selected wavefront corrector position. [A] shows fluorescence between the scanning system and the wavefront corrector, [B] is for fluorescence between the dichroic mirror and the detection pinhole, and [C] is for fluorescence after the detection pinhole. At the location [A], wavefront sensors can measure the aberrations from the specimen directly while at [B] and [C] measures the compensated aberrations by the wavefront corrector. The closed loop control configuration, [B] and [C] is proper location for the wavefront sensing. The position [C], called confocal wavefront, is better for wavefront sensing by rejecting out-of-focus light, discussed in Chap. 5.1.2.

5.1.2 Confocal Wavefront Sensor

For correct measurements of the wavefront distortion for confocal microscopy, the light at the focal point should be used for the wavefront sensing [134]. however, in confocal microscopy all the fluorophore at both in-focus and out-of-focus are excited and emit the fluorescence and this in-focus light has to be selected. As the confocal microscopy principle, a pinhole can select the light from the plane and the wavefront sensor with pinhole is called confocal wavefront sensor [196].

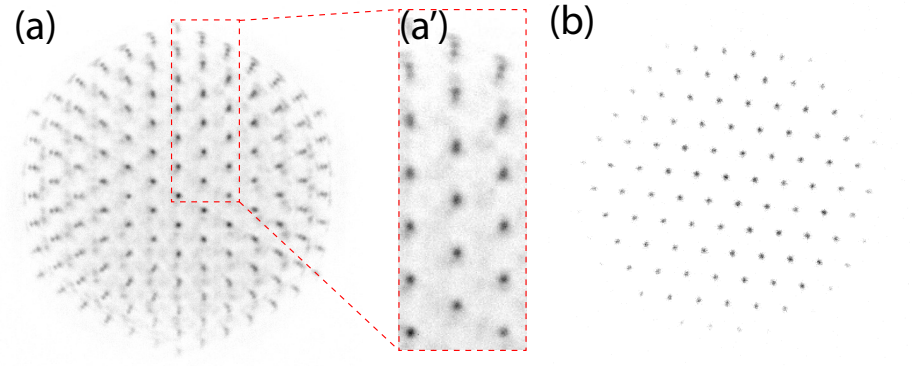

Figure 5.3: Spot images of Shack Hartmann wavefront sensor (Coolsnap HQ2 CCD Camera, Photometrics, Tucson, AZ, USA, with a lenslet array of 300 μm pitch f = 18 mm hexagonal grid, Flexible Optical B.V) (a) without pinhole (b) with 3 AU of pinhole. The light sources are fluorescence beads dispersed in 3D in polyacrylamide (PA) gel (refractive index = 1.38). An oil immersion objective (HCX PL APO 40×/1.25 NA , 506179, Leica Microsystems) is used. For detail experimental setup, see Chap. 5.4.2.

Fig. 5.2 illustrates the function of confocal wavefront sensor with sparse fluorescence beads specimen in a 3D stack. Without pinhole, the fluorescence from the out-of-focus are imaged with in-focus light and degrades the wavefront sensing performance by extending spot images. Confocal wavefront sensor can reject the fluorescence from the out of focus, and maintain the fluorescence at the focus. Fig 5.3 shows the measured WFS images with and without pinhole from fluorescence beads (FluoSpheres Carboxylate-Modified Microspheres, 0.2μm, crimson fluorescent (625/645), Life Technologies, Carlbad, CA, USA) distributed in 3D in polyacrylamide (PA) gel. The fluorescence from the out-of-focus plane blur and superpose the spot images of the lenslet while the pinhole shows the clear spot images for the lenslet image, providing a correct measurement of wavefront error.

The size of the pinhole should be selected carefully considering the trade-off of the sectioning ability and intensity degradation and wavefront distortion. The optical sectioning thickness, the range of the in-focus light defined by axial full width at half maximum, decreases by reducing pinhole size while the transmitted the signal intensity reduced as well[196]. More problem with a small pinhole is that the pinhole also rejects the light with aberrations, smoothing the measured wavefront [134, 196]. This smoothened wavefront also generates wavefront measurement errors with respect to the actual aberrations of the specimen.

Fig. 5.4 shows this trade off in terms of (a) average optical sectioning thickness (Fig.6(a) in [196]) and (b) average wavefront error caused by the finite size of the pinhole. In Fig. 5.4(a), u is normalized defocus unit defined by $u = z4kn\sin^2(\sin^{-1}(NA/n)/2)$, where z denotes axial displacement, NA is numerical aperture of objective with refractive index n, and wavenumber k. For example, the optical thickness with 5 airy unit (AU) of pinhole size provides 59 to 75 normalized defocus, corresponding to 4.54 - 5.77 μm optical section thickness for aberrations up to 0.5λ RMS wavefront error with 1.25 NA oil immersion

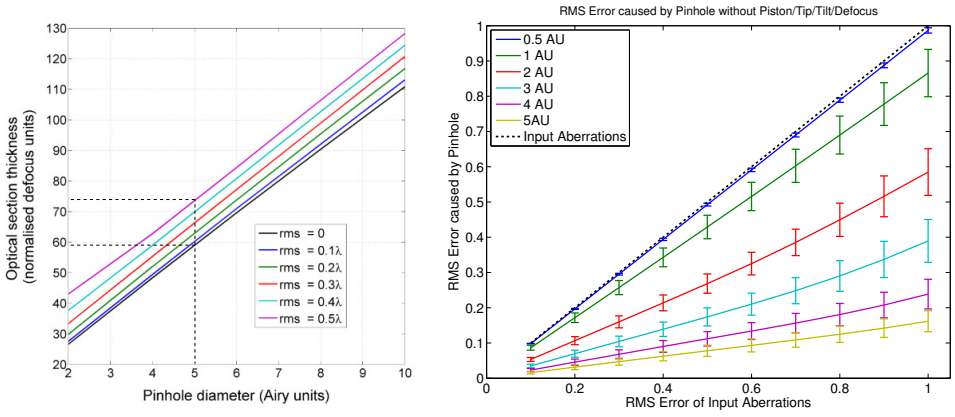

(a) Sectioning ability [196]

(b) Wavefront error by pinhole

Figure 5.4: Sectioning ability by the pinhole size (Figure is adapted from [196]) and wavefront error caused by the finite size pinhole. The sectioning thickness decreases as the pinhole size decreases while the wavefront error by pinhole increases, leading to the measurement error.

objective and 633 *nm* HeNe laser. Fig. 5.4(b) shows average wavefront error according to the actual RMS wavefront error caused by finite size pinhole. For 5 AU of the pinhole, the wavefront errors caused by the pinhole are less than 20 % of the original aberrations.

5.1.3 Anisoplanatism: Correction region of AO

Aberration correction point by point is difficult since the pixel rate is more than 0.5 MHz while the deformable mirror has kHz bandwidth. In addition wavefront sensing from weak fluorescence may take fractions of a second or even seconds to collect sufficient number of photons. By this reason, an AO correction per image is applied in the most AO developments [101, 102, 110, 125, 135]. However, the aberrations are not the same for the wide range because of different optical structure due to the specimen location and the different optical path by beam scanning points [22]. This inconsistency of aberrations by image translation is called anisoplanatism and much studied in adaptive optics to examine the coverage of guided star techniques [89, 197]. Isoplanatic angle (range) can be defined as [89, 136]

$$\sigma_\delta \quad = \quad \|\Psi(x,0) - \Psi(x,\delta)\| = 1 \; rad, \tag{5.1}$$

where δ is the size of the range, whose RMS wavefront error due to anisoplanatism equals 1 radian.

Besides its importance, there are a few work that measures the isoplanatism for microscopy. In [136] the isoplanatic range is measured from the three points measurements. The radius of anisoplanatism 19 ± 5.57 μm for $\times 40$, 0.75 NA objective lens. This concludes that a guide star for wavefront sensing can be effective approximately the range of $20\mu m$ circle for an AO correction [108, 136]. Although this range can be different by the objective and measurement conditions, the radius of $20\mu m$ (40 μm diameter) can be used as a rule of

thumb for the first AO development with commercial CLSM.

5.1.4 Wavefront Sensing with Scanning

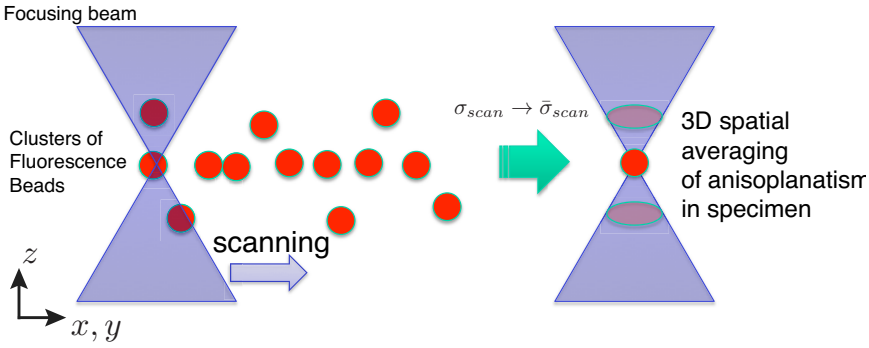

Figure 5.5: Concept of the scanning beam during wavefront sensing. The wavefront sensor corrects fluorescence from the multiple beads while the excitation light (violet double cone) is translated by the beam scanning system. By scanning, the excitation time per beads can be reduced, i.e. photobleaching per fluorophore is decresed.

As discussed in Chap. 1.3.3, fluorescence has advantages as an artificial guide star since fluorescence can be independent from the aberrations of the excitation light and can be arbitrary controlled by users using various techniques such as the bead injection technique [136] and labeling with fluorescent protein [138]. However the intensity of fluorescence is relatively weak and is even decreased due to photobleaching during the aberration correction. This signal loss leads to the low signal to noise ratio (SNR) with relatively high noise in the wavefront sensing measurements and limits the running time of AO system.

To reduce the photobleaching during the wavefront measurements, a beam scanning during wavefront sensing is proposed. For wavefront sensing from the back scattered light, the wavefront sensing during beam scanning shows to reduce the intensity fluctuation over the pupil function [134]. Fig. 5.5 shows the concept of the wavefront sensing during the scanning. The wavefront sensor accumulates photons from the multiple fluorophores while the scanning mirror stirs the excitation beam (violet double cone) in the specimen. By the scanning the exposure of the excitation beam per fluorophore can be reduced, and the AO correction time can be extended. The expected drawback is the range of scanning has to be sufficiently small so that fluorescence from multiple fluorophore can image similar aberrations.

5.1.5 Aberrations in Confocal Microscopy

The aberrations in the microscope can be categorized in two parts: system aberrations and specimen induced aberrations [108]. System aberrations are caused by the imperfect optical

system design, manufacturing tolerances, and implementation. The aberrations during scanning can be a part of system aberration since it depends on the optics design of isoplanatism. The specimen induced aberrations are aberrations by the measurement procedure depending on the specimen. These specimen induced aberrations can be categorized by refractive index mismatch, e.g. depth-dependent aberrations (between immersion media and average refractive index of specimen) and coverslip mismatch (between immersion media and coverslip glass), as well as field dependent fluctuation due to a non-homogeneous refractive index of the imaged specimen.

Specimen induced aberrations are studied by both theoretical simulation and practical measurements. The aberrations generated by a specific shape of specimen such as a layered tissue like skin and a cylindrical shape is simulated and considered for the aberration corrections [20, 172, 198]. Two deformable mirrors are analyzed and evaluated for its correction qualities regarding simulated depth dependent aberrations [173]. The measurement methods for the aberrations in microscopy are investigated using phase stepping interferometry [199], Shack Hartmann wavefront sensor [136], image quality maximization [200]. This spatial band-limited behavior is also studied as framework of atmospheric aberration description [201, 202].

In addition to the aberrations in CLSM, an aberrations can be added by implementing adaptive optics. By wavefront corrector, a fitting error is expected due to the correction principle, structure, and spacing of the wavefront corrector. For example, spatial light modulator has limited stroke and for the wrapping for the large stroke may cause high order aberrations similar to Fresnel lenses. For deformable mirror, the spacing and structure of the actuator design define the number of modes that mirror can correct and result in the different fitting error characteristics [89, 203]. For confocal wavefront sensor, the wavefront measurement contains error proportional to the total aberrations due to the confocal pinhole of a finite size γ_{ph}, besides the measurement noise of the sensor [134, 196, 204].

Assuming that the most aberration sources in microscope are all independent, then the total variance of aberrations σ^2_{tot} of confocal microscope imaging can be approximated as the sum of the variances corresponding to the specific sources as

$$\sigma^2_{tot} \approx \sigma^2_{sys} + \sigma^2_{scan} + \sigma^2_{cvsl} + \sigma^2_{depth} + \sigma^2_{fluc} + \sigma^2_{fit} + \sigma^2_{delay}, \tag{5.2}$$

where σ^2_{sys} is the variance of system aberrations generated by misalignments and design error of the optical system, σ^2_{scan} denotes the variance of aberrations by anisoplanatism during lateral or axial scanning, σ^2_{cvsl} denotes the variance of aberrations due to refractive index mismatch of coverslip and immersion media, σ^2_{depth} denotes the variance of aberrations induced by imaging depth through specimen, and σ^2_{fluc} denotes the variance of aberrations induced by fluctuations of the optical structure of the specimen. σ^2_{fit} denotes the variance of fitting errors by wavefront corrector, and σ^2_{delay} is the temporal error variance by the feedback control for time-varying aberrations. For the confocal wavefront sensors, the measurement error σ^2_{meas} also depends on the pinhole at the focus as

$$\sigma^2_{meas} \approx g(\sigma^2_{tot}, \gamma_{ph}) + \sigma^2_{meas}, \tag{5.3}$$

where $g(\cdot,\cdot)$ is a complex smoothing function of wavefront by confocal wavefront sensing by the finite-size pinhole (cf. See Chap. 7 for more discussion), σ^2_{meas} denotes the measure-

Mean (STD) [rad]	$Z_5 - Z_{45}$	$Z_{16} - Z_{45}$	$Z_{29} - Z_{45}$
RMS Error	1.94(0.39)	1.00(0.13)	0.6232(0.10)

Table 5.1: Simulated RMS wavefront error in the range of modes based on the measurement model in [196].

ment noise of the wavefront sensor.

One common observation on the aberrations in microscopy is that the Zernike coefficients tend to decrease as its order increases, as the aberrations in astronomical telescopes do. The aberration correction only with low order aberrations can increase the correction quality even though the diffraction limited resolution is not guaranteed [136, 196]. To estimate the impact of low order correction, a hundred random aberrations are generated based on the measurement model until Z_{45} of *C. elegans* specimens in [196] and is evaluated the root mean square (RMS) error according to the low order corrections. Table 5.1 shows the original RMS errors of the mode ($Z_5 - Z_{45}$) and the RMS error of the perfect correction until Z_{15} ($Z_{16} - Z_{45}$) and Z_{28} ($Z_{29} - Z_{45}$). By correction until Z_{15} can reduce the half of the original aberrations while the improvement can drop by the order increases. For verifying the concept of AO with the first design, a deformable mirror with low order correction could be sufficient as in [136].

From the simulation, peak to peak difference of the aberrations are also obtained as 2.24 ($\pm$0.4) μm. This can be used for the required stroke of the actuators in the deformable mirror.

5.2 Modifications in Leica SP5

A commercial CLSM of Leica SP5 is used for the base of the development in this thesis. Fig 5.6 shows the optical path in the Leica SP5 scanhead. The microscope contains visual light lasers such as Ar ion laser (458nm-514nm), DPSS laser (561nm), and HeNe laser (594nm and 633nm) and UV diode laser (405nm) as a light source for excitation. The laser is passing through the scanner module and is focused to the specimen by the objective. There are three detectors of PMT in the system: internal detectors with a detection pinhole, reflection light detector (RLD), and transmission light detector (TLD). Multi functional port (MFP) is usually an interface for an infrared laser for multi-photon excitation microscopy. TLD and RLD are the detector for the reflection and transmission of the excitation lasers, which are in general visual lasers.

For the adaptive optics development, MFP is chosen for the interface to the Leica SP5 CLSM. For the confocal microscopy, the wavefront correction has to be done in both excitation and illumination path [109]. MFP is usually used only for the excitation path while it is also possible to have both, excitation and illumination path design, outside of the scanhead by setting a mirror at the MFP slide (See Fig. 5.6). RLD is used as a detector for the developed AO system since it can be detached from the main microscope frame and placed freely on the optical table. This structure allows full utilization of the given Leica SP5 confocal microscope with a Leica software. Since those MFP and RLD are not with a designed purpose of the current AO development, which has different requirements mainly due to

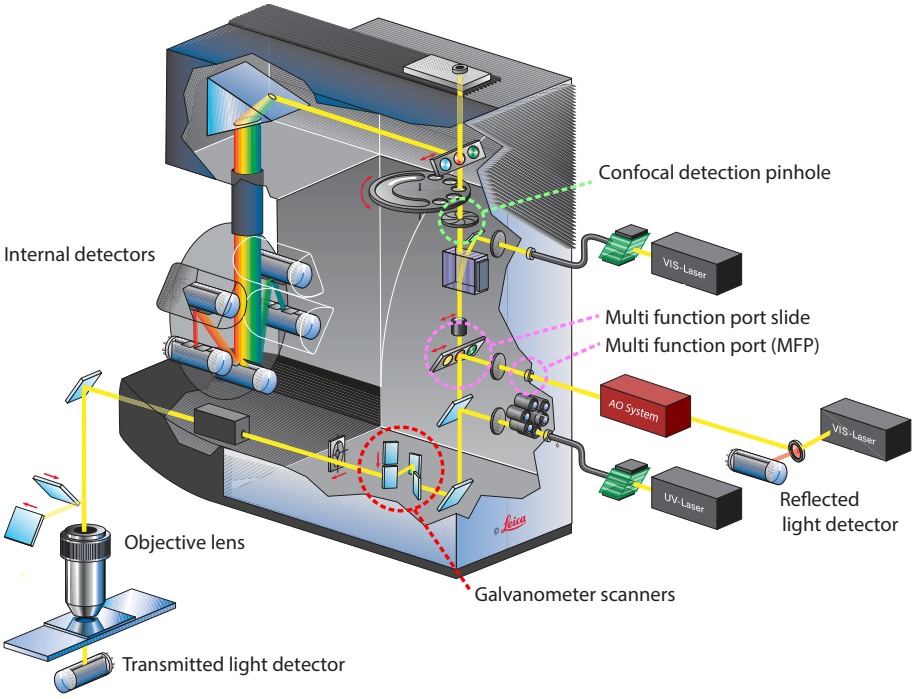

Figure 5.6: Diagram of a Leica SP5 confocal scanhead, including the beam path from source to detector (Original diagram is from Manual of SP5, Leica Microsystems).

wavelength difference, modifications are necessary. The following subsections briefly explain the performed modifications.

5.2.1 Multi Functional Port

Since the multi functional port (MFP) usually is used as an interface for the excitation path of the infrared laser, the first mirror at the MFP is initially an infrared mirror and the MFP slides consist of two short pass dichroic mirrors with a threshold of 650 *nm* and 750 *nm* and a metallic broadband mirror. Since more than 80% of the HeNe laser power is lost at the first mirror, it is replaced with a broadband dielectric mirror for the visual spectrum (400-850 nm, BB05-E02,Thorlabs) for both the excitation and the emission path. In the MFP slides, a dichroic mirror for reflection of the 633nm HeNe Laser and the transmission of fluorescence is also installed (Hereby LP650, 645nm cut on/off, zt633rdc, Chroma Technology, Chroma). This provides a strong excitation from the external HeNe laser, while the internal detector can still collect the fluorescence from the specimen.

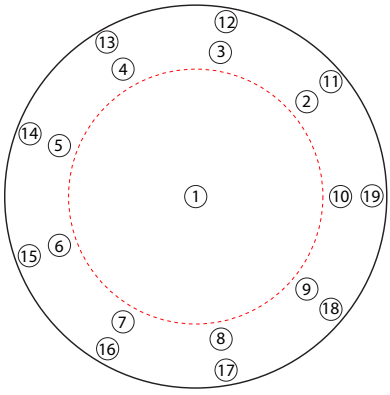

Figure 5.7: The coordination of actuator of the piezoelectric deformable mirror. The red dotted-lined circle shows a recommendable pupil size and position for preventing the aberrations due to the print-through of the actuator on the mirror surface.

5.2.2 Reflection Light Detector

The PMT in RLD is a custom-made for detecting fluorescence whose wavelength is longer than 650 *nm*. RLD can usually detect the light with a wavelength under 650 *nm*, which is common bound for the excitation laser lines for CLSM. The RLD is connected to the Leica SP5 scanhead and can be directly operated by the microscope software, which is convenient for generating and processing images.

5.3 Components of the Developed AO System

5.3.1 Piezoelectric Deformable Mirror

The adaptive optics system uses a piezoelectric deformable mirror (30 mm 19 channel PDM, Flexible Optical B.V., Rijswijk, the Netherlands), which has a special coordination specialized for the correction of low order aberrations [203]. As Fig. 5.7 shows, piezoelectric actuators are attached to the 30 mm circular mirror, one at the center and each 9 actuators on two concentric circles. The mirror is intended to use the pupil smaller than the inner concentric actuator circle, which prevents the aberrations due to the print-through of the actuators on the active mirror surface, an uncorrectable innate high order aberrations of the deformable mirror. This unique coordinate shows the less fitting wavefront error for the low order aberrations under 15th Zernike mode except tetrafoil $Z_4^{\pm 4}$ [203] The stroke of actuators is sufficient for the simulated aberration model in Chap. 5.1.5 since the stroke of piezoelectric actuator is 8 μm, Drawback of this PDM structure is that the effective strokes are reduced when the pupil size is getting smaller. Small number of actuators also limits the possible mirror shapes in high order mode errors. Because of piezoelectric actuators, nonlinearities such as hysteresis and creep can be weakness of this PDM in feedforward operations such as the identification of an influence matrix. The measurement of this nonlinearities and further discussions are summarized in Appendix B.

5.3.2 A Cooled CCD for Wavefront Sensing

For measuring the wavefront from the weak fluorescence, a CCD camera with high quantum efficiency (QE), low noise, and allows long exposure time is necessary. Regarding wavefront sensing with SH lenslet array, the total number of photon from the fluorescence is divided by the number of lenslet, which leads to hundreds times less numbers of photons per each lenslet. For example, a given CCD for wavefront sensor (UEye UI-2210SE, IDS Imaging Development Systems GmbH) cannot be used for fluorescence due to low QE and a limited exposure time shorter than 0.64 second. In addition, high readout noise also blocks the accumulation of the small intensity of the fluorescence. In literature for the wavefront sensing from fluorescence, a cooled CCD [113, 136] and an electron multiplying CCD [110] are used. In this research, a cooled CCD (Coolsnap HQ2 CCD Camera, Photometrics, Tucson, Arizona, USA) is used and considering high QE about 60% and low read noise and dark current, which also allows a long exposure time to collect enough number of photon from the fluorescence. The cooled CCD is controlled by the Matlab (Matlab 2013a, The MathWorks, Inc., Natick, Massachusetts, USA) through the Micro-manager [205] and Java interface.

5.3.3 Adjustable Pinhole

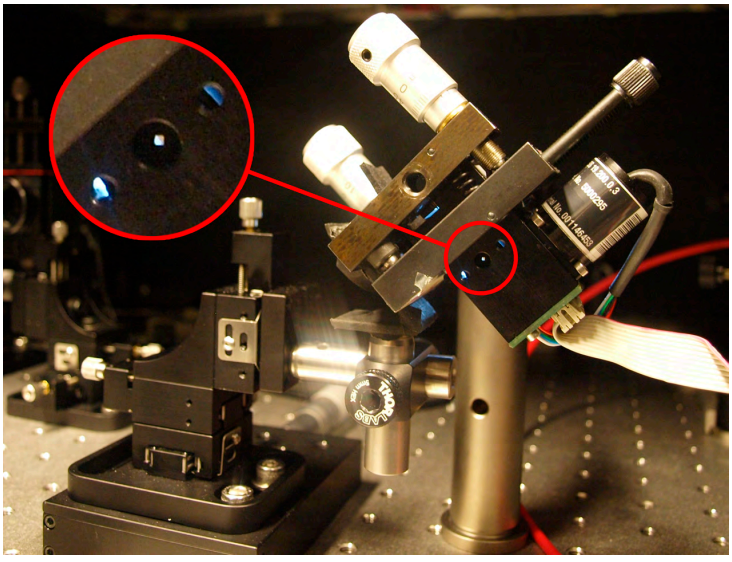

Figure 5.8: Adjustable square pinhole from Leica SP2, attached to the stages. The shining white LED in the backside shows that the shape of the pinhole is square.

For the experimental setup, a square adjustable pinhole in Fig. 5.8, a part of a commercial confocal microscope (Leica SP2, Leica Microsystems, Mannheim, Germany), is used for filtering out of focus light [206]. This allows a flexibility of the trade-off between out-of-focus light rejection and distortion of the aberration. In addition, by the narrow opening

of the pinhole in a certain extend, it can be used as a targeted point reference that can be used for correction. The peak intensity ratio between wide opening and narrow opening of the pinhole can be used a measure of the correction as well. These are discussed in the following chapter.

The adjustable pinhole module includes a stepper motor, which is operated by a stepper driver (Stellaris Stepper Motor Reference Design Kit, Texas Instruments, Dallas, TX, USA) controlled by Matlab. The size of the pinhole is controlled in open loop manner based on the calibration by a digital microscope (VHX-100, Keyence, Osaka, Japan) in advance. The initialization of the pinhole position is informed by an LED indicator connected to the photo-coupler in the pinhole module.

5.4 Verification of AO Developments

Before the first integration of the complete AO system, the PDM as well as the WFS with the cooled CCD are evaluated for the verification of the interface to the microscope and their functions. First the PDM is installed and verified to influence the image by flattening the wavefront and shaping point spread function based on the reference flat mirror. For the verification of the wavefront sensor, known aberrations such as defocus and spherical aberrations. The defocus can be obtained by z position error and spherical aberrations are generated by adjusting the coverslip correction collar.

5.4.1 Verification of DM

Since the interface via MFP is developed for an AO system, it should be verified for influencing the point spread function of the Leica CLSM, as intended. Fig. 5.9 shows the schematic of the experimental setup for the MFP and PDM verification. The external HeNe laser (633 nm, 7 mW, 1125P, JDSU) is focused on the pinhole (10 μm, Thorlabs). In front of the DM, a non-polarization cube beam splitter (50 % transmission and 50 % reflection, BS013, Thorlabs) separates the laser into two paths, to the deformable mirror and the reference flat mirror for alignment and calibration. After that, another non-polarization cube beam splitter (50 % transmission and 50 % reflection, BS013, Thorlabs) separates the input beam to the microscope and to the wavefront sensor. The MFP slide is set by the long pass dichroic mirror with a cutoff wavelength of 650 nm (LP650) for high input beam power at the objective and fluorescence detection with the internal PMT.

The first verification is an image enhancement by compensating the initial aberrations of the DM with respect to the flat reference mirror. Fig. 5.10 shows a specimen slide of convallaria majalis rhizome (CMR) with an initial distortion of DM and the flatten DM with respect to the reference mirror. A 0.4 NA dry objective is used for this imaging. It is shown that the intensity increases drastically when the initial aberrations are compensated.

The second verification is a point spread function engineering by introducing some astigmatism. An astigmatism can be applied to get an additional depth information of the fluorescence [207]. The specimen are red fluorescence beads (FluoSpheres Carboxylate-Modified Microspheres, 0.2 μm, crimson fluorescent (625/645), 2% solid, Life Technologies, Carlbad, CA, USA) sprinkled on both the coverslip and the objective glass using a poly-L-lysine coating, which is 1μm distance each other by adjusting the water in the gap.

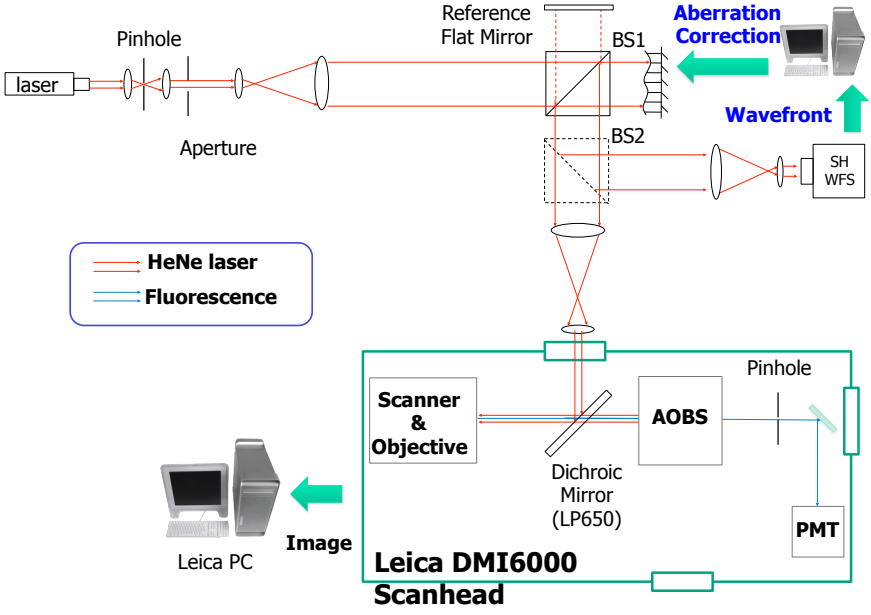

Figure 5.9: Schematics of the experimental setup for the verification of deformable mirror and MFP interface. The multi functional port slide is set as a long pass dichroic mirror (LP650) such that external HeNe laser is reflected while the fluorescence from the specimen can be imaged through the internal detectors.

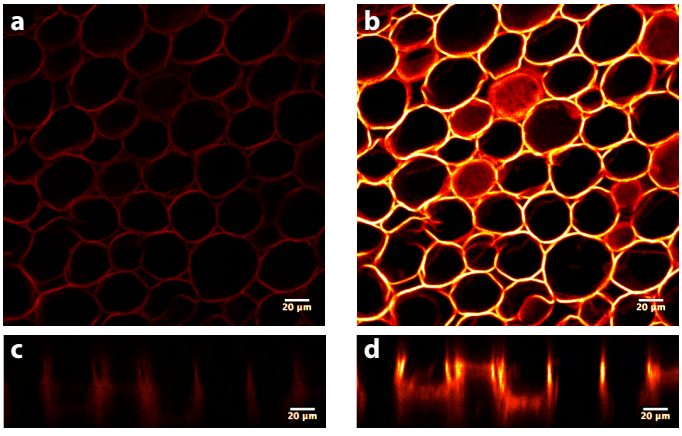

Figure 5.10: Lateral and axial images of convallaria majalis rhizome (CMR) with an inital distortion of the DM (a,c) and with the flattened DM based on the reference mirror (b,d). A 0.4 NA dry objective is used and the detection gain is the same for both images.

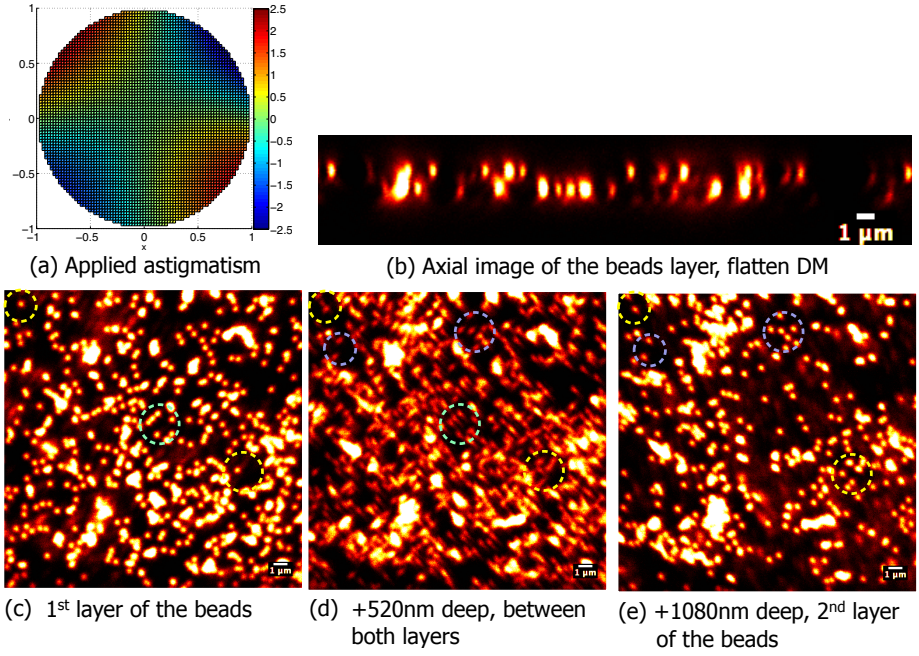

Figure 5.11: Verification of deformable mirror with an astigmatism and two layers of fluorescence beads specimen. Each layer of fluorescence is attached on the coverslip glass and objective glass. The distance between the layers is about a micrometer. The images at both layers and at the middle of two layers show the shape of the bead image along the positive and negative depth of the original beads position. Green dotted circles represent the beads on the first layer, blue dotted circles show the beads from the second layer, and yellow dotted circles contain beads image from both layers.

A 1.4 NA oil immersion objective is used for imaging. For PSF engineering, the PDM generates an astigmatism Z_5 with the coefficient of 1 radian. Fig. 5.11 shows (a) the applied astigmatism in radian, (b) the axial image of the specimen with the flattened mirror, and (c-e) the results of the experiments.

5.4.2 Verification of Wavefront Sensing from Fluorescence

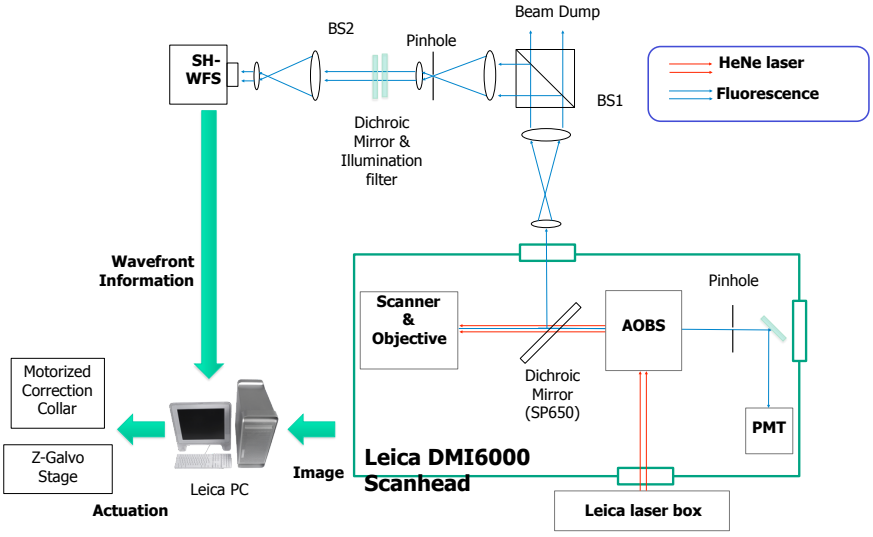

Figure 5.12: Experimental setup for the verification of the wavefront sensing from fluorescence via MFP. MFP slide is set as a short pass dichroic mirror over 650 *nm (SP650) so that internal HeNe laser can be transmitted to specimen while the fluorescence can be measured with the wavefront sensor outside of the scanhead. The amount of fluorescence that measured by internal detector is significantly reduced due to the dichroic mirror but the fluorescence still can be imaged.*

As the DM shows that it can influence the aberrations in the CLSM image via the designed MFP interface, the wavefront sensor is verified by measuring known aberrations from the fluorescence through the MFP interface. Fig. 5.12 shows the schematic of the experimental setup for the wavefront sensor verification. The internal HeNe laser is used for the fluorescence imaging, which is a fixed source while the fluorescence is collected to the SHWFS through the adjustable pinhole of 5 airy unit (AU). For the imaging, a 1.2 NA water immersion objective with a coverslip correction collar (HCX PL λ_{BL} APO 63$\times$ 1.20 NA water immersion, Leica Microsystems, Mannheim, Germany) is used. The specimen slides is also red fluorescence beads as used for the DM verification, but only on the coverslip glass. The SHWFS collects the light while the scanning is running with a small region of 3.84×3.84 μm. For the known aberration measurements, defocus and spherical aberrations are measured based on the z stage translation and the coverslip correction ring manipulation. Fig. 5.13 shows the changes of the measured aberrations by the z stage movements and the coverslip correction collar manipulation. A directional defocus is observed by moving the specimen closer to the objective (–0.6 μm z movement) and away from the objective (+0.6 μm z movement). The introduced spherical aberration via the coverslip correction collar can also be measured by the SHWFS via the MFP. During the spherical aberration measurements induced by the coverslip correction collar, the axial position (defocus) is ad-

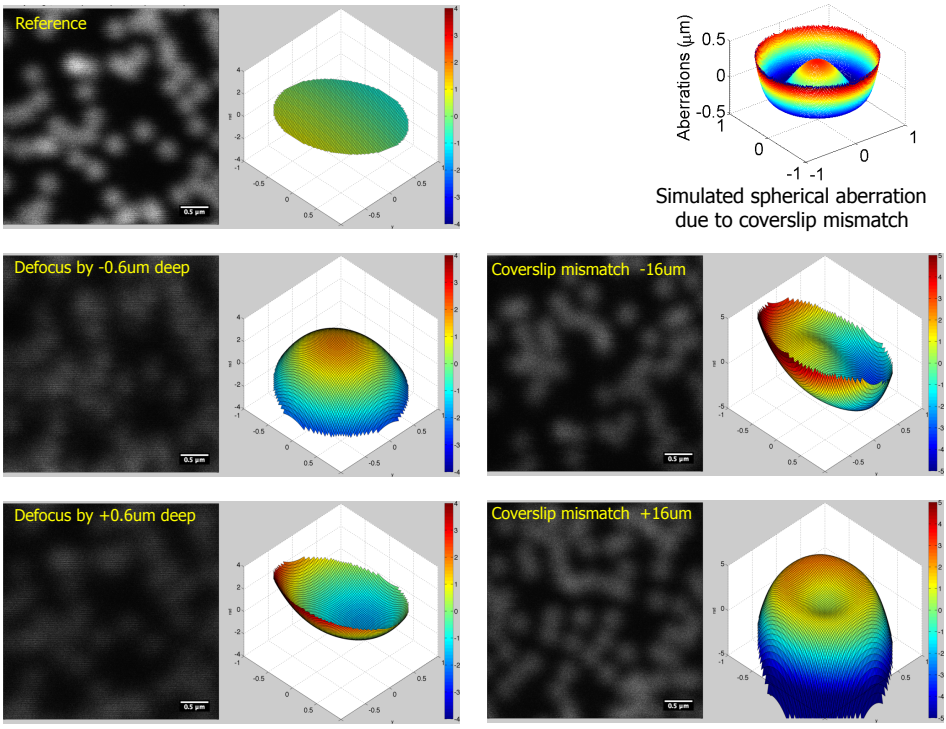

Figure 5.13: Verification of the wavefront sensor with the known aberration of defocus by the axial displacements and spherical aberrations by coverslip mismatch induced by coverslip correction collar. It is also observed that the image intensity is dropped with defocus and spherical aberrations.

justed according to the maximum intensity of the image. The results also show a directional spherical aberrations with a shape of the simulation. This proves the function of MFP interface and the SHWFS for the complete AO development, which is described in the following chapter.

5.5 Summary

For the design of AO for commercial CLSM, design choices and considerations are investigated. Based on the analysis, MFP and RLD of the Leica SP5 scan head are modified for the interface to the designed AO system. For main AO components a 19 channel PDM is chosen considering the design requirements and efficiency. For weak the fluorescence, a Coolsnap HQ2 CCD camera is chosen for wavefront sensor due to its high QE, low noise, and the capability for long exposure time because of the weak fluorescence. An adjustable pinhole from Leica SP2 confocal scanhead is installed for rejecting the out of focus light. By the experiments, the main components of AO through designed interface are verified for the complete AO developments in the following chapter.

Chapter 6

Adaptive Optics for CLSM with Adjustable Pinhole

In this chapter, an adaptive optics (AO) for the commercial confocal laser scanning microscopy (CLSM) is developed and evaluated for aberration compensation induced by biological specimen. The AO system consists of a 19ch piezoelectric deformable mirror and two Shack Hartmann wavefront sensor (SH-WFS) associate with an excitation HeNe laser and fluorescence from the specimen. The AO system is equipped with an adjustable pinhole, which can used for referencing SH-WFS. In addition a quality measure is defined based on maximum intensities with different pinhole size, which can be easily implementable with adjustable pinhole. Experimental results with fluorescence beads on the coverslip and 40 μm deep into the sphere cell cluster shows that the proposed AO system, calibration algorithm can improve the resolution up to 33.7% in axial full width at half maximum (FWHM). The proposed quality measure with different pinhole size illustrates the improvement as well.

6.1 Introduction

A pinhole is an unique component in CLSM, providing axial resolution of the images by rejecting out of focus light. This sectioning ability allows 3D imaging of the specimen, making CLSM popular in biological fluorescence imaging [1]. The size of the pinhole is directly influence the resolution and the intensity of the image [2, 208]: a bigger pinhole provides more intensity while the resolution of CLSM gets worse. For this trade-off, microscope manufactures provide adjustable pinholes in their CLSMs for users to choose the pinhole size based on their specimen condition [206].

The pinhole also plays an important role in AO for CLSM. The sensorless AO design uses the images of the microscope while the pinhole is always installed for the confocal image. The size of pinhole influences the final correction quality of the sensorless AO correction, and the small enough pinhole is necessary to achieve the high Strehl ratio [209]. For the AO with wavefront sensors such as Shack Hartmann wavefront sensors (SH-WFS), the pinhole is also important to reject out of focus light, which can cause malfunction of the SH-WFS by degraded spot image as Fig. 5.3. By this reason, the pinhole is usually

installed in most AO developments for CLSM in front of the SH-WFS for separating the targeted light source from the other sources around [112] and suppressing the light from the uninteresting out of focus region [134, 135, 138, 139, 204]. This type of wavefront sensors with pinhole are called confocal wavefront sensor (CWFS) [196]. For CWFS the selection of the size of the pinhole is also important design parameter as CLSM. For decision of the pinhole size, researchers in [135, 138] consider the maximum spatial frequency of the targeted aberrations [135, 138] and researchers in [196] uses optical sectioning ability in wavefront sensing, while they all uses a fixed size pinhole based on calculation.

In this chapter, an AO development is discussed for the commercial confocal laser scanning fluorescence microscopy to compensate for the aberration in the specimen. The AO system contains an adjustable pinhole in front of the detection path which leads to the wavefront sensor and imaging detector. Using the adjustable pinhole, a calibration method for AO system is proposed to compensate for the system aberrations in the designed light paths by improve referencing quality. A pinhole intensity ratio is also proposed to evaluate the improvement by AO, which can be easily applied for the commercial CLSMs. Experimental results with fluorescence beads on the coverslip shows the benefits of the proposed calibration methods with an adjustable pinhole. The beads in 40 μm deep into the sphere cell cluster shows that the developed AO can improve the full width half maximum (FWHM). The proposed pinhole intensity ratio with different pinhole size also clearly supports the results with FWHM.

The rest of chapter organized as follows. In Section 6.2, the design of the optical system and its control of the developed AO system is described. Then the AO calibration method using adjustable pinhole is discussed in Section 6.3. Pinhole intensity ratio for AO evaluation is given in Section 6.4. In Section 6.5 describes the experimental results for the evaluation of the calibration methods and AO correction in the specimen.

6.2 System Description

6.2.1 Optical System Design

Fig. 6.1 and Fig. 6.2 shows an experimental setup for the AO for Leica SP5 confocal microscope. The light source for excitation path is a HeNe laser (633 nm, 7 mW, 1125P, JDSU) with a polarizer for changing the intensity. L1 (f=11 mm, A397TM-A, Thorlabs, Newton, NJ, USA) and L2 (f=60 mm, AC254-060-A-ML, Thorlabs) with a fixed pinhole (10 μm, Thorlabs) generate a clear Gaussian pupil at the aperture (D1). This beam is expanded to 23 mm for a 19 channel piezoelectric actuated deformable mirror PDM (30 mm 19 channel, Flexible Optical B.V.) by L3 (f=200 mm, AC254-200-A-ML, Thorlabs) and L4 (f=750 mm, AC508-750-A-ML, Thorlabs). The size of the beam is adjusted by the aperture after L2. After a wavefront modification by PDM, the beam is contracted by L5 (f=500 mm, AC508-500-A-ML, Thorlabs) and L6 (f=150 mm, AC254-150-A-ML, Thorlabs). Then the beam is split into two by a non-polarization cube beam splitter BS1 (90% transmission and 10% reflection, BS025, Thorlabs), for the sampled beam (10% reflection) is used for the wavefront measurement by Shack Hartmann wavefront sensor WFS2 (200 μm pitch f = 10 mm orthogonal grid lenslet array, APO-Q-P192-F3.17, UEye UI-2210SE CCD camera, Flexible Optical B.V., Rijswijk, the Netherlands), which is conjugated with PDM by L9 (f=300 mm,

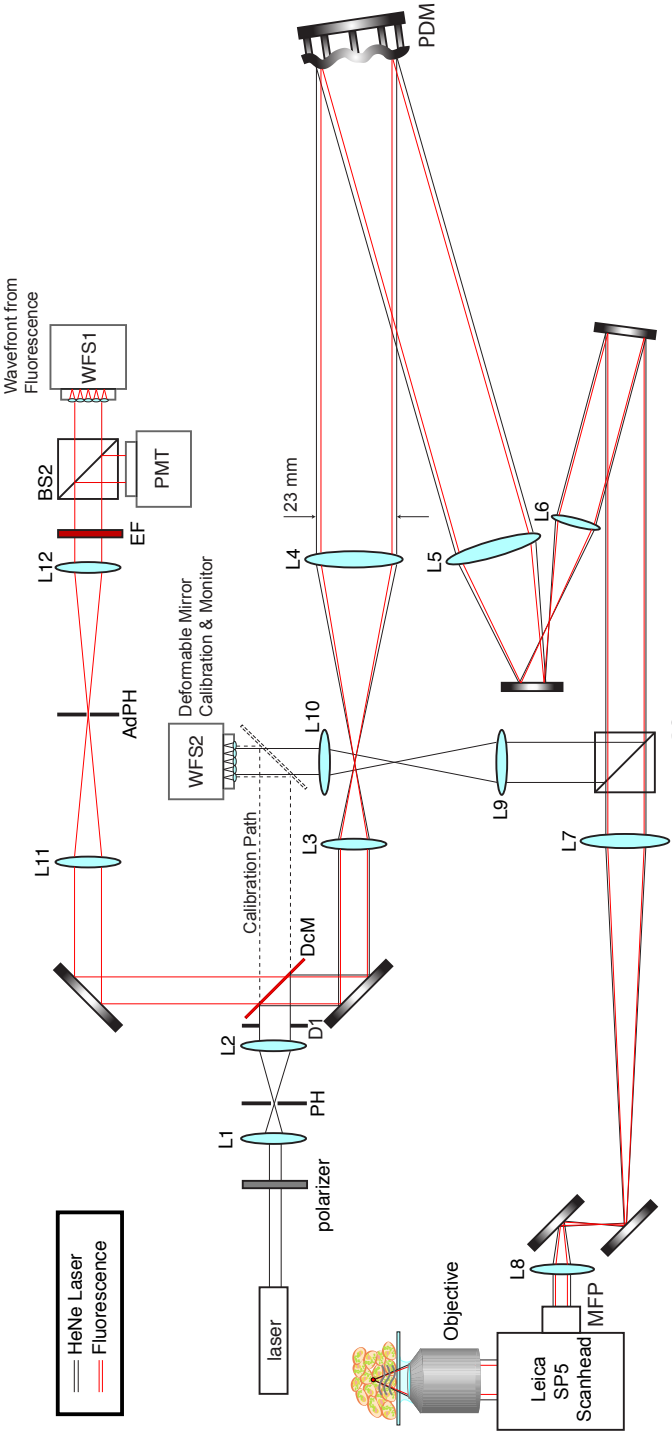

Figure 6.1: Schematics of the experimental setup for a Leica SP5 confocal microscope via multi-functional port.

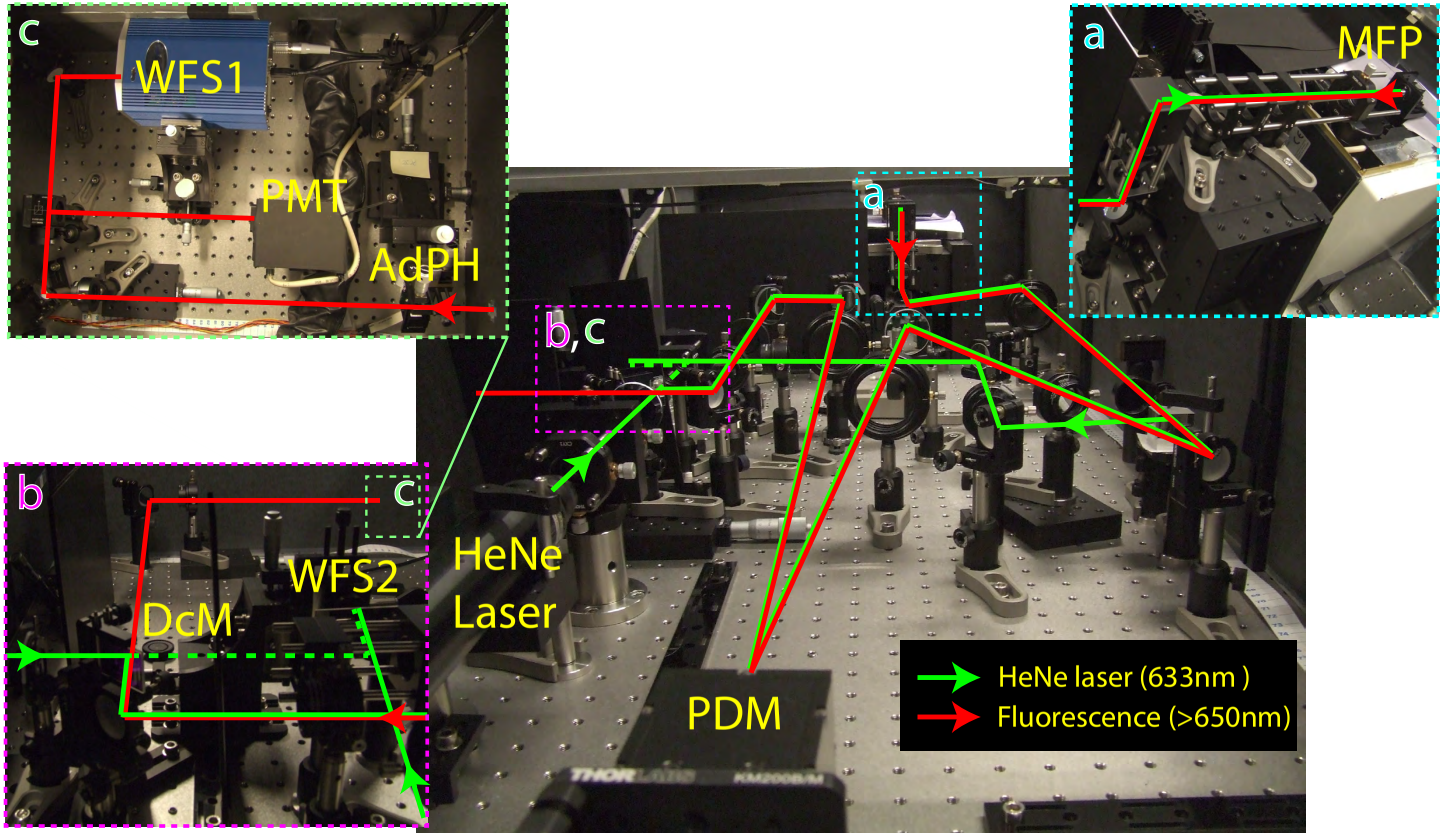

Figure 6.2: Photographs of the experimental setup. Green lines represent the HeNe laser line (633nm) and red lines represent the path of fluorescence. These colors are selected for clear presentation although both are red for human eye. The picture at center shows the main path that continues to (a) Multifunctional port and its interface. (b) dichroic mirror (DcM) that branches the detection path for fluorescence and mirror shape detection (WFS2) (c) fluorescence detection path for a photomultiplier tube (PMT, Leica RLD), and a wavefront sensor for fluorescence (WFS2) including an adjustable pinhole (AdPH).

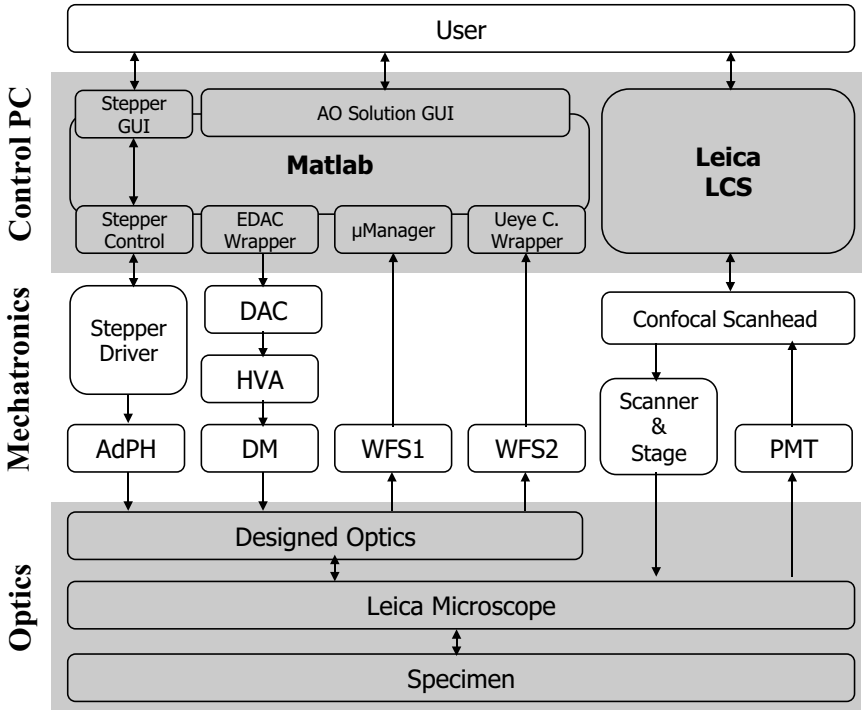

Figure 6.3: Configuration of the AO system with Leica software.

AC254-300-A-ML, Thorlabs), L10 (f=150 *mm*, AC254-150-A-ML, Thorlabs). The transmitted beam is contracted by L7 (f=750 *mm*, AC508-750-A-ML, Thorlabs), L8 (f=300 *mm*, AC254-300-A-ML, Thorlabs) and used for the excitation of the fluorescence in the specimen through Leica multi functional port (MFP). Through MFP, the PDM is conjugated with the back focal plane of the objective.

The emission of fluorescence from specimen follows the same path until a dichroic mirror DcM (651 nm cut on/off, zt638rdc, Chroma Technology). After dichroic mirror the fluorescence pass through L11 (f=500 *mm*, AC254-500-A-ML, Thorlabs) and the adjustable square pinhole (20-600 μm, TCS MR2, a part of Leica SP2 confocal microscope, Leica Microssystems). The beam after the adjustable pinhole is collimated by L12 (f=400 *mm*, AC254-400-A-ML, Thorlabs). This collimated emission beam is spectrally filtered by an emission filter (650 nm cut on/off, ET650LP, Chroma Technology, Bellows Falls, VT, USA) and separated into two paths by a non-polarization cube beam splitter BS2 (50% transmission and 50% reflection, BS013, Thorlabs). These two separated beams are collected to photomultiplier tube PMT (RLD type non-descanned detector, an order-made for fluorescence detection, Leica Microsystems) and Shack Hartmann wavefront sensor WFS1 (Coolsnap HQ2 CCD Camera, Photometrics, Tucson, AZ, USA, with a lenslet array of 300 μm pitch f = 18 *mm* orthogonal grid, Flexible Optical B.V). The WFS1 is also conjugated with PDM as WFS2. Fig. 6.3 shows the designed interface with user for running AO system and pinhole controller in parallel with Leica SP5 confocal microscope.

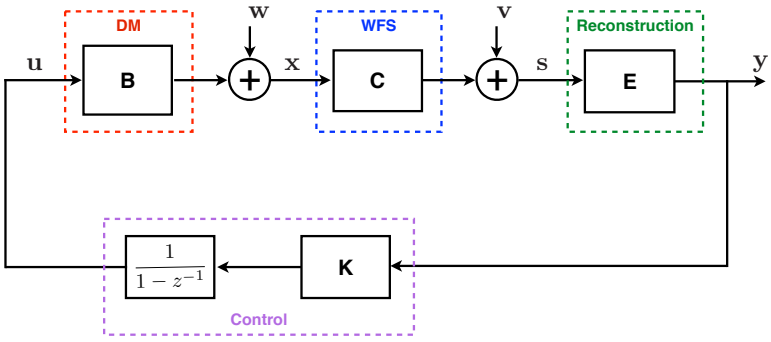

Figure 6.4: A diagram of the AO system and the feedback controller.

6.2.2 Control System Design

To run the AO system the deformable mirror has to be controlled by WFS1 from the fluorescence in the specimen. In this section a conventional wavefront reconstruction and influence matrices are discussed as the control design [190, 197, 210]. For the control design, the geometry matrix of WFS and the influence matrix of the DM are necessary to calculate the wavefront reconstruction and DM control matrices. Define the output of the WFS1 $\mathbf{y}[k] \in \mathbb{R}^n$ in Zernike modes without piston mode Z_1 at the trial k, i.e. $\mathbf{y}[k] = \begin{bmatrix} \mathbf{y}_{Z_2}[k] & \mathbf{y}_{Z_3}[k] & \cdots & \mathbf{y}_{Z_{n+1}}[k] \end{bmatrix}^T$ where $\mathbf{y}_{Z_i}[k]$ denotes the output i-th Zernike mode from WFS1. Then the output of WFS1 can be modeled by following linear equations as [197, 211],

$$\begin{aligned} \mathbf{x}[k] &= \mathbf{w} + B\mathbf{u}[k], && (6.1)\\ \mathbf{s}[k] &= C\mathbf{x}[k] + \mathbf{v}_1[k], && (6.2)\\ \mathbf{y}[k] &= E\mathbf{s}[k], && (6.3) \end{aligned}$$

where $\mathbf{u}[k] \in \mathbb{R}^m$ denotes actuator input at the trial k and $\mathbf{x}[k]$ denotes residual aberrations of the system with WFS1. C denotes the geometry matrices of the WFS1 and B denotes influence matrix which are unknown at this moment. $\mathbf{w}$ is residual aberrations of each WFS for the zero input $\mathbf{u} = 0$. For the calculation of the geometry matrices C, a modal Zernike based reconstruction is used [212]. E denotes the wavefront reconstruction matrix, usually obtained by the pseudo inverse of the geometry matrix $E = (CC^T)^{-1}C^T$ [190]. Then the output $\mathbf{y}$ is simplified into a linear equation as,

$$\mathbf{y}[k] = ECw + \underbrace{ECB}_{\mathcal{B}}\mathbf{u}[k], \qquad (6.4)$$

where $\mathcal{B}$ is a linear approximation from $\mathbf{u}[k]$ to $\mathbf{y}[k]$. Regarding the calculation of $\mathcal{B}$ from the WFS1, a filtered pseudo random input is used for the calculation of 19ch PDM. To reduce hysteresis of PDM, the every feedforward input is applied after a degauss function, which reduces hysteresis of piezoelectric actuators and provide a better linearity (See Appendix B for details) [203]. The degauss function is redesigned as a linearly attenuated sinusoidal

signal to reduces an abrupt change of the piezoelectric actuators, which may cause a possible degradation of DM. Then $\mathcal{B}$ is obtained by optimization problems as,

$$\mathcal{B} = \underset{\tilde{\mathcal{B}},\tilde{b}_z}{\operatorname{argmin}} \left\| Y_1[1:N_k] - \begin{bmatrix} \tilde{\mathcal{B}} & \tilde{b}_z \end{bmatrix} \begin{bmatrix} U[1:N_k] \\ \mathbf{1}_{1:N_k} \end{bmatrix} \right\|_F, \tag{6.5}$$

where $Y[1:N_k]$,and $U[1:N_k]$ are stacked output of WFS1 and actuator input from 1st trial to the N_k-th trial as,

$$Y[1:N_k] = \begin{bmatrix} \mathbf{y}[1] & \mathbf{y}[2] & \cdots & \mathbf{y}[N_k] \end{bmatrix}, \tag{6.6}$$

$$U[1:N_k] = \begin{bmatrix} \mathbf{u}[1] & \mathbf{u}[2] & \cdots & \mathbf{u}[k] \end{bmatrix}, \tag{6.7}$$

$$\mathbf{1}_{1:k} = \begin{bmatrix} \underbrace{1 \quad 1 \quad \cdots \quad 1}_{N_k} \end{bmatrix}. \tag{6.8}$$

and b_z are constant initial aberrations that make the output biased [125].

Then the control is given as

$$\mathbf{u}[k+1] = \mathbf{u}[k] + K\mathbf{y}[k] \tag{6.9}$$

where K are control gains regarding each wavefront sensor output. For the control, the matrix gains are applied as,

$$K = -k_g \mathcal{B}^{\ddagger} M_c, \tag{6.10}$$

$$M_c = \operatorname{diag}(\begin{bmatrix} \underbrace{0 \cdots 0}_{3} & \underbrace{1 \cdots 1}_{32} \end{bmatrix}), \tag{6.11}$$

where $\mathcal{B}^{\ddagger}$ is a control matrix using a stable pseudo inverse of $\mathcal{B}$ by truncation of small singular values [197]. k_g is a constant gain for each WFS outputs and M_c is a selection matrices of Zernike modes output of WFS1, with zeros for tip, tilt and defocus. This tip, tilt and defocus are usually ignored in the wavefront error compensation for microscopy application to remove the specimen-dependency in the wavefront measurements from the specimen, [200, 213]. Therefore, the AO is controlled based on WFS1 measurements except tip, tilt, and defocus.

6.3 WFS Calibration via Adjustable Pinhole

The quality of the reference wavefront image directly results in the compensation quality of the AO system with wavefront sensor. By principle, taking a good reference image for SH-WFS is important since it measures the relative displacement of the measurement from the reference wavefront image. This is important for the high numerical aperture objective whose image quality is sensitive to the aberrations.

Calibration of AO for the beam path from excitation laser source to the fluorescence detector, however, is not simple. One technique uses a ideal light source from the excitation beam path described by dotted black line in Fig. 6.1. It provides a flat wavefront to the wavefront sensor WFS2 and helps to calibrate the mirror surface to zero aberrations. This

allows a flat wavefront until the beam splitter BS1, however, the aberration in the optics from L8 to objective and the specimen is not considered. In addition, the optical system error from BS1 to the specimen can cause an additional error to the excitation path. This aberration in the designed optical system should be measured and calibrated to attain better quality of the microscope images.

The proposed calibration method uses an adjustable pinhole. Assume that the edge effect can be ignored, which means that the aperture is big enough comparing to the wavelength. By Fresnel approximation, the influence of the pinhole to the output pupil function is given as follows [214] (See also Chap. 7 for more detail)

$$P_{out}(\vec{\rho},\gamma_0) = \mathcal{F}\{P_{ph}(\vec{r},\gamma_0)\} * P_{in}(\vec{\xi}). \tag{6.12}$$

where P_{in}, P_{out} is the complex pupil function of input and output pupil before and after the adjustable square pinhole with size $\gamma_0 = [\gamma_{x_0}\ \gamma_{y_0}]$, and P_{ph} denotes the pupil function of the adjustable square pinhole as

$$P_{ph}(\vec{r},\gamma_0) = \begin{cases} 1 & |r_x| < \gamma_{x_0} \text{ and } |r_y| < \gamma_{y_0} \\ 0 & \text{otherwise.} \end{cases} \tag{6.13}$$

ρ, r, and ξ are coordination of the each pupil (c.f. See Fig. 7.1). Applying inverse Fourier transform to the both sides, we have the following as

$$\mathcal{F}^{-1}\{P_{out}(\vec{\rho},\gamma_0)\} = P_{ph}(\vec{r},\gamma_0) \times \mathcal{F}^{-1}\{P_{in}(\vec{\xi})\}. \tag{6.14}$$

This means that the spatial frequency bandwidth of the input pupil function can be filtered by the pupil function of the pinhole. For instance, an extremely small pinhole, a delta function, can generates an flat wavefront except tip, tilt, and defocus regardless of the input pupil function. For the implementation, the size of the adjustable pinhole should be bigger than a certain size to collect enough number of photon for the wavefront sensor. It is clearly expected from (6.14) that the wavefront after a small enough pinhole can be used as a flat wavefront reference and can improve the quality of the imaging. (cf. see simulation results in Chap. 7)

Based on this fact and idea, the small pinhole referencing algorithm can be described as follows.

1. Set a spot and reference grid for SH-WFS with a big pinhole.

2. Measure the pupil function with a small pinhole, and regard as a reference of SH-WFS

3. With a big pinhole, compensate the aberrations toward the reference with small pinhole with a closed loop control

Big and small pinhole is selected by the aberrations in the system and the intensity of the pupil. In this chapter, 5 airy unit (AU) and 1 AU pinhole, corresponding to 556.1 μm and 111.2 μm are used as a big and small pinhole, respectively.

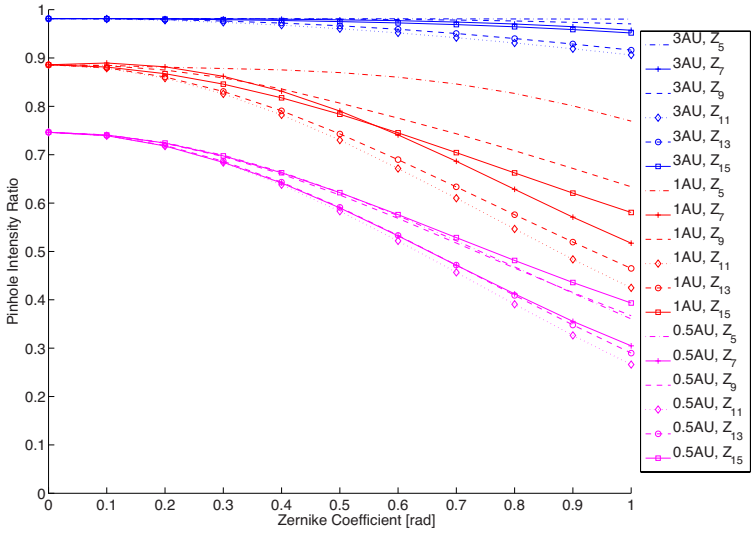

Figure 6.5: Simulation results of pinhole intensity ratio with a square adjustable pinhole for the single Zernike aberrations. The simulated small pinhole size is 3 AU, 1 AU and 0.5 AU while the size of big small pinhole is set by 5 AU. In simulation the maximum is chosen in the lateral image, i.e. 2D imaging is assumed.

6.4 Image Quality Measure using Adjustable Pinhole

Image intensity and full width at half maximum (FWHM) are traditionally used for the evaluation of the image quality [135, 138, 215]. Pinhole intensity ratio, a new quality measure of aberration for confocal microscopy, is proposed from two 3D scanned image with two different pinhole size as

$$J_r = \frac{\max I_s(x,y,z)}{\max I_b(x,y,z)}, \tag{6.15}$$

This quality criterion uses a ratio of maximum intensities of the images with a big pinhole and a small pinhole, I_b and I_s, respectively. Assuming that the source is point-like, this pinhole provides the ratio between low order term of the aberrations comparing to the aberrations as

$$J_r = \frac{\iint P_{out}(\vec{\rho},\gamma_s)d\vec{\rho}}{\iint P_{out}(\vec{\rho},\gamma_b)d\vec{\rho}} = \frac{\iint \mathcal{F}\{P_{ph}(\vec{r},\gamma_s)\} * P_{in}(\vec{\xi})d\vec{\rho}}{\iint \mathcal{F}\{P_{ph}(\vec{r},\gamma_b)\} * P_{in}(\vec{\xi})d\vec{\rho}} \tag{6.16}$$

$$= \frac{\iint P_{ph}(\vec{r},\gamma_s) \times \mathcal{F}^{-1}\{P_{in}(\vec{\xi})\}d\vec{f}_\rho}{\iint P_{ph}(\vec{r},\gamma_b) \times \mathcal{F}^{-1}\{P_{in}(\vec{\xi})\}d\vec{f}_\rho} \tag{6.17}$$

where $\vec{f}_\rho$ is the frequency components of the plane $\vec{\rho}$ and the equality between (6.16) and (6.17) holds by Parseval's theorem [216]. Similar to Strehl ratio, this quality measure usually decreased as the intensity increased since the low frequency component of the Fourier domain is dominant with low aberrations. Fig. 6.5 shows simulation results of the pinhole

intensity ratio between 5 AU and 1 AU pinhole with respect to the Zernike modes. It shows that the pinhole intensity ratio decreases with increased aberrations.

The benefit of the this measure is the amount of aberration is obtained by manipulating the motorized pinhole size. Tip and tilt does not influence this quality if the evaluation is done with 2D scanned images. By including z axis by 3D imaging, the defocus also does not influence the pinhole intensity measure.

6.5 Experimental Results

In this section the developed AO is tested with biological specimen. The referencing algorithm using an adjustable pinhole and the pinhole intensity ratio with AO for CLSM are evaluated. In the first case, the system aberration until the coverslip is compensated based on the beads on the coverslip, and the second case illustrate the compensation of deep imaging through the biological specimen. In each case, a feedback control is applied using WFS1, fluorescence from the beads. After the analysis of the image, the pinhole intensity ratio in (6.15). is applied for the evaluation of AO correction.

In the experiments, a 1.25 NA oil immersion objective (HCX PL APO 40×, 506179, Leica Microsystems) is used for the imaging. $k_g = 0.5$ and 2 *second* of exposure time for the wavefront sensor while the fluorescence beads are scanned in the given area. the correction loop stop after 20 steps of correction, which regarded sufficient to be in steady state.

6.5.1 Specimen for Evaluation

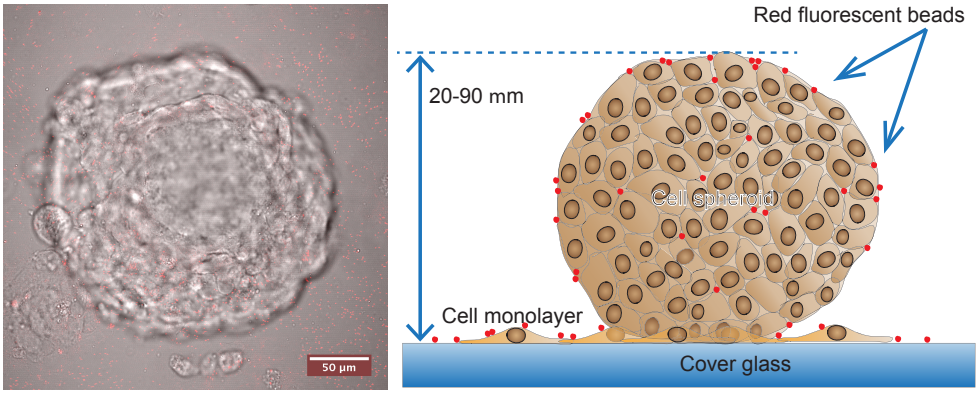

(a) Speicmen, widefield (b) Specimen Structure

Figure 6.6: Specimen for evaluation of developed AO system for system aberration correction and specimen-induced aberration correction. (Left) a wide field image of the cellular spheroid with an overlap of confocal image of the fluorescence beads (sprinkled as red in the image). The focus is at the coverslip glass. (Right) an illustration about the cellular structure and fluorescence beads (red dots). Provided courtesy of M.E. van Royen

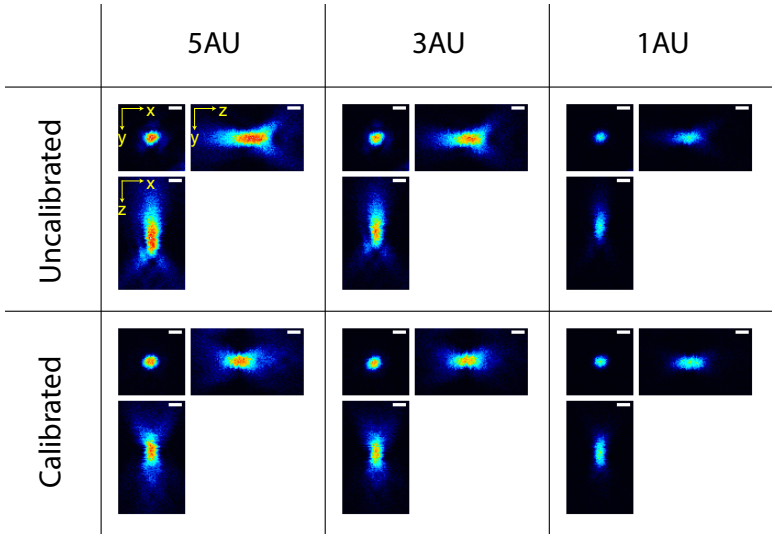

Figure 6.7: Measured point spread function (PSF) from $0.2\mu m$ *fluorescence beads on the coverslip glass. The size of the adjustable pinhole is set with 5, 3, and 1 airy unit (AU) is set for the imaging of PSF.*

Before proceeding further on the experimental results, the information of the specimen is given in this section. The specimen is developed using the cellular spheroids attached to the coverslip glass. This specimen allows to measure the aberrations in a depth of tissue consisting of a uniform cell lines. On this tissue like structure, fluorescence beads (FluoSpheres Carboxylate-Modified Microspheres, $0.2\mu m$, crimson fluorescent (625/645), 2% solid, Life Technologies, Carlbad, CA, USA) are sprinkled over the specimen for measuring point spread functions. Beads can be found inside the spheroid, which can be useful for the tests. Fig. 6.6(a) shows the widefield image of the sphere overlapped with a confocal fluorescence image of the beads and Fig. 6.6(b) shows the structure of the spheroid attached to the coverslip. For the detail information of the specimen preparation, see Appendix A.

6.5.2 Evaluation of the Calibration Method with the Adjustable Pinhole

To calibrate the AO system, compensate for the system aberrations all optics before the specimen, a small pinhole referencing method is evaluated with the beads on the coverslip, which are regarded as light sources without specimen induced aberrations. 1 AU of pinhole is used for the reference image of WFS1 as a small pinhole calibration in Section 6.3, and 5 AU of pinhole is used for AO correction afterword. For the uncalibrated setting, DM is set to shape the flat for WFS2 as the reference beam (black dotted line in Fig. 6.1), which is a conventional calibration method.

Figure 6.7 shows the lateral and axial images of the fluorescence beads with uncalibrated and AO calibrated case with 1 AU pinhole setting. After AO calibration the pinhole size of 1 AU, 3 AU and 5 AU are applied for the beads imaging to evaluate the benefits along the

pinhole size. Since different group of beads are imaged to avoid to the photobleaching, the absolute intensity in Fig 6.7 is not important but the shape and size of the measured PSF are more important for the improvement evaluation. The uncalibrated PSF shows non-symmetric and skewed in z axis while the axial PSF is symmetry after AO compensation in z axis. Fig 6.12 show the residual wavefront error and the final mirror shape of the calibration process.

To evaluate the calibration performance quantitively, full width at half maximum (FWHM) and pinhole intensity ratio is used for the beads on coverslip glass. For that shot noise need to be reduced because both performance measures uses maximum intensity of the images. Before the performance evaluation, a 3D Gaussian FIR filter is applied to smoothen shot noise in the intensity measurement [40]. The filter is designed with the filter size of $3 \times 3 \times 3$ and $\sigma = 0.56$. This 3D filtering helps analysis with FWHM more reliable by reducing sensitive of FWHM to shot noises. As a drawback, the peak intensity are smoothed, decreasing the ratio in peak intensity and widening the FWHM. Since it is relative comparison between uncalibrated and calibrated case, the measurement is still valuable for the comparison.

Measured FWHM shows the resolution improvement using a small pinhole calibration. Table 6.1 shows the mean and standard deviation (STD) of FWHM. 18 and 13 beads are used for the evaluation of the uncalibrated case and AO calibrated case. It shows that the improvement of axial FWHM by the AO correction is reduced as the pinhole size gets smaller. For the 5 AU of pinhole size, the FWHM in z axis is improved from 1.35 μm to 1.02 μm after AO correction, corresponding to 24.9% reduction. For the 3 AU, the improvement is still 11.0% but for 1 AU it is 4.81% worse than before the correction. This shows that the resolution improvement of AO correction is less as the pinhole gets smaller. The lateral resolution does not shows the drastic improvement as axial resolution, but more improvement by AO correction is shows when the pinhole is small. Up to 4.9% improvement is shown in the lateral FWHM with 1 AU of the pinhole size. Fig. 6.9 shows the cross-section of the measured lateral (y) and axial (z) PSF for FWHM calculation, shows the detail shape of the PSF. The skewness of the uncalibrated PSF is also observed compared to the PSF after AO correction.

FWHM [μm]	5 AU			3 AU			1 AU		
	x	y	z	x	y	z	x	y	z
Mean									
Uncalibrated	0.399	0.452	1.354	0.387	0.463	1.166	0.347	0.402	0.901
AO calibrated	0.406	0.436	1.018	0.396	0.442	1.038	0.340	0.382	0.944
STD									
Uncalibrated	0.018	0.022	0.043	0.017	0.020	0.068	0.013	0.019	0.097
AO calibrated	0.024	0.028	0.034	0.032	0.016	0.055	0.023	0.019	0.025

Table 6.1: Measured FWHM of the beads on the coverslip glass.

Pinhole intensity ratio of (6.15) also shows the improvement by AO correction. Table 6.2 shows the measured pinhole intensity ratio with 3 AU and 1 AU as a small pinhole and 5 AU as a big pinhole. The improvement of the pinhole intensity ratio is higher with a smaller pinhole. The pinhole intensity ratio is increased only 4.4% for 3 AU and 30.9% for 1 AU. This improvements show that the AO calibration with a small pinhole allows a less drop of

maximum intensity by the confocal detection pinhole, i.e. less light loss in detection path, besides the smaller point spread function. This shows that the maximum intensity difference between small and big pinhole is less significant after an AO correction.

Small PH Size	3 AU		1 AU	
AO Status	Uncompensated	AO corrected	Uncompensated	AO corrected
Mean	0.85	0.89	0.47	0.61
STD	0.026	0.019	0.015	0.019

Table 6.2: Measured pinhole intensity ratio of the beads on glass between 5 AU and 1 AU pinhole

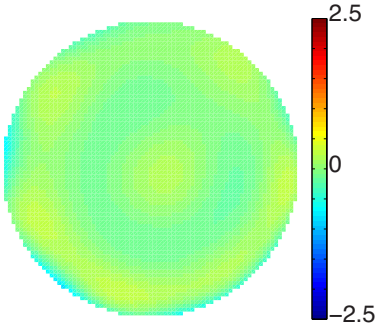

(a) Final Residual Error, WFS1

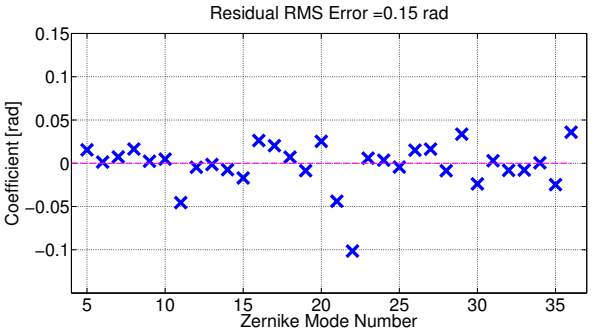

(b) Final Zernike Mode, WFS1

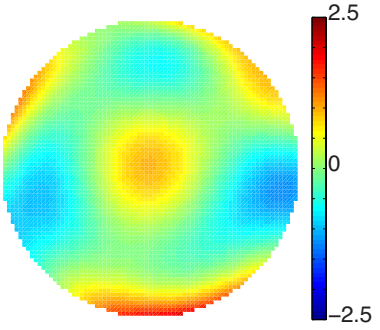

(c) Final DM Shape, WFS2

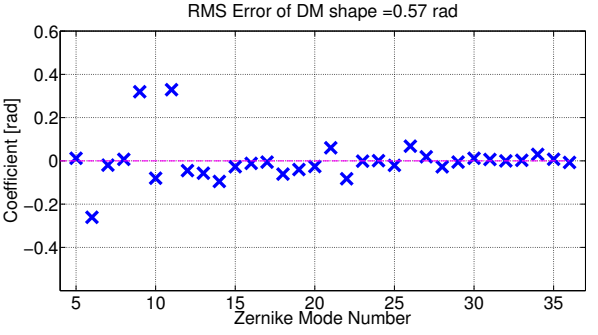

(d) Final Zernike Mode, WFS2

Figure 6.8: Residual WF and DM shape of the AO Control based on WFS1 measurement.

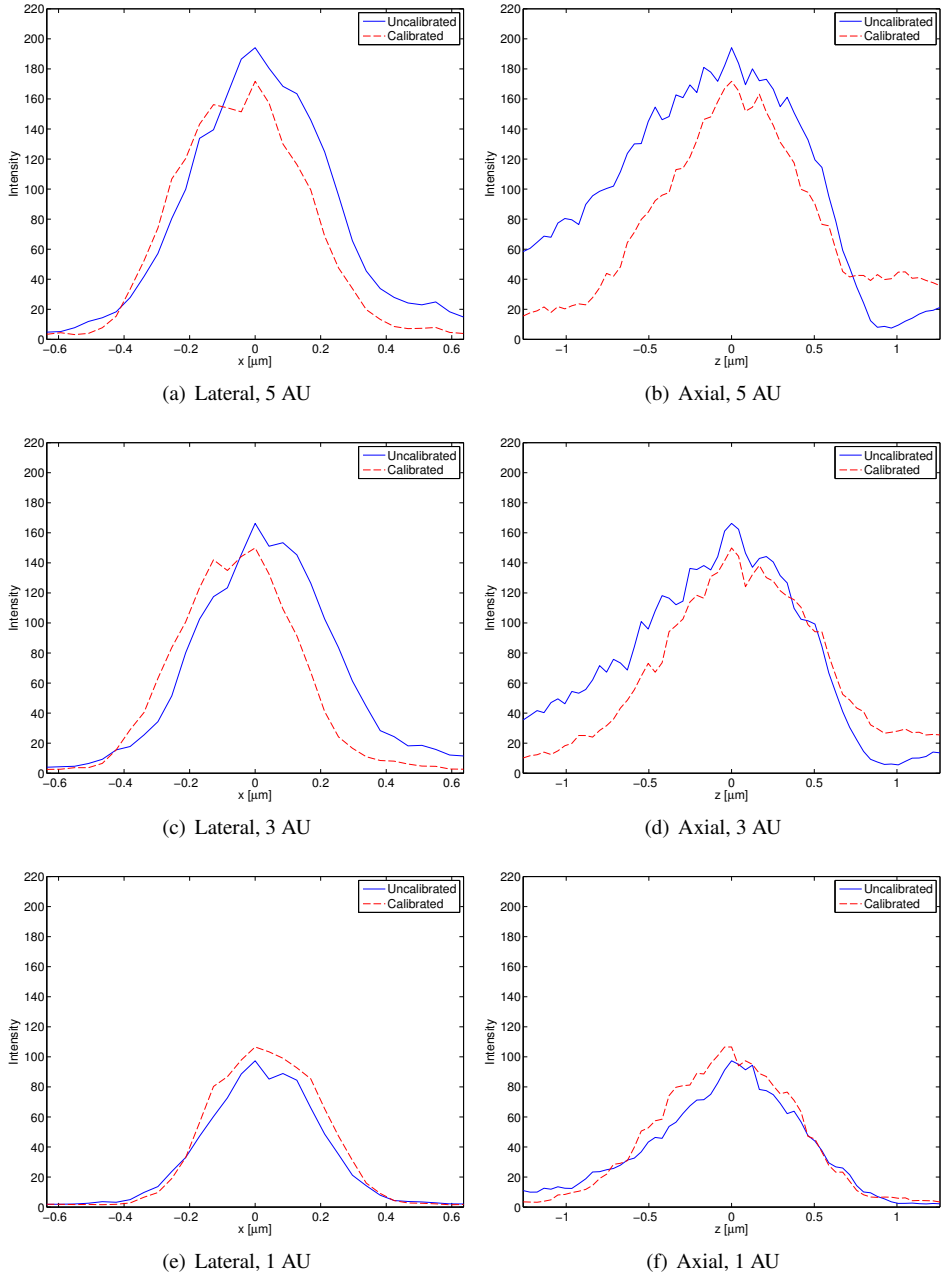

(a) Lateral, 5 AU (b) Axial, 5 AU

(c) Lateral, 3 AU (d) Axial, 3 AU

(e) Lateral, 1 AU (f) Axial, 1 AU

Figure 6.9: Lateral (y) and axial (z) profile of the measured point spread function from 0.2µm fluorescence beads on coverslip.

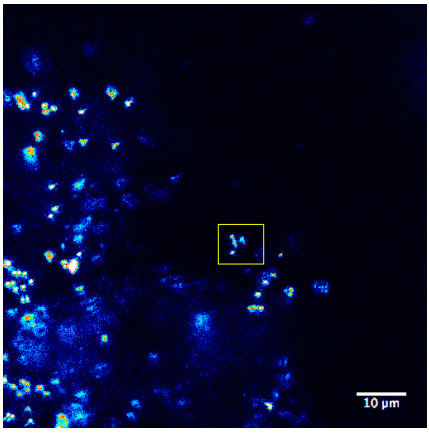

Figure 6.10: Overview at 40 μm *deep in the cellular spheroid with fluorescence beads as Fig. 6.6. The yellow box represents the scope of the correction and imaging with developed AO.*

6.5.3 Specimen Induced Aberration Correction at 40 μm Deep in the Cellular Spheroid

To demonstrate the correction with the developed AO system the fluorescence beads in the deep cellular spheroid is chosen as an test specimen for specimen induced aberrations. Fig. 6.10 shows an overview of the fluorescence beads at the 40 μm deep from the coverslip glass. The uncompensated case is the set of the DM that is calibrated using small pinhole method. Three beads in the yellows box are the scope of the wavefront detection and correction and imaging example.

Fig. 6.11 shows the lateral and axial imaging results before the AO correction and the after AO correction. Note that the intensity increase is not the indicator of improvement since the detector gain is increased after correction for the compensation of weak fluorescence by photobleaching. In the *xy* image of the uncompensated case with 5 AU pinhole, a ghosting diffraction pattern is observed at the right side of the main lobe, while it is improved by AO correction. Fig 6.12 shows the residual wavefront error and the final mirror shape.

Table 6.3 shows the measured mean and STD of the measured two beads (upper left and lower middle in Fig. 6.11) in the cellular spheroid. The FWHM of the beads at 40 μm shows the improvement by AO correction. Axial FWHM are improved from 1.94 μm to 1.28 μm (33.7%) for 5 AU detection pinhole and from 1.69 μm to 1.34 μm (20.7%) for 3AU pinhole. The axial FWHM also does not improved when the pinhole size is 1 AU as the case of fluorescence beads on the coverslip glass. The lateral FWHM in *y* axis is improves at 1 AU case most, from 0.42 μm to 0.31 μm (26.5%). Fig. 6.13 shows the cross-section of the lateral *y* and axial image of the fluorescence beads at 40 μm depth.

The pinhole intensity ratio also shows the improvement by AO correction as the beads on coverslip measurement. Table 6.4 describes the measured pinhole intensity ratio of uncompensated and AO corrected case. The pinhole intensity ratio are increased only 5.8% for 3 AU and 18.4% for 1 AU, showing a more improvement with a small pinhole as the calibration case. This shows that the maximum intensity drop between the small and big

pinhole is less significant after the AO correction, as shown with FWHM improvement.

FWHM [μm]	5 AU			3 AU			1 AU		
	x	y	z	x	y	z	x	y	z
Mean									
Uncompensated	0.414	0.496	1.937	0.418	0.489	1.685	0.336	0.421	1.084
AO corrected	0.435	0.432	1.284	0.404	0.441	1.335	0.315	0.309	1.084
STD									
Uncompensated	0.001	0.014	0.076	0.028	0.037	0.059	0.013	0.018	0.161
AO corrected	0.004	0.028	0.216	0.020	0.011	0.040	0.004	0.028	0.048

Table 6.3: Measured FWHM of the beads at 40 μm *deep in the specimen.*

Small PH Size	3 AU		1 AU	
AO Status	Uncompensated	AO corrected	Uncompensated	AO corrected
Mean	0.79	0.84	0.38	0.45
STD	0.049	0.031	0.032	0.022

Table 6.4: Pinhole intensity ratio of the 3 beads in 40 μm deep in the cellular spheroid. 3 AU and 1 AU are small pinhole sizes and 5 AU is set as the big pinhole size.

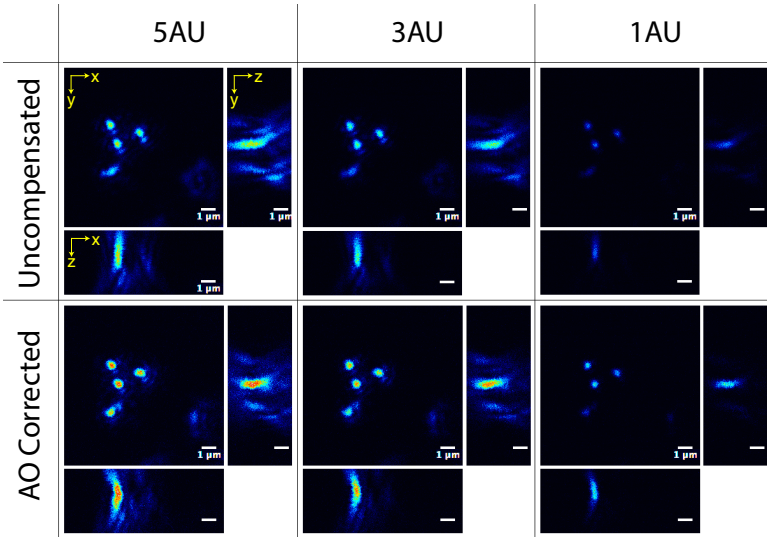

Figure 6.11: Measured PSF by 0.2 μm *fluorescence beads at* 40 μm *depth of the cellular spheroid. The size of the adjustable pinhole is set with 5, 3, and 1 AU for the imaging of PSF.*

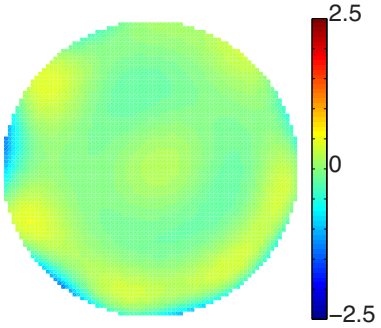

(a) Final Residual Error, WFS1

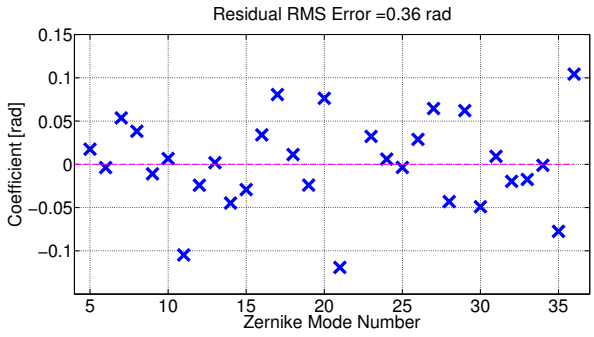

(b) Final Zernike Mode, WFS1

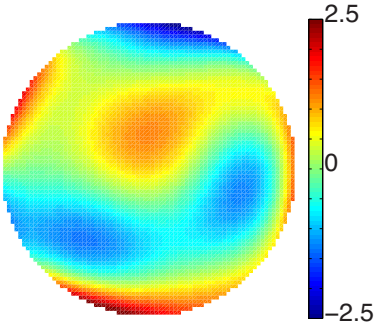

(c) Final DM Shape, WFS2

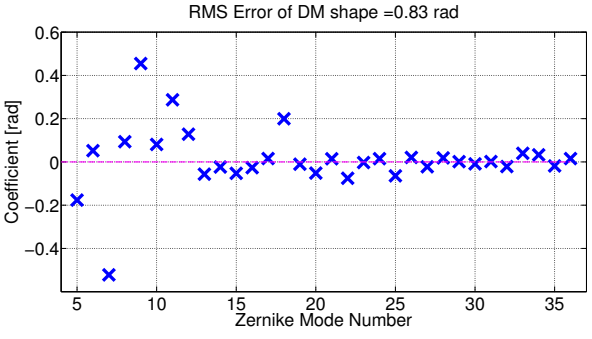

(d) Final Zernike Mode, WFS2

Figure 6.12: Residual WF and DM shape of conventional controller based on WFS1 measurement.

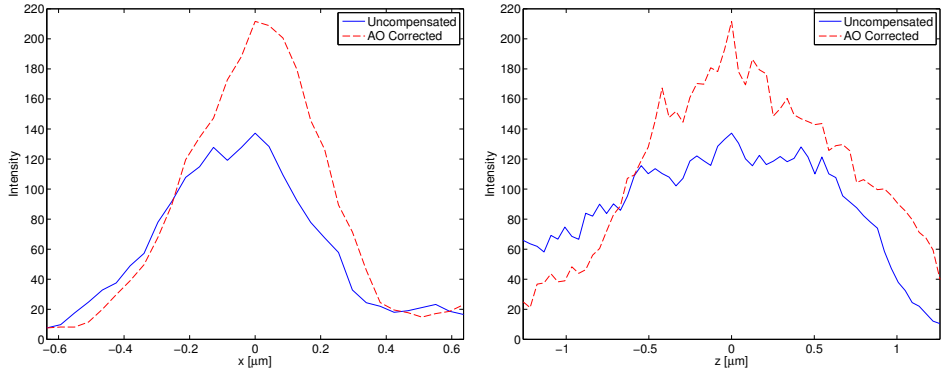

(a) Lateral, 5 AU (b) Axial, 5 AU

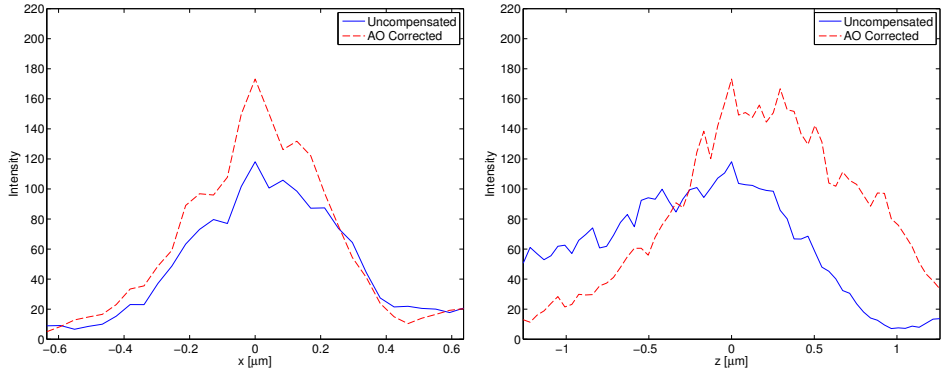

(c) Lateral, 3 AU (d) Axial, 3 AU

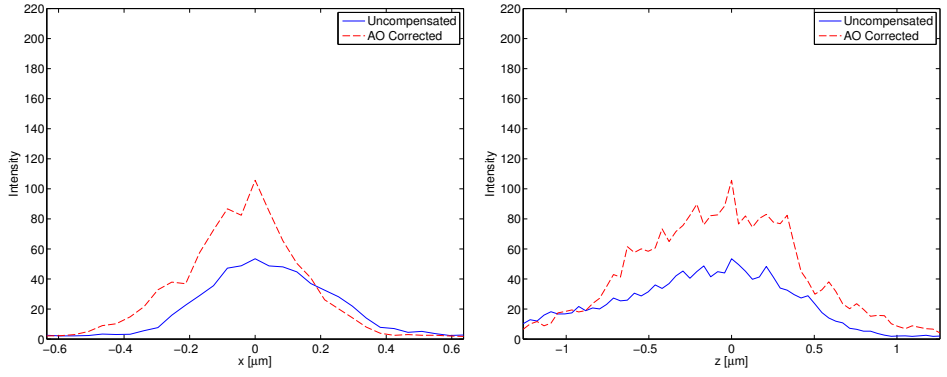

(e) Lateral, 1 AU (f) Axial, 1 AU

Figure 6.13: Lateral and Axial profile of the measured point spread function from 200 nm fluorescence beads in 40 *µm depth.*

6.6 Conclusion

In this chapter, an adaptive optics system is developed for the Leica SP5 CLSM and evaluated with fluorescence beads with biological specimen. The AO system contains an adjustable pinhole, which can be used for the WFS referencing and the evaluation of the AO correction. Experimental results with fluorescence beads on the coverslip shows that the calibration method with the adjustable pinhole can improve the resolution up to 24.9% of the axial FWHM with 5 AU pinhole and 4.9% in the lateral FWHM with 1 AU pinhole, but the improvement of axial resolution was not significantly observed with 1 AU of the pinhole. Fluorescence beads at 40 μm deep into the sphere cell cluster also shows that the improvement of axial FWHM resolution up to 33.7% for 5 AU pinhole but such improvement was not observed with 1 AU of the pinhole. Lateral FWHM is improved up to 26.5% with 1 AU of the pinhole, while it is only y-axis only. The proposed pinhole intensity ratio using the adjustable pinhole also shows 30.9% and 18.4% improvement by the correction of the aberration. These results verify the concept of AO for a commercial CLSM.

Chapter 7

Pupil Function Retrieval for Confocal WFS via Adjustable Square Pinhole

While the pinholes plays a crucial role for confocal wavefront sensing in AO for confocal microscopy by rejecting out of focus light, it also distort wavefront measurements. In this chapter, a wavefront reconstruction technique from degraded pupil function by fixed size of pinhole is proposed based on stable inversion [217]. The aberration modification by the pinhole can be modeled as 2D convolution of the pupil function in complex domain, including phase and intensity of the beam. Based on the Fresnel approximation, the 2D deconvolution problem can be simplified to a 1D deconvolution, which also allows retrieval from the measurements with diversified pinhole sizes. Simulation results of various pinhole sizes show that the distortion of the output pupil functions corresponds to the aberration model. The proposed retrieval technique from complex pupil measurements of a single as well as multiple pinhole sizes shows the improvements in magnitude and especially the phase, which can improve accuracy of AO correction in CLSM.

7.1 Introduction

The pinhole is a key component in confocal laser scanning microscopy. It allows to collect the light only nearby the focal plane and enables three dimensional (3D) imaging of the specimen at high axial resolution. Not only the axial resolution is improved, but also lateral resolution also improved by a factor of 1.6 in practice [2]. The size of the pinhole is closely related to the improvement of resolution, which has a trade off with the loss of intensity [208]. For commercial confocal microscopes, an adjustable pinhole is usually installed for users to choose its size considering the intensity from the specimen. Although the pinhole is widely used for the CLSM, however, it is argued that the pinhole is demerit since it can remove useful information from the specimen as well [1]. Wavefront aberration induced by the specimen is one of the lost information by the pinhole [134, 196].

Even though the pinhole may distort the wavefront information of the light from the

specimen, it is still a useful tool for aberration measurement in microscopy. At early developments of adaptive optics (AO) system for microscopy, which compensates for aberrations of the specimen, it is argued that the conventional wavefront sensor such as Shack Hartmann wavefront sensor (SH-WFS) is not trivial to be applied since the fluorescence from the specimen is not an point-like emitter but an extended object [92]. For the early development of adaptive optics for the microscope is mainly focused on modal wavefront sensing technique based on the image of the specimen [102, 218–220]. These image based AO techniques are less complex and cheaper without any additional hardware for wavefront sensing. However, it is usually time consuming and more chance to bleach the specimen for taking multiple images of the specimen. For fast compensation, SH-WFS is considered for wavefront sensing in the microscope [221] and widely developed with the fluorescence guide star techniques [110, 112, 135, 137, 139] or back-scattered light [134, 204]. In those AO system developments, the pinhole (or aperture) is usually installed in front of the SH-WFS for suppressing light from the uninteresting out of focus region, which is important for running the Shack Hartmann wavefront sensor in microscopy. In addition, the pinhole innately confines the illumination, which can help to degenerate the extended object to a point-like light source. Therefore the pinhole can be also useful in wavefront sensing application, while the original wavefront information is destroyed by the presence of the pinhole [134].

In this chapter, a wavefront reconstruction technique is proposed from the complex pupil measurements though the finite size of the square pinhole and extended to the reconstruction from single or multiple pupil measurements with diversified pinhole sizes. The basic idea is to recover the original wavefront information by using multiple pupil measurements with a manipulated pinhole size. The square adjustable pinhole is assumed since it is used for the commercially available confocal microscope, which also provides less interference by the optical scanning [206]. In addition there are methods for direct measurement of the complex pupil function, intensity and aberrations at the same time [222, 223]. The model of the output pupil function through the finite size of the pinhole can be modeled by a 2 dimensional convolution of the input pupil function and the Fourier transform of the pinhole. Using the separation for the square pinhole by both orthogonal axis, the 2D convolution problem can be modified into a 1 dimensional deconvolution, which allows the computational efficient algorithms and use multiple data of the pinhole size [224]. Regularization techniques such as truncated SVD and Tikhonov regularization are considered for the stable deconvolution of the pupil reconstruction problem regarding white Gaussian measurement noise [217]. Experimental results compared with simulation results of various pinholes show that the model for the problem is valid in the measurement data. Phase retrieve from a single pinhole measurement are multiple pinhole measurement are tested in simulation and show the benefits of the diversified measurements by less RMS phase error.

7.2 Problem Description

Consider an imaging system with an adjustable square pinhole as shown in Fig. 7.1. Assume that the edge effect can be ignored, which means that the aperture is big enough comparing to the wavelength. This is valid since the pinhole size ($20-600\ \mu m$) is much bigger than the wavelength of visual light ($\lambda \leq 0.7 \mu m$). By this assumption, we can use a Fresnel approximation to obtain the output pupil.

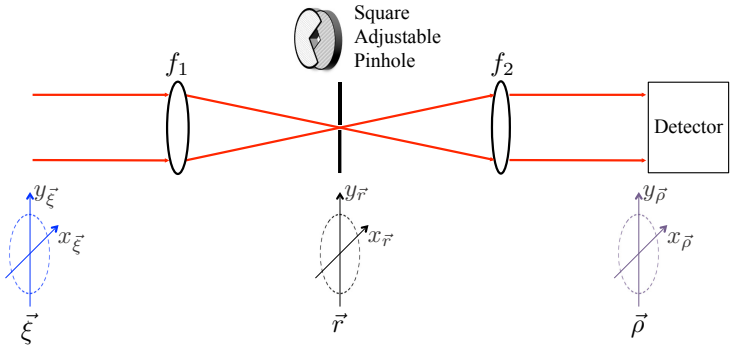

Figure 7.1: Diagram of the back focal plane and image back focal plane though the square adjustable pinhole at focus.

Let a pupil function at the aperture be as follow

$$P_{in}(\vec{\xi}) = A(\vec{\xi})e^{-j\pi\kappa\Psi_{in}(\vec{\xi})}, \tag{7.1}$$

where $A(\vec{\xi})$ is an intensity profile at the aperture, and $\Psi(\vec{\xi})$ is a given function.

First, we consider a pupil reconstruction problem from a single pinhole size. Assuming that the pinhole and the entire optical system is align correctly, the following relationship is obtained as

$$\begin{aligned} P_{out}(\vec{\rho}) &= A_{out}(\vec{\rho})e^{-j\pi\kappa\Psi_{out}(\vec{\rho})} + P_n(\vec{\rho}) \\ &= \mathcal{F}\{P_{ph}(\vec{r},\gamma_m)\} * P_{in}(\frac{1}{M}\vec{\xi}) + P_n(\vec{\rho}), \end{aligned} \tag{7.2}$$

where $P_n(\vec{\rho})$ denotes the pupil measurement noise which assumed as zero mean Gaussian in complex domain, γ_m denotes the information of the pinhole at focal plane, and $M = \frac{f_1}{f_2}$ is the magnification between the input pupil function and the output pupil function. This leads to a nonlinear least square problem for estimating the original input pupil function $P_{in}(\xi)$ by the size information of the square pinhole at the m-th trial $\gamma_m = [\gamma_x(m) \;\; \gamma_y(m)]$ where $\gamma_x(m)$ and $\gamma_y(m)$ are size of the pinhole in the coordination of $x_{\vec{r}}$ as

$$\arg\min_{P_{in}(\xi)} J\left(P_{out}(\vec{\rho}), P_{ph}(\vec{r},\gamma_m), P_{in}(\vec{\xi})\right), \tag{7.3}$$

where the cost function is given as

$$J\left(P_{out}(\vec{\rho}), P_{ph}(\vec{r},\gamma_m), P_{in}(\vec{\xi})\right) = \|\mathcal{F}\{P_{ph}(\vec{r},\gamma_m)\} * P_{in}(\vec{\xi}) - P_{out}(\vec{\rho})\|_2 \tag{7.4}$$

J denotes the cost function at the output pupil.

7.3 Methods

To reformulate the optimization problem, output pinhole image of the pinhole at the pupil function. The image of the square pinhole is modeled as follows,

$$\begin{aligned}\mathcal{F}\{P_{ph}(\vec{r},\gamma_m)\} &= \mathcal{P}_{ph}(\vec{\rho},\gamma_m)\\ &= -j\frac{\kappa}{f_1}e^{j4\pi\kappa f_1}\iint rect(\frac{1}{\gamma_x(m)}x_r)rect(\frac{1}{\gamma_y(m)}y_r)e^{-j2\pi\frac{\kappa}{f_1}\vec{r}\cdot\vec{\rho}}d\vec{r}\\ &= -j\frac{\kappa\gamma_x(m)\gamma_y(m)}{f_1}e^{j4\pi\kappa f_1}sinc(\frac{\kappa\gamma_x(m)}{f_1}x_{\vec{\rho}})sinc(\frac{\kappa\gamma_y(m)}{f_1}y_{\vec{\rho}}) \quad (7.5)\end{aligned}$$

where the focal length of the lenses f_1 and $y_{\vec{r}}$, $sinc(x)=\frac{sin\pi x}{\pi x}$. From (7.2) and (7.5), the output pupil function is rewritten as,

$$\begin{aligned}\hat{P}_{out}(\vec{\rho}) &= \mathcal{P}_{ph}(\vec{\rho},\gamma_m)*P_{in}(\frac{1}{M}\vec{\rho})+P_n(\vec{\rho})\\ &= \iint\mathcal{P}_{ph}(\vec{\rho}-\vec{\zeta},\gamma_m)P_{in}(\frac{1}{M}\vec{\zeta})d\vec{\zeta}+P_n(\vec{\rho})\\ &\simeq a(\gamma_m)\{\bar{H}(\gamma_m)\otimes H(\gamma_m)\}\,\mathrm{vec}(X^{pre})+N^{pre} \quad (7.6)\\ &= a(\gamma_m)H(\gamma_m)X^{pre}\bar{H}^T(\gamma_m)+N^{pre}, \quad (7.7)\end{aligned}$$

where $\otimes$ denotes the Kronecker product operator. Since the kernel $\mathcal{P}_{ph}$ is separable [217], the convolution integral can be discretized by Eq. (7.6), where H and $\bar{H}$ are the Toeplitz matrix determined by

$$H_{\mathbf{i},\mathbf{k}}(\gamma_m) = n^{-1}sinc\left(\frac{\kappa\gamma_x(m)}{f_1}\left(x_{\vec{\rho}}[\mathbf{i}]-x_{\vec{\zeta}}[\mathbf{k}]\right)\right), \quad (7.8)$$

$$\bar{H}_{\mathbf{j},\mathbf{l}}(\gamma_m) = n^{-1}sinc\left(\frac{\kappa\gamma_y(m)}{f_1}\left(y_{\vec{\rho}}[\mathbf{j}]-y_{\vec{\zeta}}[\mathbf{l}]\right)\right), \quad (7.9)$$

$$X^{pre}_{\mathbf{k},\mathbf{l}} = P_{in}(\frac{1}{M}x_{-\vec{\zeta}}[\mathbf{k}],\frac{1}{M}y_{-\vec{\zeta}}[\mathbf{l}]), \quad (7.10)$$

$$Y^{pre}_{\mathbf{i},\mathbf{j}}(\gamma_m) = P_{out}(x_{\vec{\rho}}[\mathbf{i}],y_{\vec{\rho}}[\mathbf{j}],\gamma_m), \quad (7.11)$$

$$N^{pre}_{\mathbf{i},\mathbf{j}} = P_n(x_{\vec{\rho}}[\mathbf{i}],y_{\vec{\rho}}[\mathbf{j}]), \quad (7.12)$$

$$a(\gamma_m) = -j\frac{\kappa\gamma_x(m)\gamma_y(m)}{f_1}e^{i4\pi\kappa f_1}. \quad (7.13)$$

The aperture of input l is defined as a circle pupil. For the output, considering the wavefront sensor, it can be restricted by the circular pupil as input. Let the number pixel of discretized pupil be s as Fig. 7.2, and a binary selection matrix be $S\in\mathbb{Z}^{s\times n^2}$, satisfying $SS^T=I_{s\times s}$, which maps from a square pupil to the circular pupil. Then the available output is defined as

$$Y(\gamma_m) = S\times\mathrm{vec}\left(Y^{pre}(\gamma_m)\right), \quad (7.14)$$

$$X = S\times\mathrm{vec}(X^{pre}). \quad (7.15)$$

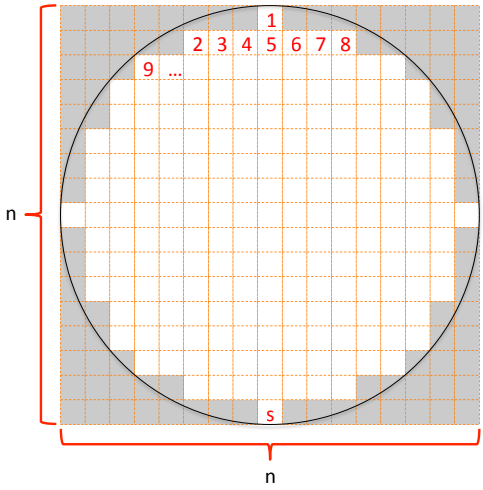

Figure 7.2: Mapping and indexing of the binary selection matrix S for a circular pupil function. The binary selection matrix arranges non-zero elements in the discretized pupil function.

The physical meaning of the input pupil $S \times \mathrm{vec}(X_{pre})$ is a zero padding of the unrelated area of the circular input pupil, since the outsize of the pupil has no intensity and does not contribute the output pupil. This property is normal for the most application, which has a finite input beam diameter. Regarding the output pupil, it is not necessary to be bounded to the circular pupil with S, while for the consistency of measurement, it is applied without loss of generality.

Based on this, a pupil function retrieve problem from a single pinhole γ_m measurement is defined as

$$\arg\min_{X} J_1(Y(\gamma_m), H(\gamma_m), X), \tag{7.16}$$

where

$$J_1(Y(\gamma_m), H(\gamma_m), X) = \|Y(\gamma_m) - a(\gamma_m) S\{\bar{H}(\gamma_m) \otimes H(\gamma_m)\} S^T X\|_2. \tag{7.17}$$

In practice this least square problem suffers from the numerically unstable to the small perturbation [217]. This numerical instability can be reduced by applying a regularization method as

$$\begin{aligned} J_{1,reg}(Y(\gamma_m), X, H(\gamma_m), \lambda_T) &= \|Y(\gamma_m) - a(\gamma_m) S\{\bar{H}(\gamma_m) \otimes H(\gamma_m)\} S^T X\|_2 \\ &+ \lambda_T \|X\|_p, \end{aligned} \tag{7.18}$$

where λ_T is a regularization parameter [217]. When p = 2, the problem is defined as Tikhonov regularization. The truncation of the singular value decomposition (TSVD) can be also considered with (7.17). Including TSVD and Tikhonov regularization, a number of

regularization approaches are available with open-source solvers [224, 225].

Since the pupil function retrieval problem with the a square pinhole results in 1-D least square problem, it can be easily extended to the various problem settings. For example, the pupil recovery problem of (7.16) can be simply extended to the pupil recovery problem with diversified pinhole sizes, γ_m, $m = 1, 2, \cdots, N_m$, by stacking the Kernel matrix and measurement serially as,

$$J_D(\mathbf{Y}, X, \mathbf{H}) \quad = \quad \|\mathbf{Y} - \mathbf{H}X\|_2. \tag{7.19}$$

where

$$\mathbf{Y} = \begin{bmatrix} Y(\gamma_1) \\ Y(\gamma_2) \\ \vdots \\ Y(\gamma_{N_m}) \end{bmatrix}, \quad \mathbf{H} = \begin{bmatrix} a(\gamma_1) S \{\bar{H}(\gamma_1) \otimes H(\gamma_1)\} S^T \\ a(\gamma_2) S \{\bar{H}(\gamma_2) \otimes H(\gamma_2)\} S^T \\ \vdots \\ a(\gamma_{N_m}) S \{\bar{H}(\gamma_{N_m}) \otimes H(\gamma_{N_m})\} S^T \end{bmatrix}. \tag{7.20}$$

As the single pinhole approximation, regularization methods such as TSVD and Tikhonov regularization can be also used to improve numerical stability of the calculation. By extending with multiple measurements with diversified pinhole sizes, less error can be expected with the same maximum size of pinhole. In the simulation results, it is discussed while

7.4 Model Verification

7.4.1 Experimental Setup

Before proceeding on the simulation of the algorithm, the discretized pupil function model with the square pinhole in (7.14) is verified by experimental results. Fig. 7.3 and Fig. 7.4 illustrate the schematics and photographs of the experimental setup for the wavefront sensing through an adjustable square pinhole. The light source is a He-Ne laser (633 nm, 7 mW, 1125P, JDSU) with a polarizer for changing the intensity. L1 (f=11 *mm*, A397TM-A, Thorlabs, Newton, NJ, USA) and L2 (f=60 *mm*, AC254-060-A-ML, Thorlabs) with a fixed pinhole (10μm, Thorlabs) generates a clear Gaussian pupil at the aperture D1 and the aperture generated truncated circular Gaussian profile. This beam is expanded to 23 mm to non-polarizing beam splitter BS1(50% transmission and 50% reflection, BS013, Thorlabs) by L3 (f=200 *mm*, AC254-200-A-ML, Thorlabs) and L4 (f=750 *mm*, AC508-750-A-ML, Thorlabs). The beam splitter separated the beam into two for a 19 channel piezoelectric actuated deformable mirror PDM (30 mm 19 channel, Flexible Optical B.V.) and also allows the flat reference mirror (broadband dielectric mirror,BB2-E02, 400-750 nm, Thorlabds), which is only used for alignment and calibration of the optical system and wavefront sensors. After the wavefront is modified by PDM, the beam is contracted by L5 (f=200*mm*, AC508-200-A-ML, Thorlabs) and L6 (f=50 *mm*, AC254-050-A-ML, Thorlabs), 23 mm to 5.75 mm. Then the beam is split into two paths, DM calibration path and pupil measurement through the pinhole ,by a non-polarization cube beam splitter BS2 (50% transmission and 50% reflection, BS013, Thorlabs).

For the calibration path, the beam is contracted by L7 (f=300 *mm*, AC254-300-A-ML, Thorlabs) and L8 (f=150 *mm*, AC254-150-A-ML, Thorlabs) and its wavefront is measured

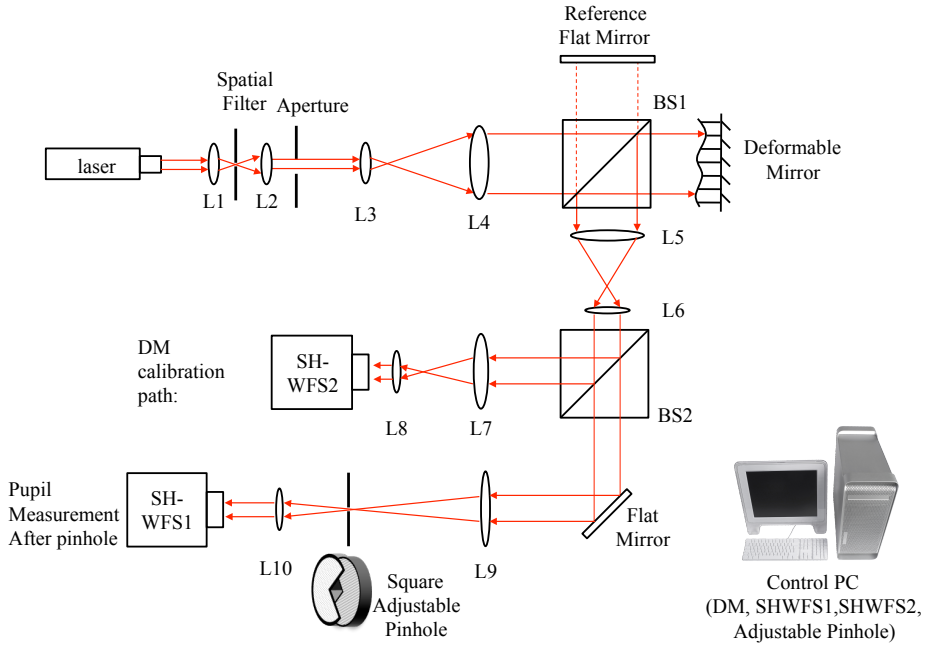

Figure 7.3: Schematics of the experimental setup for the verification of the aberration model with square pinhole (7.14).

by a Shack-Hartmann wavefront sensor SH-WFS2 (200 μm pitch f = 10mm orthogonal grid lenslet array, APO-Q-P192-F3.17, UEye UI-2210SE CCD camera, Flexible Optical B.V., Rijswijk, the Netherlands) that regulates the shape of deformable mirror during the experiment.

In the pupil measurement path thorough the pinhole, the beam is focused on the adjustable square pinhole (20-600 μm, TCS MR2, a part of Leica SP2 confocal microscope, Leica Microsystems) by L9 (f=500 mm, AC254-500-A-ML, Thorlabs), which results in the diameter of 1 AU as 134 μm. The adjustable pinhole module includes the stepper motor, which is operated by a stepper driver (Stellaris Stepper Motor Reference Design Kit, Texas Instruments, Dallas, TX, USA) and its developed Matlab software. The size of the pinhole is controlled in offline control manner after the pinhole is calibrated by a digital microscope (VHX-100, Keyence, Osaka, Japan) in advance. The initialization of the pinhole position can be informed by an LED indicator connected to the photo-coupler in the pinhole module. The spatially filtered beam after the pinhole are diverged to L10 (f=400 mm, AC254-400-A-ML, Thorlabs) and its phase is measured by Shack Hartmann wavefront sensor SH-WFS2 (Coolsnap HQ2 CCD Camera, Photometrics, Tucson, AZ, USA, with a lenslet array of 300 μm pitch f = 18 mm orthogonal grid, Flexible Optical B.V). The deformable mirror is conjugated with both SH-WFS1 and SH-WFS2.

Experiments are designed to measure the wavefront variation by the pinhole size. SH-WFS2 measures the phase variation after the square pinhole and the square pinhole changes it size from 0.25 to 4 AU. For each pinhole size, 10 wavefront measurements of SH-WFS2 are taken and averaged for the analysis. During measurements, the DM is constantly con-

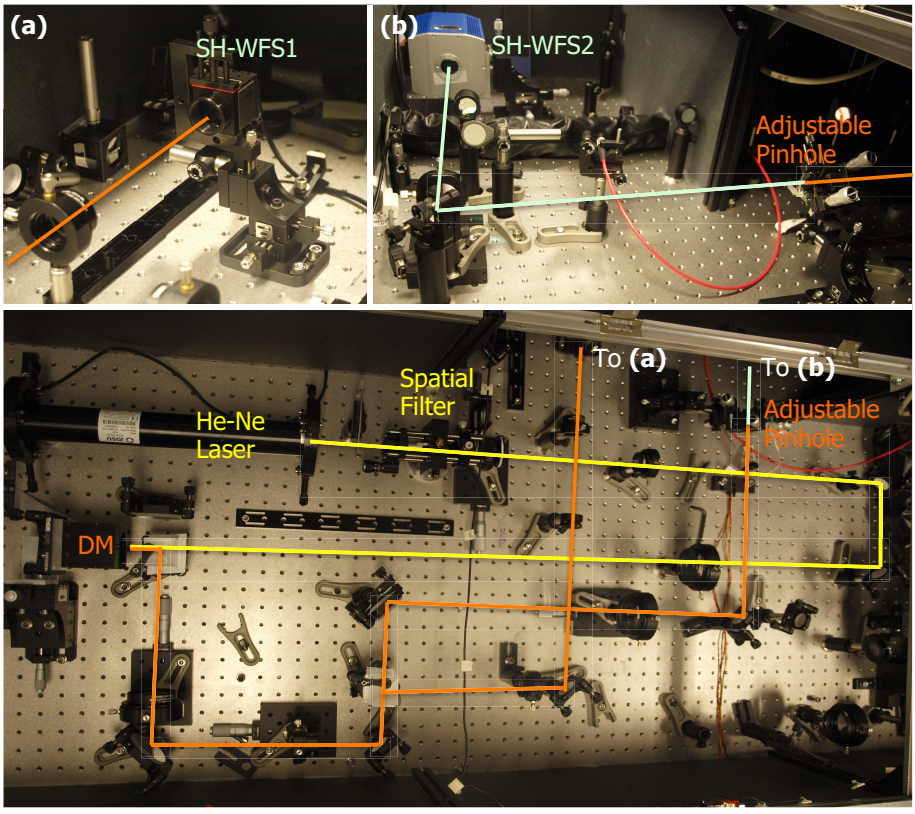

Figure 7.4: Photographs of the experimental setup. Each color of lines represents the beam with specific aberration, i.e. yellow lines are regarded without aberrations by spatial filtering after the HeNe laser, orange lines are the aberrations induced by deformable mirror, and cyan lines are for the spatially filtered aberrations by adjustable square pinhole. The picture below shows the main path from laser with deformable mirror, which lines to the two wavefront sensor paths: (a) DM calibration path with SH-WFS1 and (b) pupil measurements path through adjustable square pinhole by SH-WFS2.

trolled by SH-WFS2 to stably generate an arbitrary shape of the deformable mirror. The measurement noise of each measurements is obtained by standard deviation of 10 measurements with scaling by $\sqrt{10}$.

7.4.2 Experimental Results and Analysis

A simulation for Fig. 7.1 is designed and evaluated for comparing aberrations by experiments. We assume a truncated Gaussian intensity aperture with $\sigma = 5.75\ mm$. For the simulation, the pupil functions at ξ and ρ are discretized by 62 μm, i.e. $n = 95$ and the image plane is at r are discretized by 5 μm, 27×27) pixels for 1 AU. The simulation is performed with 1024×1024 pixel. The simulation uses Fresnel approximation based on the Matlab

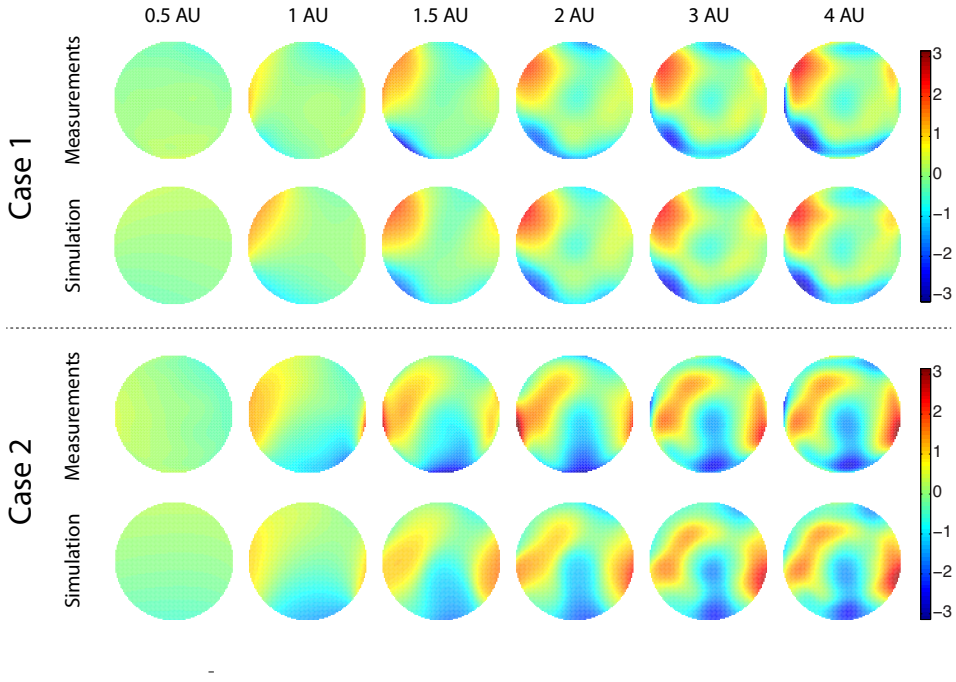

Figure 7.5: Measured wavefronts and simulation results of two arbitrary aberrations.

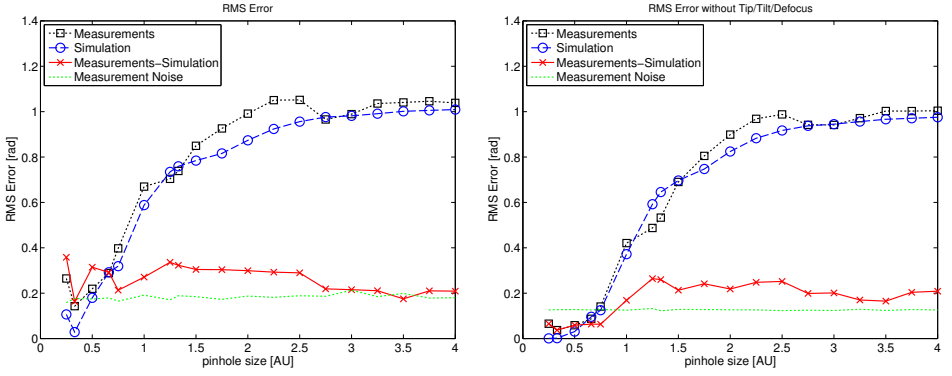

(a) Case 2, RMS WF error

(b) Case 2, RMS WF error without tip, tilt and defocus

Figure 7.6: RMS wavefront error of the measured data (dotted black line with square marks) and the model (blue solid line with o marks), and its difference (red solid line with x marks). The measurement noise is given as green dotted line.

codes in [226]. The final input aberrations assumed with the measurement result with 4 AU because it is the best measurement data with the maximum pinhole size and without for the mismatch between SH-WFS1 and SH-WFS2. Reference of for SH-WFS1 and SH-WFS2 are taken with reference flat mirror. For the model verification phase is only considered and

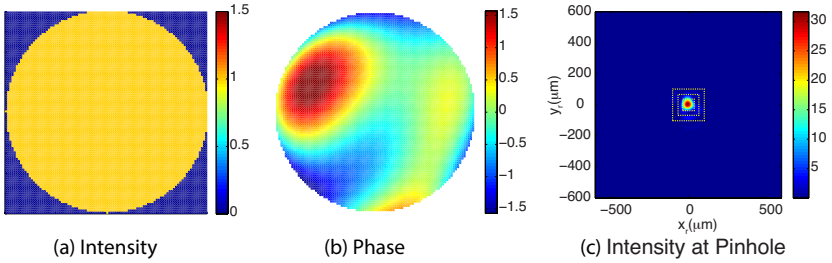

Figure 7.7: Input pupil function with aberrations and the image at the focus. Dotted magenta squares at the image at the focus represent different sizes of the pinhole (0.5, 1.0, and 1.5 AU).

compared with since the pupil intensity can be assumed as a truncated Gaussian after the spatial filtering and the phase comparison could be enough for verifying the behavior of the pinhole. In addition, the phase modification by the pinhole is of interest for the adaptive optics development. For the complex pupil measurement and parameterization with intensity profile, an additional techniques may be necessary [223], which is not covered in this thesis.

Fig. 7.5 shows the comparison between the simulation and experimental data for two random aberrations, case 1 and case 2. As the pinhole size decreases, the amplitude of the aberrations decreases and the feature in high order modes are blurred. The tendency of the aberration change in Fig.7.5 is similar in both simulation and measurements. Fig. 7.9 shows RMS errors of the experimental measurements (dotted black line with square marks) and simulation (blue solid line with o marks) of Case 2 and its RMS difference between simulation and measurements (red solid line with x marks) for each pinhole size. The mean noise floor of SH-WFS2 after the pinhole is also shown as well (green dotted line). For larger pinhole size than 1 AU, total RMS error between simulation and the measurements in Fig. 7.9(a) shows a good agreement about the measurement noise. The measurement and simulation shows a better agreement without tip, tilt, and defocus of Fig. 7.9(b), since tip, tilt, and defocus may caused by vibrations of the optical system. the difference of simulation and experiments at 4 AU is not zeros since the 4 AU with simulation still blur and change the aberrations. This verifies the model of (7.14) for the simulation results in the following section.

7.5 Simulation Results

7.5.1 Pupil Function Retrieval via Single and Diversified Pinhole Sizes

The simulation study about the retrieval of the pupil function is discussed from the complex pupil measurement with Gaussian random noise. The input pupil function has 5.75mm diameter with an uniform intensity with only aberrations. The aberrations are chosen based on the finite Zernike polynomials until Z_{15}. Fig. 7.7 shows the input pupil function in terms of intensity and phase and the intensity profile at the focal plane. The yellow squares represent the square pinhole of 1 AU (135μm), 1.5 AU (205μm), and 2 AU (275 μm). The phase wrapping is observed since the aberrations are over π. The noise is assumed as an

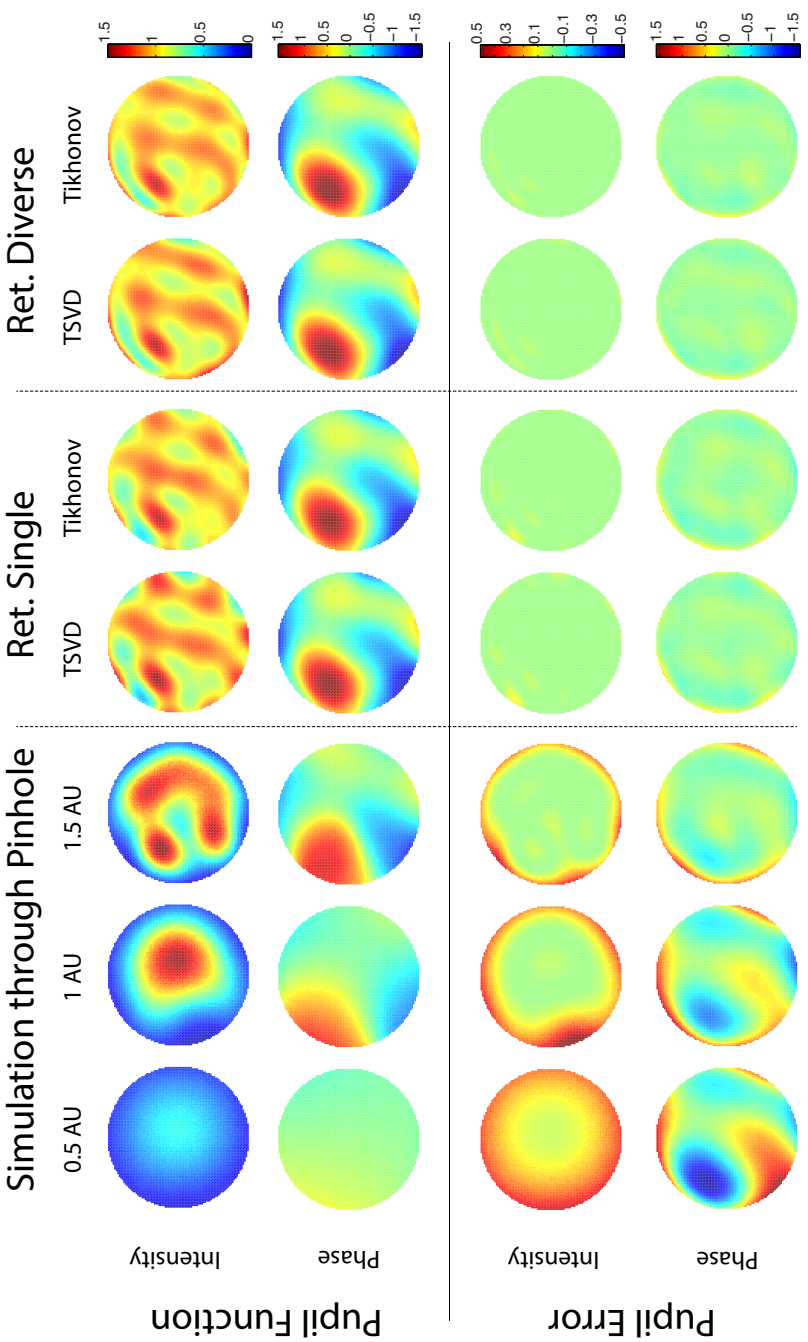

Figure 7.8: Simulation results of the output pupil functions (intensity, phase) through the square pinhole of 0.5, 1.0, and 1.5 AU with additive Gaussian noise, retrieved pupil function from the output pupil function with a pinhole of 1.5AU (single pinhole size) and all three (0.5, 1, 1.5 AU) measurements (diversified pinhole size) using truncated SVD and Tikhonov regularization. The error with respect to the input pupil is shown for each cases.

additive white Gaussian noise (AWGN) with zero mean and a standard deviation $\sigma = 0.01$ in both real and imaginary sides. It shows that the output pupil function has a distortion in both intensity and the phase at the same time.

Fig.7.8 illustrate the magnitude and the phase of the output pupil function after pinhole, and retrieved pupil functions by the single measurement of 1.5 AU pinhole size, and diversified pinhole size 0.5, 1, and 1.5 AU. and the error of pupil function compared to the input pupil function in Fig 7.7. For the regularization, TSVD and Tikhonov regularization and the regulation parameter λ is selected from L-curve [217, 225]. In all case, TSVD and Tikhonov regularization show the meaningful retrieval which recover the main features of peak and troughs while Tikhonov shows the slight better representation than TSVD. Multiple measurements with diversified pinhole sizes also show a better retrieval quality in Tikhonov regularization retrieval. Table 7.1 shows RMS of the total error in complex value, magnitude error, and phase error of the output pupil after the finite size pinhole and the retrieved pupil function from the pupil measurements of single or multiple pinhole sizes. It shows that the improvement of the phase error is up to 46.4% while the magnitude and overall error is only up to 26.3% and 25.5%. This shows that the propose retrieval methods shows more significant correction in phase than magnitude.

RMS Err [rad]	Output Pupil			Retrieval Single		Retrieval Multiple	
	0.5AU	1AU	1.5AU	TSVD	Tik. Reg.	TSVD	Tik. Reg.
Total	0.5341	0.4126	0.2797	0.1171	0.1108	0.0916	0.0852
Magnitude	0.3906	0.2993	0.2221	0.0775	0.0667	0.0647	0.0560
Phase	0.5308	0.3777	0.2214	0.0882	0.0902	0.0645	0.0641

Table 7.1: RMS error of the pupil function based on the total, magnitude only, and phase only. It is shown that the proposed retrieval methods improve the RMS errors, especially the phase.

7.5.2 Wavefront Measurement Improvement with Arbitrary Aberrations

To verify the wavefront improvement by the proposed algorithm, random aberrations are evaluated to improve the aberration measurement by a pinhole. Ten aberrations are randomly generated based on the biological tissue measurements [196]. The aberrations are scaled from 0.1 to 1 radian RMS Error, and the algorithms of (7.16) with Tikhonov regularization are applied as the conditions in the previous section. Fig. 7.9 shows RMS total error and RMS wavefront error of the output pupil function with each pinhole size and of the retired pupil function by (7.16) as the RMS phase error of the input pupil function increases. The results show that the algorithm improves the wavefront measurements from 1.5 AU to nearly 3 AU, leading to a more accurate wavefront measurements with a confined optical sectioning region.

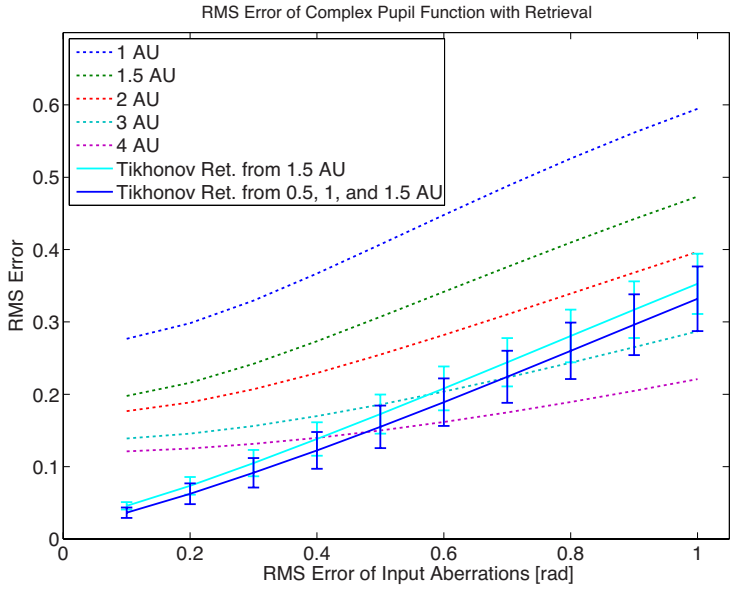

(a) RMS total error

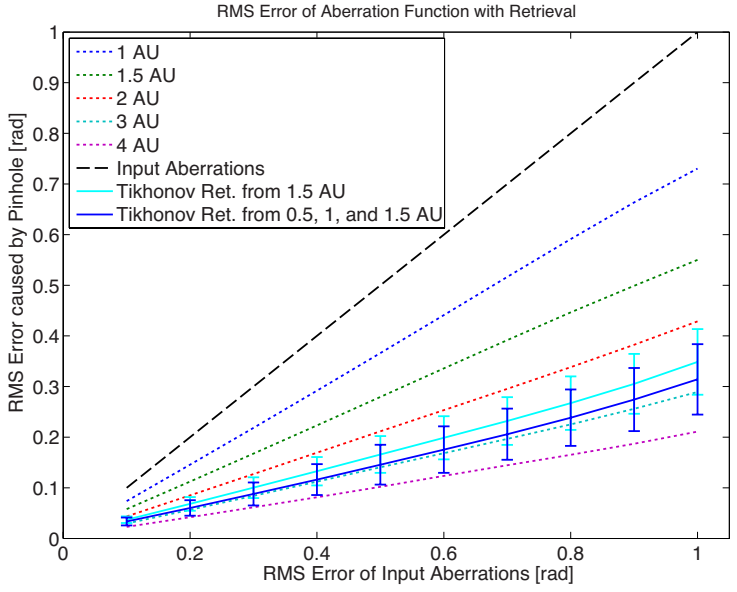

(b) RMS wavefront error

Figure 7.9: Retrieved RMS wavefront error from single (1.5 AU of the pinhole, cyan solid line, standard deviation) and multiple measurements (0.5, 1.0, 1.5 AU of the pinhole, blue solid line with standard deviation) and mean RMS wavefront error of each pinhole sizes (dotted lines with various color), according the RMS wavefront error of input pupil function. (7.7).

7.6 Conclusion

The pupil function retrieval techniques from the distorted output pupil functions after focusing into the finite size of square pinhole is studied in this chapter. Based on the model of the square finite pinhole, which can be separated, 2-dimensional deconvolution problem can be simplified into 1-D problem that a number of efficient solvers are available for. This structure also allows an easy extension for pupil function retrieval from the multiple pupil function measurements. The simulation results with noisy output pupil function measurements verify that stable inversion techniques such as TSVD and Tikhonov regularization provide the meaningful retrieval that recover the features of the pupil function. The proposed retrieval techniques reduced the phase error induced by the pinhole, which allows high accuracy of the confocal wavefront sensor with a high sectioning ability.

Chapter 8

Conclusions and Recommendations

8.1 Conclusions

In this thesis, optomechatronics design and control are discussed for improving temporal and spatial resolution of confocal laser scanning microscopy (CLSM). For the temporal resolution, iterative learning control has been investigated for fast and accurate scanning of the galvanometer scanner (Chapter 2-3). For the spatial resolution improvement, the aberrations in the CLSM, e.g. coverslip mismatch and specimen induced aberrations, are the main targets to compensate for to improve imaging quality. Two main applications, automated coverslip correction collar (Chapter 4) and adaptive optics (AO) system for CLSM (Chapter 5-6), have been developed to verify the concept of the image improvements by optomechatronics design and control. As an extension of AO for CLSM, an algorithm for improving confocal wavefront sensor is also discussed (Chapter 7).

To improve the imaging speed and precision of the galvanometer scanner in CLSM, iterative learning control (ILC) has been proposed to achieve a high speed, linear, and accurate bidirectional scanning. Based on two stable inversion methods, zero phase approximation and time delay approximation, two model based ILCs are designed for enabling a wide control bandwidth over two resonance modes by the mirror and encoder. Experimental results verify the benefits of ILCs, demonstrating up to 73 times smaller root mean square (RMS) error than a conventional feedback controller.

For high rate ILC implementation, non-collocated sensing by the encoder hampers the accuracy of the beam scanning, resulting in a tracking error of the actual beam position although the encoder measurement matches the reference signal. For this non-collocated sensing of the galvanometer scanner, a transformation-based ILC has been proposed to achieve accurate image scanning. The proposed ILC has been extended from the conventional ILC design by adding a reference transformation filter, which is obtained by the transfer functions of the mirror and the encoder. Theoretical analysis show that the proposed ILC can reduce the error of the actual beam scanning. Experimental results with the proposed ILC show a better tracking accuracy as compared to previous ILC design solely

with non-collocated encoder signal.

These ILCs demonstrate the potential of control algorithms to improve the speed and the accuracy of the galvanometer scanner significantly, answering the main research question 1 with yes. However, transformation-based ILC has to be polished for the future research since the residual harmonics are still observed.

To improve imaging quality of CLSM, three optomechatronics systems and their controls are designed and evaluated. For spherical aberrations due to coverslip thickness mismatch, an automated adjustment of the coverslip correction collar is proposed. The automatic coverslip mismatch correction consists of a motorized correction collar and the model based correction algorithms by the image quality measures such as the maximum intensity, sharpness, and entropy to search for the best correction collar adjustment. The benefits of the proposed automated correction are demonstrated with various coverslips with biological specimens, keeping the improved resolution of the confocal microscope.

For the general aberrations, an adaptive optics (AO) system for a commercial CLSM has been developed. The AO system consists of 19ch piezoelectric deformable mirror and two Shack Hartmann wavefront sensor (SHWFS), associated with the excitation HeNe laser and the fluorescence. The AO system also has an adjustable pinhole, which can be used for the WFS referencing and the evaluation of the AO correction. Experimental results with fluorescence beads through the biological specimen show that the developed AO system and algorithms with the adjustable pinhole can improve the resolution, which proves the feasibility of the AO development.

For the phase degradation of the finite size pinhole of confocal wavefront sensor, a pupil function retrieval based on the adjustable square pinhole is proposed based on the stable inversion techniques of regularization. The model is verified with an experimental results, which support the formulation of the algorithm. Simulation results show that the input pupil function can be partly retrieved from the output pupil functions, which improves 46 % RMS wavefront errors of the distorted pupil by the pinhole. The simulation with random aberrations shows that the proposed algorithm can improve the wavefront measurements with 1.5 AU pinhole up to the wavefront error of 3 AU of the pinhole, allowing to measure the wavefront more accurately.

For the main research question 2, the result with automatized coverslip corrections clearly shows the image quality improvement by compensating for spherical aberrations. In AO development for the general aberrations, more complex with various modes, the improvement is vividly given mainly on axial resolution with a large pinhole, showing potentials for correcting aberrations. However, there are still rooms for improvement concerning PSF quality and more verification is necessary about the improvement with different pinhole sizes. The algorithms for minimizing distortions in confocal wavefront sensor are verified in the simulations while it is not in the experimental data yet. At these points, the main research question 2 can be tentatively answered with yes considering potentials of the results while further research is necessary to provide meaningful benefits to the users of CLSM.

8.2 Recommendations

As history of the science and engineering repeatedly shows, the development and analysis dealt with in the thesis have some limitations, which can be improved and extended

by researchers in future. For the, several unsolved issues and challenges that have to be investigated further are described along the main developments in this thesis.

- **ILC for Galvanometer Scanner:** While ILCs showed its capabilities in tracking error, the improvement of the CLSM imaging has not been tested yet. The proposed ILC with a galvanometer scanner can be implemented for the commercial CLSM to verify benefits in imaging. For the non-collocated sensing and transformation ILC design, a robust design would be of interest to minimize the residual vibrations in the active region.

- **Automated Coverslip Correction Collar:** The main challenge of this automatic correction is a sensing method of the aberration. In image based algorithms, less image acquisition is desirable for reducing correction time and chances of photobleaching. Other mean such as wavefront sensing can be an option for the fast correction as well. In the meantime, an automatic compensation of the aberrations in general, including non-spherical aberrations, is of interest in the scanning confocal microscopy by means of adaptive optics. Since the aberration in deep imaging has a similar model with coverslip mismatch problem, the analysis and algorithm in this results can be extended to minimize the aberrations in the tissue imaging.

- **Adaptive Optics for CLSM:** The urgent work to be done for future AO development is applying the other laser lines such as Ar laser, which are popular for the biological study. HeNe laser is widely used in physics study while it is not much popular in biological study and only a few kind of fluorephore are available. Based on the additional laser line, the image improvements of the biological specimen can be evaluated by the proposed approach. For the fast calibration and compensation process is also necessary for less photobleaching since the signal loss by photobleaching is a serious problem for running AO for CLSM. Using the knowledge of the senseless AO, a hybrid control scheme using both wavefront sensored AO and wavefront sensorless AO can be an interesting topic for control engineers, which may provides fast convergence and higher image quality after all.

- **Pupil Function Retrieval via Pinhole Diversity** The challenges of the applying the proposed pupil functional retrieval are the sensing methods of the output pupil function. A new pupil function sensing method is desirable since the accuracy and its resolution has to be improved for applying this algorithm. An analysis on the specific sensors and noise characteristics are important for the complex pupil measurement such as SHWFS to realize and evaluate the proposed method.

Bibliography

[1] J. B. Pawley, ed., *Handbook of biological confocal microscopy*. Springer Science Business Media, 3rd ed., 2006.

[2] J. Mertz, *Introduction to Optical Microscopy*. Roberts and company publisher, 1st ed., 2009.

[3] W. Denk, J. Strickler, and W. Webb, "Two-photon laser scanning fluorescence microscopy," *Science*, vol. 248, pp. 73–76, Apr. 1990.

[4] P. J. Campagnola and L. M. Loew, "Second-harmonic imaging microscopy for visualizing biomolecular arrays in cells, tissues and organisms," *Nature biotechnology*, vol. 21, pp. 1356–1360, Nov. 2003.

[5] M. G. L. Gustafsson, "Surpassing the lateral resolution limit by a factor of two using structured illumination microscopy.," *Journal of microscopy*, vol. 198, pp. 82–87, May 2000.

[6] S. W. Hell and J. Wichmann, "Breaking the diffraction resolution limit by stimulated emission: stimulated-emission-depletion fluorescence microscopy," *Optics Letters*, vol. 19, no. 11, p. 780, 1994.

[7] W. Lukosz, "Optical Systems with Resolving Powers Exceeding the Classical Limit," *Journal of the Optical Society of America*, vol. 56, no. 11, p. 1463, 1966.

[8] E. A. Ash and G. Nicholls, "Super-resolution Aperture Scanning Microscope," *Nature*, vol. 237, pp. 510–512, June 1972.

[9] M. Minsky, "Microscopy apparatus, us 3013467," 1957.

[10] W. B. Amos and J. G. White, "How the Confocal Laser Scanning Microscope entered Biological Research," *Biology of the Cell*, vol. 95, pp. 335–342, Jan. 2012.

[11] A. P. Baader, L. Buchler, L. Bircher-Lehmann, and A. G. Kleber, "Real time, confocal imaging of Ca2+ waves in arterially perfused rat hearts," *Cardiovasc Res.*, vol. 53, no. 1, pp. 105–115, 2002.

[12] P. Saggau, "New methods and uses for fast optical scanning," *Current Opinion Neurobiology*, vol. 16, pp. 543–550, 2006.

[13] M. D. Egger and M. Petran, "New reflected-light microscope for viewing unstained brain and ganglion cells," *Science*, vol. 157, pp. 305–307, 1967.

[14] M. Petráň, M. Hadravský, M. D. Egger, and R. Galambos, "Tandem-Scanning Reflected-Light Microscope," *Journal of the Optical Society of America*, vol. 58, no. 5, p. 661, 1968.

[15] G. Q. Xiao and G. S. Kino, "A Real-Time Confocal Scanning Optical Microscope," in *Hague International Symposium* (L. J. Balk and T. Wilson, eds.), pp. 107–113, SPIE, Aug. 1987.

[16] K. Carlsson, P. E. Danielsson, R. Lenz, A. Liljeborg, L. Majlöf, and N. Åslund, "Three-dimensional microscopy using a confocal laser scanning microscope," *Optics Letters*, vol. 10, no. 2, p. 53, 1985.

[17] V. Duma, A. Podoleanu, and M. Nicolov, "Modeling a galvanoscanner with an optimized scanning function," *SYROM*, pp. 539–548, 2009.

[18] A. Diaspro, M. Faretta, and P. Sapuppo, *Confocal Microscopy*. Leica Microsystems CMS, 2008.

[19] S. Hell, G. Reiner, C. Cremer, and E. H. K. Stelzer, "Aberrations in confocal fluorescence microscopy induced by mismatches in refractive index," *Journal of microscopy*, vol. 169, no. 3, pp. 391–405, 1993.

[20] M. J. Booth, M. A. A. Neil, and T. Wilson, "Aberration correction for confocal imaging in refractive-index-mismatched media," *Journal of microscopy*, vol. 192, no. 2, pp. 90–98, 1998.

[21] Z. Kam, B. Hanser, M. Gustafsson, D. A. Agard, and J. W. Sedat, "Computational adaptive optics for live three-dimensional biological imaging," in *Proceedings of the National Academy of Sciences*, vol. 98, pp. 3790–3795, 2001.

[22] J. Zeng, P. Mahou, M.-C. Schanne-Klein, E. Beaurepaire, and D. Débarre, "3D resolved mapping of optical aberrations in thick tissues," *Biomedical Optics Express*, vol. 3, no. 8, p. 1898, 2012.

[23] J. Crest, S. Kotadia, and W. Sullivan, "Telescopes, stars, and cells: adaptive optics microscopy," *SPIE Newsroom*, Oct. 2011.

[24] B. N. Giepmans, S. R. Adams, M. H. Ellisman, and R. Y. Tsien, "The Fluorescent Toolbox for Assessing Protein Location and Function," *Science*, vol. 312, no. 5771, pp. 217–224, 2006.

[25] X. X. Zhou and M. Z. Lin, "Photoswitchable fluorescent proteins: ten years of colorful chemistry and exciting applications," *Curr. Opin. Chem. Biol.*, vol. 17, no. 4, pp. 682–690, 2013.

[26] D. Ehrhardt, "GFP technology for live cell imaging," *Curr. Opin. Plant Biol.*, vol. 6, no. 6, pp. 622–628, 2003.

[27] R. N. Germain, E. A. Robey, and M. D. Cahalan, "A Decade of Imaging Cellular Motility and Interaction Dynamics in the Immune System," *Science*, vol. 336, no. 6089, pp. 1676–1681, 2012.

[28] R. M. Hoffman, "The multiple uses of fluorescent proteins to visualize cancer in vivo," *Nat. Rev. Cancer*, vol. 5, no. 10, pp. 796–806, 2005.

[29] M. R. Fein and M. Egeblad, "Caught in the act: revealing the metastatic process by live imaging," *Dis. Model. Mech.*, vol. 6, no. 3, pp. 580–593, 2013.

[30] L. Bakota and R. Brandt, "Chapter 2 Live–Cell Imaging in the Study of Neurodegeneration," in *Int. Rev. Cell Mol. Biol.*, vol. 276, pp. 49–103, Academic Press, 2009.

[31] C. Weissmann and R. Brandt, "Mechanisms of neurodegenerative diseases: Insights from live cell imaging," *J. Neurosci. Res.*, vol. 86, no. 3, pp. 504–511, 2008.

[32] B. Valeur and M. N. Berberan-Santos, "A Brief History of Fluorescence and Phosphorescence before the Emergence of Quantum Theory," *Journal of Chemical Education*, vol. 88, pp. 731–738, June 2011.

[33] R. Y. Tsien, "The information age in optics: Measuring the transmission matrix," *Annu. Rev. Biochem*, vol. 67, pp. 509–544, 1998.

[34] N. C. Shaner, P. A. Steinbach, and R. Y. Tsien, "A guide to choosing fluorescent proteins," *Nature methods*, vol. 3, pp. 905–909, December 2005.

[35] R. Yuste, ed., *Imaging: A Laboratory Manual*. Cold Spring Harber Protocols, 2011.

[36] M. Y. Lee, H. Song, J. Nakai, M. Ohkura, M. I. Kotlikoff, S. P. Kinsey, V. A. Golovina, and M. P. Blaustein, "Local subplasma membrane Ca2+ signals detected by a tethered Ca2+ sensor," *Proceedings of the National Academy of Sciences*, vol. 103, pp. 13232–13237, Aug. 2006.

[37] A. Sakaue-Sawano, H. Kurokawa, T. Morimura, A. Hanyu, H. Hama, H. Osawa, S. Kashiwagi, K. Fukami, T. Miyata, H. Miyoshi, T. Imamura, M. Ogawa, H. Masai, and A. Miyawaki, "Visualizing Spatiotemporal Dynamics of Multicellular Cell-Cycle Progression," *Cell*, vol. 132, pp. 487–498, Feb. 2008.

[38] N. P. from the Nobel Committee for Chemistry, "The nobel prize in chemistry 2008 - illustrated presentation," 2008.

[39] P. W. Hawkes and J. C. H. Spence, *Science of Microscopy: Volume II*. Springer Science Business Media, 1st ed., 2007.

[40] Q. Wu, F. Merchant, and K. Castleman, *Microscope Image Processing*. Academic Press, 2008.

[41] A. Weigel, *Qualtitation strategies in optically sectioning fluorescence microscopy*. PhD thesis, Georg August University Göttingen, 2006.

[42] D. J. Stephens and V. J. Allan, "Light Microscopy Techniques for Live Cell Imaging," *Science Signaling*, vol. 300, p. 82, Apr. 2003.

[43] N. Ji, H. Shroff, H. Zhong, and E. Betzig, "Advances in the speed and resolution of light microscopy," *Current Opinion Neurobiology*, vol. 18, pp. 605–616, 2008.

[44] Leica Microsystems, *Leica TCS SP5 II: The only broadband confocal technical documentation.* Order No. 1593101008.

[45] V.-F. Duma, K.-S. Lee, P. Meemon, and J. P. Rolland, "Experimental investigation of the scanning functions of galvanometer-based scanners with applications in oct," *Applied Optics*, vol. 50, no. 29, pp. 5735–5749, 2011.

[46] P. Xi, Y. Liu, and Q. Ren, "Scanning and Image Reconstruction Techniques in Confocal Laser Scanning Microscopy," in *cdn.intechopen.com* (C.-C. Wang, ed.), InTech, Apr. 2011.

[47] V.-F. Duma, "Mathematical functions of a 2-d scanner with oscilating elements," *Modeling, Simulation and Control of Nonlinear Engineering Dynamical Systems*, pp. 243–253, 2009.

[48] S. Chen, X. Feng, Y. Li, C. Zhou, P. Xi, and Q. Ren, "Software controlling algorithms for the system performance optimization of confocal laser scanning microscope," *Biomedical Signal Processing and Control*, vol. 5, pp. 223–228, July 2010.

[49] J. G. White, "An evaluation of confocal versus conventional imaging of biological structures by fluorescence light microscopy," *The Journal of cell biology*, vol. 105, pp. 41–48, July 1987.

[50] K. H. Kim, C. Buehler, and P. T. C. So, "High-Speed, Two-Photon Scanning Microscope," *Applied Optics*, vol. 38, no. 28, p. 6004, 1999.

[51] N. Callamaras and I. Parker, "Construction of a confocal microscope for real-time x-y and x-z imaging," *Cell Calcium*, vol. 26, no. 6, pp. 271–279, 1999.

[52] S. R. Goldstein, T. Hubin, and S. Rosenthal, "A confocal video-rate laserbeam scanning reflected-light microscope with no moving parts," *J. Microscope*, vol. 127, pp. 29–38, 1990.

[53] A. Bullen, S. S. Patel, and P. Saggau, "High-speed, random-access fluorescence microscopy: I. high- resolution optical recording with voltage-sensitive dyes and ion indicators," *Biophys J*, vol. 73, pp. 477–491, 1997.

[54] V. Iyer, B. E. Losavio, and P. Saggau, "Dispersion compensation for acousto-optic scanning two-photon microscopy," *Progress in Biomedical Optics and Imaging*, vol. 3, pp. 281–292, 2002.

[55] G. D. Reddy and P. Saggau, "Fast three-dimensional laser scanning scheme using acousto-optic deflectors," *Journal of Biomedical Optics*, vol. 10, p. 64038, 2005.

[56] G. Duemani Reddy, K. Kelleher, R. Fink, and P. Saggau, "Three-dimensional random access multiphoton microscopy for functional imaging of neuronal activity," *Nature Neuroscience*, vol. 11, pp. 713–720, Apr. 2008.

[57] G. Q. Xiao, T. R. Corle, and G. S. Kino, "Real-time confocal scanning optical microscope," *Applied Physics Letters*, vol. 53, no. 8, pp. 716–718, 1988.

[58] A. Ichihara, T. Tanaami, K. Isozaki, Y. Sugiyama, and Y. Kosugi, "High-speed confocal fluorescence microscopy using a nipkow scanner with microlenses for 3d imaging of single fluorescence molecule in real time," *Bioimages*, vol. 4, pp. 57–62, 1996.

[59] T. Tanaami, S. Otsuki, N. Tomosada, Y. Kosugi, M. Shimizu, and H. Ishida, "High-speed 1-frame/ms scanning confocal microscope with a microlens and nipkow disks," *Applied Optics*, vol. 41, pp. 4704–4708, 2002.

[60] J. Bewersdorf, R. Pick, and S. W. Hell, "Multifocal multiphoton microscopy," *Optics Letters*, vol. 23, no. 9, pp. 655–657, 1998.

[61] M. Liang, R. L. Stehr, and A. W. Krause, "Confocal pattern period in multiple-aperture confocal imaging systems with coherent illumination," *Optics Letters*, vol. 22, no. 11, pp. 751–753, 1997.

[62] M. Ehrenberg, "The Nobel Prize in Chemistry 2014 - Advanced Information." http://www.nobelprize.org/nobel_prizes/chemistry/laureates/2014/advanced.html, Dec. 2014.

[63] S. W. Hell, "Toward fluorescence nanoscopy," *Nature biotechnology*, vol. 21, pp. 1347–1355, Nov. 2003.

[64] R. P. J. Nieuwenhuizen, K. A. Lidke, M. Bates, D. L. Puig, D. Grünwald, S. Stallinga, and B. Rieger, "Measuring image resolution in optical nanoscopy," *nAture methods*, vol. 10, pp. 557–562, Apr. 2013.

[65] F. de Lange, A. Cambi, R. Huijbens, B. de Bakker, W. Rensen, M. Garcia-Parajo, N. van Hulst, and C. Figdor, "Cell biology beyond the diffraction limit: near-field scanning optical microscopy," *Journal of Cell Science*, vol. 114, pp. 4153–4160, 2001.

[66] Y. Oshikane, T. Kataoka, M. Okuda, S. Hara, H. Inoue, and M. Nakano, "Observation of nanostructure by scanning near-field optical microscope with small sphere probe," *Science and Technology of Advanced Materials*, vol. 8, no. 3, pp. 181–185, 2007.

[67] M. G. L. Gustafsson, L. Shao, P. M. Carlton, C. J. R. Wang, I. N. Golubovskaya, W. Z. Cande, D. A. Agard, and J. W. Sedat, "Threedimensional resolution doubling in wide-field fluorescence microscopy by structured illumination," *Biophysical Journal*, vol. 94, pp. 4957–4970, 2008.

[68] P. Kner, B. B. Chhun, E. R. Griffis, L. Winoto, and M. G. L. Gustafsson, "Super-resolution video microscopy of live cells by structured illumination," *Nature Method*, vol. 6, no. 5, pp. 339–342, 2009.

[69] V. Westphal and S. W. Hell, "Nanoscale resolution in the focal plane of an optical microscope," *Physical Reveiw Letters*, vol. 94, p. 143903, 2005.

[70] V. Westphal, S. O. Rizzoli, M. A. Lauterbach, D. Kamin, R. Jahn, and S. W. Hell, "Video-rate far-field optical nanoscopy dissects synaptic vesicle movement," *Science*, vol. 320, pp. 246–249, 2008.

[71] E. Betzig, G. H. Patterson, R. Sougrat, O. W. L. S. Olenych, J. S. Bonifacino, M. W. Davidson, J. Lippincott-Schwartz, and H. F. Hess, "Imaging intracellular fluorescent proteins at nanometer resolution," *Science*, vol. 313, pp. 1642–1645, 2006.

[72] M. J. Rust, M. Bates, and X. Zhuang, "Sub-diffraction-limit imaging by stochastic optical reconstruction microscopy (STORM)," *nAture methods*, vol. 3, pp. 793–796, Aug. 2006.

[73] S. T. Hess, T. P. K. Girirajan, and M. D. Mason, "Ultra-High Resolution Imaging by Fluorescence Photoactivation Localization Microscopy," *Biophysical Journal*, vol. 91, pp. 4258–4272, Dec. 2006.

[74] M. Uchiyama, "Formulation of high-speed motion pattern of a mechanical arm by trial (in Japanese)," *Trans. SICE (Soc. Instrum. Control Eng.)*, vol. 14, pp. 706–712, 1978.

[75] S. Arimoto, S. Kawamura, and F. Miyazaki, "Bettering operation of dynamic systems by learning: a new control theory for servomechanism or mechatronic system," in *Proceedings of 23rd Conference on Decision and Control*, p. 1064–1069, 1984.

[76] H.-S. Ahn, Y. Chen, and K. L. Moore, "Iterative Learning Control: Brief Survey and Categorization," *IEEE Transactions on Systems, Man and Cybernetics, Part C (Applications and Reviews)*, vol. 37, no. 6, pp. 1099–1121, 2007.

[77] R. Longman, "Iterative learning control and repetitive control for engineering practice," *International Journal of Control*, vol. 73, no. 10, pp. 930–954, 2000.

[78] Y. Wang, F. Gao, and F. J. Doyle, "Survey on iterative learning control, repetitive control, and run-to-run control," *Journal of Process Control*, vol. 19, no. 10, pp. 1589–1600, 2009.

[79] A. J. Fleming and K. K. Leang, *Design, Modeling and Control of Nanopositioning Systems*. London, UK: Springer, 2014.

[80] Y. Li and J. Bechhoefer, "Model-free iterative control of repetitive dynamics for high-speed scanning in atomic force microscopy," *Review of Scientific Instruments*, vol. 80, p. 013702, Jan. 2009.

[81] O. Trepte, "Enhanced scanning control in a confocal scanning laser microscope," *Scanning*, vol. 18, pp. 356–361, 1996.

[82] B. Potsaid, J. T.-Y. Wen, M. Unrath, D. Watt, and M. Alpay, "High performance motion tracking control for electronic manufacturing," *Journal of Dynamic Systems, Measurement, and Control*, vol. 129, pp. 767–776, 2007.

[83] K. K. Leang and S. Devasia, "Design of hysteresis-compensating iterative learning control for piezo-positioners: Application to atomic force microscopes," *Mechatronics*, vol. 16, pp. 141–158, 2006.

[84] S. Tien, Q. Zou, and S. Devasia, "Iterative control of dynamics-coupling-caused errors in piezoscanners during high-speed AFM operation," *IEEE Transactions on control systems technology*, vol. 13, pp. 921–931, 2006.

[85] G. Schitter, "Improving the speed of AFM by mechatronic design and modern control methods," *Technisches Messen*, vol. 76, no. 5, pp. 266–273, 2009.

[86] G. M. Clayton, S. Tien, K. K. Leang, Q. Zou, and S. Devasia, "A Review of Feedforward Control Approaches in Nanopositioning for High-Speed SPM," *Journal of Dynamic Systems, Measurement, and Control*, vol. 131, no. 6, p. 061101, 2009.

[87] K. Leang, Q. Zou, and S. Devasia, "Feedforward control of piezoactuators in atomic force microscope systems," *IEEE Control Systems Magazine*, vol. 29, pp. 70–82, Feb. 2009.

[88] W. M. K. Observatory, "Keck Next: Next Generation Adaptive Optics." http://www.keckobservatory.org/support/ngao, 2010.

[89] J. W. Hardy, ed., *Adaptive Optics for Astronomical Telescopes*. Oxford University Press, USA, 1998.

[90] R. W. Duffner, *The Adaptive Optics Revolution*. University of New Mexico Press, 2009.

[91] J. Palca, "For Sharpest Views, Scope The Sky With Quick-Change Mirrors ." http://www.npr.org/2013/06/24/190986008/for-sharpest-views-scope-the-sky-with-quick-change-mirrors, June 2013.

[92] M. J. Booth, "Adaptive optics in microscopy," *Philosophical Transactions of the Royal Society A: Mathematical, Physical and Engineering Sciences*, vol. 365, pp. 2829–2843, Dec. 2007.

[93] R. D. Ferguson, Z. Zhong, D. X. Hammer, M. Mujat, A. H. Patel, C. Deng, W. Zou, and S. A. Burns, "Adaptive optics scanning laser ophthalmoscope with integrated wide-field retinal imaging and tracking," *Journal of the Optical Society of America A*, vol. 27, no. 11, p. A265, 2010.

[94] M. Zacharria, B. Lamory, and N. Chateau, "Biomedical imaging: New view of the eye," *Nature Photonics*, vol. 5, pp. 24–26, Jan. 2011.

[95] R. W. Bowman, A. J. Wright, and M. J. Padgett, "An SLM-based Shack–Hartmann wavefront sensor for aberration correction in optical tweezers," *Journal of Optics*, vol. 12, p. 124004, Nov. 2010.

[96] R. K. Tyson, "Bit-error rate for free-space adaptive optics laser communications," *J. Opt. Soc. Am. A*, vol. 19, no. 4, pp. 753–758, 2002.

[97] N. Ishii, T. Muroi, N. Kinoshita, K. Kamijo, and N. Shimidzu, "Wavefront compensation method using novel index in holographic data storage," *Journal of the European Optical Society: Rapid Publications*, vol. 5, no. 0, p. 10036s, 2010.

[98] J. W. Hardy, "Active optics: A new technology for the control of light," *Proceedings of the IEEE*, vol. 66, pp. 651–697, June 1978.

[99] H. Song, R. Fraanje, G. Schitter, H. Kroese, G. Vdovin, and M. Verhaegen, "Model-based aberration correction in a closed-loop wavefront-sensor-less adaptive optics system," *Optics Express*, vol. 18, no. 23, p. 24070, 2010.

[100] J. Antonello, M. Verhaegen, R. Fraanje, T. van Werkhoven, H. C. Gerritsen, and C. U. Keller, "Semidefinite programming for model-based sensorless adaptive optics," *J. Opt. Soc. Am. A*, vol. 29, no. 11, pp. 2428–2438, 2012.

[101] D. Debarre, E. J. Botcherby, M. J. Booth, and T. Wilson, "Image based adaptive optics through optimisation of low spatial frequencies," *Optics Express*, vol. 15, no. 13, pp. 8176–8190, 2007.

[102] D. Debarre, E. J. Botcherby, T. Watanabe, S. Srinivas, M. J. Booth, and T. Wilson, "Image-based adaptive optics for two-photon microscopy," *Optic Letters*, vol. 34, no. 16, pp. 2495–2497, 2009.

[103] L. M. Mugnier, A. Blanc, and J. Idier, "Phase Diversity: a technique for Wave-front sensing and for diffraction-limitted imaging," *Advances in Imaging and Electron Physics*, vol. 141, p. 76, 2006.

[104] W. J. Wild, "Linear phase retrieval for wave-front sensing," *Optics Letters*, vol. 23, no. 8, pp. 573–575, 1998.

[105] L. A. Thompson and R. M. Castle, "Experimental demonstration of a Rayleigh-scattered laser guide star at 351 nm," *Optics Letters*, vol. 17, no. 20, p. 1485, 1992.

[106] M. Lloyd-Hart, J. R. P. Angel, B. Jacobsen, D. Wittman, R. Dekany, D. McCarthy, E. Kibblewhite, W. Wild, B. Carter, and J. Beletic, "Adaptive optics experiments using sodium laser guide stars," *The Astrophysical Journal*, vol. 439, pp. 455–473, Jan. 1995.

[107] R. K. Tyson, *Topics in Adaptive Optics*. InTech, 2012.

[108] J. Kubby, ed., *Adaptive optics for biomedical imaging*. CRC Press, 2013.

[109] M. J. Booth., M. A. A. Neil, and T. Wilson, "New modal wave-front sensor: application to adaptive confocal fluorescence microscopy and two-photon excitation fluorescence microscopy," *Journal of the Optical Society of America A: Optics, Image Science and Vision*, vol. 19, no. 10, pp. 2112–2120, 2002.

[110] X. Tao, B. Fernandez, O. Azucena, M. Fu, D. Garcia, Y. Zuo, D. C. Chen, and J. Kubby, "Adaptive optics confocal microscopy using direct wavefront sensing," *Optics Letters*, vol. 36, no. 7, p. 1062, 2011.

[111] P. Kner, J. Sedat, D. Agrad, and Z. Kam, "High-resolution wide-field microscopy with adaptive optics for spherical aberration correction and motionless focusing," *Journal of Microscopy*, vol. 237, p. 136.147, 2010.

[112] P. Vermeulen, E. Muro, T. Pons, V. Loriette, and A. Fragola, "Adaptive optics for fluorescence wide-field microscopy using spectrally independent guide star and markers," *Journal of Biomedical Optics*, vol. 16, no. 7, p. 076019, 2011.

[113] O. Azucena, J. Crest, S. Kotadia, W. Sullivan, M. R. Xiaodong Tao, D. Gavel, S. Olivier, and J. Kubby, "Adaptive optics wide-field microscopy using direct wavefront sensing ," *Optics Letter*, vol. 36, no. 6, 2011.

[114] A. Jesacher, A. Thayil, K. Grieve, D. Débarre, T. Watanabe, T. Wilson, S. Srinivas, and M. Booth, "Adaptive harmonic generation microscopy of mammalian embryos," *Optics Letters*, vol. 34, no. 20, pp. 3154–3156, 2009.

[115] C.-E. Leroux, I. Wang, J. Derouard, and A. Delon, "Adaptive optics for fluorescence correlation spectroscopy," *Optics Express*, vol. 19, no. 27, pp. 26839–26849, 2011.

[116] A. J. Wright, S. P. Poland, J. M. Girkin, C. W. Freudiger, C. L. Evans, and X. S. Xie, "Adaptive optics for enhanced signal in CARS microscopy," *Optics Express*, vol. 15, no. 26, p. 18209, 2007.

[117] C. Bourgenot, C. D. Saunter, J. M. Taylor, J. M. Girkin, and G. D. Love, "3D adaptive optics in a light sheet microscope," *Optics Express*, vol. 20, no. 12, p. 13252, 2012.

[118] B. R. Patton, D. Burke, and M. J. Booth, "Adaptive optics from microscopy to nanoscopy," in *SPIE BiOS* (A. Periasamy, P. T. C. So, and K. König, eds.), p. 894802, SPIE, Feb. 2014.

[119] D. Debarre, E. J. Botcherby, M. J. Booth, and T. Wilson, "Adaptive optics for structured illumination microscopy," *Optics Express*, vol. 16, no. 13, pp. 9290–9305, 2008.

[120] I. Izeddin, M. El Beheiry, J. Andilla, D. Ciepielewski, X. Darzacq, and M. Dahan, "PSF shaping using adaptive optics for three-dimensional single-molecule super-resolution imaging and tracking," *Optics Express*, vol. 20, no. 5, p. 4957, 2012.

[121] T. J. Gould, D. Burke, J. Bewersdorf, and M. J. Booth, "Adaptive optics enables 3D STED microscopy in aberrating specimens," *Optics Express*, vol. 20, no. 19, p. 20998, 2012.

[122] M. J. Booth, D. Débarre, and A. Jesacher, "Adaptive Optics for Biomedical Microscopy," *Optics and Photonics News*, vol. 23, no. 1, pp. 22–29, 2012.

[123] M. A. A. Neil, R. Juskatis, M. J. Booth, T. Wilson, T. Tanaka, and S. Kawata, "Adaptive aberration correction in a two-photon microscope," *Journal of Microscopy*, vol. 200, pp. 105–108, 2000.

[124] M. J. Booth, "Wavefront sensorless adaptive optics for large aberrations," *Optic Letters*, vol. 32, no. 1, pp. 5–7, 2007.

[125] J. Antonello, T. van Werkhoven, M. Verhaegen, H. H. Truong, C. U. Keller, and H. C. Gerritsen, "Optimization-based wavefront sensorless adaptive optics for multiphoton microscopy," *J. Opt. Soc. Am. A*, vol. 31, no. 6, pp. 1337–1347, 2014.

[126] N. Ji, D. E. Milkie, and E. Betzig, "Adaptive optics via pupil segmentation for high-resolution imaging in biological tissues," *Nature Method*, vol. 7, no. 2, pp. 141–147, 2010.

[127] D. E. Milkie, E. Betzig, and N. Ji, "Pupil-segmentation-based adaptive optical microscopy with full-pupil illumination," *Optics Letters*, vol. 36, no. 21, pp. 4206–4208, 2011.

[128] N. Ji, T. R. Sato, and E. Betzig, "Characterization and adaptive optical correction of aberrations during in vivo imaging in the mouse cortex," *Proceedings of the National Academy of Sciences*, vol. 109, pp. 22–27, January 2012.

[129] J. Scrimgeour and J. E. Curtis, "Aberration correction in wide-field fluorescence microscopy by segmented-pupil image interferometry," *Optics Express*, vol. 20, no. 13, pp. 14534–14541, 2012.

[130] J. Antonello, *Optimization-based wavefront sensorless adaptive optics for microscopy*. PhD thesis, Techniche Universiteit Delft, 2014.

[131] M. Rueckel, J. A. Mack-Bucher., and W. Denk, "Adaptive wavefront correction in two-photon microscopy using coherence-gated wavefront sensing," in *Proceedings of the National Academy of Sciences*, vol. 103, pp. 17137–17142, 2006.

[132] T. I. M. van Werkhoven, J. Antonello, H. H. Truong, M. Verhaegen, H. C. Gerritsen, and C. U. Keller, "Snapshot coherence-gated direct wavefront sensing for multi-photon microscopy," *Optics Express*, vol. 22, no. 8, p. 9715, 2014.

[133] C. Bourgenot, C. D. Saunter, G. D. Love, and J. M. Girkin, "Comparison of closed loop and sensorless adaptive optics in widefield optical microscopy," *Journal of the European Optical Society: Rapid Publications*, vol. 8, no. 0, p. 13027, 2013.

[134] S. A. Rahman and M. J. Booth, "Direct wavefront sensing in adaptive optical microscopy using backscattered light," *Applied Optics*, vol. 52, no. 22, p. 5523, 2013.

[135] J. W. Cha, J. Ballesta, and P. T. C. So, "Shack-Hartmann wavefront-sensor-based adaptive optics system for multiphoton microscopy," *Journal of Biomedical Optics*, vol. 15, no. 4, p. 046022, 2010.

[136] O. Azucena, J. Crest, J. Cao, W. Sullivan, P. Kner, D. Gavel, D. Dillon, S. Olivier, and J. Kubby, "Wavefront aberration measurements and corrections through thick tissue using fluorescent microsphere reference beacons," *Optics Express*, vol. 18, no. 16, pp. 17521–17532, 2010.

[137] X. Tao, O. Azucena, M. Fu, Y. Zuo, D. C. Chen, and J. Kubby, "Adaptive optics microscopy with direct wavefront sensing using fluorescent protein guide stars," *Optics Letters*, vol. 36, no. 17, p. 3389, 2011.

[138] X. Tao, J. Crest, S. Kotadia, O. Azucena, D. C. Chen, W. Sullivan, and J. Kubby, "Live imaging using adaptive optics with fluorescent protein guide-stars," *Optics Express*, vol. 20, no. 14, pp. 15969–15982, 2012.

[139] X. Tao, Z. Dean, C. Chien, O. Azucena, D. Bodington, and J. Kubby, "Shack-Hartmann wavefront sensing using interferometric focusing of light onto guidestars," *Optics Express*, vol. 21, no. 25, p. 31282, 2013.

[140] H. W. Yoo, S. Ito, M. Verhaegen, and G. Schitter, "Iterative Learning Control of a Galvanometer Scanner for Fast and Accurate Scanning Laser Microscopy," in *Mechatronics 2012, 17-19 Sep, Linz, Austria*, pp. 537–543, 2012.

[141] H. W. Yoo, S. Ito, M. Verhaegen, and G. Schitter, "Transformation-based iterative learning control for non-collocated sensing of a galvanometer scanner," in *2013 European Control Conference (ECC)*, pp. 1204–1209, IEEE, July 2013.

[142] H. W. Yoo, M. Verhaegen, M. E. van Royen, and G. Schitter, "Automated adjustment of aberration correction in scanning confocal microscopy," in *IEEE International Instrumentation and Measurement Technology Conference*, pp. 1083–1088, 2012.

[143] H. W. Yoo, M. E. van Royen, W. A. van Cappellen, A. B. Houtsmuller, M. Verhaegen, and G. Schitter, "Automated spherical aberration correction in scanning confocal microscopy," *Review of Scientific Instruments*, vol. 85, p. 123706, Dec. 2014.

[144] R. P. Aylward, "Advanced galvanometer-based optical scanner," *Sensor review*, vol. 23, no. 3, p. 2160222, 2003.

[145] E. Meijering, I. Smal, and G. Danuser, "Tracking in molecular bioimaging," *IEEE Signal Processing Magazine*, vol. 23, no. 3, pp. 46–53, 2006.

[146] O. Trepte and A. Liljeborg, "Computer control for a galvanometer scanner in a confocal scanning laser microscope," *Optical Engineering*, vol. 33, no. 11, pp. 3774–3780, 1994.

[147] Leica Microsystems, *Leica TCS SP5 User Manual*. Order No.: 156500002.

[148] J.-Y. Yen, Y.-C. Yeh, Y.-H. Peng, and J.-F. Lee, "Application of the continuous no-reset switching iterative learning control on a novel optical scanning system," *Mechatronics*, vol. 19, pp. 65–75, 2009.

[149] R. M. Schmidt, G. Schitter, A. Rankers, and J. van Eijk, *The design of high performance mechatronics: high-tech functionality by multidisciplinary system integration*. Delft University Press, 2nd ed., 2014.

[150] S. Skogestad and I. Postlethwaite, *Multivariable feedback control: analysis and design*. John Wiley & Sons, Ltd, 2nd ed., 2005.

[151] M. Tomizuka, "Zero phase error tracking algorithm for digital control," *Jounal of Dynamic Systems, Measurement, and Control*, vol. 109, pp. 65–68, 1987.

[152] Z. Cai, C. T. Freeman, P. L. Lewin, and E. Rogers, "Iterative learning control for a non-minimum phase plant based on a reference shift algorithm," *Control Engineering Practice*, vol. 16, pp. 633–643, 2008.

[153] D. A. Bristow, M. Tharayil, and A. G. Alleyne, "A survey of iterative learning control: a learning based method for high-performance tracking control," *IEEE Control System Magazine*, vol. 26, no. 3, pp. 96–114, 2006.

[154] M. Norrlöf and S. Gunnarsson, "Time and frequency domain convergence properties in iterative learning control," *International Journal of Control*, vol. 75, no. 14, pp. 1114–1126, 2002.

[155] B. P. Rigney, L. Y. Pao, and D. A. Lawrence, "Nonminimum Phase Dynamic Inversion for Settle Time Applications," *IEEE Transactions on Control Systems Technology*, vol. 17, pp. 989–1005, Jan. 2009.

[156] J. T. Wen and B. Potsaid, "An experimental study of a high performance motion control system," in *American Control Conference*, (Boston, MA, USA), pp. 5158–5163, IEEE, Feb. 2004.

[157] J. A. Butterworth, L. Y. Pao, and D. Y. Abramovitch, "Analysis and comparison of three discrete-time feedforward model-inverse control techniques for nonminimum-phase systems," *Mechatronics*, vol. 22, pp. 577–587, Aug. 2012.

[158] K. J. Åström and T. Hägglund, *Advanced PID Control*. ISA - The Instrumentation, Systems, and Automation Society; Research Triangle Park, NC 27709, 2006.

[159] J. A. Butterworth, L. Y. Pao, and D. Y. Abramovitch, "A Discrete-Time Single-Parameter Combined Feedforward/Feedback Adaptive-Delay Algorithm With Applications to Piezo-Based Raster Tracking," *IEEE Transactions on Control Systems Technology*, vol. 20, pp. 416–423, Mar. 2012.

[160] G. E. Fantner, P. Hegarty, J. H. Kindt, G. Schitter, G. A. G. Cidade, and P. K. Hansma, "Data acquisition system for high speed atomic force microscopy," *Rev. of Sci. Instrum.*, vol. 76, p. 026118, Jan. 2005.

[161] A. J. Fleming and A. G. Wills, "Optimal periodic trajectories for band-limited systems," *IEEE Trans. on Control Syst. Technol.*, vol. 17, pp. 552–562, May 2009.

[162] N. C. Singer and W. P. Seering, "Using acausal shaping techniques to reduce robot vibration," in *Proc. of the IEEE International Conference on Robotics and Automation*, vol. 3, pp. 1434–1439, 1988.

[163] W. Singhose, "Command Shaping for Flexible Systems: A Review of the First 50 Years," *Int. J. Preccision Engineering and Manufacturing*, vol. 10, no. 4, pp. 153–168, 2009.

[164] G. Schitter, P. J. Thurner, and P. K. Hansma, "Design and input shaping control of a novel scanner for high-speed atomic force microscopy," *Mechatronics*, vol. 18, pp. 282–288, 2008.

[165] F. P. Martial and N. A. Hartell, "Progammable illumination and high-speed, multi-wavelength, confocal microscopy using digital micromirror," *PLOS ONE*, vol. 7, no. 8, p. e43942, 2012.

[166] J. Wallén, M. Norrlöf, and S. Gunnarsson, "A Framework for analysis of observer-based-ILC," *Asian Journal of Control*, vol. 13, no. 1, pp. 1–12, 2011.

[167] J. Wallén, I. Dressler, A. Robertsson, M. Norrlöf, and S. Gunnarsson, "Observer-based ilc applied to the gantry-tau parallel kinematic robot," in *Proceedings of 18th IFAC World Congress*, (Milano, Italy), pp. 992–998, Aug. 2011.

[168] B. A. Francis and W. M. Wonham, "The internal model principle of control theory," *Automatica*, vol. 12, pp. 457–465, 1976.

[169] R. M. Schmidt and G. Schitter, *The design of High Performance Mechatronics: High-tech functionality by multidisciplinary system integration*. Delft University Press, 2011.

[170] Y. Wu, Q. Zou, and C. Su, "A current cycle feedback iterative learning control approach for AFM imaging," *IEEE Trans. on NanoTech.*, vol. 8, no. 4, pp. 515–527, 2009.

[171] Leica microsystems, *Glycerol Objective*, April 2004.

[172] M. J. Booth and T. Wilson, "Strategies for the compensation of specimen-induced spherical aberration in confocal microscopy of skin," *J. Microscopy*, vol. 200, no. 1, pp. 68–74, 2000.

[173] M. Shaw, S. Hall, S. Knox, R. Stevens, and C. Paterson, "Characterization of deformable mirror for spherical aberration correction in optical sectioning microscope," *Opt. Express*, vol. 18, no. 7, pp. 6900–6913, 2010.

[174] R. Liang, *Optical Design for Biomedical Imaging*. SPIE Press, 2010.

[175] M. Shimada, Y. Shimada, and H. Kitagawa, 2003. US Patent 6,563,634.

[176] M. Karasawa, A. Yoshikawa, and K. Hayashi, 2010. US Patent 7,825,360.

[177] W. Knebel, T. Bauer, and P. Euteneuer, 21 January 2014. US Patent 8,724,103.

[178] C. Monks, "Optical spherical aberration correction," *Imaging and Microsc.*, vol. 3, pp. 2–3, 2004.

[179] M. Schwertner, M. J. Booth, and T. Wilson, "Simple optimization procedure for objective lens correction collar setting," *Journal of microscopy*, vol. 217, no. 3, pp. 184–187, 2004.

[180] P. Török, P. Varga, Z. Laczik, and G. R. Booker, "Electromagnetic diffraction of light focused through a planar interface between materials of mismatched refractive indices: an integral representation," *J. Opt. Soc. Am. A*, vol. 12, no. 2, pp. 325–332, 1995.

[181] M. J. Booth and T. Wilson, "Refractive-index-mismatch induced aberrations in single-photon and two-photon microscopy and the use of aberration correction," *Journal of Biomedical Optics*, vol. 6, no. 3, pp. 266–272, 2001.

[182] K. Carlsson, "The influence of specimen refractive index, detector signal integration, and non-uniform scan speed on the imaging properties in confocal microscopy," *J. Microscopy*, vol. 163, no. 2, pp. 167–178, 1991.

[183] W.-L. Chen, Y.-Y. Lee, C.-Y. Chang, H.-M. Huang, T.-C. Lu, and Y.-M. Chang, "Depth-resolved confocal micro-Raman spectroscopy for characterizing GaN-based light emitting diode structures," *Rev. Sci. Instrum.*, vol. 84, p. 113108, Nov. 2013.

[184] D. N. Baldwin and K. J. Batchelder, "Confocal Raman Microspectroscopy through a Planar Interface," *Appl. Spectrosc.*, vol. 55, pp. 517–524, May 2001.

[185] H. L. V. Trees, *Detection, Estimation, and Modulation Theory, Part I*. Wiley-Interscience, 2001.

[186] M. Bravo-Zanoguera, B. von Massenbach, A. L. Kellner, and J. H. Price, "High-performance autofocus circuit for biological microscopy," *Rev. Sci. Instrum.*, vol. 69, no. 11, pp. 3966–3977, 1998.

[187] A. Buffington, F. S. Crawford, R. A. Muller, A. J. Schwemin, and R. G. Smits, "Correction of atmospheric distortion with an image-sharpening telescope," *J. Opt. Soc. Am.*, vol. 67, no. 3, pp. 298–303, 1977.

[188] L. P. Murray, J. C. Dainty, and E. Daly, "Wavefront correction through image sharpness maximisation," *Proc. SPIE Opto-Ireland 2005: Imaging and Vision*, vol. 5823, no. 40, 2005.

[189] Y. Sun, S. Duthaler, and B. J. Nelson, "Autofocusing in computer microscopy: Selecting the optimal focus algorithm," *Microsc. Res. and Techniq.*, vol. 65, no. 3, pp. 139–149, 2004.

[190] R. K. Tyson, *Principles of Adaptive Optics*. CRC Press, 3rd ed., 2011.

[191] K. Drabek, M. van Ham, T. Stepanova, K. Draegestein, R. van Horssen, C. L. Sayas, A. Akhmanova, T. ten Hagen, R. Smits, R. Fodde, F. Grosveld, and N. Galjart, "Role of CLASP2 in Microtubule Stabilization and the Regulation of Persistent Motility," *Current Biology*, vol. 16, no. 22, pp. 2259–2264, 2006.

[192] C. Conde and A. Cáceres, "Microtubule assembly, organization and dynamics in axons and dendrites," *Nature Reviews Neuroscience*, vol. 10, no. 5, pp. 319–332, 2009.

[193] M. E. van Royen, W. A. van Cappellen, C. de Vos, A. B. Houtsmuller, and J. Trapman, "Stepwise androgen receptor dimerization," *J. Cell Sci.*, vol. 125, pp. 1970–1979, 2012.

[194] M. E. van Royen, S. M. Cunha, M. C. Brink, K. A. Mattern, A. L. Nigg, H. J. Dubbink, P. J. Verschure, J. Trapman, and A. B. Houtsmuller, "Compartmentalization of androgen receptor protein-protein interactions in living cells," *J. Cell Biol.*, vol. 177, pp. 63–72, 2007.

[195] T. van Werkhoven, H. Truong, J. Antonello, R. Fraanje, H. Gerritsen, M. Verhaegen, and C. Keller, "Coherence-gated wavefront sensing for microscopy using fringe analysis," *Proc. SPIE 8253, MEMS Adaptive Optics VI*, pp. 82530E–82530E–7, Feb. 2012.

[196] M. Shaw, K. O'Holleran, and C. Paterson, "Investigation of the confocal wavefront sensor and its application to biological microscopy," *Optics Express*, vol. 21, no. 16, pp. 19353–19362, 2013.

[197] F. Roddier, *Adaptive optics in astronomy*. Cambridge University Press, 1999.

[198] M. Schwertner, M. J. Booth, and T. Wilson, "Characterizing specimen induced aberrations for high NA adaptive optical microscopy," *Optics Express*, vol. 12, no. 26, pp. 6540–6552, 2004.

[199] M. Schwertner, M. J. Booth, M. A. A. Neil, and T. Wilson, "Measurement specimen-induced aberration of biological samples using phase stepping interferometry," *Journal of microscopy*, vol. 213, no. 1, pp. 11–19, 2004.

[200] J. Zeng, P. Mahou, M.-C. Schanne-Klein, E. Beaurepaire, and D. Débarre, "3D resolved mapping of optical aberrations in thick tissues," *Biomedical Optics Express*, vol. 3, no. 8, p. 1898, 2012.

[201] J. Schmitt and G. Kumar, "Turbulent nature of refractive index variation in biological tissue," *Optics Letter*, vol. 21, no. 16, 1996.

[202] P. Wang, R. K. Bista, W. Qui, W. E. Khalbuss, L. Zhang, R. E. Brand, and Y. Liu, "An insight into statistical refractive index properties of internal structure via low coherence statistica amplitude microscopy," *Optics Express*, vol. 18, no. 21, 2010.

[203] G. Vdovin, O. Soloviev, M. Loktev, S. Savenko, and L. Dziechciarczyk, "Optimal correction and feedforward control of low-order aberrations with piezoelectric and membrane deformable mirrors," in *SPIE Optical Engineering + Applications*, pp. 81650W–81650W–10, SPIE, Sept. 2011.

[204] S. A. Rahman and M. J. Booth, "Adaptive optics for high-resolution microscopy: wave front sensing using back scattered light," in *MEMS Adaptive Optics VI,*, Nov. 2012.

[205] A. Edelstein, N. Amodaj, K. Hoover, R. Vale, and N. Stuurman, *Computer Control of Microscopes Using μManager, in Current Protocols in Molecular Biology*. John Wiley & Sons, Inc., 2010.

[206] J. Engelhardt, H. Gugel, and H. Ulrich, "Optical arrangement provided for a spectral fanning out of a light beam," us patent 6801359, 10 2004.

[207] R. Henriques, M. Lelek, E. F. Fornasiero, F. Valtorta, C. Zimmer, and M. M. Mhlanga, "QuickPALM: 3D real-time photoactivation nanoscopy image processing in ImageJ," *nAture methods*, vol. 7, pp. 339–340, May 2010.

[208] T. Wilson and A. R. Carlini, "Three-dimensional imaging in confocal imaging systems with finite sized detectors," *Journal of microscopy*, vol. 149, pp. 51–66, Aug. 1988.

[209] M. A. R. Jewel, V. Akondi, and B. Vohnsen, "On pinhole size optimization in wavefront sensorless adaptive optics," in *Adaptive Optics: Methods, Analysis and Applications*, (Washington, D.C.), p. OTu1A.3, OSA, 2013.

[210] H. Song, R. Fraanje, G. Schitter, G. Vdovin, and M. Verhaegen, "Controller Design for a High-Sampling-Rate Closed-Loop Adaptive Optics System with Piezo-Driven Deformable Mirror," *European Journal of Control*, vol. 17, pp. 290–301, Jan. 2011.

[211] H. Song, *Model-based Control in Adaptive Optical Systems*. PhD thesis, Techniche Universiteit Delft, 2011.

[212] G.-m. Dai, "Modified Hartmann-Shack Wavefront Sensing and Iterative Wavefront Reconstruction," *SPIE Vol. 2201 Adaptive Optics in Astronomy (1994)*, pp. 1–12, Jan. 1994.

[213] M. Rueckel, J. A. Mack-Bucher, and W. Denk, "Adaptive wavefront correction in two-photon microscopy using coherence-gated wavefront sensing," *Proceedings of the National Academy of Sciences*, vol. 103, pp. 17137–17142, Nov. 2006.

[214] M. Gu, *Advanced Optical Imaging Theory*. Springer, 2000.

[215] A. J. Wright, D. Burns, B. A. Patterson, S. P. Poland, G. J. Valentine, and J. M. Girkin, "Exploration of the optimisation algorithms used in the implementation of adaptive optics in confocal and multiphoton microscopy," *Microscopy Research and Technique*, vol. 67, no. 1, pp. 36–44, 2005.

[216] J. W. Goodman, *Introduction to fourier optics*. Roberts & Company Publishers, 3rd ed., 2005.

[217] P. C. Hansen, "Deconvolution and Regularization with Toeplitz Matrices - Springer," *Numerical Algorithms*, vol. 29, no. 4, pp. 323–378, 2002.

[218] M. A. A. Neil, M. J. Booth, and T. Wilson, "New modal wave front sensor: A theoretical analysis," *Journal of the Optical Society of America A: Optics, Image Science and Vision*, vol. 17, pp. 1098–1107, 2000.

[219] M. A. A. Neil, M. J. Booth, and T. Wilson, "Closed-loop aberration correction using a modal Zernike wave-front sensor," *Optic Letters*, vol. 25, pp. 1083–1085, 2000.

[220] M. J. Booth, M. A. A. Neil, R. Juskaitis, and T. Wilson, "Adaptive aberration correction in a confocal microscope," in *Proceedings of the National Academy of Sciences*, vol. 99, pp. 5788–5792, 2002.

[221] J. L. Beverage, R. V. Shack, and M. R. Descour, "Measurement of the three-dimensional microscope point spread function using a Shack-Hartmann wavefront sensor," *Journal of microscopy*, vol. 205, pp. 61–75, Jan. 2002.

[222] F. J. Rigaut, J.-P. Véran, and O. Lai, "Analytical model for Shack-Hartmann-based adaptive optics systems," in *Astronomical Telescopes & Instrumentation* (D. Bonaccini and R. K. Tyson, eds.), pp. 1038–1048, SPIE, Sept. 1998.

[223] T. A. Rhoadarmer, J. D. Barchers, and E. J. Spillar, "Complex field reconstruction using gradient and intensity measurements from a Shack-Hartmann wave front sensor," in *International Symposium on Optical Science and Technology* (R. K. Tyson, D. Bonaccini, and M. C. Roggemann, eds.), pp. 233–244, SPIE, Feb. 2002.

[224] P. C. Hansen, J. G. Nagy, and D. P. O'leary, *Deblurring images: matrices, spectra, and filtering*, vol. 3. Siam, 2006.

[225] P. C. Hansen, "Regularization Tools version 4.0 for Matlab 7.3," *Numerical Algorithms*, vol. 46, pp. 189–194, Nov. 2007.

[226] D. Voelz, *Computational Fourier Optics A Matlab Tutorial*. SPIE Press, Aug. 2011.

[227] "FluoSpheres® Carboxylate-Modified Microspheres, 0.2 μm, crimson fluorescent (625/645), 2% solids." https://www.lifetechnologies.com/order/catalog/product/F8806.

[228] S. Vieira, "The behavior and calibration of some piezoelectric ceramics used in the STM," *IBM Journal of Research and Development*, vol. 30, pp. 553–556, Sept. 1986.

[229] C. V. Newcomb and I. Flinn, "Improving the linearity of piezoelectric ceramic actuators," *Electronics Letters*, vol. 18, no. 11, p. 442, 1982.

[230] H. Kaizuka and B. Siu, "A Simple Way to Reduce Hysteresis and Creep When Using Piezoelectric Actuators," *Japanese Journal of Applied Physics*, vol. 27, pp. L773–L776, May 1988.

[231] K. R. Koops, P. M. L. O. Scholte, and W. L. de Koning, "Observation of zero creep in piezoelectric actuators," *Applied Physics A: Materials Science & Processing*, vol. 68, pp. 691–697, June 1999.

[232] H. Jung, J. Y. Shim, and D. Gweon, "Tracking control of piezoelectric actuators," *Nanotechnology*, vol. 12, pp. 14–20, Jan. 2001.

[233] R. Changhai and S. Lining, "Hysteresis and creep compensation for piezoelectric actuator in open-loop operation," *Sensors and Actuators A: Physical*, vol. 122, pp. 124–130, July 2005.

[234] H. Song, G. Vdovin, R. Fraanje, G. Schitter, and M. Verhaegen, "Extracting hysteresis from nonlinear measurement of wavefront-sensorless adaptive optics system," *Optics Letters*, vol. 34, no. 1, pp. 61–63, 2009.

[235] C. Vogel, "Hysteresis modeling and go-to control of deformable mirrors in adaptive optics," in *IEEE Aerospace Conference 2012*, pp. 1 – 5, 2012.

[236] R. J. Noll, "Zernike polynomials and atmospheric turbulence," *Journal of the Optical Society of America*, vol. 66, no. 3, pp. 207–211, 1976.

[237] V. N. Mahajan, "Zernike Circle Polynomials and Optical Aberrations of Systems with Circular Pupils," *Applied Optics*, vol. 33, no. 34, pp. 8121–8124, 1994.

Appendix A

Specimen Preparation Protocol with Fluorescence Beads

To determine aberrations via fluorescence, which are introduced by cells or tissue, several types of specimen with fluorescence beads have been developed. These protocol are provided with courtesy of Martin E. van Royen.

Fluorescent beads directly on glass

Several dilutions of fluorescent beads (FluoSpheres Carboxylate-Modified Microspheres, 0.2 μm, crimson fluorescent (625/645), 2% solid, Life Technologies, Carlbad, CA, USA) are added to 1 *ml* Dulbecco's Phosphate Buffered Saline (DPBS) in a well of a Polystyrene 6 Wells Cell Culture Cluster (Corning B.V. Life Sciences, Schiphol-Rijk, Netherlands) that contains a Ø24 *mm* coverglass (thinkness: $0.13-0.16$ *mm* (#1.5) Menzer-Gläser/Menzel Gerhard GmbH, Braunschweig, Germany). The beads are allowed to spread over the cover glass for 30 minutes and embedded in Vectashield (Vector Laboratories, Inc. Burlingame, US) and mounted to a glass microscope slide for imaging.

Fluorescent beads in a polyacrylamide gel (Fig. 1.4)

Fluorescent beads (FluoSpheres Carboxylate-Modified Microspheres, 0.2 μm, crimson fluorescent (625/645), 2% solid, Life Technologies, Carlbad, CA, USA) are rapidly mixed with a 20% polyacrylamide gel and allowed to polymerize in a well of a 8 wells chambered coverglass (Lab-Tek^{TM}Chambered Coverglass, Thermo Scientific Inc., Waltham, MA, US). Alternatively, custom made plastic spacers (~ 0.75 *mm*) with a round spacing in the center are glued to a microscope slide to generate a well. The mix of fluorescent beads in polyacrylamide gel is poured in the generated well, covered with a Ø24 *mm* coverglass (thinkness: $0.13-0.16$*mm* (#1.5) Menzer-Gläser / Menzel Gerhard GmbH, Braunschweig, Germany) and allowed to polymerize.

Fluorescent beads on a cell monolayer

Human hepatocellular carcinoma cells (Hep3B cells) are grown on Ø24 *mm* coverglasses (thinkness: 0.13-0.16 mm (#1.5) Menzer-Gläser/Menzel Gerhard GmbH, Braunschweig, Germany) for minimally 16 hours to a confluency of $\sim$70% in Alfa Minimal Essential Medium (αMEM-Bio-Whittaker/Cambrex, Verviers, Belgium) supplemented with 2 *mM* L-glutamine (Bio-Whitaker/Cambex), 100 U/ml Penicillin / 100 $\mu g/ml$ Streptomycin (Bio-Whitaker/Cambrex) and 5% triple 0.1 μM sterile filtered fetal bovine serum (HyClone, South Logan, UT). Similarly as for fluorescent beads on glass, beads are spread over the cell monolayer, allowed to adhere to the cells for 1 hour, after which the cells are fixed with 4% paraformaldehyde (PFA). After fixation the coverslip is embedded in Vectashield and mounted to a glass microscope slide, as described above.

Fluorescent beads covering cellular spheroids (Fig. 6.6)

Human hepatocellular carcinoma cells (Hep3B cells) are grown in 25 cm^2 cell culture flasks with an ultra-low attachment surface to allow the growth of cells in spheroid formation. After 2-7 days the culture with spheroids are centrifuged at 1000rpm and the pellet is re-suspended in 500 μl αMEM culture medium and added to a glass coverslip with a 70% confluent Hep3B cell monolayer (as above). The spheroids are allowed to attach to the cells for maximally 2 hours. After 1 hour fluorescent beads are spread over the cells covering both the cell monolayer as well the attached cell spheroids. After attachment of cell sheroids and fluorescent beads, the samples are fixed with 4% paraformaldehyde for 1-2 hours, washed with DPBS, embedded in Vectashield and mounted to microscope slide with a ($\sim$ 0.75 *mm*) custom made spacer, as described above.

Absorption and emission spectra of fluorescence beads

Fig. A.1 shows an excitation and emission spectrum of red fluorescence beads (FluoSpheres Carboxylate-Modified Microspheres, 0.2μm, crimson fluorescent (625/645), used in the experiments.

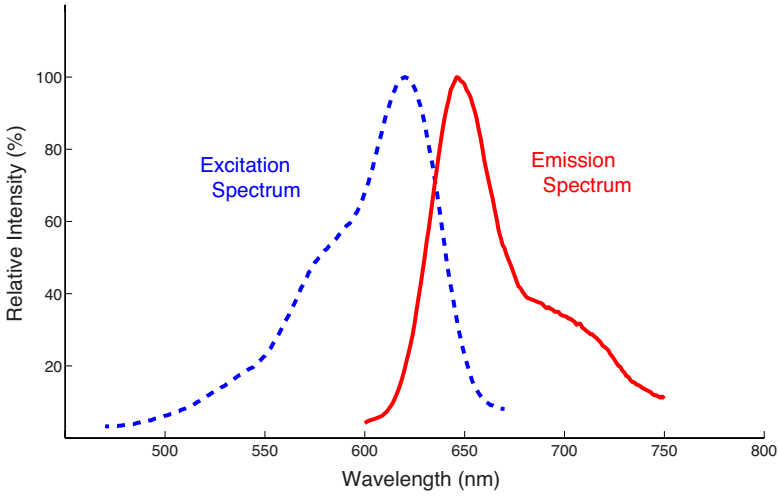

Figure A.1: Excitation and emission spectrum of FluoSpheres Carboxylate-Modified Microspheres, 0.2 μm, crimson fluorescent (625/645) [227].

Appendix B

Nonlinearities of Piezoelectric Deformable Mirror

Since the DM uses piezoelectric actuators, there are innate nonlinearities such as hysteresis and creep during the manipulation of the DM. Hysteresis of PDM shows the generated aberrations from the given input is not a function of the current input only, but also of the previous input trajectory and the current mirror shape. As a result, the wavefront of the PDM in open loop control, also known as feedforward control, usually have errors which is not easy to compensate. Fig. B.1(a) shows a measurement of defocus of PDM by change only the 1st piezoelectric actuator at the center of pupil. About 1 μm peak to peak defocus error is observed by the overall 8 μm peak to peak defocus actuation. Regarding other 18 actuators on the concentric circles, similar hysteresis is expected which causes a wavefront error during the open-loop control.

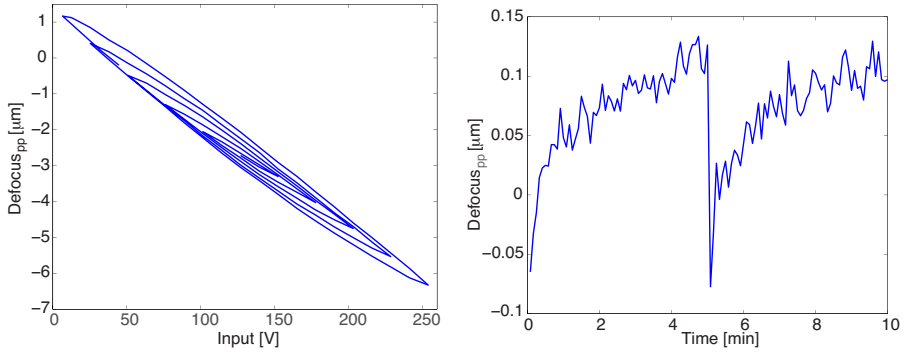

(a) Hysteresis (b) Creep

Figure B.1: Nonlinearities of the piezoelectric deformable mirror via defocus measurements

Creep of the piezo actuator also results in wavefront correction error. Creep is a slow drift of actuator without change of the input voltage, mainly caused by the remnant polar-

izations in piezoelectric material. [228] The change of creep is known as a logarithmically linear in time. Fig B.1(b) shows the change of defocus due to the creep of PDM, while a closed loop control for flattening the PDM is being applied every 5 minutes. For 5 minutes, 0.2 μm peak to peak defocus changes due to the creep of PDM while its logarithmical behavior in time clearly observed.

A simple way to reduce this hysteresis and creep is a closed loop control by monitoring the displacement of actuator directly and applying the error correction promptly. In some cases, however, this direct displacement measurement of the piezoelectric actuator is not available and is usually expensive if available. A number of solutions for compensating these nonlinearities of piezo actuators has been proposed such as a charge control [229, 230], input trajectory shaping [231], nonlinear model inversion[232, 233]. Especially regarding PDM, an hysteresis compensation algorithm based on an nonlinear inversion [99, 234, 235] and degaussing [203] are reported.

Appendix C

Zernike Polynomials

Zernike Polynomials

Zernike polynomials are a smooth orthogonal basis set for the two dimensional circular domain. For the circular aperture, the wavefront aberrations are usually approximated with the finite set of Zernike modes [197, 236]. For polar coordinates (ρ,θ), $\rho \in [0,1]$ and $\theta \in [0,2\pi]$, the Zernike polynomials can be defined as

$$Z_n^m(\rho,\theta) = \begin{cases} N_n^m R_n^{|m|}(\rho)\cos m\theta & m \geq 0 \\ -N_n^m R_n^{|m|}(\rho \sin m\theta & m < 0 \end{cases} \tag{C.1}$$

where n is the radial order, $n = 0,\ 1,\ 2,\ \cdots$, m is the azimuth order $m = 2k-n$, i.e. $m = -n,\ -n+2,\ -n+4,\ \cdots,\ n$ and

$$N_n^m = \sqrt{\frac{2(n+1}{1+\delta_{m=0}}} \tag{C.2}$$

$$R_n^{|m|}(\rho) = \sum_{s=0}^{(n-|m|)/2} \frac{(-1)(n-s)!}{s!(0.5(n+|m|)-s)!(0.5(n-|m|)-s)!}\rho^{n-2s} \tag{C.3}$$

Based on the orthogonality of the basis, the aberration can be represented by the weighted sum of the Zernike polynomials as,

$$\Phi(\rho,\theta) = \sum_n \sum_m W_n^m Z_n^m(\rho,\theta) \tag{C.4}$$

where $W_n^m \in \mathbb{R}$ are weight of the Zernike Modes. These weights can be a reasonable finite approximation of the phase of the 2D pupil function. By the orthonormality of Zernike polynomials, the root mean square wavefront error can be defined as [197]

$$\sigma = \sqrt{\sum_n \sum_m W_n^m}. \tag{C.5}$$

Table C.1: Zernike polynomials until 15th mode

Name	n	m	Zernike Mode
Piston	0	0	$Z_1 = 1$
Tip/Tilt	1	1	$Z_2 = 2\rho\cos\theta$ $Z_3 = 2\rho\cos\theta$
Defocus	2	0	$Z_4 = \sqrt{3}(2\rho^2 - 1)$
Astigmatism	2	2	$Z_5 = \sqrt{6}\rho^2\sin 2\theta$ $Z_6 = \sqrt{6}\rho^2\cos 2\theta$
Coma	3	1	$Z_7 = \sqrt{8}(3\rho^3 - 2r)\sin\theta$ $Z_8 = \sqrt{8}(3\rho^3 - 2r)\cos\theta$
Trepoly	3	3	$Z_9 = \sqrt{8}\rho^3\sin 3\theta$ $Z_{10} = \sqrt{8}\rho^3\cos 3\theta$
Spherical	4	0	$Z_{11} = \sqrt{5}(6\rho^4 - 6\rho^2 + 1)$
Astigmatism (2nd)	4	2	$Z_{12} = \sqrt{10}(10\rho^4 - 3\rho^2)\sin 2\theta$ $Z_{13} = \sqrt{10}(10\rho^4 - 3\rho^2)\cos 2\theta$
Tetrapoly	4	4	$Z_{14} = \sqrt{10}\rho^4\sin 4\theta$ $Z_{15} = \sqrt{10}\rho^4\cos 4\theta$

In practice, Noll's index, Z_i, which starts from the lower order to the higher order of radial order and azimuth order, is used instead of Z_n^m [236, 237]. Table. C.1 shows the first 15th mode from piston.

General Pupil Representation by Zernike Polynomials

The pupil function, a complex function with both intensity and phase variations, can be generally expressed with Zernike polynomials both real and imaginary part as

$$P(\vec{\xi}, W) \quad = \quad e^{-j\kappa\sum_{i=1}^{N_z} W_i Z_i(\vec{\xi})}, \tag{C.6}$$

where $W = [W_1\ W_2\ \cdots\ W_{N_z}]$ are a complex coefficient vector associated with a Zernike polynomials Z_j where $j \leq N_z$ is Noll's index. The real part of the β_j denotes the aberrations in the pupil while the imaginary part represent the amplitude fluctuation of the pupil.

Glossary

List of symbols and notations

Below follows a list of the most frequently used symbols and notations in this thesis. Symbols particular to power network applications are explained only in the relevant chapters.

x, y, z	Lateral and axial position of image
r	Angular position of coverslip correction ring
j	$\sqrt{-1}$
J	Performance index
$\theta_i(t),\ \Theta_i(s)$	Angle of ith inertia and its trenasfer function
$J_1,\ J_2,\ J_3$	Inertia
k_l, k_{12}, k_{13}	Stiffness coefficients
b_l, b_{12}, b_{13}	Damping coefficients
$\mathbf{x}, \mathbf{y}, \mathbf{u}, \mathbf{e}$	Vectors (scalar) of state, output, input, and error
$\mathbf{s}$	Centroid output of Shack Hartmann wavefront sensor
$\mathbf{y}^{ref}$	Output tracking reference
$\mathbf{u}^i, \mathbf{y}^i, \mathbf{y}^i_m, \mathbf{y}^i_c$	input and output at trial i
$\mathbf{e}^i, \mathbf{e}^i_m, \mathbf{e}^i_c$	error at trial i
$\mathbf{w}, \mathbf{v}$	Disturbance to the input and measurement noise to output
$B(\mathrm{z}), A(\mathrm{z})$	Numerator and denominator of transfer function
s	Complex frequency variable for Laplace transform
ω	frequency variable for Fourier transform
k	Index of time
q	Delay operator
z	Complex frequency variable for Z transform
P, P_m, P_c	Galvanometer model
$H(q), H(\mathrm{z}), H(j\omega)$	Reference transformation filter
L	Learning filter
Q	Q-filter
$I_i, I_f, I_{xy},$	Light Intensity
κ	Wavenumber
f, f_1, f_c	focus position
γ	a ratio between two media
ζ	Reflectance
β	Radial coordinate

I_0, I_1, I_2	Diffraction integrals
n, n_1, n_2, n_3	Refractive index
Ψ	Aberration function
B, C, E	Influence, geometry, reconstruction matrices
K	Control gain matrices
P_{in}, P_{out}	A complex pupil function of input pupil and output pupil
$\mathcal{P}$	Fourier transform of the complex pupil function
$\vec{\xi}$, $\vec{r}$, $\vec{\rho}$	2D coordination of the pupil/focus/image plane
Y, Y_d	Measured vectorized output pupil function
X	Vectorized input pupil function
$H_{\mathbf{i},\mathbf{k}}$	**i**-th and **j**-th element of matrix H
$\gamma_m = [\gamma_x(m)\ \gamma_y(m)]$	m-th pinhole size
rect	Rectangle function
sinc	Sinc function
vec	Matrix to vector operator
$\otimes$	Kronecker product

List of abbreviations

The following abbreviations are used in this thesis:

3D	Three Dimensional
AdPH	Adjustable Pinhole
AFM	Atomic Force Microscopy (AFM)
AO	Adaptive Optics
AOD	Acousto-Optic Deflectors
AR	Androgen Receptor
AU	Airy Unit
AWGN	Additive White Gaussian Noise
CCD	Charge Coupled Device
CLSM	Confocal Laser Scanning Microscopy
CMR	Convallaria Majalis Rhizome
DcM	Dichroic Mirror
DM	Deformable Mirror
FIR	Finite Impulse Response
FWHM	Full Width at Half Maximum
GF/MGF	Gaussian Fitting / Mixed Gaussian Fitting
GFP/YFP/CFP	Green/Yellow/Cyan Fluorescence Protein
GP	Gold Particles
ILC	Iterative Learning Control
LGS	Laser Guide Star
LP	Long Pass filter
MEFs	Mouse Embryonic Fibroblasts
MFP	Multi functional port
NA	Numerical Aperture
NSOM/SNOM	Near-field scanning optical microscopy

PALM	Photoactivated Localization Microscopy
PD	Proportional-Derivative
PDM	Piezoelectric Deformable Mirror
PH	Pinhole
PMT	Photomultiplier Tube
PSD	Position Sensitive Detector
PSF	Point Spread Function
QE	quantum efficiency
RC	Repetitive Control
RMS	Root Mean Square
SHWFS	Shack Hartmann Wavefront Sensor
SIM	Structured Illumination Microscopy
SISO	Single Input Single Output
SNR	Signal to Noise Ratio
SP	Short Pass filter
SPM	Scanning Probe Microscopy
STD	Standard Deviation
STED	Stimulated Emission Depletion
STORM	Stochastic Optical Reconstruction Microscopy
SVD	Singular Value Decomposition
TIRF	total internal reflection fluorescence
TLD/RLD	Transmission Light Detector / Reflection Light Detector
TSVD	Truncated SVD
WF	Wavefront
WFS	Wavefront Sensor

Summary

Optomechatronics Design and Control for Confocal Laser Scanning Microscopy

Han Woong Yoo

Confocal laser scanning microscopy (CLSM) is considered as one of the major advancements in microscopy in the last century and is widely accepted as a 3D fluorescence imaging tool for biological studies. For the emerging biological questions CLSM requires fast imaging to detect rapid biological processes and aberration-corrected imaging to localize the targeted biomolecule precisely through optical disturbances by specimen. In this thesis, optomechatronics design and control are discussed for improving this temporal and spatial resolution of CLSM to respond the needs in biological research.

To improve temporal resolution of CLSM imaging, the scanning speed has to be improved. For galvanometer scanners as the most popular scanner of commercial CLSM, iterative learning control (ILC) is proposed to achieve a high speed, linear, and accurate bidirectional scanning control. Two stable inversion methods of zero phase shifts and phase fitting by input delays are used for designing stable ILCs enabling a wide control bandwidth. Experimental results verify the benefits of ILCs allowing a faster scanning over 2000 lines per second with high accuracy without a phase lag and a gain mismatch, achieving up to a 73 times smaller root mean square (RMS) error than a conventional feedback controller.

Although the encoder measurements follow the reference signal by the developed ILC, actual beam trajectories can have errors at high scanning rates due to non-collocation sensing by the encoder. A transformation-based iterative learning control is proposed to improve the accuracy of fast beam scanning with the non-collocated galvanometer scanner. The proposed ILC is extended from the previous ILC design by adding a reference transformation filter, which is based on the transfer functions between the mirror and the encoder. An error analysis in theory shows that the proposed ILC can reduce the error of the actual mirror angle, especially for the image scanning applications. Experimental results with the proposed transformation based ILC show up to 7.5 times better beam accuracy as compared to the previous ILC.

To improve spatial resolution in CLSM, the spherical aberrations induced by coverslip thickness mismatch have to be corrected. An automated adjustment of the coverslip correction collar is proposed to compensate for the spherical aberrations by means of motorization of the collar with a correction algorithms. An axial image model is derived to suppress noise of the measured axial image and to analyze of the influence of the spherical aberrations by

the coverslip thickness mismatch. To search for the best correction collar adjustment, axial scans of the coverslip reflection are recorded, processed, and evaluated by correction quality measures such as the maximum intensity, sharpness, and entropy. The benefits of the proposed automated correction are demonstrated with various coverslips with biological specimens. The Imaging examples illustrate the improved resolution with sharp and accurate multicolor images of the confocal microscope.

For the general aberration correction in the deep tissue imaging, an adaptive optics (AO) is developed for the commercial CLSM to verify its concept. The AO system consists of a piezoelectric deformable mirror and a Shack Hartmann wavefront sensor (SH-WFS), which measures the wavefront of the fluorescence from the specimen. The wavefront sensor is equipped with an adjustable pinhole for confocal wavefront sensing (CWFS) to confine the optical thickness of wavefront measurements. Using the adjustable pinhole, a referencing method of the SH-WFS and the evaluation of the AO correction quality, pinhole intensity ratio, are proposed. Experimental results with fluorescence beads on the coverslip and $40\mu m$ deep in a sphere cell cluster show that the developed AO system and proposed algorithms with adjustable pinhole can improve the measured full width at half maximum (FWHM). The proposed pinhole intensity ratio using the adjustable pinhole can also show the improvement of imaging quality by the proposed AO.

For CWFS, a small pinhole is desirable for rejecting out-of-focus light while it can degrade the wavefront measurement qualities. A wavefront reconstruction technique is proposed to recover the degraded phase information by the finite size of pinhole. The aberration modification by the pinhole can be modeled as a 2D convolution of the pupil function in complex domain, i.e. phase and intensity of the beam. Based on the Fresnel approximation, the 2D deconvolution problem can be simplified to the 1D deconvolution, which also allows retrieval from multiple measurements by diversified pinhole sizes. With the verified model by experimental results, the simulation results of various pinhole sizes show that the distortion of the output pupil functions by the finite pinhole can be recovered by the proposed retrieval technique, reducing the RMS phase error up to 46 %. The proposed retrieval technique is evaluated for arbitrary aberrations generated from statistics of the wavefront measurements of a biological specimen. Simulation results show that about the wavefront errors level with 3 airy unit (AU) can be achieved by the recovery algorithm and the pupil measurement with 1.5 AU pinhole, allowing an accurate wavefront sensing with higher optical sectioning ability.

Samenvatting

Optomechatronics ontwerp en controle voor confocale laser scanning microscopie

Han Woong Yoo

Confocale laser scanning microscopie (CLSM) wordt gezien als een van de grootste vooruitgangen in microscopie van de afgelopen eeuw, en wordt breed geaccepteerd als een 3D-fluorescentie-beeldvormingstechniek voor biologische studies. Voor de opkomende biologische vraagstukken is snelle beeldvorming met CLSM nodig om snelle biologische processen te kunnen waarnemen.Daarnaast is aberratie-gecorrigeerde beeldvorming nodig om biomoleculen precies te kunnen lokaliseren in optische verstoringen van het monster. Dit proefschrift behandelt het opto-mechatronisch ontwerp en de regeltechniek voor het verbeteren van de temporele en spati ele resolutie van CLSM, om aan de vragen van biologisch onderzoek te voldoen.

Om de temporele resolutie van CLSM te verbeteren moet de scansnelheid worden verhoogd. De meeste commerci ele CLSM systemen gebruiken galvanometers voor het scannen. Voor deze systemen is een iteratief lerende regelstrategie (ILC) voorgesteld om een snelle, lineaire en nauwkeurige scanregeling te verkrijgen in twee richtingen. Twee stabiele inversiemethoden zijn gebruikt om een stabiele ILC te verkrijgen met grote regelbandbreedte, gebaseerd op nul fase verschuiving en het plaatsen van ingangsvertragingen. Experimentele resultaten bevestigen de voordelen van ILC door een snellere scanbeweging van meer dan 2000 lijnen per seconde op hoge nauwkeurigheid zonder faseachterstand of versterkingsfouten. De kwadratisch gemiddelde van de servofout is 73 keer lager dan in geval van een conventionele terugkoppelregelaar.

Hoewel bij ILC de positiesensormetingen het referentiesignaal volgen, kan bij hoge snelheden het werkelijke traject van de bundel fouten bevatten door het niet juist samenvallen van het sensorsignaal met de positie van ontkoppelde massa's. Een transformatiegebaseerde ILC-methode is voorgesteld om de nauwkeurigheid te verbeteren van snelle bundelscans met galvanometers waarbij de spiegelposities niet direct samenvallen met de sensorposities. De voorgestelde ILC-methode is uitgebreid met een referentietransformatiefilter, gebaseerd op een overdrachtsfunctie tussen de spiegel en de positiesensor. Een theoretische foutenanalyse laat zien dat de voorgestelde ILC-methode de hoekfouten van de spiegel kan reduceren, vooral voor de beeldscantoepassingen. Experimentele resultaten met de voorgestelde transformatiegebaseerde ILC- methode laten een verbeterde bundelnauwkeurigheid zien van 7,5 keer ten opzichte van de eerdere ILC-methode.

Om de spati ele resolutie van CLSM te verbeteren zijn de sferische aberraties die voortkomen uit de diktevariaties van het dekglaasje gecorrigeerd. Een geautomatiseerde verstelling van de dekglascorrectiekraag is voorgesteld om te compenseren voor de sferische aberraties met behulp van een gemotoriseerde kraag en een correctie-algoritme. Een axiaal beeldmodel is afgeleid om de ruis te onderdrukken in het gemeten axiale beeld en om te analyseren wat de invloed is van sferische aberraties als gevolg van foutieve diktes van het dekglaasje. Om de juiste correctiekraaginstelling te vinden worden de reflecties van het dekglaasje opgenomen, verwerkt en ge evalueerd op basis van maximumintensiteit, scherpte en entropie. De voordelen van de voorgestelde automatische correctie zijn gedemonstreerd met verschillende dekglaasjes en monsters waarbij verbeterde meerkleuren afbeeldingen zijn verkregen met de confocale microscoop, met hogere resolutie en nauwkeurigheid.

Voor de algehele aberratie correctie in de beeldvorming van diep weefsel is adaptieve optiek (AO) ontwikkeld voor de commerci ele CLSM ter verificatie van het concept. Het AO systeem bevat een piezo-elektrische deformeerbare spiegel en een Shack-Hartmann golffront sensor (SH-WFS), die is geassocieerd met de fluorescentie van het monster. Het AO systeem is uitgerust met een verstelbaar naaldgat voor de confocale golffront sensor (CWFS) om de optische dikte van de golffrontmetingen af te bakenen. Op basis van het verstelbare naaldgat is een referentie methode van de SH-WFS voorgesteld en een evaluatie van de AO correctie kwaliteit, ofwel de naaldgat intensiteit ratio. Experimentele resultaten met fluorescentie kralen op het dekglaasje en 40 μm diep in een bol cel cluster, laten zien dat het ontwikkelde AO systeem en de voorgestelde algoritmen met verstelbare naaldgat de gemeten halfwaardebreedte kunnen verbeteren. Het voorgestelde naaldgat intensiteitsratio op basis van het verstelbare naaldgat kan ook de verbetering van de beeldkwaliteit weergeven van het AO systeem.

Voor de CWFS is een klein naaldgat wenselijk om uit-focus licht te onderdrukken, hoewel dit de kwaliteit van de golffrontmeting kan verstoren. Een golffront reconstructie techniek is voorgesteld om de fase informatie te herstellen die gedegradeerd wordt door de eindige grootte van het naaldgat. De aberratie-verandering door het naaldgat kan gemodelleerd worden als een 2D convolutie van de pupilfunctie in het complexe domein, of wel de fase en intensiteit van de bundel. Op basis van een Fresnel benadering kan het 2D deconvolutie probleem worden vereenvoudigd tot een 1D deconvolutie probleem, wat ook het terugwinnen van meerdere metingen door vari erende naaldgatgroottes mogelijk maakt. Op basis van het experimenteel geverifieerde model laten simulaties van verschillende naaldgatgroottes zien dat de verstoring van de uitgangspupilfuncties door het eindige naaldgat gereconstrueerd kunnen worden met de voorgestelde hersteltechniek, met een reductie van de RMS golffrontfout tot 46%. De voorgestelde terugwintechniek is ge evalueerd met arbitraire aberraties gebaseerd op een model van biologische monsters en geeft een meetfout van 3 arbitraire eenheden (AU) bij het kleinere naaldgat van 1.5 AU, wat een nauwkeurige golffront meting toestaat met hogere optische doorsnede mogelijkheden.

Curriculum vitae

Han Woong (Hans) Yoo was born on October 23, 1980 in Seoul, Republic of Korea (South Korea). After finishing his high school diploma in 1999, he studied at Yonsei University in Seoul, Republic of Korea for the bachelor degree in Electrical and Electronic Engineering and received it in 2005. During the undergraduate study, he studied in Engineering Systems Laboratory at Aoyama Gakuin University in Kanagawa, Japan, under Prof. Ken Tomiyama's supervision, designing electronics and software for a prototype of the robot for health professionals. He continued his study in Electrical Engineering at Seoul National University in Seoul, Republic of Korea under the supervision of Prof. Wook Hyun Kwon. His master thesis is about receding horizon control of input delay systems based on linear quadratic and H_∞, and linear quadratic Gaussian costs, for which he received his master degree in 2007. After a short research program in Science & Technology Research Laboratories of Japan Broadcasting Corporation (NHK STRL) in Tokyo, Japan, he worked in Samsung Advanced Institute of Technology (SAIT) and Samsung Electronics co. LTD, semiconductor business in Gyunggido, Republic of Korea from 2007 to 2009. During his work, he conducted researches on low power digital front end for digital RF and operating algorithms for reliability of multi-level non-volatile memories.

In May 2010 Han Woong Yoo started his PhD project at Delft Center for Systems and Control (DCSC), Delft University of Technology, Delft, the Netherlands. As a part of "Integrated Smart Microscopy" project of STW, his PhD project mainly focus on the design of the optomechatronics and its control for fast and aberration-corrected imaging of confocal laser scanning microscopy. His PhD project was supervised by Prof.dr.ir. M. Verhaegen and Univ.Prof.Dr.sc.techn. Georg Schitter and collaborated with the other project members in Erasmus MC, Leica Microsystems, and Flexible Optical B.V. For the researches on fast scanning of the galvanometer scanner, he conducted his research in Automation and Control Institute (ACIN) at Vienna University of Technology, Vienna, Austria. In his work, his paper about automated coverslip correction in confocal laser scanning microscopy received Graduate Student Best Paper Award of the 2012 IEEE International Instrumentation and Measurement Technology Conference (I2MTC) the second place. He also supported lectures and lab sessions for MSc courses and supervised a master student during his PhD.

Since June 2014, Han Woong Yoo joined ACIN at Vienna University of Technology, Vienna, Austria. His main research interests are mechatronics systems, precision motion control, adaptive optics, and biomedical imaging.

List of Publications

Journal articles

- **H. W. Yoo**, S. Ito, M. Verhaegen, and G. Schitter. Iterative Learning Control of a Galvanometer Scanner for Fast and Accurate Scanning Laser Microscopy. Mechatronics, submitted.
- **H. W. Yoo**, M. E. van Royen, A. B. Houtsmuller, W. A. van Cappellen, M. Verhaegen, G. Schitter, "Automated spherical aberration correction in scanning confocal microscopy", Review of Scientific Instruments, Vol 85, No. 12, 123706, 2014.
- R. Paris, T. Thurner, T. Berndorfer, **H. W. Yoo**, G. Schitter, "Intelligente Kameras in der Messtechnik", Elektrotechnik & Informationstechnik, Vol 129, No.1, pp. 34-41, 2012
- **H. W. Yoo**, S. Han, Y. S. Lee, "Receding Horizon H_∞ Control for Input-Delayed Systems", Mathematical Problems in Engineering, A. id 927213, 2012
- **H. W. Yoo**, Y. S. Lee, S. Han, "Constrained Receding Horizon Controls for Nonlinear Time-delay Systems", Nonlinear Dynamics, Vol. 69, No. 1-2, pp. 149-158, 2012
- J. H. Park, **H. W. Yoo**, S. Han, W. H. Kwon, "Receding horizon control for input delayed systems", IEEE Transactions on Automatic Control, pp. 1746-1752, 2008

Conference proceedings

- **H. W. Yoo**, S. Ito, M. Verhaegen, G. Schitter, "Transformation-based Iterative Learning Control for Non-collocated Sensing of a Galvanometer Scanner. European Control Conference", pp. 1204-1209, July 17-19, Zürich, Switzerland, 2013,
- **H. W. Yoo**, S. Ito, M. Verhaegen, G. Schitter, "Iterative Learning Control of a Galvanometer Scanner for Fast and Accurate Scanning Laser Microscopy," in Mechatronics 2012, pp. 537-543, 17-19 Sep, Linz, Austria, 2012
- **H. W. Yoo**, M. Verhaegen, G. Schitter, "Automated adjustment of aberration correction in scanning confocal microscopy, IEEE International Instrumentation and Measurement Technology Conference, pp. 1083-1088, 13-16 May, Graz, Austria, 2012
- J. H. Park, **H. W. Yoo**, S. Han, W. H. Kwon, "Receding horizon control for input delayed systems", Decision and Control, 46th IEEE Conference on, pp. 1368-1373 12-14 Dec.USA , 2007
- **H. W. Yoo**, Y. Miyaji, K. Tomiyama, "Design of controller for the care-worker support robot: considering psychological safety issue" RoboMEC of JSME Conference on Robotics and Mechatronic, Nagoya, Japan 2004
- H. Takeuchi, T. Yanadori, N. Kiuchi, **H. W. Yoo**, Y. Miyaji, K. Tomiyama, "Construction of Care worker Support robot in terms of Virtual KANSEI", Proceedings of the 5th Annual Conference of JSKE, Tsukuba, Japan 2003

Patents, granted

- H. Son, **H. W. Yoo**, J. J. Kong, H. Eun, “Program method of multi-bit memory device and data storage system using the same”, US 8441862 B2
- H. Son, **H. W. Yoo**, J. Kim, J. J. Kong, “Flash memory device, memory system and method of operating the same”, US 8411510 B2
- H. Eun, J. H. Kim, J. Kim, D. H. Choi, S. H. Song, **H. W. Yoo**, J. J. Kong, Y. H. Lee, K. Cho, Y. J. Kim, “Flash memory device, program method and read method for the same”, US 8339846 B2
- **H. W. Yoo**, S. H. Song, H. Eun, J. J. Kong, “Nonvolatile memory device system, and related methods of operation”, US 8422307 B2
- **H. W. Yoo**, J. Kim, J. J. Kong, “Nonvolatile memory device and related programming method”, US 8284599 B2
- Y. J. Kim, H. Eun, **H. W. Yoo**, J. Kim, H. Son, “Storage device and method for reading the same”, US 8422291 B2
- Y. J. Kim, J. J. Kong J. Kim, **H. W. Yoo**, “Memory system and defective block management methods related thereto”, US 8417988 B2
- **H. W. Yoo**, J. Kim, J. J. Kong, “Methods of accessing storage device”, US 8310876 B2
- **H. W. Yoo**, S. H. Song, H. Eun, K. Cho, “Access method of nonvolatile memory device”, US 8503230 B2, CN 101847439 A
- **H. W. Yoo**, S. H. Song, H. Eun, J. Kim , “Non-volatile memory device and program method thereof”, US 8331144 B2
- **H. W. Yoo**, S. H. Song, J. J. Kong, J. Kim “Method of analyzing threshold voltage distribution in nonvolatile memory”, US 8116141 B2
- I. Kwon, J. Lee, **H. W. Yoo**, “Interference signal removing apparatus and receiving using the same”, US 8320582 B2

Thesis

- **H. W. Yoo**, “Receding horizon control for linear input delay systems”, Master thesis, Seoul National University, Seoul, Republic of Korea, 2007

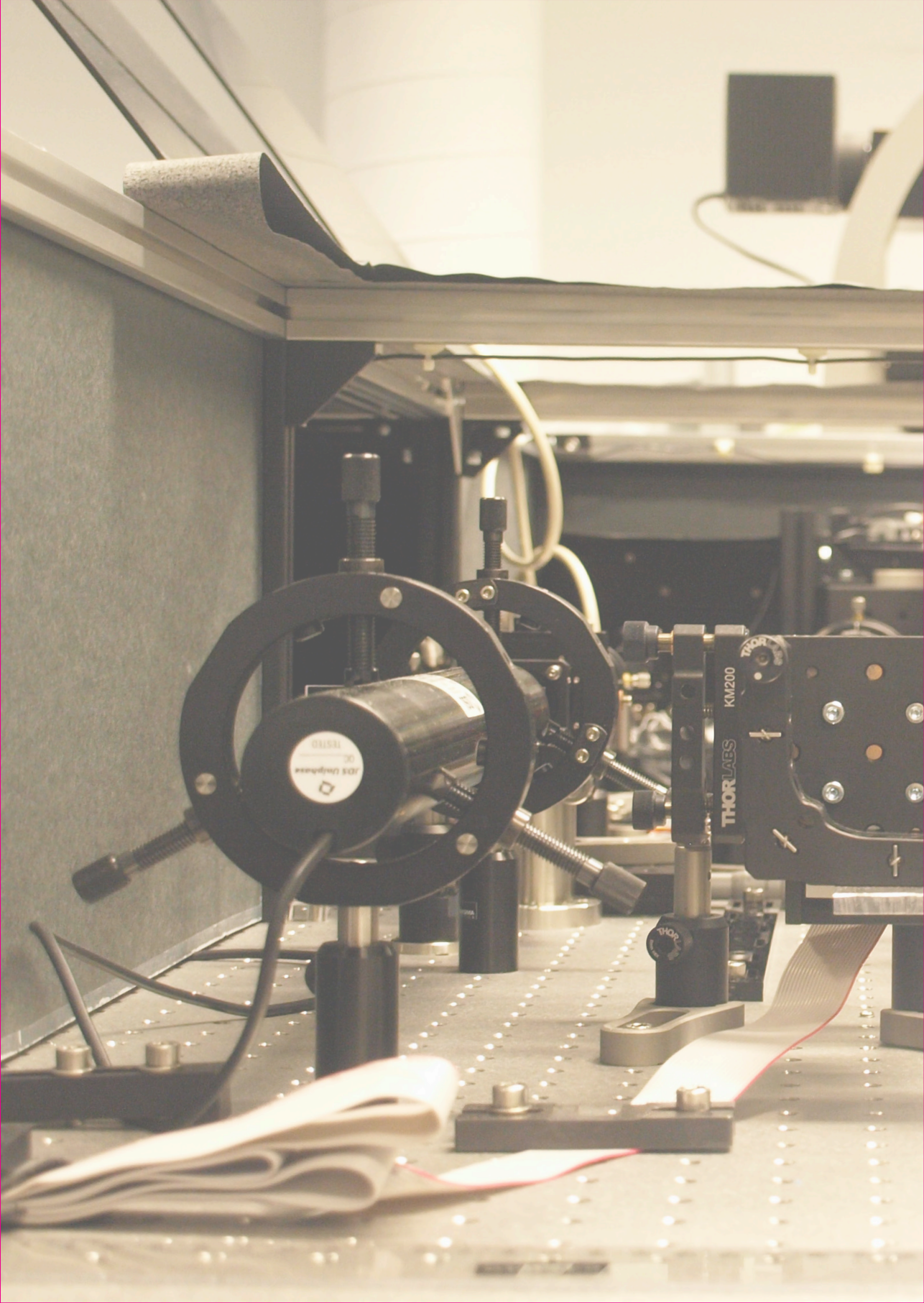
THORLABS
KM200